THE UNIVERSITY OF CHICAGO

MULTI-PRONGED STUDIES OF DIFFUSE HALO GAS AROUND MASSIVE QUIESCENT GALAXIES

A DISSERTATION SUBMITTED TO
THE FACULTY OF THE DIVISION OF THE PHYSICAL SCIENCES
IN CANDIDACY FOR THE DEGREE OF
DOCTOR OF PHILOSOPHY

DEPARTMENT OF ASTRONOMY AND ASTROPHYSICS

BY

FAKHRI SALEH ZAHEDY

CHICAGO, ILLINOIS

AUGUST 2019

To my dear parents, and to all curious minds...

TABLE OF CONTENTS

LIST OF FIGURES

LIST OF TABLES

ACKNOWLEDGMENTS

The past six years that I have spent pursuing my Ph.D at the University of Chicago have been a time of great professional and personal growth for me. I owe an enormous debt of gratitude to so many people, without whom none of this would have been possible.

Thank you foremost to my advisor, Hsiao-Wen Chen, who gave me the incredible opportunity to grow as an astronomer under her tutelage. I am very grateful that you took me on as your student six years ago, and since then it has been my great privilege to learn from you. I know no other scientist with as great a commitment to mentoring and as creative a scientific mind as you, and I am thankful for your wisdom, encouragement, and patience. I feel extremely lucky that we were able to work closely on many different projects, and I hope that you are proud of the work I have done with you. I relied on your guidance as a student, and I hope to continue to seek your advice in the future as your colleague and friend.

I am deeply indebted to Michael Rauch who offered his guidance and friendship during and after my visit to Carnegie. Michael, thank you for making sure that everything went smoothly during my visit, and I am grateful to you and your family for always making me feel at home in Pasadena. I would also like to thank the Carnegie staff for welcoming me as one of their own during my stay at Carnegie, especially John Mulchaey, Gwen Rudie, and Steve Shectman. I look forward to being your colleagues in the near future.

Thank you to Ann Zabludoff for her enthusiastic support and advice, especially during the past year. I am especially grateful for Ann's always thoughtful advice on the scientific contents, the presentation, and the writing of the papers we have worked on together.

I would like to thank the current and former members of my dissertation committee: Wendy Freedman, Nick Gnedin, Rich Kron, and Scott Dodelson. Thank you for serving in my committee, and I am grateful for your advice and guidance on this process.

I was fortunate to have shared my time in graduate school with the fantastic graduate students and other student researchers in the Astronomy & Astrophysics department, especially those I had the privilege to share an office with. Rebecca Diesing, Yun-Hsin Huang,

Sean Johnson, Cameron Liang, Rebecca Pierce, and Vadim Semenov, thank you for all the meaningful discussions, the shared laughs, and the times you all graciously provided to read the various drafts of my work over the years.

My time in Chicago would not have gone as smoothly as it has without the help of the staff at the Astronomy & Astrophysics department, especially Laticia Rebeles, Jennifer Smith, and Julia Brazas. I am particularly thankful to Laticia, who has done so much for me and my fellow graduate students over the years. I would also like to thank Valeri Galtsev for his always-excellent computing support and assistance.

As a Chicago graduate student, I was privileged to conduct astronomical observations at the Las Campanas Observatory in Chile, arguably the best astronomical research site in the world. I would like to thank the observatory staff, telescope operators for the Magellan twins, and instrumental specialists. Because of their excellent work, each of my many visits to these state-of-the-art telescopes was such an joyful experience. My dissertation also involved extensive observations using the Hubble Space Telescope. I am very grateful to the NASA astronauts who took such a good care of Hubble over its many servicing missions, and to the staff of the Space Telescope Science Institute who work tirelessly to ensure Hubble's continuing productivity for years to come.

I would like to acknowledge earlier scientific mentors of mine. I am thankful to the late Djuhana Widjajakusumah who kindly answered all the astronomy questions I had asked him during numerous phone calls almost two decades ago. Next, I would like to thank Hakim Malasan of ITB for his mentorship and support, and for his confidence in my abilities to pursue a higher education and career in astronomy. I am similarly grateful to Yohanes Surya for the excellent education he gave me in basic physics during the time I spent as a part of his physics olympiads team. Finally, I would like to acknowledge my undergraduate research mentors for introducing me to the world of astronomical research, which convinced me to pursue a Ph.D in astronomy. Thanks to MIT professors Jacqueline Hewitt and the late James Elliot for the mentorship and support they provided as my UROP advisors. I'd also

like to express my gratitude to Deidre Hunter for taking me on to work with her during the MIT Astronomy Field Camp at the Lowell Observatory, during which I first became exposed to extragalactic research.

I would like to express my deepest admiration and appreciation to the American people, who have welcomed me as a guest in this great country for the past ten years that I have spent pursuing my undergraduate and graduate studies. Your openness and kindness as a people made this transformative experience possible, and you will always have my friendship.

I am especially grateful for the constant support and love I have received from my family over the last six years and throughout my entire life. Thank you to my siblings *Kak* Ulma (and *Mas* Bayu) and Ihsan, I could not have done it all without you! I am thankful to Mpok Wati for caring for me over the years. Finally, no words can express how grateful I am for my parents, Destiana and Darwin. Mama and Papa, you have been the true constants in my life. The two of you nurtured in my childhood self the sense of wonder for the natural world and the joy of discovery. You always encouraged me to aim high and be my best possible self. You shared my joy when I succeeded, but you also picked me up when I failed, and for that I am grateful. Although we are often half a world away from each other and we do not get to spend much time together during the last few years, my sincerest hope is that I have done you proud with this effort and the person that I have become. I thank you most of all, and I dedicate this work to you.

The work presented in this dissertation was made possible by funding from The University of Chicago, the National Aeronautics and Space Administration, the Brinson Foundation and the Carnegie Institution for Science. I am grateful for the generous support from these institutions.

ABSTRACT

While significant progress has been made in galaxy formation studies in the past few decades, a self-consistent explanation for the diffuse gaseous halos (also known as the circumgalactic medium; CGM) surrounding galaxies still eludes us. Particularly puzzling is the high incidence of cool ($T \sim 10^4$ K) gas in the gaseous halos of massive quiescent galaxies, which is at odds with their lack of recent star-formation activity and the theoretical expectation that their diffuse baryons are predominantly hot. Characterizing the physical properties of the gaseous halos of massive quiescent galaxies is necessary to build an empirical understanding of the coevolution of galaxies and gas over cosmic time.

This dissertation is based on a series of observational studies that investigate the physical characteristics, origin, and fate of the gaseous halos of intermediate-redshift ($z \sim 0.5$) massive quiescent galaxies with stellar masses $M_{\rm star} \gtrsim 10^{11}{\rm M}_{\odot}$, using precision analysis of QSO absorption-line spectroscopy. Chapter 2 investigates the properties of cool gas in the vicinity (projected distances $d < 20$ kpc) of three massive quiescent lensing galaxies at $z = 0.4 - 0.7$. Whenever cool gas is detected, it exhibits a high and super-solar Fe/α abundance ratio, indicating that the inner gaseous halos of massive quiescent galaxies have been highly enriched by Type Ia supernovae (SNe Ia).

Chapter 3 examines how chemical compositions (specifically the Fe/α ratio) in the CGM depends on both distance from and star-formation history of the galaxy, using a sample of intermediate-redshift quiescent and star-forming galaxies probed by background QSO sightlines. The data show that passive galaxies exhibit higher Fe/α than star-forming galaxies at all radii in their CGM. Furthermore, the Fe/α ratio in the gaseous halos of passive galaxies declines with increasing distance. While super-solar Fe/α gas is common in the inner halo ($d \lesssim 50$ kpc), at larger distances ($d \gtrsim 100$ kpc) the gas is predominantly Fe-poor, consistent with gas originating from the intergalactic medium (IGM). These observations indicate that feedback by SNe Ia is relatively localized to the inner halos of passive galaxies.

Chapter 4 presents the first detection of extended neutral hydrogen (H I) gas in the

interstellar medium (ISM) of a massive elliptical galaxy beyond the local universe ($z = 0.4$), which subsequently allows the total mass of the cool ISM to be estimated. The mass of cool ISM is $\approx 5\%$ the inferred mass of the hot ISM ($T > 10^6$ K) in this galaxy, which implies the presence of an effective heating source in the ISM.

Chapter 5 presents a systematic investigation of the physical conditions and elemental abundances in the gaseous halos of massive elliptical galaxies at $z \sim 0.5$. Based on the results of a detailed ionization analysis of the observed gas, Chapter 5 finds that the CGM of massive elliptical galaxies is a multi-phase mixture of gasses with different physical origins and poor chemical mixing. Furthermore, the typical massive elliptical galaxy at $z \sim 0.5$ is surrounded by a significant mass of cool gas in its gaseous halo, $M_{\rm cool} \sim 10^{10}\,{\rm M}_{\odot}$, which is comparable in mass to the halo gas reservoirs of L^* star-forming galaxies. At the same time, the observed radial velocity dispersion of the cool gas clumps is sub-virial, which implies that the cool clouds and are subjected to dissipative interactions which cause them to fall toward the galaxy.

Chapter 6 moves to the high-redshift Universe ($z \approx 2.8$) to investigate the gaseous environment of three Lyα emitters (LAEs), the high-redshift precursors of today's luminous galaxies. Combined evidence from the observed elemental abundances, kinematics, and projected spatial alignment of the observed gas relative to the LAEs suggests the presence of an accretion stream of low-metallicity gas in the IGM which are likely feeding the growth of these galaxies.

This dissertation concludes in Chapter 7 with a discussion of the significant insights this work has provided into the gaseous environment of massive quiescent galaxies, the implications on future research, and work in progress investigating the multi-phase nature of the ISM of massive quiescent galaxies.

CHAPTER 1

INTRODUCTION

1.1 Prologue: a Brief Historical Context

The development of extragalactic science owed a great deal to the works of astronomers affiliated with the University of Chicago. During the early 20th century, George Ellery Hale played a central role in developing the largest reflecting telescopes of the day and establishing professional astronomy journals in the United States. Using one of these state-of-the-art telescopes, Edwin Hubble measured the distances to many known spiral nebulae and provided the first empirical evidence that these nebulae are in fact galaxies in their own right which are located far outside our own Milky Way Galaxy (Hubble 1926; 1929).

In the 1950s, Guido Münch discovered clouds of gas that appeared to be situated far (~ 1 kpc) above the Galactic disk, based on prominent absorption lines from neutral sodium (Na I) and singly ionized calcium (Ca II) ions they produced in the spectra of hot O- and B-stars at high Galactic latitudes (Münch & Zitrin 1961; see also York 1999). The presence of strong absorption from these low-ionization metal species indicate that the clouds are cool ($T \lesssim 10^4$ K) and dense ($n_{\rm H} \sim 10$ hydrogen atoms cm^{-3}). Moreover, the observability of these cool clouds implies that they are prevented from evaporation by pressure confinement, which motivated Spitzer (1956) to postulate that these cool clouds are embedded within a hot and diffuse ($T \sim 10^6$ K; $n_{\rm H} \sim 10^{-4}$ cm^{-3}) gaseous corona that surrounds the Galaxy.

The aforementioned studies by Münch and Spitzer illustrate the potency of absorption-line spectroscopy for detecting and characterizing intervening gas along the line of sight. This observational technique experienced its first revolution in the next decade, with the discovery of a class of blue point sources now known as quasi-stellar objects (QSOs). After Schmidt (1963) and Oke (1963) demonstrated that QSOs are extragalactic objects situated at large cosmological distances, researchers began exploring the possibility of using these high-redshift point sources to detect tenuous gas outside the local Universe (Bahcall & Salpeter

1965; 1966; Rees & Sciama 1966). Within a couple of years, researchers discovered that intervening absorption lines are a ubiquitous feature in the spectra of QSOs (e.g., Burbidge et al. 1966; Greenstein & Schmidt 1967; Bahcall et al. 1967). Bahcall & Spitzer (1969) proposed that a majority of these absorption lines are produced by diffuse gas in the extended gaseous halos surrounding galaxies.

The first associations between galaxies and QSO absorption-line systems would come about a decade later, when a number of studies identified galaxies with redshifts coincident with metal absorption species, specifically the Ca II $\lambda\lambda 3934, 3969$ and Mg II $\lambda\lambda 2796, 2803$ doublets previously detected in QSO spectra (e.g., Boksenberg & Sargent 1978; Boksenberg et al. 1980; Bergeron 1986). These authors noted the large projected distances between the QSO sightlines and the galaxies they identified, often far exceeding the size of the disk, which supported the extended halo scenario proposed by Bahcall & Spitzer (1969).

Since these pioneering works, the study of the diffuse gaseous halo surrounding galaxies (also known as the circumgalactic medium; CGM) has continued to rely on the absorption lines imprinted by the intervening gas in the spectra of bright background objects. The advent of the *Hubble Space Telescope* (*HST*) and large ground-based telescopes in the 1990s triggered a second revolution of the field by allowing systematic studies to characterize the extended gaseous halos of galaxies using large samples of background QSO-foreground galaxy pairs (e.g., Lanzetta et al. 1995; Steidel et al. 1997; Chen et al. 1998; 2001; 2010). Over the past two decades, the works of these astronomers and many others have gradually built a deeper understanding of the nature of diffuse gas within, around, and in between galaxies, and more importantly, the critical role that gas plays in galaxy evolution. This dissertation stands on the shoulders of these giants and continues their endeavors by probing the connection between gas and galaxies in a poorly understood regime: that of massive quiescent halos.

1.2 Major Problems of the Study of Galaxy Evolution

Modern cosmology epitomizes the triumph of the scientific method. A principal success of today's concordance cosmology, also known as the ΛCDM (Lambda Cold Dark Matter) model, is to explain and connect the observed large-scale structures of the present-day Universe, based on large spectroscopic surveys of galaxies, to the primordial density and temperature fluctuations in the infant Universe, based on the anisotropy in the power spectrum of the Cosmic Microwave Background (see a recent review by Bullock & Boylan-Kolchin 2017). The observed large scale properties of the Universe are consistent with a present-day Universe which is dominated by dark energy ($\approx 70\%$ of the energy budget) and cold dark matter ($\approx 25\%$ of the energy density), with ordinary matter or baryons constituting fewer than five percent of the energy density of the observable Universe (Planck Collaboration 2016). While significant success has been achieved in explaining the origin of large-scale structures ($\gtrsim$ 10 Mpc scales) and their evolution over more than 13 Gyr of cosmic time, major questions remain on physical processes acting on smaller scales. This smaller scale ($\lesssim$ 1 Mpc) is the realm of the astrophysics of galaxy formation and evolution.

In the ΛCDM paradigm, primordial matter overdensities grow over time, only to eventually collapse due to their self-gravity to form dark-matter halos. The initial fate of baryonic matter, being subdominant to dark matter in terms of mass, is to be dragged into the gravitational potential wells of dark matter halos. Over time, these accreted baryons cool radiatively and condense as they fall deeper into the center of a halo (Rees & Ostriker 1977; White & Rees 1978), eventually forming high-density gas clouds from which stars are born. The primary objective of galaxy evolution studies is to explain how such seemingly simple beginning—the conversion of gas into stars—results in the incredibly diverse population of galaxies observed across space and time. I will motivate this dissertation by outlining several major problems in galaxy evolution studies, and discussing how diffuse gas is inextricably linked to each one.

1.2.1 Why Do Galaxies Produce Significantly Fewer Stars Than Predicted by Cosmology?

During the 1990s, researchers performed cosmological N-body and semi-analytic calculations to simulate structure formation in the Universe, incorporating both gravitational physics and well-understood gas physics (e.g., radiative cooling, pressure gradients). The resulting simulated universes were found to contain too many low- and high-mass galaxies when compared to observations. Furthermore, the simulated galaxies had stellar masses which indicated that most of their host halos' baryons had been converted into stars (e.g. Cole 1991; Navarro & Benz 1991; Navarro & White 1994; Navarro et al. 1995). Observationally, it is well-established that star formation is a highly inefficient process on both sub-galactic and galactic scales, where only a small fraction of available baryons is converted to stars over Gyr timescales (e.g., Schmidt 1959; Kennicutt & Evans 2012). Therefore, the shortcomings of these simulations illustrate that their underlying calculations were based on incomplete physics, and that additional baryonic processes are necessary to suppress star formation in both high- and low-mass galaxies.

At the same time, a number of studies have been carried out to draw a connection between dark matter halos predicted in cosmological simulations and galaxies found in the observable Universe, by matching the expected abundance of dark matter halos of different masses with the observed stellar mass function of galaxies. These abundance-matching exercises assume a direct correspondence between the total stellar content of galaxies with the total mass of dark matter halos hosting them: more massive galaxies reside in higher-mass dark matter halos. The stellar-to-halo mass ratio is found to peak at halos hosting Milky Way-sized galaxies but rapidly decrease for both higher- and lower-mass halos (e.g., Moster et al. 2010; Guo et al. 2010; Behroozi et al. 2010, 2013; Kravtsov et al. 2018). While dark-matter halos of L^* galaxies like the Milky Way appear to be the most efficient at turning their gas into stars, even then only $\approx 20\%$ of the halo's expected baryon contents are locked up in stars. In contrast, halos hosting both massive super-L^* galaxies and dwarf sub-L^* galaxies are found

to have converted $\lesssim 5-10\%$ of their baryons into stars.

The strong mass dependence of a galaxy's mass-to-light ratio indicates that different physical processes are at play in galaxies of different masses to regulate star formation (e.g., Benson et al. 2003). These "feedback" mechanisms are thought to provide additional heating to reduce gas cooling in the halo and prevent the overproduction of stars. For low-mass halos, the low baryon fraction in stars has been attributed to inefficient cooling (Rees & Ostriker 1977), photoionization heating (Efstathiou 1992; Navarro & Steinmetz 1997), and feedback from core-collapse supernovae of massive stars (e.g., Dekel & Silk 1986; Cole et al. 2000).

For galaxies more massive than the Milky Way (those with halo masses of $M_{\rm h} \gtrsim 10^{12} M_{\odot}$), it is generally thought that feedback from supernova-driven winds alone is insufficient to prevent excessive cooling in the halo (e.g., Benson et al. 2003; Silk 2010). Instead, energetic feedback from active galactic nuclei (AGN) powered by supermassive black hole (SMBH) is often invoked to be responsible for quenching star formation, thereby explaining the decreased stellar-to-halo mass ratios in massive quiescent galaxies (e.g., Silk & Rees 1998; McNamara & Nulsen 2007; Benson et al. 2010; Kravtsov et al. 2018). This explanation is supported by the observed correlation between the mass of a galaxy's bulge and the mass of its central SMBH (e.g., Ferrarese & Merritt 2000; Gebhardt et al. 2000; Sahu et al. 2019), which suggests a coevolutionary relationship between galaxies and SMBHs. However, direct observations of AGN feedback on scales of galaxy halos ($\sim$ 100 kpc) have proven to be challenging in all but a few extreme cases (see Fabian 2012 for a recent review of the observational efforts). Alternative feedback mechanisms have also been proposed, including gravitational heating (e.g., Johansson et al. 2009) and heating from evolved stellar populations (e.g., Conroy et al. 2015), but empirical constraints remain scarce.

1.2.2 Where Are the Rest of the Baryons, and What Are They Doing?

It has been estimated that stars and interstellar gas account no more than $\sim$ 10 percent of the cosmological baryon budget in the present-day Universe (e.g., Persic & Salucci 1992;

Fukugita et al. 1998; Fukugita 2004; Fukugita & Peebles 2004). If a majority of baryons are not locked into stars or gas within galaxies, where are they and what are their physical conditions? There are several possible answers to this question.

The first possibility is that most baryons have not been incorporated into galaxy halos to begin with, and they remain in the intergalactic medium (IGM) instead. While observations of the Lyman-alpha (Lyα) forest indicate that this is the case at high redshifts ($z > 2$, e.g., Rauch et al. 1997; Weinberg et al. 1997; Rauch 1998), where as much as 90% of the cosmic baryons are accounted for in the form of cool ($T \sim 10^{4-5}\,\mathrm{K}$) intergalactic gas, the cool IGM's share of the cosmic baryon budget appears to be a factor of two to three lower in the local Universe (e.g., Penton et al. 2004 ; Lehner et al. 2007; Shull et al. 2012). Another possibility is that a large fraction of baryons were once accreted into overdense regions, but they had subsequently been heated and possibly expelled out of halos due to accretion shocks and feedback from galaxies, and they now reside in a warm-hot phase of the IGM (WHIM; e.g., Cen & Ostriker 1999, 2006; Davé 2001; Bregman 2007). However, detecting WHIM is extremely challenging due to the expected low densities and high temperatures ($T \sim 10^{5-7}\,\mathrm{K}$; $n_\mathrm{H} < 10^{-4}\,\mathrm{cm}^{-3}$) of the gas, and robust constraints on their baryonic content remain lacking today (McQuinn 2016).

The final scenario is that baryons reside within dark matter halos, but unlike interstellar gas they are too diffuse and therefore difficult to detect in emission. This circumgalactic medium (CGM), commonly defined to be the space enclosed within the virial radius of the dark matter halo (e.g., Chen 2017; Tumlinson et al. 2017), is the interface between galaxies, where star formation takes place, and the IGM, where a majority of baryons are situated at high redshifts. Due to its unique location, the CGM is expected to be strongly influenced by the complex interplay between gas accretion from the IGM, feedback processes originating from galaxies, and interactions among different galaxies. For that reason, characterizing the CGM of different populations of galaxies at both low and high redshifts is a promising avenue to build an empirical understanding of how the flow of diffuse baryons in and out of

galaxies drives galaxy evolution over cosmic time.

1.2.3 How Do Massive Quiescent Galaxies Become and Stay Red and Dead?

Among different populations of galaxies, massive quiescent galaxies present some of the most perplexing problems in galaxy evolution studies. These massive galaxies, with total stellar masses of $M_{\rm star} \gtrsim 10^{11} M_{\odot}$ and total halo masses including dark matter of $M_{\rm h} \gtrsim 10^{13} M_{\odot}$, consist of predominantly old ($\gtrsim$ 5 Gyr) stellar populations (e.g., Caldwell et al. 2003; Roseboom et al. 2006; Tojeiro et al. 2011). Unlike disk galaxies, massive elliptical galaxies show little ongoing star formation and appear to have been quiescent since as early as $z \sim 1$ (e.g., Ferreras et al. 2009). The quiescent nature of massive ellipticals leads to their common characterization as "red and dead."

A natural explanation for the quiescence of elliptical galaxies is that they are devoid of cool gas which is needed to sustain star formation (e.g., Kereš et al. 2005; 2009). Theoretical studies suggest that the gaseous halos of massive ellipticals remain hot at close to the virial temperature ($T \sim 10^{6-7}$ K), because cooling is impeded by the feedback mechanisms thought to be responsible for the decreased stellar-to-halo mass ratios in these massive halos (see Section 1.2.1). This physical picture is supported by the near-ubiquity of X-ray emitting gas observed around nearby ellipticals.

Contrary to theoretical expectations, systematic surveys of 21-cm and sub-mm emissions around local elliptical galaxies have revealed significant amounts of cool atomic and molecular gas around approximately a third of nearby ellipticals (e.g.,Young et al. 2011; Serra et al. 2012; Davis et al. 2016). While some evidence suggests that at least some of the gas may originate from recent galaxy mergers (e.g., Davis et al. 2019), the physical origin and fate of the gas is largely unknown.

Beyond the nearby universe, we know little about the cool interstellar gas properties of massive quiescent galaxies. However, absorption-line surveys against background QSOs

have uncovered a widespread presence of cool ($T \sim 10^4$ K), chemically enriched gas on 100-kpc scales in the gaseous halos around distant massive ellipticals at redshifts $z \sim 0.5$ (e.g., Gauthier et al. 2009, 2010, 2011; Lundgren 2009; Bowen & Chelouche 2011; Huang et al. 2016). These findings are based on observations of Mg II absorption in the gaseous halos of large number of massive quiescent galaxies discovered by the Sloan Digital Sky Survey (SDSS; York et al. 2000). In principle, the observed cool CGM gas at $z \sim 0.5$ could be a precursor of the colder and denser neutral ISM observed in present-day ellipticals. However, the continuing lack of significant star formation activity in massive ellipticals over the last $5 - 10$ Gyr of cosmic time is clearly at odds with this scenario.

The presence of significant gas reservoirs in the gaseous halos of massive ellipticals challenges the expectation that the absence of star formation is directly caused by a dearth of cool gas supply. More importantly, it underscores our incomplete understanding of galaxy formation, in particular how the interplay of accretion and feedback regulates star formation on galactic scales over time.

1.3 This Dissertation: Multi-Pronged Studies of Diffuse Halo Gas around Massive Quiescent Galaxies

Existing body of research shows that diffuse gas surrounding galaxies is involved in a number of major problems of galaxy evolution studies, as outlined in the previous section. Solving these problems necessitates an empirical understanding of the relationship between galaxies and their gaseous halos, and how they coevolve over time. Doing so, however, requires knowledge of not only the incidence and extent of the gaseous halos around galaxies, but also the detailed physical conditions of the gas, including its thermal state, ionization state, and chemical enrichment.

This dissertation presents the results from observational studies I have conducted to characterize the gaseous halos of intermediate-redshift ($z \sim 0.5$) massive quiescent galaxies

with $M_{\rm star} \gtrsim 10^{11} M_{\odot}$. These studies share a common theme of investigating the chemical enrichment of the gas using absorption spectroscopy of neutral hydrogen and different ionic metal features that probe the halo gas under different thermal and ionization conditions. The emphasis on elemental abundances in the gaseous halos is motivated by the simple fact that hydrogen is a primordial element that constitutes the bulk of baryons, whereas metals are produced by stars within galaxies. Consequently, the chemical enrichment level and elemental abundance pattern in the gaseous halo are expected to be particularly sensitive to the interactions between accretion from the IGM and feedback and other physical processes within galaxies.

The focus on massive quiescent galaxies is motivated by several reasons. First, characterizing the physical conditions in the gaseous halos of quiescent galaxies is the first step toward reconciling the well-established presence of cool gas in the gaseous halos of a significant fraction of both local and distant elliptical galaxies (Section 1.2.3) with the persistent lack of star-formation activity in these galaxies over cosmic time. Secondly, the strong clustering of these passive galaxies indicate that they reside in massive dark-matter halos of $M_{\rm h} \gtrsim 10^{13} M_{\odot}$. Because a large majority ($\gtrsim 80\%$) of galaxies with $M_{\rm star} \gtrsim 10^{11} M_{\odot}$ are quiescent in the present-day Universe (e.g., Peng et al. 2010), characterizing the CGM properties of the massive ellipticals will bear significantly on our overall understanding of both the feedback processes in and the baryonic contents of massive halos in general (see Sections 1.2.1 and 1.2.2). Finally, empirical information on the physical properties of the gas will facilitate future quantitative comparisons between observations and theoretical predictions on the gas content of massive dark matter halos, a hitherto unchartered territory.

Taken together, the following chapters form the first comprehensive study of the physical properties and chemical enrichment in massive halos beyond the local Universe, and they offer new insights into the origin and fate of the gaseous halos of massive galaxies, as well as the dominant feedback mechanisms in massive halos. Chapter 2 presents a detailed study of gas kinematics and chemical abundance ratios in the inner halos (projected distances

$d \lesssim 20$ kpc) of massive elliptical galaxies, based on multi-sightline absorption spectroscopy of three massive elliptical lens galaxies at $z = 0.4 - 0.7$. Chapter 3 investigates how chemical compositions (specifically the Fe/α ratio) in the cool CGM depend on both distance from and star-formation history of the galaxy, using a sample of 27 intermediate-redshift quiescent and star-forming galaxies probed by background QSO sightlines. Chapter 4 presents the first detection of extended neutral hydrogen (H I) gas in the interstellar medium (ISM) of a massive elliptical galaxy beyond the local universe ($z = 0.4$), and investigates the elemental abundances and the mass budget of the cool ISM. Chapter 5 presents a systematic investigation of the physical properties and elemental abundances in the CGM within $d < 160$ kpc of 16 massive elliptical galaxies at $z \sim 0.5$, to shed light on the origin and fate of cool gas in the gaseous halos of massive elliptical galaxies. Moving to the high-redshift Universe, Chapter 6 investigates the gaseous environment of three Lyα emitters at $z \approx 2.8$, and infers the presence of accreting gas from the IGM based on the observed elemental abundances, kinematics, and spatial alignment of the gas relative to the Lyα emitters. Finally, in Chapter 7 I highlight ongoing work and outline future research in the topic.

CHAPTER 2

PROBING THE COOL INTERSTELLAR AND CIRCUMGALACTIC GAS OF THREE MASSIVE LENSING GALAXIES AT $z = 0.4 - 0.7$

The contents of this chapter were previously published in the Monthly Notices for the Royal Astronomical Society as Zahedy, F. S., Chen, H.-W., Rauch, M., Wilson, M. L., & Zabludoff, A. 2016, MNRAS, 458, 2423. They are reproduced here in accordance with the copyright agreement and with permission from the Oxford University Press.

2.1 Introduction

For over two decades, QSO absorption spectroscopy has provided a sensitive probe of low-density intergalactic gas, circumgalactic medium (CGM), and interstellar medium (ISM) which are otherwise too diffuse to be detected in emission beyond the local universe (e.g., Verheijen et al. 2007). Traditionally, the physical properties of the extended gas around galaxies, such as spatial extent, mean covering fraction, and total mass content, are characterized using a statistical approach over an ensemble of projected galaxy–background QSO pairs. This approach has yielded statistically significant constraints for the chemically-enriched CGM around both star-forming and quiescent galaxies based on searches of strong absorption transitions, including the Mg II $\lambda\lambda$ 2796, 2803 absorption doublet (e.g., Bowen et al. 1995; Chen et al. 2010; Lovegrove & Simcoe 2011; Kacprzak et al. 2011) and the hydrogen Lyman series (e.g., Lanzetta et al. 1995; Chen et al. 1998; Tripp et al. 1998; Rudie et al. 2013; Tumlinson et al. 2013; Liang & Chen 2014; Johnson et al. 2015). In contrast, absorption-line observations of diffuse gas in interstellar space have been limited because the ISM of distant galaxies has a much smaller cross section and closely projected QSO and galaxy pairs are rare.

Despite significant progress in characterizing the CGM, the origin of cool, metal-enriched

gas around galaxies remains ambiguous. Possible mechanisms to produce cool gas in a hot halo include outflows from super-galactic winds (e.g., Murray et al. 2011; Booth et al. 2013), stripped satellites due to tidal interactions or ram pressure (e.g., Wang 1993; Agertz et al. 2009; Gauthier 2013), gas accreted from the intergalactic medium (IGM, e.g., Rauch et al. 1997; Nelson et al. 2013), as well as in-situ cloud formation from thermal instabilities (e.g., Mo & Miralda-Escude 1996; Maller & Bullock 2004; Sharma et al. 2012).

A number of CGM observations targeting star-forming galaxies have suggested that one or a combination of the above scenarios are at play, such as outflows (Bordoloi et al. 2011) or a combination of outflowing and infalling gas (e.g., Bouché et al. 2012; Kacprzak et al. 2012). These findings have been based on a simple assumption that outflows occur along the rotation (minor) axis, while accretion proceeds along the disk plane (major axis). However, complications arise when considering the required energetics to drive the observed velocity field of the gas (e.g., Gauthier & Chen 2012) and possible spin-filament alignment with the cosmic web (e.g., Tempel et al. 2013) which, in the absence of galactic-scale outflows, would also give rise to an elevated incidence of absorbers along the minor axis of disk galaxies.

To better discriminate between different scenarios for the origin of metal-line absorbers, both spatially resolved gas kinematics and knowledge of galaxy star formation history are necessary. As shown in multi-wavelength imaging observations of local starburst galaxies (e.g., Suchkov et al. 1996; Cecil et al. 2001), stronger constraints for gas flows in galactic halos can be obtained from the observed spatial variations in the velocity field and physical conditions of the gas. In a pilot project, Chen et al. (2014) also demonstrated that multi-sightline observations of the CGM using a quadruply-lensed QSO, coupled with high resolution imaging of the associated galaxies, enable direct measurements of the velocity gradient and coherence length of the absorbing gas. In turn, these measurements provide critical constraints for distinguishing between different gas flow models.

An added advantage of studying lensed QSO fields is the opportunity of probing distant ISM by targeting the lensing galaxies. In this chapter, we apply three multiply-lensed QSOs,

HE 0047−1756, HE 0435−1223, and HE 1104−1805, to study the inner halo gas content of their lensing galaxies at $z = 0.4 - 0.7$. By targeting the lensing galaxies, our study focuses on the cool gas around massive, early-type galaxies (e.g., Keeton et al. 1998). These galaxies exhibit optical colors and spectral features that are characteristic of nearby elliptical galaxies. Although these evolved galaxies exhibit little/no on-going star formation, they are not all devoid of cold gas. Systematic H I and CO searches have uncovered a non-negligible amount of neutral gas in roughly 40% of nearby ellipticals (e.g., Oosterloo et al. 2010; Young et al. 2014), suggesting that some feedback processes are in effect to prevent continuing star formation in these gas-rich quiescent galaxies (e.g., McNamara & Nulsen 2007; Conroy et al. 2015). In addition, morphologies of the detected neutral gas span a broad range, from regular disk- or ring-like structures to irregular distributions of clumps and/or streams (e.g., Oosterloo et al. 2007; Serra et al. 2012) with roughly 1/4 displaying centralized disk or ring-like structures (Serra et al. 2012). These different morphologies indicate possibly different origins of the gas in different galaxies, including left-over materials from previous mergers and newly accreted gas from the CGM/IGM. These gas-rich, quiescent galaxies therefore provide an important laboratory for studying the physical processes that regulate/terminate star formation in the presence of cold gas in massive galaxies.

Incidentally, QSO absorption-line spectroscopy carried out in the vicinities of red galaxies at intermediate redshift, $z \sim 0.5$, continues to uncover extended cool halo gas to projected distances beyond $d \approx 100$ kpc (e.g., Gauthier et al. 2009, 2010; Bowen & Chelouche 2011; Thom et al. 2012; Huang et al. 2016), demonstrating that there may indeed be sufficient supplies of cool gas in these massive quiescent halos. Absorption spectroscopy along multiple sightlines in the vicinities of lensing galaxies is particularly interesting, because the small projected distances of these lensed QSO sightlines from the lensing galaxies at $d = 3 - 15$ kpc (or $d = 1 - 2\,r_e$) provide an unprecedented opportunity to probe and spatially resolve the cool gas content both in the interstellar space and in the halos of quiescent galaxies.

The fields are chosen because of the available high-quality optical and near-infrared imag-

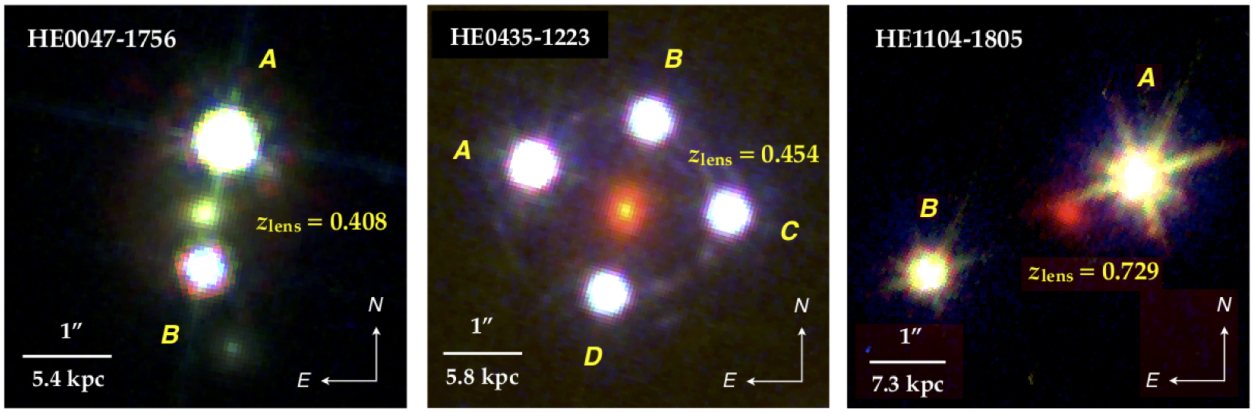

Figure 2.1: False color composite images of three gravitational lens systems in our study. The composite images were produced using the HST/ACS WFC and the F555W and F814W filters and NICMOS and the F160W filter for HE0047−1756, HST/WFC3 UVIS channel and the F275W filter and ACS WFC and the F555W and F814W filters for HE 0435−1223, and HST/WFC3 UVIS channel and the F275W filter and WFPC2 and the F555W and F814W filters for HE 1104−1805 (see Table 2.1 for details). The imaging data were retrieved from the HST data archive (see Section 2.2.1 for descriptions). For each system, the lensing galaxy is located at the center of each panel with the horizontal bar in the lower-left corner indicating the 1″ angular scale and the corresponding physical distance at the redshift of the lens. Using absorption spectra of the lensed QSOs, we are able to probe halo gas around the lens on projected distance scales of $d \sim 3 - 15$ kpc across the center of each lensing galaxy. Note that the lensing galaxy of HE 0047−1756 exhibit consistently red colors as those of HE 0435−1223 and HE 1104−1805 (see Tables 3 & 4). The available F275W images for the fields around HE 0435−1223 and HE 1104−1805 provide strong contraints for a lack of young stars in these lensing galaxies. As a result, the lensing galaxies appear to be red in the composite images that include the F275W band. However, an UV image is not available for the field around HE 0047−1756. Including available optical and NIR images results in the apparent bluer color of this lensing galaxy.

ing data in the *Hubble Space Telescope* (*HST*) archive, which enable a detailed morphological study of galaxies near the QSO sightlines. In addition, we have targeted relatively wide-separation gravitational lens systems with angular separations $\theta \gtrsim 1.5''$ and relatively bright lensed QSO images with g-band magnitude of $g \lesssim 19.5$. These selection criteria are chosen to facilitate high-resolution echelle spectroscopy of the lensed QSOs on the ground. The wide separation ensures that the lensed QSO images are not blended under typical sub-arcsecond seeing conditions on the ground, allowing these lensed QSO images to serve as independent probes of the foreground CGM at multiple locations. The brightness limit ensures a relatively high observing efficiency of QSO echelle spectroscopy under limited observing resources.

As described in Section 2.2.3 below, all three lensing galaxies presented here are old and massive with stellar masses in the range of $\log\, M_{\rm star}/M_{\odot} = 10.9 - 11.4$. The available QSO echelle spectra cover a spectral range from ≈ 3300 Å to beyond 6000 Å, which allow us to search for absorption features due to Fe II, Mg II, Mg I, and Ca II transitions at the redshift of each lensing galaxy. These transitions are commonly seen in the diffuse interstellar and circumgalactic gas of temperature $T \sim 10^4$ K in the Milky Way and in distant galaxies (e.g., Savage & Sembach 1996; Rao et al. 2006). The presence of such cool gas, together with the expected presence of a hot X-ray emitting halo around massive elliptical galaxies (e.g., O'Sullivan et al. 2001), would indicate a multiphase nature of extended gas around these lensing galaxies. The observed velocity gradient across the lensing galaxy, together with the relative abundance pattern between different ions, also offers a unique opportunity to directly test the origin of the observed cool gas in these massive, quiescent halos.

This chapter is structured as follows. In Section 2.2, we describe relevant imaging and spectroscopic observations and data reduction. In Section 2.3, we describe the empirical properties that can be extracted from available imaging and spectroscopic data. Specifically, we summarize the general observable quantities of the lensing galaxies in Section 2.3.1 and absorbing gas properties in Section 2.3.2. Observational findings of individual fields are presented in Section 2.4, and analysis of absorbing gas properties, including the ionization

state, chemical abundance pattern, and spatial coherence in gas kinematics, is presented in Section 2.5. We discuss the implications for the origin of chemically-enriched cool gas near massive, quiescent galaxies in Section 2.6, and present a summary of our findings/conclusions in Section 2.7. We adopt a Λ cosmology, $\Omega_{\rm M} = 0.3$ and $\Omega_{\Lambda} = 0.7$, with a Hubble constant $H_0 = 70$ km s^{-1} Mpc^{-1} throughout the chapter. All magnitudes and colors reported here are in the AB system.

2.2 Observations and Data Reduction

The study presented in this chapter focuses on three multiply-lensed QSO fields, HE 0047−1756, HE 0435−1223, and HE 1104−1805, with the lensing galaxies identified at $z = 0.4 - 0.7$. Figure 2.1 shows the lensing configurations of these fields. The relatively wide separation ($\theta_{\rm lens} \gtrsim 1.5''$) enables the application of these lensed QSO images as independent probes of the inner gaseous halo around each of the lensing galaxies based on QSO absorption spectra obtained on the ground. Here we describe relevant imaging and spectroscopic data of the lensing galaxies, as well as echelle spectroscopy of the lensed QSOs.

2.2.1 Imaging Observations

Exquisite optical and near-infrared images of the lensed QSO fields were retrieved from the *Hubble Space Telescope* (HST) data archive. Details of the imaging observations are summarized in Table 2.1. All imaging data were processed using the standard HST reduction pipeline, and individual dithered exposures were drizzle-combined using the AstroDrizzle package in each bandpass. Given slight differences in WCS solutions between different bandpasses, the co-added images were then registered to a common origin using point sources in each field. In Figure 2.1 we show false color composite images of the three lens systems, where it can be seen that at the redshift of each lens, absorption spectroscopy of the lensed QSOs allows us to probe the gaseous halo on projected distance scales of $d \sim 3 - 15$ kpc

Table 2.1: Journal of imaging observations with the HST

Field	Instrument	Filter	Exptime (s)	PID	PI
HE 0047−1756	ACS-WFC	F555W	670	9744	C. Kochanek
	ACS-WFC	F814W	670	9744	C. Kochanek
	NICMOS	F160W	2620	9744	C. Kochanek
HE 0435−1223	WFC3-UVIS	F275W	11360	11732	C. Kochanek
	ACS-WFC	F555W	760	9744	C. Kochanek
	ACS-WFC	F814W	1440	9744	C. Kochanek
	WFC3-IR	F160W	9580	12889	S. Suyu
HE 1104−1805	WFC3-UVIS	F275W	12620	11732	C. Kochanek
	WFPC2-PC	F555W	9600	9138	C. Impey
	WFPC2-PC	F814W	8500	9138	C. Impey
	WFC3-IR	F160W	14380	12889	S. Suyu

from the center of each lensing galaxy.

2.2.2 Galaxy Spectra

Optical spectra of two of the lensing galaxies, HE 0047−1756 and HE 0435−1223, were published in Eigenbrod et al. (2006), and kindly made available to us by F. Courbin. A brief description of the spectroscopic observations and spectra extraction is provided here.

The low-resolution spectra ($R \equiv \lambda/\Delta\lambda = 210$ at 5900 Å) of the lenses were obtained using the FOcal Reducer and low dispersion Spectrograph (FORS1) mounted on the European Southern Observatory Very Large Telescope (ESO/VLT). The observations were carried out using a $1''$ slit under mean seeing conditions of FWHM $\approx 0.5" - 0.6"$. Due to a significant amount of contaminating light in the galaxy spectra from the lensed QSO images, Eigenbrod et al. (2006) employed a spectral deconvolution algorithm to optimally extract the spectrum of the lensing galaxy. These authors applied the wavelength dependent spatial profiles of known stellar (PSF) sources to deconvolve the observed two-dimensional spectra of both the lensing galaxy and the lensed QSO based on their known relative positions along the slit. The extracted galaxy spectra show minimal residual presence of broad emission features expected from the QSO, demonstrating the success of the spectral deconvolution algorithm

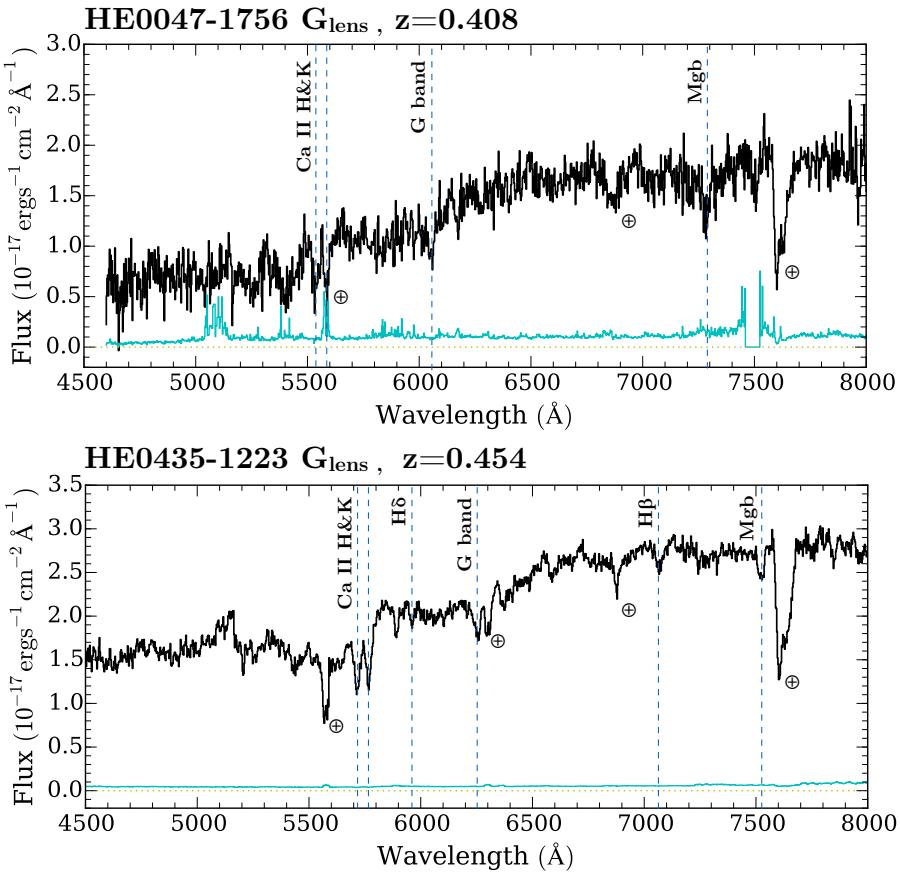

Figure 2.2: Optical spectra of the lensing galaxies of HE 0047−1756 (top panel) and HE 0435−1223 (bottom panel) at respective redshifts of $z = 0.408 \pm 0.001$ and $z = 0.454 \pm 0.001$ from Eigenbrod et al. (2006). The corresponding 1-σ error spectrum of each galaxy is shown in cyan above the zero flux line (dotted line). The galaxy spectra are dominated by prominent absorption lines such as Ca II H&K, G-band, and Mg b as by dashed lines. Night-sky absorption bands and emission line residuals are also marked by an earth symbol.

employed by Eigenbrod et al. (2006). Flux calibrations of the galaxy spectra were performed using the same PSF stars adopted in the deconvolution routine. Wavelengths were calibrated to air.

These optical spectra allow us to check the redshifts of the galaxies based on vacuum wavelengths, providing the rest frame necessary for studying halo gas kinematics using QSO absorption spectroscopy, and to characterize the stellar population and star formation history based on various line indices. We present in Figure 2.2 the extracted spectra of the lensing galaxies for HE0047−1756 in the top panel and for HE0435−1223 in the bottom

panel, along with their corresponding 1-σ error spectra. Both spectra show the prominent absorption features such as Ca II H&K doublet, G-band, and Mg b, and a strong 4000-Å spectral discontinuity that are characteristic of a quiescent galaxy with no trace of on-going star formation. Using a cross-correlation analysis with model spectra constructed from the eigen spectra of the Sloan Digital Sky Survey (SDSS) spectroscopic galaxy sample (e.g. Chen et al. 2010), we estimate the redshift of the lensing galaxy at $z = 0.408 \pm 0.001$ for HE 0047−1756, consistent with previous measurements of Eigenbrod et al. (2006) and Ofek et al. (2006). The lens redshift of HE 0435−1223 was estimated to be $z = 0.454 \pm 0.001$, consistent with the measurements of Eigenbrod et al. (2006) and Morgan et al. (2005). The redshift accuracy is clearly limited by the spectral resolution and the broad absorption width of available spectral features.

We do not have the optical spectrum of the HE 1104−1805 lens and therefore adopt the published redshift of $z = 0.729 \pm 0.001$ from Lidman et al. (2000) as the rest frame of the galaxy in the subsequent analysis.

2.2.3 QSO Echelle Spectroscopy

High-resolution echelle spectra of the doubly lensed QSO HE 0047−1756 and the quadruply-lensed QSO HE 0435−1223 were obtained using the MIKE echelle spectrograph (Bernstein et al. 2003) on the Magellan Clay Telescope. Following Chen et al. (2014), echelle spectroscopic observations were carried out in the fall semester of 2013 using a $1''$ slit and an aggressive binning of 2×4 (spatial $\times$ spectral) during readout to increase observing efficiency of these relatively faint QSOs. The mean seeing conditions over the observing period were $\approx 0.5'' - 0.7''$. The observing setup delivers a spectral resolution of FWHM ≈ 12 km s^{-1} over the spectral range from $\lambda = 3200$ Å to $\lambda = 1\,\mu$m. While the heavy binning does not allow us to fully resolve individual resolution components, it is sufficient to resolve velocity structures on scales as small as ~ 10 km s^{-1}. A summary of MIKE observations is presented in Table 2.2.

Table 2.2: Journal of QSO echelle spectroscopy

QSO Image	$z_{\rm em}$	Instrument	Exptime (s)	Date
HE 0047−1756 A	1.676	MIKE	7200	2013/11
HE 0047−1756 B	1.676	MIKE	5700	2013/11
HE 0435−1223 A	1.689	MIKE	5400	2013/11
HE 0435−1223 B	1.689	MIKE	5400	2013/11
HE 0435−1223 C	1.689	MIKE	10800	2013/11
HE 0435−1223 D	1.689	MIKE	10800	2013/10
HE 1104−1805 A	2.305	HIRES	19300	1997/02
		UVES	19000	2001/06
HE 1104−1805 B	2.305	HIRES	51200	1997/02
		UVES	19000	2001/06

The MIKE spectra were reduced using a custom data reduction pipeline described in Chen et al. (2014). In summary, each raw spectral image was bias-subtracted and corrected for pixel-to-pixel variations using twilight flats obtained through a diffuser. A ThAr comparison frame, obtained immediately following every science exposure, was used to create a two-dimensional wavelength map, which was corrected to vacuum and heliocentric wavelengths. For each echelle order, the QSO spectrum was optimally extracted using a Gaussian profile that matched the spatial profile of the QSO. To prevent possible contamination from neighboring QSO images (in the case of HE 0435−1223) that were rotated into the slit during individual exposures, we made sure to mask the trace of neighboring objects during the spectral extraction procedure. Relative flux calibrations were performed using a sensitivity function determined from observations of a spectrophotometric standard star taken during the same night as the QSO observations. Individual flux-calibrated echelle orders from different exposures were co-added and combined to form a single continuous spectrum per QSO image. Finally, the combined spectrum was continuum normalized using a low-order polynomial function that fits the spectral regions free of strong absorption features. In the spectral region around the systemic redshifts of the lensing galaxies, the mean S/N per resolution element is found to be $\approx 20 - 50$ for the two QSO images of HE 0047−1756, and

$S/N \approx 10 - 15$ per resolution element for all four images of HE 0435−1223.

High-resolution echelle spectra of the doubly lensed QSO HE 1104−1805 were obtained using High Resolution Echelle Spectrometer (HIRES; Vogt et al. 1994) on the Keck I Telescope. The observations were carried out in February 1997 (Rauch et al. 2001) using a $0.86''$ slit that delivered a spectral resolution of FWHM $\approx$ 6.6 km s^{-1} over the spectral range from $\lambda = 3600$ Å to $\lambda = 6100$ Å. Additional echelle observations of the QSOs were obtained using the VLT UV-Visual Echelle Spectrograph (UVES) in June 2001 (Lopez et al. 2007) and kindly provided to us by Dr. Sebastián López. The final combined spectra cover a wavelength range from $\lambda = 3050$ Å to $\lambda = 6850$ Å with a spectral resolution of FWHM $\approx$ 6.7 km s^{-1}. The mean S/N for image A is $S/N \approx 80$ per pixel and $S/N \approx 50$ per pixel for image B. Comparisons of absorption line profiles between the continuum normalized HIRES and UVES spectra show excellent agreement between the two datasets. The additional UVES spectra offer coverage for the Ca II λ3934 absorption transition at the redshift of the lensing galaxy. A summary of the HIRES and UVES observations is also included in Table 2.2.

2.3 Lensing Galaxy and Absorbing Gas Properties

A principal goal of our multi-sightline study is to examine whether/how spatially resolved halo gas kinematics from high-resolution QSO absorption spectroscopy correlate with the observed properties of the lensing galaxy. In this section, we describe the galaxy properties and halo gas absorption properties that were extracted from the data described in Section 2.2.

2.3.1 Galaxy Properties

The available imaging and spectroscopic data of the lensing galaxies described in Section 2.2.1 and Section 2.2.2 allow us to examine in detail their optical morphologies and stellar population, thereby constraining the stellar structure and star formation history.

To analyze the morphologies of the lensing galaxies, we have developed a custom computer program to obtain a best-fit two-dimensional surface brightness profile of each of the lensing galaxies. The results of the surface brightness analysis include morphological parameters (such as effective radius, ellipticity, etc.), and total flux.

The first step in our surface brightness analysis is a careful subtraction of lensed QSO images, a necessity given the close angular separations (typically $\approx 1''$) between the lensing galaxy and the lensed QSO images. The QSO image subtraction was performed using a model point spread function (PSF) generated from the TINYTIM software (Krist 1995) for individual cameras. We scale the input PSF to match both the observed peak brightness and position of each lensed QSO image, and subtract the best-fit point source model profile from the QSO image. Following the QSO image subtraction, we characterize the two-dimensional surface brightness profile of each lensing galaxy, μ, as a function of galactocentric radius, R, following a Sérsic profile,

$$\mu(R) = \mu_0 \exp\left\{-b_n\left[\left(\frac{R}{r_e}\right)^{\frac{1}{n}} - 1\right]\right\}, \tag{2.1}$$

where μ_0 is the central surface brightness, r_e is the effective (also called half-light) radius, n is the Sérsic index, and b_n is a constant whose value is defined by n (b_n can be precisely estimated by a polynomial in n, see Ciotti & Bertin 1999). The observed projected distance, r_{ij}, of each pixel (i, j) in the image is related to the deprojected galactocentric radius, R_{ij}, according to,

$$R_{ij} = r_{ij}\sqrt{1 + \sin^2(\alpha_{ij} - \mathrm{PA})\tan^2(\cos^{-1}\, b/a)}, \tag{2.2}$$

where α_{ij} is the azimuthal angle of the pixel (i, j) and PA is the position angle of the major axis of the galaxy, both measured north through east, and b/a is the minor-to-major axis ratio. The model surface brightness profile is then convolved with a TINYTIM PSF model computed at the location of the lensing galaxy. Finally, the resulting PSF-convolved two-dimensional model surface brightness profile is compared with the observation to obtain

Table 2.3: Summary of Galaxy Structural and Photometric Properties

Galaxy	n	r_e (kpc)	b/a	PA[a] (°)	M_B (mag)	$(g-r)_{\rm rest}$	$\log {\rm M_{star}/M_\odot}$	L_B/L_*	SFR(UV)[b] ($\rm M_\odot$ / yr)
HE 0047 $\rm G_{lens}$	3.87 ± 0.55	2.6 ± 0.6	0.78 ± 0.02	114 ± 3	-20.7	0.77	10.9	0.9	...
HE 0435 $\rm G_{lens}$	3.51 ± 0.04	4.4 ± 0.1	0.82 ± 0.01	176 ± 1	-21.4	0.74	11.1	1.7	< 0.01
HE 1104 $\rm G_{lens}$	4.36 ± 0.17	8.2 ± 0.2	0.77 ± 0.01	56 ± 2	-22.4	0.71	11.4	3.5	< 0.1

[a]Position angle of the major axis of the lens galaxy is measured North through East.

[b]Unobscured SFR based on the observed F275W flux limits and the SFR calibrator from Kennicutt & Evans (2012).

the best-fit morphological parameters based on a χ^2 analysis. Error bars in the best-fit parameters are estimated from the diagonal terms of the covariance matrix returned from the χ^2 analysis.

Of the images available in each field (Table 2.1), the F814W images offer the best combination of fine spatial sampling and sufficient sensitivity for tracing the dominant stellar population in the rest-frame optical window. While the two-dimensional surface brightness profile analysis is performed for all bandpasses, we adopt the best-fit morphological parameters as the fiducial model for characterizing each lensing galaxy. Cross examinations of the best-fit morphological parameters in different bandpasses show that the best-fit model based on the F814W image is consistent with those obtained in other bandpasses for all three fields, except for the F555W image of the HE 1104−1805 lens. The discrepancy is understood as due to a lack of young stars contributing to the rest-frame near-ultraviolet light that is recorded in the observed F555W frame. We present the best-fit morphological parameters from the F814W images in columns (3) to (6) of Table 2.3.

The total flux of each galaxy in each filter is determined by integrating the best-fit Sérsic profile within the half-light radius r_e and multiplying the result by a factor of two (yielding the total flux, by definition of the Sérsic profile)[1]. Error in the total flux is estimated by adding in quadrature the systematic error in the best-fit Sérsic profile due to uncertainties

1. It is possible that there exists an underlying faint disk that has been missed in the glare of the QSO images. We show in the right most panel of Figures 2.3, 2.5, & 2.7 that the 2-sigma limit on the surface brightness at $d > r_e$ of each lensing galaxy is typically fainter than $\mu \approx 23 - 23.5\,{\rm mag/arcsec^2}$. Taking a disk scale length of $r_s \approx 8$ kpc, which is typical of nearby elliptical/S0 galaxies (see e.g., de Jong et al. 2004), we estimate that the disk component, if present, would have added $< 35\%$ of the total light.

in the best-fit model parameters and statistical errors due to photon counting. Next, the rest-frame absolute magnitudes and rest-frame $g-r$ colors, and total stellar mass $M_{\rm star}$ of each galaxy are calculated using the IDL K-correct library version 4.2 (Blanton & Roweis 2007), which performs k-correction using a library of templates generated using Bruzual & Charlot (2003) stellar population synthesis code together with emission line models from Kewley et al. (2001). For the lensing galaxies in the HE 0435−1223 and HE 1104−1805 fields, constraints on the unobscured star formation rate (SFR) are also derived using the observed flux limit in the F275W bandpass and the SFR calibrator from Kennicutt & Evans (2012). At the redshifts of the lensing galaxies, the F275W bandpass corresponds to roughly rest-frame $1500-1800$ Å. The results are also summarized in Table 2.3.

The available optical spectra of two of the lensing galaxies described in Section 2.2.2 (Figure 2.2) exhibit prominent absorption features such as Ca II H&K doublet, G-band, and Mg b, and a strong 4000-Å spectral discontinuity that are characteristic of a quiescent galaxy with no on-going star formation. We measure the D4000 index, which is defined as the continuum flux ratio between two spectral regions, $4000-4100$ Å and $3850-3950$ Å, bracketing the 4000-Å discontinuity, D4000 $\equiv f_{4000-4100}/f_{3850-3950}$, as well as the H$\delta$ absorption and [O II] emission equivalent width following the spectral index definitions of Balogh et al. (1999). The results are summarized in Table 2.4. Based on the observed equivalent width upper limits for [O II] emission, we apply the SFR conversion of Kewley et al. (2004) and place a 2-σ upper limit for the unobscured SFR at $\approx 0.07\,M_{\odot}$/yr. In addition, the relatively large D4000 indices indicates that the two lensing galaxies have a minimum stellar age of $\gtrsim 1$ Gyr (e.g., Kauffmann et al. 2003). We note that the presence of residual QSO flux blueward of the 4000-Å spectral discontinuity would result in underestimated D4000 indices, implying an even older stellar population for these galaxies.

Table 2.4: Summary of Galaxy Spectroscopic Properties

Galaxy	z	D4000	EW(Hδ)[a] (Å)	EW([O II])[b] (Å)	SFR[O II][c] ($M_\odot$ / yr)
HE 0047 G_{lens}	0.408	1.4 ± 0.4	2.8 ± 0.8	< 1.9	< 0.07
HE 0435 G_{lens}	0.454	1.4 ± 0.2	1.7 ± 0.2	< 0.4	< 0.06
HE 1104 G_{lens}	0.729[d]	...	...	...	...

[a] Rest-frame absorption equivalent width
[b] 2-σ upper limit of [O II] emission.
[c] Unobscured SFR based on the observed flux limits for [O II] emission line and the conversion from Kewley et al. (2004).
[d] Lidman et al. (2000).

2.3.2 Absorbing Gas Properties

The echelle spectroscopy described in Section 2.2.3 produces high-resolution absorption spectra of gas along multiple sightlines around three lensing galaxies. These spectra enable a detailed study of how halo gas properties around massive quiescent galaxies vary with different physical locations. At the redshifts of the three lensing galaxies, the echelle spectra provide a wavelength coverage for observing prominent absorption transitions Fe II λ 2600, Mg II $\lambda\lambda$ 2796, 2803, Mg I λ 2852, and Ca II $\lambda\lambda$ 3934.

To characterize halo gas around the lensing galaxies, we perform two sets of measurements following what is described in Chen et al. (2014). First, we measure the total, integrated absorption equivalent widths along individual sightlines. Measurements of total integrated absorption equivalent widths along individual sightlines offer a baseline comparison between absorbers residing in massive galaxy halos and the general absorber population from random sightline surveys (e.g. Rao et al. 2006; Zhu & Ménard 2013; Seyffert et al. 2013). Next, we perform a Voigt profile analysis on a component-by-component basis to constrain the gas column densities and Doppler parameters of individual components. Measurements of individual absorption components allow us to examine detailed kinematic structures and investigate possible variations in relative ionic abundances both along and across individual sightlines.

To carry out the Voigt profile analysis, we developed a custom software to analyze both

heavily binned MIKE spectra and unbinned UVES and HIRES data. For each observed absorption line system, we first generate a theoretical absorption line profile based on the minimum number of discrete components, n_c, that is needed to explain the observed Mg II absorption kinematics. We focus on the Mg II absorption doublet for setting the number of necessary components, because among all observable features (Fe II, Mg II, Mg I, and Ca II absorption) the lines of the doublet are expected to be the strongest features in diffuse gas. For each absorbing component, the Voigt profile is uniquely defined by three free parameters: the velocity offset of the line center relative to the systemic redshift of the lensing galaxy (v_c), the absorption column density of ion X ($\log N_c$[X]), and the Doppler parameter (b_c). Next, the theoretical absorption profile is convolved with a Gaussian line spread function with the FWHM set by the appropriate instrumental resolution, which is FWHM $\approx$ 12 km s^{-1} for MIKE and FWHM $\approx$ 6.7 km s^{-1} for UVES and HIRES. Following this step, the convolved model Voigt profile is binned according to the adopted spectral binning of the data. Finally, the resulting binned model spectrum is compared with the observed absorption spectrum, and the best-fit parameters are determined based on a χ^2 analysis. We perform the Voigt profile fitting procedure to all available transitions of a given absorption system. The velocity offsets of individual components are fixed across all transitions, whereas $\log N_c$ and b_c are allowed to vary freely for different transitions. The results of the Voigt profile analysis also allow us to determine the total velocity widths that enclose 90% of total optical depth, which enable a direct comparison of the mean velocity field across different sightlines. Finally, we note that because both HIRES and UVES spectra are available for HE 1104−1805, the best-fit model parameters were found by a simultaneous χ^2 fit to the HIRES and UVES spectra. The two spectra were combined for display purposes only (Figure 2.8).

A summary of the integrated absorption properties along individual sightlines is presented in Table 2.5. For each lensed QSO sightline, we present its angular separation θ and the corresponding projected distance d to the lensing galaxies, the relative azimuthal angle ϕ of the lensed QSO image from the major axis of the lens, the rest-frame absorption equivalent

Table 2.5: Integrated absorption properties along lensed QSO sightlines near the three lensing galaxies

			Fe II λ 2600		Mg II λ 2796		Mg I λ 2852		Ca II λ 3934	
	θ^b ($''$)	d^c (kpc/r_e)	W_r (Å)	$\delta\, v_{90}$ (km/s)	W_r (Å)	$\delta\, v_{90}$ (km/s)	W_r (Å)	$\delta\, v_{90}$ (km/s)	W_r (Å)	$\delta\, v_{90}$ (km/s)
HE 0047−1756 lens at $z = 0.408$										
A	0.85	4.6/1.8	2.29 ± 0.04	590	4.46 ± 0.02	609	0.80 ± 0.02	603	0.32 ± 0.02	584
B	0.61	3.3/1.3	2.03 ± 0.10	462	3.69 ± 0.04	482	0.72 ± 0.04	473	0.12 ± 0.02	74
HE 0435−1223 lens at $z = 0.454$										
A	1.30	7.5/1.7	< 0.04	...	< 0.03	...	< 0.01	...	< 0.03	...
B	1.17	6.7/1.5	< 0.04	...	< 0.03	...	< 0.01	...	< 0.04	...
C	1.30	7.5/1.7	< 0.03	...	< 0.03	...	< 0.01	...	< 0.03	...
D	1.07	6.2/1.4	< 0.06	...	< 0.04	...	< 0.02	...	< 0.03	...
HE 1104−1805 lens at $z = 0.729$										
A	1.11	8.1/1.0	0.34 ± 0.01	332	0.64 ± 0.01	331	0.09 ± 0.01	333	0.06 ± 0.01	334
B	2.08	15.1/1.8	< 0.01	...	< 0.01	...	< 0.01	...	< 0.04	...

[a]For non-detections, we present a 2-σ upper limit to the absorption equivalent width. For HE 1104−1805B, the limits are estimated over the same velocity interval as in HE 1104−1805A. For HE 0435−1223 A,B,C,D, the limits are estimated over twice the resolution element (10 km/s).

[b]θ: angular separation between the lens and lensed QSO image.

[c]d: Projected distance in units of kpc or half-light radius r_e.

width (W_r), and velocity width enclosing 90% of the total optical depth ($\delta\, v_{90}$) of each absorption transition. Uncertainties in $\delta\, v_{90}$ are of order the size of the spectral pixel, which is 10 km s^{-1} for HE 0047−1756 and HE 0435−1223, and 2.6 km s^{-1} for HE 1104−1805.

The results of the Voigt profile analysis for individual fields are summarized in Tables 2.6, 2.7, and 2.8, and the best-fit model absorption profiles are presented in Figures 2.4, 2.6, and 2.8 below for comparison with observations. Uncertainties listed in the tables represent only formal errors from the χ^2 analysis, not including systematic uncertainties due to continuum fitting errors. For non-detected Fe II, Mg I, and Ca II absorbing components, we first measure the 2-σ equivalent width limits of the strongest transitions using the error spectrum over a spectral window that is twice the FWHM of the corresponding Mg II component. When Mg II absorption features are absent (namely for HE 0435−1223 and for HE 1104−1805B), the upper limits are evaluated over a spectral window that is twice the spectral resolution element. Then we calculate the corresponding 2-σ upper limits to the component column densities, assuming that the gas is optically thin.

Because our MIKE spectra have a pixel resolution comparable to the instrument spectral

resolution, it is important to understand and quantify possible systematic uncertainties in the Voigt profile analysis that may result from an undersampled line spread function. For this reason, we perform a series of Monte Carlo simulations to assess the accuracy of the best-fit Voigt profile parameters. Specifically, we first generate a set of synthetic Mg II and Fe II absorption lines with varying column densities and Doppler parameters, convolve the synthetic absorbers with the instrumental line spread function, apply a pixel binning of 10 km s^{-1}, and add noise to the synthetic spectra based on the 1-σ error spectrum associated with each lensed QSO spectrum. Next, we perform the Voigt profile analysis using the resulting synthetic spectrum to determine the best-fit column density and Doppler parameter of each component. Finally, we repeat the process 1000 times to record the distribution of best-fit model parameters relative to the input values.

The Monte Carlo simulations demonstrate that despite an undersampled line spread function, the input column density and Doppler parameter are well-recovered for relatively broad components ($\gtrsim 7$ km s^{-1}). For these broad components, the 95% confidence interval is less than 5% of the best-fit column density and b values. For narrower components ($b < 7$ km s^{-1}), we found that while the input values are well-recovered for weak transitions ($\log N \lesssim 13.0$), the intrinsic line profiles begin to saturate when the column density exceeds $\log N \approx 13.0$. The simulations show that for these narrow and saturated components the best-fit column density and b value become degenerate and the uncertainties in column density can be as high as 0.1 dex for absorbers of $\log N \lesssim 13.5$ and up to 0.3 dex for strong absorbers of $\log N > 14$. For Mg II components, we note that all narrow component are weak and saturation is therefore not a significant issue. For Fe II components, including weaker transitions, such as Fe II λ 2586, allows us to recover the underlying N(Fe II) to better than 0.1 dex accuracy for components as strong as $\log N(\mathrm{Fe\,II}) \approx 14$. Based on the results of the simulations, we conclude that the column density measurements are robust for relatively isolated components.

Complications arise when two saturated components are blended together. This is the

case for components 1 & 2 in sightline B of HE 0047−1756 (see Figure 2.4 below). A simultaneous Voigt profile analysis of the two components yields two local χ^2 minima at $(\log N_c, b_c) = (16.5, 6.9)$ and (13.7, 18.0) for component 1, and $(\log N_c, b_c) = (16.8, 14.9)$ and (14.9, 23.2), for component 2. For these two components, we apply a prior based on the known N(Mg I) and the CLOUDY photo-ionization calculation (see Section 2.5.1, and adopt the second local minimum as the best-fit values. This is justified by the implied N(Mg I)/N(Mg II) ratio which, at the first local minimum, would place the component in an unrealistically low gas density regime, $n_{\rm H} < 10^{-4}\,{\rm cm}^{-3}$ (see Figure 2.9 below), leading to an unphysically large cloud size that exceeds 300 kpc for optically thin gas with solar metallicity.

2.4 Description of Individual Lensing Galaxies

With the separate measurements of galaxy and absorption-line properties presented in Section 2.3, here we proceed with a joint analysis of the stellar population and halo gas properties of each lensing galaxy.

2.4.1 The HE 0047−1756 Lens at $z = 0.408$

The lensing galaxy of HE 0047−1756 at $z = 0.408$ was spectroscopically identified by Ofek et al. (2006) and confirmed by Eigenbrod et al. (2006). Our two-dimensional surface brightness profile analysis has yielded a best-fit Sérsic index of $n = 3.9 \pm 0.6$, a half-light radius of $r_e = 2.6$ kpc, and an axis ratio of $b/a = 0.78 \pm 0.02$ (Figure 2.3). The best-fit morphological parameters characterize the lens as an elliptical galaxy, which is consistent with the relatively old age (> 1 Gyr) and a lack of on-going star formation (SFR $< 0.07\,{\rm M}_\odot\,{\rm yr}^{-1}$) inferred from the spectral indices presented in Table 2.4. Integrating the best-fit Sérsic profile, we estimate the total apparent magnitudes in the F555W, F814W, and F160W bandpasses, and find AB(F555W) $= 21.64 \pm 0.07$, AB(F814W) $= 19.71 \pm 0.05$, and AB(F160W) $=$

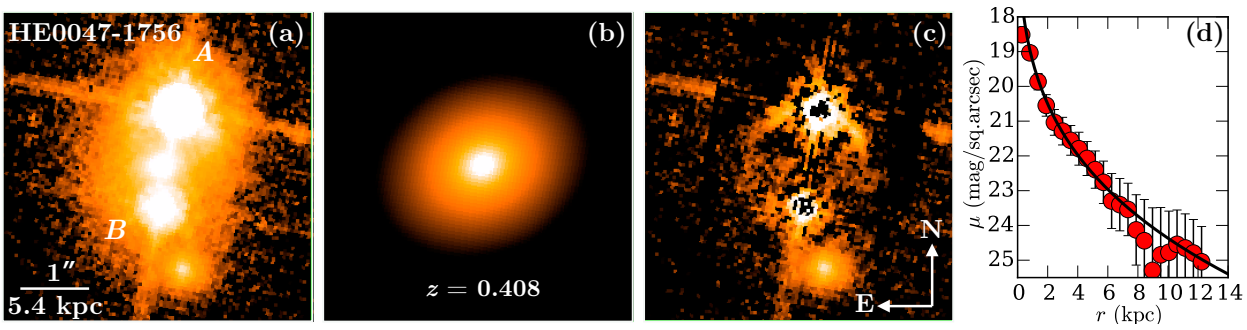

Figure 2.3: (a) HST/ACS F814W image of the field around HE 0047−1756. The lensing galaxy at $z = 0.408$ is at the center of the panel surrounded by the doubly-lensed QSO at $z_{\rm QSO} = 1.67$ (Wisotzki et al. 2004). We note that the redshift of the fainter source at $1.5''$ south of the lens is not known. Panel (b) displays the best-fit Sérsic model surface brightness profile, which is characterized by a Sérsic index of $n = 3.9 \pm 0.6$, half-light radius $r_e = 2.6 \pm 0.6$ kpc, and an axis ratio of $b/a = 0.78 \pm 0.02$. The best-fit morphological properties are consistent with those expected from an elliptical galaxy. Panel (c) displays the residual image after subtracting the QSO PSFs and the best-fit Sérsic model. Panel (d) displays an azimuthally-averaged surface brightness profile of the lensing galaxy in the F814W bandpass. Each data point is calculated from an elliptical annulus of 0.1" (2 pixels) in width, and the associated error bar represents photon counting noise, which is driven primarily by the contaminating QSO light at large radii. The best-fit Sérsic from the 2D analysis is shown as a black line. We note that the deviant points at $8 - 10$ kpc are due to large residuals from subtracting the QSO light.

18.64 ± 0.06. Following the procedures described in Section 2.3.1, the observed apparent magnitudes translate to a rest-frame B-band absolute magnitude of $M_B = -20.7$, which is roughly $0.9\,L_*$ at $z = 0.4$ according to Faber et al. (2007). In addition, we find a rest-frame optical color of $g - r = 0.77$ and a total stellar mass of $\log M_{\rm star}/M_\odot = 10.9$ for the lensing galaxy. Adopting the stellar-to-halo-mass relations of Behroozi et al. (2013) and Kravtsov et al. (2014), we further infer a total dark matter halo mass of $\log M_h/M_\odot = 12.4 - 12.7$. In summary, we find that the lensing galaxy of HE 0047−1756 is a quiescent L_* galaxy with structural and photometric properties typical of intermediate-redshift early-type galaxies (e.g., Rutkowski et al. 2012).

We note the presence of an extended source at $\approx 1.6''$ southwest of the lensing galaxy. This object appears to be bluer than the lensing galaxy (see left panel of Figure 2.1). We have also performed a two-dimensional surface brightness profile analysis for this object and found

a best-fit Sérsic index of $n = 2.05 \pm 0.08$, consistent with the more extended morphology displayed in the HST images. No redshift measurement is available for this object. However, Chantry et al. (2010) noted that this galaxy is likely a major contributor to the shear term in the lens model that is needed to reproduce the image configuration of the lensed QSOs. Assuming this object is at the same redshift as the lensing galaxy, Chantry et al. (2010) calculated a velocity dispersion of $\sigma = 88$ km s^{-1} for this galaxy, which is comparable to the characteristic velocities of large satellite galaxies like the Large Magellanic Cloud (e.g., Alves & Nelson 2000).

At $z = 0.408$, the projected distance between the lens and QSO image A is $d_{\rm A} = 4.6$ kpc or $1.8\,r_e$, and the projected distance between the lens and QSO image B is $d_{\rm B} = 3.3$ kpc or $1.3\,r_e$. The two sightlines probe both the gaseous halo at small projected distances and the interstellar medium of an elliptical galaxy where the gas is expected to be hot. Adopting the correlation between X-ray luminosity and B-band luminosity L_B of local elliptical galaxies from O'Sullivan et al. (2001), we infer an X-ray luminosity of $L_X \approx 10^{41}\,{\rm erg\,s^{-1}}$ for the lens of HE 0047−1756. The expected luminous X-ray flux indicates that, similar to nearby elliptical galaxies, the lensing galaxy is likely surrounded by a hot halo.

At the same time, the absorption spectra show that not only abundant cool gas is present along both A and B sightlines in the inner halo of the galaxy, but the velocity spread is also very large. The total rest-frame equivalent width is found to be $W_r(2796) = 4.46 \pm 0.02$ Å along sightline A at $d = 4.6$ kpc ($1.8\,r_e$) north of the lens and $W_r(2796) = 3.69 \pm 0.04$ Å along sightline B at $d = 3.3$ ($1.3\,r_e$) kpc south of the lens. These ultra-strong absorbers are often attributed to starburst driven outflows (e.g., Nestor et al. 2011). In the case of the lensing galaxy, however, the lack of on-going star formation together with a dominant old stellar population makes a starburst driven outflow origin an unlikely scenario. On the other hand, Rao et al. (2006) showed that strong Mg II absorbers of $W_r(2796) > 0.6$ Å at $z < 1.65$ have a mean H I column density of $\langle\, N({\rm H\,I})\,\rangle = (3.5 \pm 0.7) \times 10^{20}\,{\rm cm^{-2}}$ which, together with the relative line ratios between Mg II, Fe II, and Mg I, indicate a high probability ($> 40\%$)

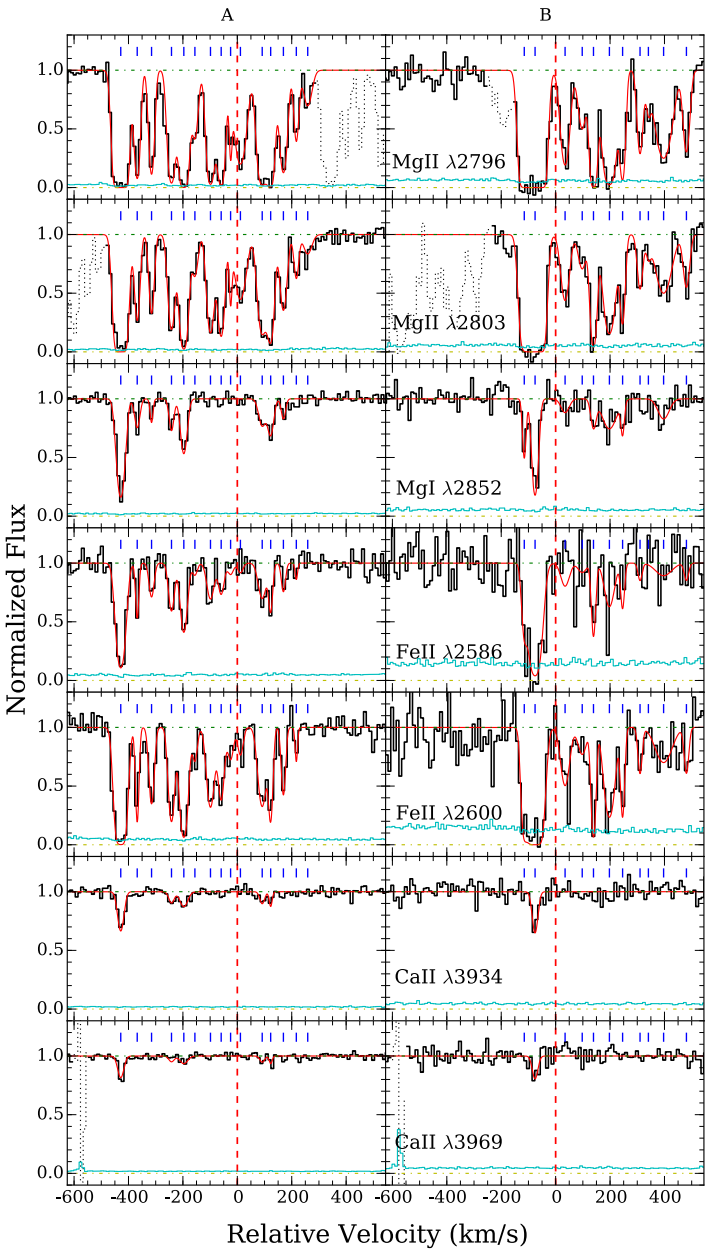

Figure 2.4: Continuum normalized absorption profiles of different transitions along the lensed QSO sightlines HE 0047−1756 A (left) at $d = 4.6$ kpc (or $1.8\,r_e$) and B (right) at $d = 3.3$ kpc (or $1.3\,r_e$) from the HE 0047−1756 lens. Zero velocity corresponds to the systemic redshift of the lensing galaxy at $z = 0.408$. The 1-σ error spectrum is included in thin, cyan curve above the zero flux level. The blue tickmarks at the top of each panel indicate the location of individual components included in the Voigt profile analysis (see Section 2.3.2), and the best-fit Voigt profile models are included in red. Contaminating features have been dotted out for clarity. Despite showing no sign of recent star formation, the inner halo of the lensing galaxy harbors a significant amount of cool gas with complex kinematic profiles that span $\approx 500 - 600$ km s^{-1} in line-of-sight velocity and exhibit a large velocity shear of $\Delta\, v \approx 350$ km s^{-1} across the two sightlines separated by merely ≈ 8 kpc.

Table 2.6: Absorption properties around the HE 0047−1756 Lens.

			v_c	Fe II		Mg II		Mg I		Ca II	
Sightline	n_c	component	(km/s)	log N_c	b_c (km/s)	log N_c	b_c (km/s)	log N_c	b_c (km/s)	log N_c	b_c (km/s)
A	15	1	−428.4	14.23 ± 0.03	19.1 ± 0.7	14.34 ± 0.16	19.2 ± 1.4	12.63 ± 0.02	17.1 ± 0.8	12.23 ± 0.03	14.3 ± 1.4
		2	−367.9	13.32 ± 0.08	5.5 ± 1.1	13.12 ± 0.03	11.0 ± 0.9	11.68 ± 0.21	11.7 ± 0.2	< 11.0	...
		3	−315.2	13.21 ± 0.05	11.0 ± 1.6	13.04 ± 0.03	10.8 ± 0.8	11.35 ± 0.12	4.4 ± 5.4	< 11.1	...
		4	−241.9	13.45 ± 0.04	12.8 ± 1.3	13.31 ± 0.03	14.5 ± 1.3	11.69 ± 0.08	10.4 ± 3.4	11.57 ± 0.12	12.3 ± 5.5
		5	−196.6	13.75 ± 0.03	15.5 ± 1.2	13.70 ± 0.06	15.5 ± 1.7	12.11 ± 0.04	14.7 ± 1.8	11.86 ± 0.08	18.9 ± 4.8
		6	−155.9	12.70 ± 0.13	10.7 ± 5.0	12.71 ± 0.08	13.9 ± 3.4	< 10.9	...	< 11.0	...
		7	−98.6	13.39 ± 0.04	16.7 ± 2.0	13.37 ± 0.03	15.2 ± 1.3	< 10.9	...	< 11.1	...
		8	−59.3	13.22 ± 0.06	12.9 ± 2.7	13.39 ± 0.03	14.1 ± 1.3	< 10.9	...	< 11.1	...
		9	−24.7	12.75 ± 0.16	13.2 ± 7.2	12.78 ± 0.27	3.2 ± 1.4	< 10.7	...	< 10.8	...
		10	+11.4	12.64 ± 0.15	12.0 ± 6.8	13.22 ± 0.03	25.7 ± 2.0	< 11.0	...	< 11.2	...
		11	+91.5	13.42 ± 0.04	18.4 ± 2.3	13.47 ± 0.09	19.0 ± 2.8	11.77 ± 0.10	16.4 ± 4.9	11.55 ± 0.12	10.6 ± 4.9
		12	+122.6	13.31 ± 0.06	8.2 ± 1.6	13.46 ± 0.09	13.6 ± 2.3	11.85 ± 0.07	13.7 ± 2.8	11.45 ± 0.12	4.8 ± 6.7
		13	+169.4	13.04 ± 0.06	8.3 ± 2.0	13.13 ± 0.03	15.4 ± 1.3	11.42 ± 0.16	9.0 ± 7.0	< 11.1	...
		14	+216.9	12.62 ± 0.10	5.3 ± 2.2	12.64 ± 0.05	10.2 ± 2.1	< 10.8	...	< 11.1	...
		15	+258.8	< 12.2	...	12.46 ± 0.09	19.5 ± 5.1	< 10.9	...	< 11.1	...
B	11	1	−115.3	13.60 ± 0.16	10.9 ± 3.5	$13.74^{+0.10}_{-0.08}$	18.0 ± 1.6	11.92 ± 0.11	6.3 ± 3.2	< 11.5	...
		2	−75.6	14.49 ± 0.12	24.5 ± 2.6	$14.88^{+0.29}_{-0.23}$	23.2 ± 2.0	12.51 ± 0.06	13.1 ± 1.6	12.21 ± 0.05	12.6 ± 2.4
		3	+34.7	13.24 ± 0.16	20.1 ± 6.2	13.11 ± 0.04	19.0 ± 2.2	11.52 ± 0.27	19.7 ± 8.9	< 11.5	...
		4	+97.7	12.82 ± 0.20	20.0 ± 4.5	12.72 ± 0.09	18.4 ± 5.6	< 11.3	...	< 11.5	...
		5	+139.1	13.59 ± 0.14	8.1 ± 4.2	13.55 ± 0.10	12.0 ± 1.5	11.68 ± 0.20	11.9 ± 4.6	< 11.4	...
		6	+197.6	13.62 ± 0.07	23.0 ± 4.2	13.57 ± 0.04	24.8 ± 2.7	12.12 ± 0.12	34.3 ± 6.8	< 11.6	...
		7	+246.1	13.25 ± 0.17	7.3 ± 3.8	13.12 ± 0.07	10.2 ± 1.8	11.59 ± 0.21	6.4 ± 7.6	< 11.4	...
		8	+310.2	12.80 ± 0.18	8.4 ± 6.2	12.82 ± 0.06	12.1 ± 2.6	< 11.2	...	< 11.5	...
		9	+340.9	< 12.6	...	12.22 ± 0.20	10.0 ± 6.0	< 11.1	...	< 11.4	...
		10	+396.8	13.24 ± 0.12	40.0 ± 6.8	13.30 ± 0.03	36.4 ± 3.7	11.83 ± 0.15	27.4 ± 6.4	< 11.7	...
		11	+480.7	12.83 ± 0.18	9.5 ± 7.5	12.85 ± 0.05	13.9 ± 2.4	< 11.2	...	< 11.5	...

that the strong Mg II absorbers found in the inner regions of the lensing galaxy are damped Lyα absorbers (DLAs), in which the gas is expected to be mostly neutral (e.g., Wolfe et al. 2005).

It is clear from the echelle absorption spectra that the large equivalent widths are driven by complex multi-component structures that span $\approx 500-600$ km s^{-1} in line-of-sight velocity (Table 2.5 and Figure 2.4). The observed velocity spread along an individual sightline exceeds the maximum circular velocity, $v_{\rm max} \approx 240$ km s^{-1}, expected for halos of $\sim 2.5 \times 10^{12}\, M_\odot$. In addition, the absorption profiles exhibit an edge-leading signature commonly seen in rotating disks with the highest column density gas moving (blueshifted) at the highest velocity toward the observer. Based on a grid of photo-ionization models discussed in Section 2.5.1 below, we find that component 1 along sightline A and component 2 along sightline B are indeed likely strong Lyman limit absorbers (or possibly DLAs) of log N(H I) > 19 which have a significant neutral fraction. Other weaker components remain in the optically thin regime with log N(H I) $\lesssim 17$. The lower N(H I) is also reflected in the observed declining N(Mg II) (by nearly 2 dex) with increasing receding velocity along the line of sight. Such

edge-leading kinematic signatures are present along both sightlines.

At $d = 3 - 5$ kpc, the QSO sightlines probe both halo gas at $r \sim 100$ kpc (in front of and behind the lens) and the ISM at $r \sim 5 - 10$ kpc. It is possible that a coherent structure in the ISM contributes predominantly to the absorption profiles, which drives the strong resemblance in the edge-leading signature, and that independent gas clumps in the halo contribute to the absorption separately along different sightlines, which adds noise to the profiles. To examine possible spatial coherence between the gas revealed along the two sightlines, we perform a cross-correlation analysis of the absorption profiles observed along A and B sightlines and found a clear maximum at velocity offset of $\Delta\, v \approx 350$ km s^{-1} between the two sightlines. Applying an velocity offset of $\Delta\, v = -350$ km s^{-1}, we find good match between components 1, 2, 5, 7, and 8 along sightline B and components 1, 5, 7, and 9 along sightline A, both in their relative absorption strengths and in velocity offsets. The observed kinematic profiles suggest strong coherence on scales of ~ 8 kpc in the gas motion across the inner halo (a more complete discussion follows in Section 2.5.3). However, the matched components span a light-of-sight velocity range of ≈ 420 km s^{-1}, still exceeding the maximum circular velocity, $v_{\rm max} \approx 240$ km s^{-1}, expected for halos of $\sim 2.5 \times 10^{12}\, M_{\odot}$.

2.4.2 HE 0435−1223 Lens Galaxy at $z = 0.454$

The lensing galaxy of HE 0435−1223 at $z = 0.454$ was spectroscopically identified by Morgan et al. (2005) and confirmed by Eigenbrod et al. (2006). This lens resides in a galaxy group with 12 spectroscopically confirmed members and a group velocity dispersion of $\sigma_{\rm group} = 520^{+70}_{-80}$ km s^{-1} (Wilson et al.2016). We note, however, that galaxy G22 in Morgan et al. (2005) at $4.4''$ from the lensing galaxy is spectroscopically identified at $z = 0.7818$ by Chen et al. (2014), and is therefore not part of the group. Our two-dimensional surface brightness profile analysis has yielded a best-fit Sérsic index of $n = 3.51 \pm 0.04$, a half-light radius of $r_e = 4.4$ kpc, and an axis ratio of $b/a = 0.82 \pm 0.01$ (Figure 2.5), consistent with measurements of Kochanek et al. (2006). The best-fit morphological parameters characterize

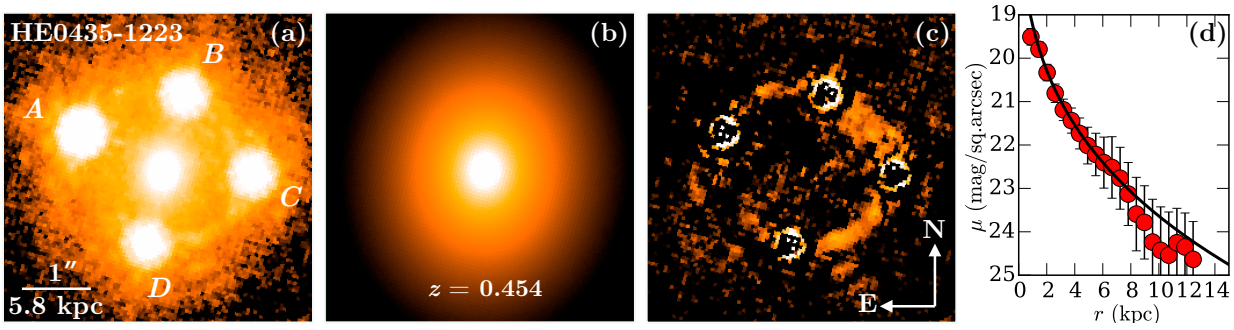

Figure 2.5: (a) HST/ACS F814W image of the field around HE 0435−1223. The lensing galaxy at $z = 0.454$ is at the center of the panel surrounded by the quadruply-lensed QSO at $z_{\rm QSO} = 1.69$ (Wisotzki et al. 2002). Panel (b) displays the best-fit Sérsic model surface brightness profile, which is characterized by a Sérsic index of $n = 3.51 \pm 0.04$, half-light radius $r_e = 4.4 \pm 0.1$ kpc, and an axis ratio of $b/a = 0.82 \pm 0.01$. The best-fit morphological properties are consistent with those expected from an early-type galaxy. Panel (c) displays the residual image after subtracting the QSO PSFs and the best-fit Sérsic model. Panel (d) displays an azimuthally-averaged surface brightness profile of the lensing galaxy in the F814W bandpass. Each data point and the associated error are calculated from an elliptical annulus of 0.1" (2 pixels) in width. The best-fit Sérsic from the 2D analysis is shown as a black line. We note that the deviant points at > 8 kpc are due to large residuals from subtracting the QSO light.

the lens as an early-type galaxy, consistent with the old stellar population (> 1 Gyr) and a lack of on-going star formation (SFR $< 0.07\,{\rm M}_\odot\,{\rm yr}^{-1}$) inferred from both the rest-frame UV continuum flux (Table 2.3) and the spectral indices presented in Table 2.4. Integrating the best-fit Sérsic profile, we find the total apparent magnitudes in the F555W, F814W, and F160W bandpasses of $AB({\rm F555W}) = 21.30 \pm 0.04$, $AB({\rm F814W}) = 19.36 \pm 0.03$, and $AB({\rm F160W}) = 18.34 \pm 0.04$. Our photometry for this lens galaxy is in general agreement with the magnitudes reported by Kochanek et al. (2006). The observed apparent magnitudes translate to a rest-frame B-band absolute magnitude of $M_B = -21.4$ (corresponding to $1.7\,L_*$ at $z = 0.45$), a rest-frame optical color of $g - r = 0.74$, and a total stellar mass of $\log M_{\rm star}/M_\odot = 11.1$ for the lensing galaxy. The inferred dark matter halo mass is $\log M_h/M_\odot = 12.7 - 13.4$, consistent with $\log M_h/M_\odot = 13.3 \pm 0.4$ from Kochanek et al. (2006) based on the lensing properties of this system. In summary, we find that the lensing galaxy of HE 0435−1223 is a quiescent super L_* galaxy.

At $z = 0.454$, the projected distances between the lensing galaxy and four lensed QSO

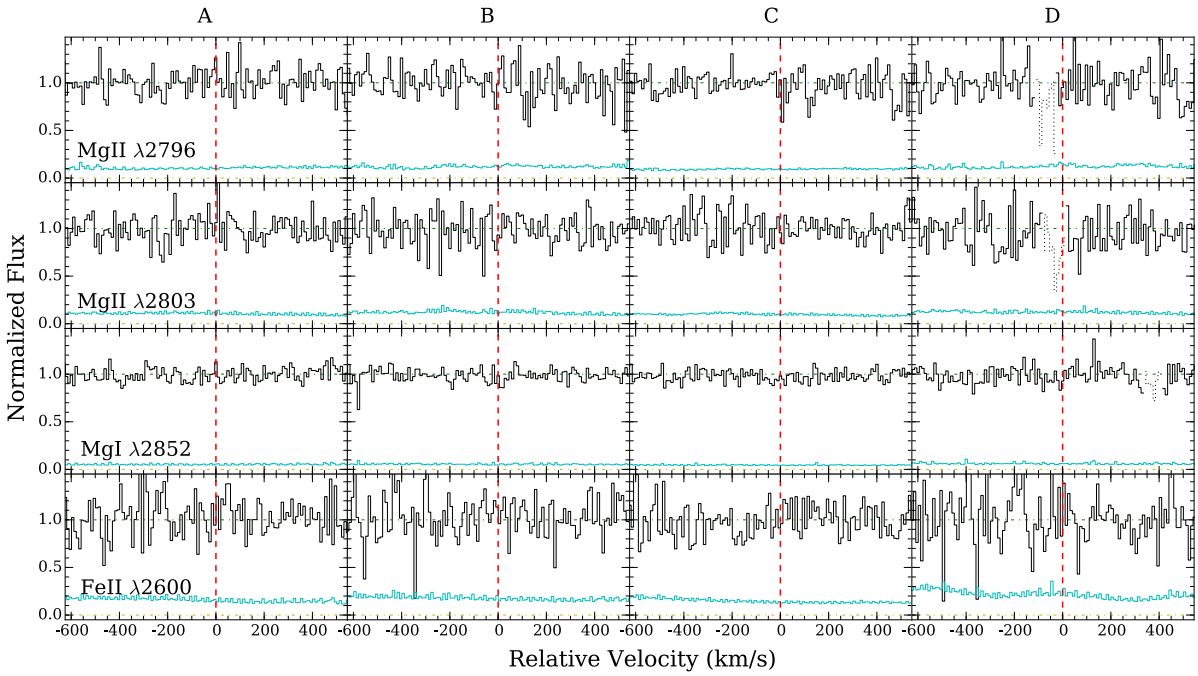

Figure 2.6: Continuum normalized spectra along the lensed QSO sightlines HE 0435−1223 A, B, C, D, at $d = 7.5, 6.7, 7.5$, and 6.2 kpc (or 1.7, 1.5, 1.7, $1.4\,r_e$), respectively. Zero velocity corresponds to the systemic redshift of the lensing galaxy at $z = 0.454$. The 1-σ error spectrum is included in thin, cyan curve above the zero flux level. Contaminating features have been dotted out for clarity. In stark contrast to the ultra-strong Mg II absorber detected along both sightlines of HE 0047−1756 (Figure 2.5), none of the four sightlines near the HE 0435−1223 lens reveals any cool gas.

images are $d = 7.5, 6.7, 7.5$, and 6.2 kpc or 1.7, 1.5, 1.7, $1.4\,r_e$ for images A, B, C, and D, respectively. Similar to the doubly lensed QSO HE 0047−1756, the quadruply-lensed QSO sightlines probe both the gaseous halo at small projected distances and the interstellar medium of a massive, early-type galaxy. Adopting the same L_x-L_B relation of O'Sullivan et al. (2001), we infer $L_x \approx (2 - 3.5) \times 10^{41}\,\mathrm{erg\,s^{-1}}$ for the lensing galaxy.

In contrast to the ultra-strong Mg II absorbers found in the vicinities of the HE 0047−1756 lens, no trace of ionic absorption is detected near the HE 0435−1223 to sensitive limits. We measure 2-σ upper limits of the underlying gas column densities for all observed transitions based on the absorption equivalent width limits presented in Table 2.5. The column density constraints are presented in Table 2.7. In Figure 2.6, we present the continuum-normalized QSO spectra within $\pm\,500$ km s^{-1} of the systemic redshift of the lensing galaxy. The strong

Table 2.7: Constraints on the absorption properties around the HE 0435−1223 Lens.

	log N(Fe II)	log N(Mg II)	log N(Mg I)	log N(Ca II)
A	< 12.5	< 11.8	< 11.0	< 11.5
B	< 12.5	< 11.9	< 11.0	< 11.6
C	< 12.4	< 11.8	< 10.9	< 11.5
D	< 12.6	< 12.0	< 11.1	< 11.5

limits afforded by the MIKE spectra indicates a lack of cool gas in the inner halo of this massive, quiescent galaxy.

2.4.3 HE 1104−1805 Lens Galaxy at $z = 0.729$

The lensing galaxy of HE 1104−1805 at $z = 0.729$ was spectroscopically identified by Lidman et al. (2000). Our two-dimensional surface brightness profile analysis has yielded a best-fit Sérsic index of $n = 4.4 \pm 0.2$, a half-light radius of $r_e = 8.2$ kpc, and an axis ratio of $b/a = 0.77 \pm 0.01$ (Figure 2.7). The best-fit morphological parameters indicate that the lens is also an elliptical galaxy, consistent with a lack of on-going star formation (SFR $< 0.1\,\mathrm{M}_\odot\,\mathrm{yr}^{-1}$) inferred the rest-frame UV continuum flux (Table 2.3). Integrating the best-fit Sérsic profile, we estimate the total apparent magnitudes in the F555W, F814W, and F160W bandpasses, and find $AB(\mathrm{F555W}) = 22.42 \pm 0.06$, $AB(\mathrm{F814W}) = 20.04 \pm 0.04$, and $AB(\mathrm{F160W}) = 18.77 \pm 0.06$. The observed apparent magnitudes translate to a rest-frame B-band absolute magnitude of $M_B = -22.4$, corresponding to $3.5\,L_*$ at $z = 0.7$ according to Faber et al. (2007). In addition, we find a rest-frame optical color of $g - r = 0.71$ and a total stellar mass of $\log M_{\mathrm{star}}/M_\odot = 11.4$ for the lensing galaxy. The inferred dark matter halo mass is $\log M_h/M_\odot = 13.3 - 14.3$. In summary, we find that the lensing galaxy of HE 1104−1805 is a massive, quiescent galaxy.

At $z = 0.729$, the projected distance between the lens and QSO image A is $d_{\mathrm{A}} = 8.1$ kpc or $\approx r_e$, and the projected distance between the lens and QSO image B is $d_{\mathrm{B}} = 15.1$ kpc or $1.8\,r_e$. Similar to the previous two lenses, the two sightlines probe both the gaseous halo

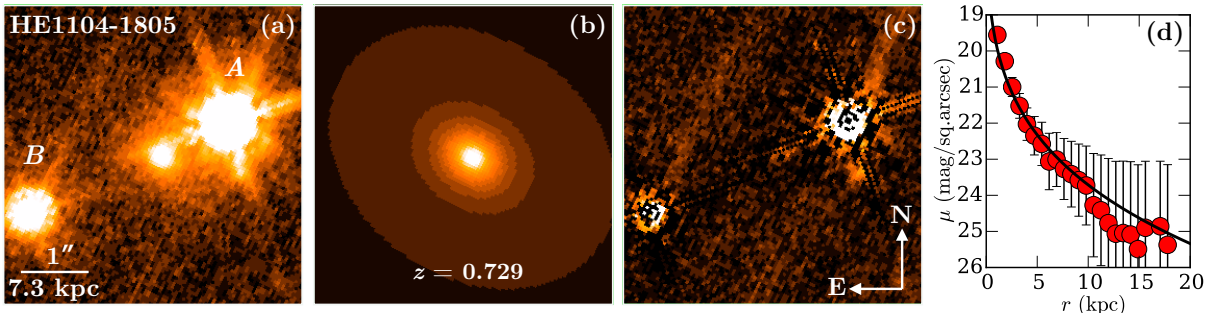

Figure 2.7: (a) HST/WFPC2-PC F814W image of the field around HE 1104−1805. The lensing galaxy at $z = 0.729$ is at the center of the panel surrounded by the doubly-lensed QSO at $z_{\rm QSO} = 2.31$ (Wisotzki et al. 2000). Panel (b) displays the best-fit Sérsic model surface brightness profile, which is characterized by a Sérsic index of $n = 4.4 \pm 0.2$, half-light radius $r_e = 8.2 \pm 0.2$ kpc, and an axis ratio of $b/a = 0.77 \pm 0.01$. The best-fit morphological properties are consistent with those expected from an early-type galaxy. Panel (c) displays the residual image after subtracting the QSO PSFs and the best-fit Sérsic model. Panel (d) displays an azimuthally-averaged surface brightness profile of the lensing galaxy in the F814W bandpass. Each data point is calculated from an elliptical annulus Each data point and the associated error are calculated from an elliptical annulus of 0.1" (2.5 pixels) in width. The best-fit Sérsic from the 2D analysis is shown as a black line. We note that the deviant points at > 10 kpc are due to large residuals from subtracting the QSO light.

at small projected distances and the interstellar medium of an elliptical galaxy. Adopting the L_x-L_B relation of O'Sullivan et al. (2001), we infer $L_x \approx 3 \times 10^{42}\,{\rm erg\,s^{-1}}$ for the lens of HE 1104−1805.

For the two lensed QSO sightlines, we have high S/N and high spectral resolution echelle spectra, and interestingly the inner halo of the HE 1104−1805 lens exhibits absorption properties that lie between the two previous cases. Only sightline A at $d = 8.1$ kpc (or $\approx r_e$) exhibits a modest amount of cool gas, as indicated by the presence of a moderately strong Mg II absorber with $W_r(2796) = 0.6$ Å (Smette et al. 1995). Associated Fe II, Mg I, and Ca II absorption transitions are also detected at this location (Table 2.5). Sightline B at about twice the distance away, $d = 15.1$ kpc (or $1.8\,r_e$), does not show any trace of cool gas. We place a 2-σ upper limit of $W_r(2796) = 0.01$ Å for possible underlying cool gas (Table 2.5).

Similar to the Mg II absorbers found in the vicinities of the HE 0047−1756 lens, the strongest components (3 & 5) along HE 1104−1805 A may contain a non-negligible amount

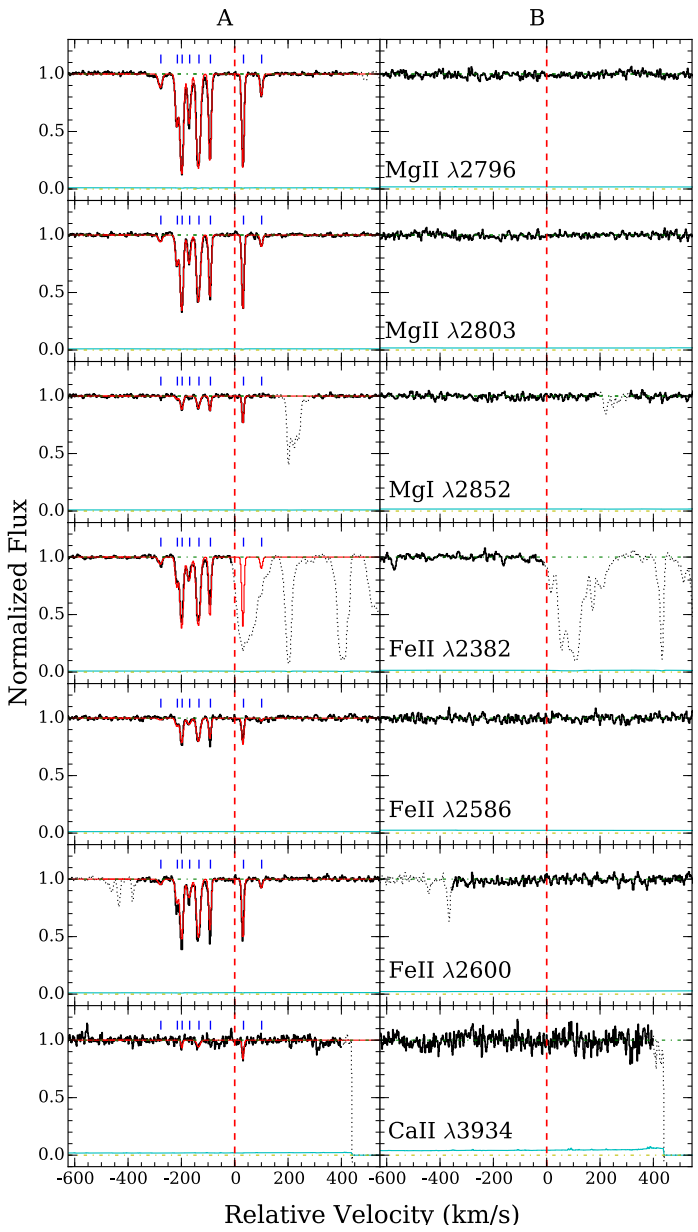

Figure 2.8: Continuum normalized absorption profiles of different transitions along the lensed QSO sightlines A (left) at $d = 8.1$ kpc (or $\approx r_e$) and B (right) at $d = 15.1$ kpc (or $1.8\,r_e$) from the HE 1104−1805 lens. Zero velocity corresponds to the systemic redshift of the lensing galaxy at $z = 0.729$. The 1-σ error spectrum is included in thin, cyan curve above the zero flux level. The blue tickmarks at the top of each left panel indicates the location of individual components included in the Voigt profile analysis (see Section 2.3.2), and the best-fit Voigt profile models are included in red. The best-fit model parameters were found by a simultaneous χ^2 analysis to the HIRES and UVES spectra. The HIRES and UVES spectra were combined for display purposes only, as shown here. Contaminating features have been dotted out for clarity. Only sightline A exhibits chemically-enriched cool gas characterized by six primary absorbing components that span ≈ 330 km s^{-1} in line-of-sight velocity, while sightline B exhibits no low-ionization transitions in the HIRES or UVES spectrum.

Table 2.8: Absorption properties around the HE 1104−1805 Lens.

			v_c	Fe II		Mg II		Mg I		Ca II	
Sightline	n_c	component	(km/s)	log N_c	b_c (km/s)	log N_c	b_c (km/s)	log N_c	b_c (km/s)	log N_c	b_c (km/s)
A	8	1	−277.7	11.78 ± 0.06	8.9 ± 1.8	11.69 ± 0.03	8.9 ± 0.9	< 10.2	...	< 10.8	...
		2	−215.7	12.34 ± 0.02	6.4 ± 0.4	12.27 ± 0.01	6.2 ± 0.3	10.41 ± 0.12	5.8 ± 2.9	< 10.7	...
		3	−197.3	12.87 ± 0.01	6.7 ± 0.2	12.82 ± 0.01	6.3 ± 0.1	11.08 ± 0.03	6.2 ± 0.7	10.96 ± 0.27	1.0 ± 5.6
		4	−169.8	12.33 ± 0.02	8.9 ± 0.6	12.25 ± 0.01	6.7 ± 0.2	< 10.1	...	< 10.7	...
		5	−134.9	12.92 ± 0.01	8.6 ± 0.2	12.80 ± 0.01	8.1 ± 0.1	11.08 ± 0.03	7.0 ± 0.7	11.16 ± 0.09	7.8 ± 2.4
		6	−91.5	12.66 ± 0.01	4.3 ± 0.2	12.61 ± 0.01	4.4 ± 0.1	11.00 ± 0.02	3.5 ± 0.6	< 10.7	...
		7	+32.1	12.75 ± 0.02	3.4 ± 0.3	12.74 ± 0.01	3.5 ± 0.1	11.28 ± 0.01	2.7 ± 0.4	11.39 ± 0.04	2.4 ± 1.2
		8	+101.3	11.80 ± 0.10	4.7 ± 2.2	11.75 ± 0.02	5.1 ± 0.5	< 10.1	...	< 10.7	...
B	...	...	0.0	< 11.0	...	< 10.8	...	< 10.3	...	<11.0	...

of H I with $\log N(\mathrm{H\,I}) \gtrsim 17$ while the remaining weaker components are optically thin absorbers. Unlike the the HE 0047−1756 lens, however, no edge-leading signature is found for the absorber near the HE 1104−1805 lens. The absorption kinematics in the vicinities of the HE 1104−1805 lens is shown in Figure 2.8. The moderately strong Mg II absorber at $d = 8.1$ kpc (or $1\,r_e$) is resolved into six dominant components of comparable strength, spanning ≈ 330 km s^{-1} in line-of-sight velocity. The observed velocity spread along sightline A is comparable to the maximum circular velocity, $v_{\rm max} \approx 340$ km s^{-1}, expected for halos of $5 \times 10^{12}\,M_\odot$. Results from our Voigt profile analysis are presented in Table 2.8.

2.5 Analysis and Results

Our multi-sightline absorption-line search has revealed a diverse range of halo gas properties at $d = 1 - 2\,r_e$ from three lensing galaxies at $z = 0.4 - 0.7$. While strong Mg II, Fe II, and Mg I absorption features are found at the redshift of the double lens for HE 0047−1756 in both sightlines, these absorption features are observed in only one of the two sightlines at the redshift the HE 1104−1805 lens and no absorbers are found in any of the four sightlines near the lens for HE 0435−1223. Incidentally, HE 0435−1223 is the only one of the three lenses in our study known to reside in a group environment (Wilson et al. 2016). Here we examine the physical properties (such as temperature and ionization state), relative abundance pattern, and spatial coherence of gas kinematics in the vicinities of the two

lensing galaxies in HE 0047−1756 and HE 1104−1805.

2.5.1 Photo-ionized Cool Gas Associated with Lensing Galaxies

All Mg II absorbers detected in our study have associated absorption transitions due to Fe II λ2600, Fe II λ2586, Mg I λ2852, and Ca II λ3934. Comparisons of the relative line widths and absorption strengths between these transitions allow us to constrain both the temperature and ionization state of the gas. It is immediately clear from Tables 6 & 8 that for each component, different ionic transitions are found to share a consistent best-fit Doppler parameter which is roughly $1-2$ times the instrument resolution. Recall from Section 2.3.2 that our Voigt profile analysis was carried out with the velocity offsets of individual components fixed across all transitions, but letting log N_c and b_c vary freely for different transitions. Fixing the b_c value of each component for all transitions would lead to < 0.1 dex differences in the best-fit column density. The consistent best-fit b_c between Mg^0 and Mg^+ states lends strong support for the hypothesis that these different ions originate in the same gaseous clouds. In addition, the consistent b_c between Fe^+ and Mg^+, which differ in mass by a factor of two, indicates that the line broadening is driven by non-thermal motions and confirms the expectation that Mg II absorbing gas is typically cool with temperature $T \lesssim$ a few $\times\, 10^4$ K (e.g., Bergeron & Stasińska 1986).

Given the relatively cool gas temperature, we consider the scenario in which the gas is being photo-ionized and determine the ionization state based on the observed relative abundances between Mg^0 and Mg^+ ions. Under the photo-ionization scenario, a key factor is the ionization parameter U, which is defined as the number of ionizing photons ϕ relative to the total hydrogen number density $n_{\rm H}$, $U \equiv \phi / c\, n_{\rm H}$. For a fixed radiation field, lower gas densities lead to higher U parameters, and the gas is expected to be more highly ionized. Conversely, higher gas density lead to lower U parameters, and the gas is more neutral. We perform a series of photo-ionization calculations using the CLOUDY package (Ferland et al. 2013; v. 13.03) and construct a grid of models that span a range in U, from

$\log U = -6$ to $\log U = -1$ and a range in gas metallicity, from 1/100 solar to solar. We consider both optically-thin gas with $\log N(\mathrm{H\,I})/\mathrm{cm}^{-2} = 15$ and optically-thick gas with $\log N(\mathrm{H\,I})/\mathrm{cm}^{-2} = 19$, which are representative of the expected H I column density range for the absorbing clouds found near the lensing galaxies. For each photo-ionization model, we assume a plane-parallel geometry for the absorbing gas of $T = 10^4$ K, which is illuminated by an updated version of the Haardt & Madau (2001) ionizing radiation field (HM05 in CLOUDY) at $z = 0.5$. Then we compute the expected relative abundance ratios between Mg^0, Mg^+, and Fe^+ for gas that follows a solar abundance pattern. While no empirical knowledge is available for the neutral hydrogen column density of the Mg II absorbers found in the vicinities of the lensing galaxies, the photo-ionization models can be constrained based on the observed column density ratio between Mg^0 and Mg^+. Finally, we note that the CLOUDY models we constructed are dust-free, although we will discuss the effects of dust depletion in Section 2.5.2.

The top panel of Figure 2.9 shows the expected $N(\mathrm{Mg\,I})/N(\mathrm{Mg\,II})$ versus U for photo-ionized gas of 1/10 solar metallicty and different $\log N(\mathrm{H\,I})$ (solid and dotted curves), in comparison to obserations from Tables 2.6 & 2.8 (blue lines and associated bands to indicate the 1-σ uncertainties. The observed Mg I to Mg II column density ratios constrain the ionization parameter in the range from $\log U \approx -3.9$ to $\log U \approx -2$ or gas density from $n_\mathrm{H} \lesssim 0.04\,\mathrm{cm}^{-3}$ to $n_\mathrm{H} \lesssim 4 \times 10^{-4}\,\mathrm{cm}^{-3}$. The results are insensitive to the adopted gas metallicity. The allowed U range is consistent with previous findings for weak Mg II absorbers of $W_r(2796) < 0.3$ Å (e.g., Rigby et al. 2002) or for Lyman limit systems at similar redshifts (e.g., Lehner et al. 2013).

2.5.2 Uniform Super-solar (Fe/Mg) Across $\gtrsim 400$ km s^{-1} at $d \approx 1 - 2\,r_e$

The observed column density ratio between Fe^+ and Mg^+ ions allows us to estimate the underlying total elemental abundance ratio between iron and magnesium, (Fe/Mg), even though we cannot constrain the gas metallicity due to unknown $N(\mathrm{H\,I})$ for these absorbers.

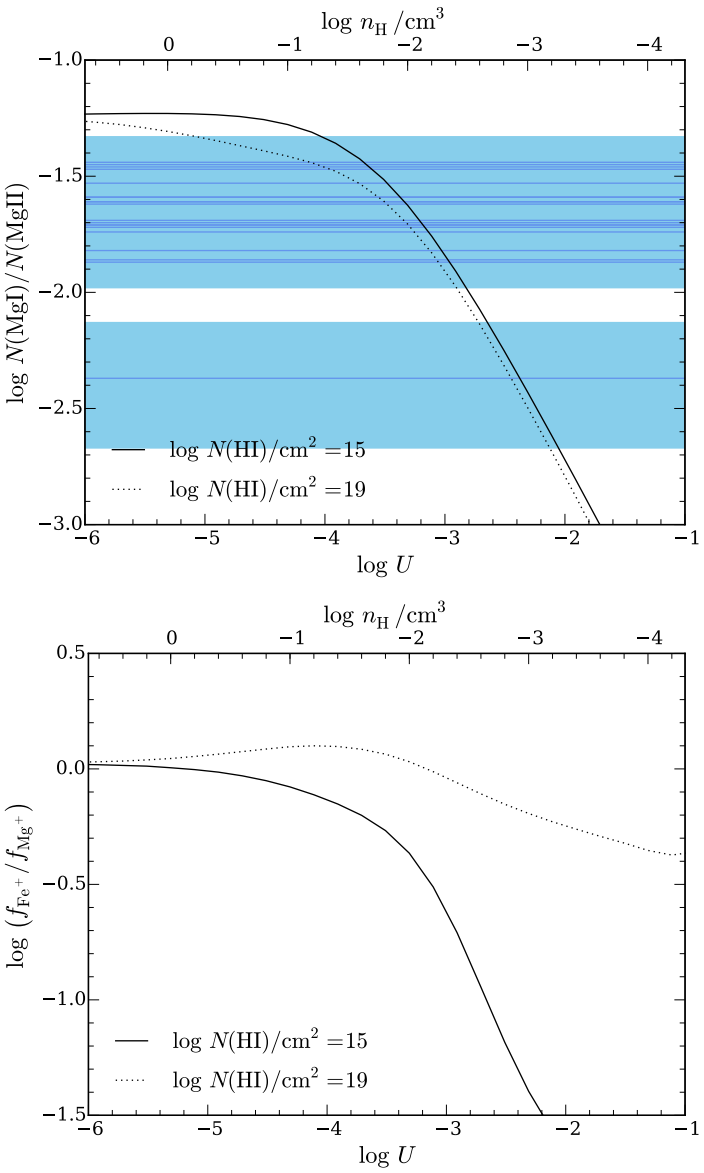

Figure 2.9: Expectations from CLOUDY photo-ionization calculations (Ferland et al. 2013; v. 13.03). The *top* panel shows the expected $N(\mathrm{Mg\,I})/N(\mathrm{Mg\,II})$ versus U for photo-ionized gas of $T = 10^4$ K, 0.1 solar metallicity, and two different $N(\mathrm{H\,I})$. The observed Mg I to Mg II column density ratios (Tables 6 & 8) are displayed in horizontal blue lines, with the band showing the 1-σ measurement uncertainties. Comparisons between observations and model predictions for both optically-thin ($\log N(\mathrm{H\,I})/\mathrm{cm}^{-2} = 15$) and optically-thick ($\log N(\mathrm{H\,I})/\mathrm{cm}^{-2} = 19$) gas constrain U to be between $\log U \approx -3.9$ and $\log U \approx -2$ Experimenting with different gas metallicities (from 0.01 solar to solar) does not change the result. The *bottom* panel shows the ionization fraction of Fe^+ relative to that of Mg^+ as a function of U. The model predictions show that independent of gas metallicity the observed $N(\mathrm{Fe\,II})/N(\mathrm{Mg\,II})$ ratio represents a conservative lower limit of the underlying (Fe/Mg) for optically thin gas ($\log N(\mathrm{H\,I})/\mathrm{cm}^{-2} = 15$), while in the optically thick regime the observed relative ionic abundance roughly reflects the underlying total (Fe/Mg) ratio.

Constraining the relative abundance between iron and magnesium is particularly interesting, because both core collapse and Type Ia supernovae (SNe) contribute to the observed iron abundance (e.g., Tsujimoto et al. 1995) while magnesium is an α element generated primarily in massive stars and core-collapse SNe (e.g., Nomoto et al. 2006). Specifically, every Type Ia supernova is expected to release $\sim 0.7\,M_{\odot}$ of iron, while at the same time producing $\lesssim 0.02\,M_{\odot}$ of magnesium (e.g., Thielemann et al. 1986; Iwamoto et al. 1999). The relative [Fe/Mg] ratio therefore provides a quantitative measure of the relative contribution of massive stars to the chemical enrichment in galaxies (e.g., Tsujimoto et al. 1995; Ferreras & Silk 2002; de Plaa et al. 2007).

Furthermore, Mg^{+} and Fe^{+} share similar ionization potentials (15 eV and 16.2 eV, respectively) and are the dominant ionization states of the respective species in both neutral and cool photo-ionized medium. Observations of $N(\mathrm{Fe\,II})/N(\mathrm{Mg\,II})$ should reflect closely the intrinsic total elemental abundance ratio, (Fe/Mg). Specifically,

$$\log\left(\frac{\mathrm{Fe}}{\mathrm{Mg}}\right) = \log\,\frac{N(\mathrm{Fe\,II})}{N(\mathrm{Mg\,II})} - \log\,\frac{f_{\mathrm{Fe}^{+}}}{f_{\mathrm{Mg}^{+}}}, \tag{2.3}$$

where $f_{\mathrm{Fe}^{+}}$ is the fraction of Fe in singly ionized state and $f_{\mathrm{Mg}^{+}}$ is the fraction of Mg in singly ionized state. The bottom panel of Figure 2.9 shows the ratio of the ionization fractions for the Fe^{+} and Mg^{+} states as a function of U. Adopting the model predictions for photo-ionized gas, we expect that the observed $N(\mathrm{Fe\,II})/N(\mathrm{Mg\,II})$ ratio represents a conservative lower limit of the underlying (Fe/Mg) for optically-thin gas, which is likely the case for weak components of $\log N(\mathrm{Mg\,II}) < 14$ near the lensing galaxies (Tables 6 & 8). In the optically-thick regime, which is likely the case for the strong components (e.g., component 2 along HE 0047−1756 B), the observed $N(\mathrm{Fe\,II})/N(\mathrm{Mg\,II})$ reflects the underlying total (Fe/Mg) ratio.

We present the observed $N(\mathrm{Fe\,II})/N(\mathrm{Mg\,II})$ versus velocity offset, $\Delta\,v$, for individual components in Figure 2.10. Observations for both sightlines A and B of HE 0047−1745 are

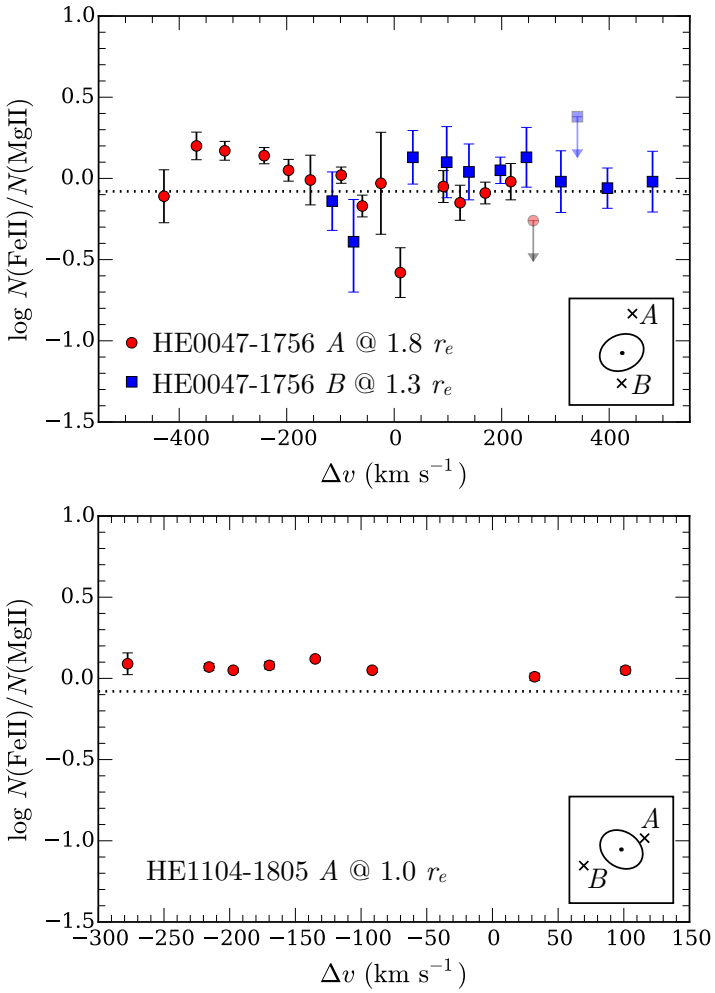

Figure 2.10: The observed column density ratio of Fe^+ to Mg^+ versus velocity offset, Δv, for individual components along both sightlines A and B of HE 0047−1745 in the *top* panel and along sightline A of HE 1104−1805 in the *bottom* panel. Error bars associated with individual data points represent the 1-σ uncertainties, with upper limits indicating an absence of Fe II absorption. The dotted line indicates the expected solar (Fe/Mg) ratio of $\log(\mathrm{Fe/Mg}) = -0.08$ (Asplund 2006) for visual comparisons. The inset shows the geometric alignment between the lensing galaxy shown as the ellipse and the lensed QSO images. Both the axis ratio and position angle of the ellipse are representative of the observed morphological properties of the lens.

presented in the *top* panel and observations for sightline A of HE 1104−1805 in the *bottom* panel. Error bars associated with individual data points represent the 1-σ uncertainties, with upper limits indicating absence of Fe II absorption.

Figure 2.10 displays two striking features. First, the observed $N(\mathrm{Fe\,II})/N(\mathrm{Mg\,II})$ ratios are high, exceeding the typical solar abundance pattern. Second, the dispersion in the observed $N(\mathrm{Fe\,II})/N(\mathrm{Mg\,II})$ ratio is small among different components across the full velocity range. The only exceptions are components 10 & 15 along HE 0047−1756 A and possibly component 2 along HE 0047−1756 B. Excluding these outliers, we find a median of $\langle \log N(\mathrm{Fe\,II})/N(\mathrm{Mg\,II}) \rangle \approx 0$ and dispersion of 0.11 and 0.09 dex, respectively, for sightlines A and B near HE 0047−1756. For HE 1104−1805 A, we find a median of $\langle \log N(\mathrm{Fe\,II})/N(\mathrm{Mg\,II}) \rangle = 0.06$ and dispersion of 0.03 dex.

Such homogeneity in abundance ratio across multiple components is not commonly seen in absorbers uncovered along random sightlines. For example, weak Mg II absorbers often display a component-to-component $N(\mathrm{Fe\,II})/N(\mathrm{Mg\,II})$ ratio that varies by ≈ 0.3 dex to more than 0.4 dex over $\Delta v \approx 50$ km s^{-1} (e.g., Narayanan et al. 2008) and high-redshift DLAs display up to 0.9 dex difference between components separated by $\Delta v \lesssim 100$ km s^{-1} (e.g., Fox et al. 2014). In contrast, the scatter of the observed $N(\mathrm{Fe\,II})/N(\mathrm{Mg\,II})$ in the vicinities of the two massive lensing galaxies is < 0.1 dex across $\Delta v > 400$ km s^{-1}.

For comparisons, we include in Figure 2.11 the observed $N(\mathrm{Fe\,II})/N(\mathrm{Mg\,II})$ versus $N(\mathrm{Fe\,II})$ for individual components found in weak Mg II absorbers of $W_r(2796) < 0.3$ Å at $z = 0.4 - 2.4$ from Rigby et al. (2002) and Narayanan et al. (2008), and in DLAs or sub-DLAs at $z = 1.8 - 2.4$ from Dessauges-Zavadsky (2004), Crighton et al. (2013), and Fox et al. (2014), together with the observations for individual components found near lensing galaxies. It is immediately clear that the relatively high $N(\mathrm{Fe\,II})/N(\mathrm{Mg\,II})$ ratios are not common among QSO absorption-line systems found along random sightlines. While weak Mg II absorbers have on average lower $N(\mathrm{Fe\,II})$ per component and exhibit a significant scatter in the observed $N(\mathrm{Fe\,II})/N(\mathrm{Mg\,II})$ ratio, only a few components have been found to show en-

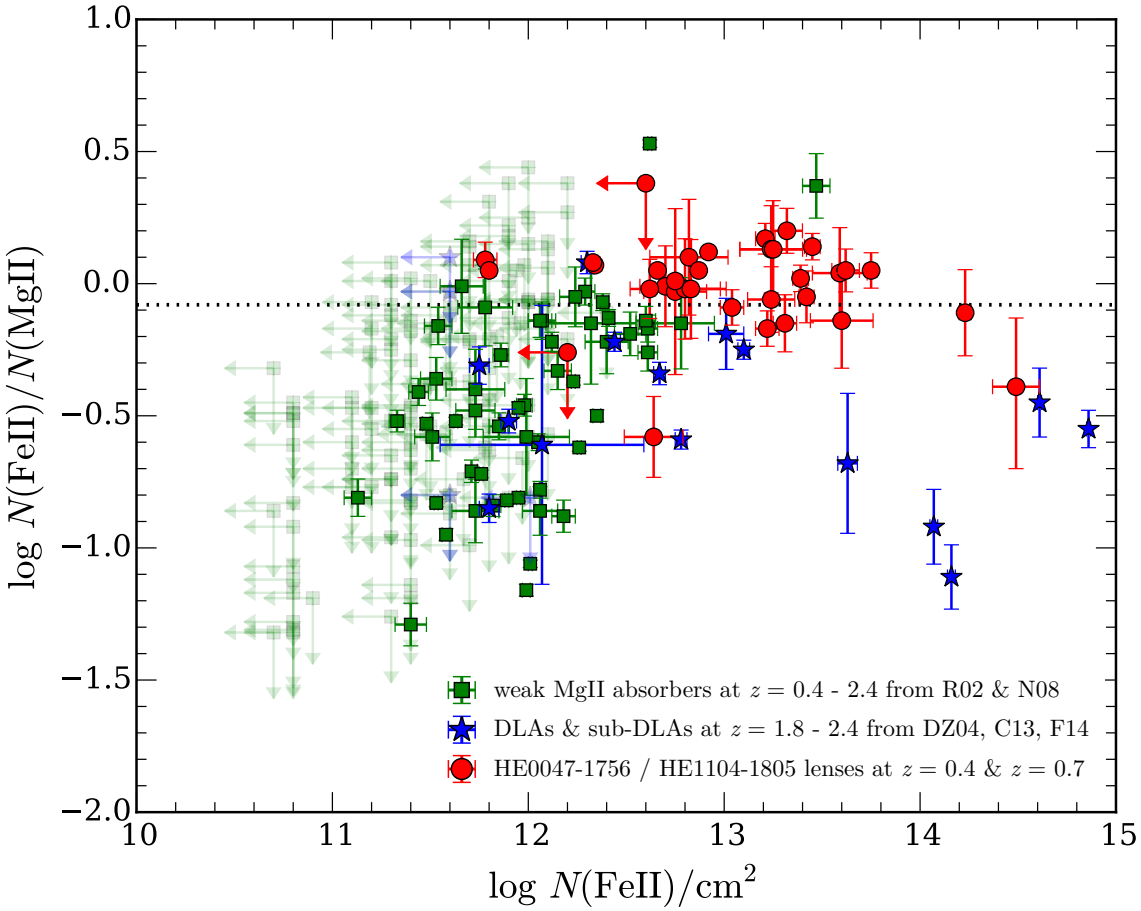

Figure 2.11: Observed Fe II to Mg II column density ratios versus N(Fe II) both for absorbers selected from random sightlines and for halo gas around lensing galaxies from our study. Each data point represents a single absorbing component resolved in high-resolution QSO spectra. Our observations near lensing galaxies are presented in red, circles with error bars showing the corresponding measurement uncertainties. Measurements from high-redshift ($z = 1.8-2.4$) DLAs and sub-DLAs from Dessauges-Zavadsky (2004), Crighton et al. (2013), and Fox et al. (2014) are shown in blue star symbols. Measurements for weak Mg II absorbers of $W_r(2796) < 0.3$ Å at $0.4 < z < 2.4$ from Rigby et al. (2002) and Narayanan et al. (2008) are shown in green squares. Absorbing components with no associated Fe II absorption transitions are shown as downward and left-pointing arrows with the data point indicating the 2-σ upper limit in N(Fe II). We have grayed out weak Mg II data points without associated Fe II detections for clarity. Like Figure 2.10, the dotted line indicates the solar (Fe/Mg) abundance pattern for visual calibrations. With the exception of three outlying points, halo clouds around lensing galaxies occupy a unique log N(Fe II)/N(Mg II)–log N(Fe II) space, separated from either the weak Mg II absorber group or DLAs/sub-DLAs. The scatter in log N(Fe II)/N(Mg II) is small, ~ 0.1 dex, in the halos around lensing galaxies. Including necessary ionization fraction corrections, our observations imply a super solar Fe to Mg abundance pattern for the halo gas around these lensing galaxies.

hancement in $N(\mathrm{Fe\,II})$ relative to $N(\mathrm{Mg\,II})$. DLAs and sub-DLAs, which are thought to originate in young star-forming galaxies, have on average higher $N(\mathrm{Fe\,II})$ per component and exhibit a significant α-element enhancement abundance pattern. Neither one of these absorber populations occupies the same parameter space as the Fe-rich components found near the lensing galaxies. The observed discrepancy strongly suggests a different origin for the gas found along the sightlines near the two lensing galaxies.

From the CLOUDY photo-ionization models presented in the bottom panel of Figure 2.9, we find $\log\,(f_{\mathrm{Fe^+}}/f_{\mathrm{Mg^+}}) \lesssim -0.3$ for the allowed range of U in the optically thin regime and $-0.3 \lesssim \log\,(f_{\mathrm{Fe^+}}/f_{\mathrm{Mg^+}}) \lesssim 0$ in the optically thick regime. Applying these conditions to Equation (2.3) leads to

$$\log\,(\mathrm{Fe/Mg}) > \log\,N(\mathrm{Fe\,II})/N(\mathrm{Mg\,II}). \tag{2.4}$$

We therefore conclude that the observed $N(\mathrm{Fe\,II})/N(\mathrm{Mg\,II})$ represents a conservative minimum for the underlying total elemental abundance ratio, (Fe/Mg), particularly in relatively weak components of $\log\,N(\mathrm{Mg\,II})/\mathrm{cm}^{-2} < 14$, for which the gas is likely optically thin to the ionizing radiation field. Adopting a solar abundance pattern of $\log\,(\mathrm{Fe/Mg})_\odot = -0.08$ (Asplund et al. 2006), we estimate a super solar Fe to Mg abundance pattern of $[\mathrm{Fe/Mg}] \equiv \log\,(\mathrm{Fe/Mg}) - \log\,(\mathrm{Fe/Mg})_\odot \gtrsim 0.1$ for individual absorbing components across a velocity range of ≈ 400 km s^{-1}.

We note that the presence of Ca II absorption (Tables 6 & 8) also strongly implies the presence of dust (e.g., Savage & Sembach 1996; Wakker & Mathias 2000), which would further alter the observed elemental abudance pattern if not accounted for. Observations of local interstellar clouds have shown that Fe is more depleted in cool phase by as much as 0.5 dex relative to Mg (Savage & Sembach 1996; Lauroesch et al. 1996). If differential dust depletion is significant, then the inferred [Fe/Mg] will be even higher.

2.5.3 Probing Spatial Coherence of Gas Kinematics Across $d \approx 8$ kpc of the HE 0047−1756 Lens

A primary goal of the multi-sightline study is to examine the spatial coherence of chemically-enriched gas across the halo (e.g., Chen et al. 2014). In our current study, the doubly lensed HE 0047−1756 exhibits an ultra-strong Mg II absorber along both lensed QSO sightlines separated by $\approx$ 8 kpc in projected distance, and offers a unique opportunity to examine possible correlation in the gas kinematics at $d \approx 1.5\, r_e$ on the opposite sides of the lensing galaxy. We have noted two remarkable similarities in the absorption signatures between the two sightlines: (1) an edge-leading signature with the strongest absorption component moving at the highest blueshifted velocity and (2) strong correlation between a large number of components over a velocity range of $\approx$ 420 km s^{-1} along each sightline (see Section 2.4.1). These observed kinematic signatures suggest strong coherence on scales of 8 kpc in the gas motion across the inner halo of the HE 0047−1756 lens galaxy, similar to the strong coherence found on scales of 10 kpc at $d \approx 40 - 50$ kpc from a blue, L_* galaxy at $z = 0.4188$ by Chen et al. (2014). A natural explanation of the edge-leading signature is a rotating disk (e.g., Lanzetta & Bowen 1992). However, if the two sightlines probe the opposite sides of a rotating disk, then the edge-leading feature of the second sightline is expected to be flipped from the first (e.g., Prochaska & Wolfe 1997). This is not what is observed. Instead, the edge-leading profiles are merely offset by $\Delta\, v \approx 350$ km s^{-1} between the two sightlines. It is not clear a gaseous stream connecting to the lensing galaxy would produce such consistent edge-leading profiles on the opposite sides of the galaxy.

Further insights into the connection between the observed absorbing gas along two closely separated sightlines may be gained from comparing the chemical abundance pattern. In Section 2.5.3 and in Figure 2.10, we show that while the majority of the absorbing components in HE 0047−1756 exhibit a uniform super solar [Fe/Mg] relative abundance with a small scatter, three components have non-negligible likelihood of being Mg-rich (α-element enhanced). These are components 10 & 15 along sightline A and component 2 along sightline B. We

note that component 2 in sightline B is especially interesting, given the observed large gas column density that exceeds all other components found near this lens. The large error bar in the Fe/Mg ratio indicates that there is a non-negligible probability that this gas may be Mg-rich. Because Mg-rich gas does not share the same SNe Ia enhanced chemical enrichment history as Fe-rich gas, these possible Mg-rich components could provide additional clues for the nature of the gas along these two sightlines.

Using the observed Fe/Mg ratio to identify absorption components sharing a common origin, we reproduce the best-fit absorption profiles of Mg II λ 2796, Fe II λ 2600, and Mg I λ 2852 transitions from Figure 2.4 in the bottom left panel of Figure 2.12 but highlight the few possibly Mg-rich components in shaded green. Excluding possible Mg-rich components, we find that the correlation between the absorption profiles along sightlines A and B weakens, with no clear maximum between $\Delta\, v = 0$ and $\Delta\, v = 600$ km s^{-1}, due to a diminishing edge-leading signature along sightline B. We therefore caution that line-of-sight kinematics alone may not be sufficient to determine the spatial coherence of gas at multiple locations.

2.6 Discussion

The widely dispersed line-of-sight gas kinematics around the lens of HE 0047−1756 is especially remarkable when compared to the H I gas detected in nearby elliptical/S0 galaxies (e.g., Oosterloo et al. 2007; Serra et al. 2012). Roughly 40% of nearby elliptical/S0 galaxies exhibit extended H I gas out to ~ 30 kpc in radius with increasing velocity shear up to ± 200 km s^{-1} at the edges of the observed H I structures (e.g., Serra et al. 2012). The observed line-of-sight velocity spread around the HE 0047−1756 lens would still exceed the largest velocity dispersion (≈ 250 km s^{-1}) known at the peak H I emission near the center of local elliptical galaxies (see Figure 6 of Serra et al. 2012). Alternatively, the observations of the HE 0047−1756 lens can be explained if these gas-rich nearby ellipticals are surrounded by high-dispersion low column density clouds that fall below the typical column density limit of N(H I) $\approx 5 \times 10^{19}$ cm^{-2} in local 21 cm observations.

The observed relative (Fe/Mg) abundance pattern offers new clues for understanding the origin of chemically-enriched cool gas in massive quiescent halos. In particular, strong metal-line absorbers are commonly attributed to starburst driven outflows (e.g., Murray et al. 2011; Booth et al. 2013). However, it is difficult to explain the presence of metal-enriched cool gas near quiescent galaxies based on the outflow scenario. Additional explanations that have been proposed include stripped satellites due to tidal interactions or ram pressure force (e.g., Wang 1993; Agertz et al. 2009; Gauthier 2013), gas accreted from the IGM (e.g., Rauch et al. 1997; Nelson et al. 2013), as well as in-situ cloud formation from thermal instabilities (e.g., Mo & Miralda-Escude 1996; Maller & Bullock 2004; Sharma et al. 2012). Different scenarios would predict different chemical abundance patterns. For example, if the gas is pre-enriched by early-generation star formation (which is expected for newly accreted IGM as well as ISM in and or stripped from blue satellites), then it is also expected to be α-element enriched (e.g., Rauch et al. 1997). On the other hand, if the gas has significant contribution from SNe Ia ejecta (which is expected for ISM in or stripped from red satellites), then it is expected to show Fe enhancement.

For the cool, Fe-rich gas, the observed super solar (Fe/Mg) ratio indicates a significant contribution to the chemical enrichment from SNe Ia. For reference, the expected SNe Ia contribution relative to total (Type Ia and core-collapse SNe combined) in the solar abundance pattern is $f_{\rm Ia} \approx 15\%$ (e.g., Tsujimoto et al. 1995; de Plaa et al. 2007). Here we estimate $f_{\rm Ia}$ for the observed Fe-rich gas around massive lensing galaxies based on the observed $N({\rm Fe\,II})/N({\rm Mg\,II})$, which shows a median of $\langle \log\, N({\rm Fe\,II})/N({\rm Mg\,II}) \rangle \approx 0 - 0.06$ (Section 2.5.2). From Equation (2.4), these values represent conservative lower bounds for $\log({\rm Fe/Mg})$. Adopting the expected yields for Type Ia and core-collapse SNe from Iwamoto et al. (1999), we estimate a minimum fractional contribution of SNe Ia to the chemical enrichment of $f_{\rm Ia} \approx 20\%$. The estimated SNe Ia contribution around massive, lensing galaxies is comparable to what is found for intracluster medium (e.g., de Plaa et al. 2007). Furthermore, SNe Ia occur in low-mass, evolved stars (e.g., Maoz et al. 2014) with long

lifetimes, which also implies that the gas has been enriched to relatively high metallicities by previous generations of massive stars. Indeed, observations of stellar atmospheres find an increasing Fe abundance with increasing metallicity (e.g., McWilliam 1997). We therefore expect the Fe-rich halo gas to also have a high metallicity. This expectation is at least consistent with what is found for the few Fe-rich, weak Mg II absorbers by Rigby et al. (2002).

Based on the uniform super solar (Fe/Mg) ratios with a small dispersion and the expected high metallicity, we argue that the Fe-rich absorbing components (which dominate the total absorption width) originate in SNe Ia enriched inner regions at radius $r \sim d$ from the lensing galaxies. The large velocity spread ($\Delta\, v \gtrsim 400$ km s^{-1}) can be attributed to recent SNe Ia ejecta (Figure 2.12). In addition to chemically enriching their environment, SNe Ia ejecta can interact with the surrounding gas and deposit thermal energy that increases the velocity dispersion of the gas. We consider stellar winds from low-mass stars an unlikely source for the observed Fe-rich gas, because observations of nearby elliptical galaxies have uncovered a predominantly α-enhanced abundance pattern in these stars (e.g., Kuntschner et al. 2010).

A SNe Ia origin is qualitatively consistent with previous finding that the radial distribution of Type Ia SNe in early-type galaxies is consistent with the Sérsic profile describing the stellar light of the galaxies (Förster & Schawinski 2008). Recall also that the lensed QSO sightlines that have revealed this cool, Fe-rich gas pass through the interstellar space of the lensing galaxies at merely $1 - 1.8\, r_e$.

Alternatively, the observed kinematic and chemical signatures may be explained by Fe-rich gas expelled from red satellites. Large-scale surveys of nearby galaxies have shown that massive, red galaxies have a significantly higher fraction of red satellites (e.g., Prescott et al. 2011). Star formation in these red satellites is shut off as a result of gas removal upon entering the host halo (e.g., Larson et al. 1980; Kawata & Mulchaey 2008). As the remaining stars continue to evolve in the satellites, we also expect increased contribution from SNe Ia to the chemical enrichment in the surrounding gas, resulting in increasingly Fe-rich abundance

patterns.

The absence of absorption features along sightline B at $1.8\,r_e$ from the lens for HE 1104−1805 and in all four sightlines at $1.4-1.7\,r_e$ from the lens for HE 0435−1223 is qualitatively consistent with the partial gas covering fraction expected from either stripped satellites or clumpy SNe Ia ejecta. However, additional factors from the galactic environments may have also played an important role in depleting the cool gas near the quad-lens of HE 0435−1223. This lensing galaxy is the only one of the three lenses in our study known to reside in a group environment (e.g., Morgan et al. 2005; Wilson et al. 2016) and the only one that appears to be devoid of cool gas at small projected distances to the lens. A similar example is found by Johnson et al. (2014), who reported a transparent sightline at $d < 20$ kpc from a pair of interacting galaxies. Interactions between group members may have heated or tidally stripped cool gas from the inner halo of the lens galaxy. Follow-up studies of the galaxy environments of the other two fields will cast important insights into possible environmental role in the CGM properties of these lenses.

It has been shown that chemically-enriched, cool gas is not uncommon in massive, quiescent halos (see e.g., Gauthier et al. 2009, 2010; Bowen & Chelouche 2011; Zhu et al. 2014). The mean gas covering fraction is found to be $\kappa_{\rm Mg\,II} > 15\%$ at $d \lesssim 100$ kpc (Gauthier & Chen 2011; Huang et al. 2016). However, the physical nature of such gas remains unknown. Based on the suppressed velocity dispersion between Mg II gas and galaxies, and the observed preferential geometric alignment of Mg II absorbers with filaments, Huang et al. (2016) have recently argued that the observed Mg II absorbers are best-explained by a combination of cool clouds formed in thermally unstable hot halos and satellite accretion through filaments. We expect that Mg II gas produced in these processes should exhibit an abundance pattern that reflects an α-element enhancement.

Interestingly, the strongest component (component 2) at $\Delta\,v \approx -75$ km s^{-1} in sightline B and a moderately strong component (component 10) at $\Delta\,v \approx 11$ km s^{-1} in sightline A of the HE 0047−1756 lens are consistent with an α-element enhancement, although we cannot

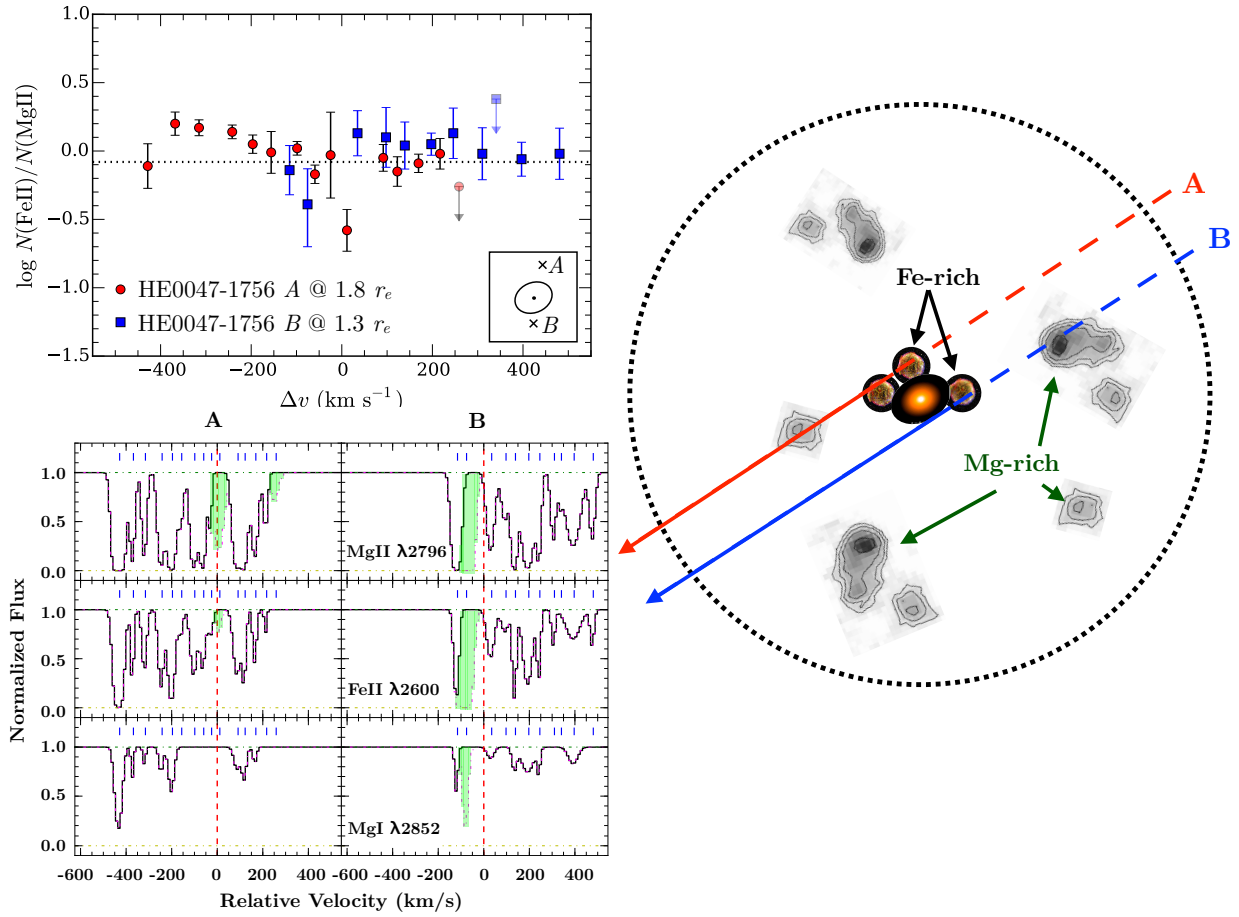

Figure 2.12: Cartoon illustrating the possibility of combining the observed $N(\mathrm{Fe\,II})/N(\mathrm{Mg\,II})$ of individual components (upper-left panel) and their kinematic signatures (lower-left panel) for identifying the origins of the absorbing clouds in the diagram on the right. We adopt observations for the HE 0047−1756 lens for the illustration. In the absorption profiles panel, we present the best-fit model absorption profiles from Figure 2.4 for Mg II λ 2796, Fe II λ 2600, and Mg I λ 2852 transitions, but with possible Mg-rich components dotted out and shaded in pale-green. The resemblance in the kinematic signatures of Fe-rich absorbing gas between sightlines A and B is weakened. Because of the required SNe Ia contributions to the elevated Fe enrichment, as well as the remarkably uniform (Fe/Mg) relative abundances for these Fe-rich absorbing components, we propose that these components originate in the inner regions at radius $r \sim d$, with the observed large velocity spread driven by recent SNe Ia ejecta (the schematic diagram on the right). While the large velocity shear (≈ 350 km s^{-1}) between the Fe-rich gas across two sightlines may be explained by bulk rotation, we consider this scenario unlikely because the edge-leading features along sightlines on the opposite sides of the rotating disk are expected to be flipped from each other (Lanzetta & Bowen 1992; Prochaska & Wolfe 1997), contrary to what is observed here. We highlight the possibility of Mg II-rich components originating in stripped gas from blue satellites or condensed halo clouds at larger distances ($r \gg d$) that were enriched by early episodes of star formation.

rule out Fe-rich gas as the origin of component 2 in sightline B. We note that component 2 toward HE 0047−1756 B contains a significant amount of neutral gas with log N(H I) > 19. The inferred large H I column density resembles the high velocity clouds (HVCs) found in the Milky Way Halo or DLAs and sub-DLAs found along random QSO sightlines. Both HVCs and DLAs exhibit α-element enhancement driven by core collapse SNe (e.g., Richter 2006; Wolfe et al. 2005), and both are primarily found in/near star-forming galaxies. This is, however, inconsistent with the old stellar population found for the lensing galaxy with no trace of a cool interstellar medium. Incidentally, a blue galaxy is seen at $\approx$ 1.6" southwest of the lens. At $z = 0.408$, this galaxy would be at $d \approx 5.4$ kpc from sightline B and nearly twice the distance from sightline A which shows weaker Mg-rich components. It is possible that this gas, if Mg-rich, originates in an infalling gas cloud or stripped gas from a blue satellite as it orbits around the lensing galaxy (see the cartoon illustration in Figure 2.12).

While it is also possible that this possibly Mg-rich gas arises in the ISM or halo gas of a faint satellite that is missed in the glare of the QSO light, we consider this an unlikely scenario. Both Gauthier et al. (2010) and Huang et al. (2016) have estimated possible contributions from the CGM of satellite galaxies to the observed Mg II absorption around massive luminous red galaxies (LRGs), assuming that the satellites can retain their gas content while moving in the hot halos of LRGs. These authors found that the expected contribution from the CGM of satellites is $< 20\,(10)\%$ at $d < 50\,(100)$ kpc. Considering only ISM, however, which is roughly 10 times smaller in size than the CGM, we expect a contribution of $< 2\,(1)\%$ at $d < 50\,(100)$ kpc. Because the cross section of blue satellites is negligible, the observed Mg-rich gas is unlikely to originate in an unresolved blue satellite. Follow-up spectroscopy to measure the redshift and star-forming properties of the blue object will provide necessary data for further studies.

In summary, if the observed ISM gas of massive galaxies is locally enriched by SNe Ia and and the halo is more dominated by pre-enriched gas from early-generation of young stars, then a radial dependence in [Fe/Mg] should be observed, with sightlines at small

projected distances showing a higher fraction of high [Fe/Mg] absorbers. We plan to test this hypothesis using a larger sample of luminous red galaxy and QSO pairs.

2.7 Conclusions

We have carried out multi-sightline absorption spectroscopy of cool gas around three lensing galaxies at $z = 0.4 - 0.7$, HE 0047−1756, HE0435−1223, and HE 1104−1805. The fields are selected from wide-separation gravitational lens systems with angular separations $\theta \gtrsim 1.5''$, which ensure that each lensed QSO serves as an independent probe of the foreground lensing galaxy. All three lensing galaxies are massive with estimated total stellar masses of $\log M_{\rm star}/M_\odot = 10.9 - 11.4$. They exhibit spectral and photometric properties that are characteristic of nearby elliptical galaxies with half-light radii of $r_e = 2.6 - 8$ kpc.

For each lensing galaxy, the lensed QSO sightlines occur at projected distances of $1-2\,r_e$, providing for the first time an opportunity to probe spatial variations of the cool gas content both in the interstellar space at $r \sim r_e$ and in the halos at larger radii $r \gg r_e$ of quiescent galaxies. The main results from our absorption-line analysis of halo gas properties at the redshift of the lensing galaxies are summarized below.

1. We observe a diverse range of absorbing gas properties among the three lensing galaxies. Specifically, both sightlines at $1.8\,r_e$ and $1.3\,r_e$ on the opposite sides of the lens for HE 0047−1756 exhibit an ultra-strong Mg II absorber at the redshift of the lens. The lensing galaxy of HE 1104−1805 exhibits a moderately strong Mg II absorber along sightline A at $\approx r_e$, but no trace of absorption within a sensitive upper limit along sightline B at $1.8\,r_e$. The strong absorbers found near the two lensing galaxies are resolved into $8 - 15$ narrow components with line-of-sight velocity spread of $\Delta\,v \approx 300 - 600$ km s^{-1}. In contrast, none of the four sightlines at $d = 1.4 - 1.7\,r_e$ from the quadruple lens for HE 0435−1223 exhibits detectable Mg II absorption, and this is the only one of the three lenses in our study known to reside in a group environment.

2. The strong Mg II absorbers with associated Fe II, Mg I, and Ca II absorption at $d = 1 - 2\,r_e$ reveal chemically-enriched cool gas ($T \lesssim$ a few $\times\ 10^4$ K) around massive, evolved galaxies at intermediate redshifts. The observed large column densities for Mg^+, Fe^+, and Ca^+ suggest a significant neutral gas fraction, similar to Lyman limit clouds. The two strongest components may even be DLAs.

3. The majority of the absorbing components exhibit a super solar Fe/Mg ratio with only three components displaying a likely Mg-rich (α-element enhancement) abundance pattern. All three possible Mg-rich components occur at the redshift of the lens for HE 0047−1756. The Fe-rich components, along both sightlines of the lens for HE 0047−1756 and one sightline of the lens for HE 1104−1805, show a uniform super solar (Fe/Mg) ratio with a dispersion of < 0.1 dex, across the full velocity range of the absorbers ($\Delta\,v \approx 300 - 600$ km s^{-1}).

4. The absorbers uncovered on the opposite sides of the lens for HE 0047−1756 appear to share a common edge-leading absorption signature, suggesting a spatial coherence on scales of $\gtrsim 8$ kpc. However, the spatial coherence is diminished when excluding possible Mg-rich gas. The kinematic signatures of the remaining components share little resemblance between the two sightlines.

Given the predominantly old stellar populations in the lensing galaxies and the observed small scatter in Fe/Mg, we argue that the Fe-rich gas (which dominates the total absorption width) originates in the inner regions (at radius $r \sim 1-2\,r_e$) of the lensing galaxies, with the observed large velocity spread driven by recent SNe Ia ejecta. Stellar winds from low-mass stars are an unlikely source for the observed Fe-rich gas, because observations of nearby elliptical galaxies have uncovered a predominantly α-enhanced abundance pattern in these stars.

We consider the possibility that the few possible Mg-rich components arise in either stripped gas or pre-enriched halo gas at larger distances $r \gg d$, where the chemical enrich-

ment is likely driven by young stars. Incidentally, a candidate gas-rich companion is seen in deep HST images of HE 0047−1756. Follow-up studies of the galaxy environment will provide further insights into the physical origin of these components.

In summary, we show that additional spatial constraints in line-of-sight velocity and relative abundance ratios afforded by a multi-sightline approach provide a powerful tool to resolve the origin of chemically-enriched cool gas in massive halos. Our study of three lensing galaxies uncovers a broad range of absorbing gas properties around massive, evolved galaxies. A larger sample of lensing galaxies is clearly necessary to determine whether the super solar Fe/Mg abundance pattern is representative of cool gas at small projected distances from evolved galaxies. At the same time, single QSO probes of foreground luminous red galaxies over a wide range of projected distances should yield important constraints for the radial dependence of [Fe/Mg], which will provide further insights into the chemical enrichment history in massive halos.

CHAPTER 3

ON THE RADIAL PROFILE OF GAS-PHASE Fe/α RATIO AROUND DISTANT GALAXIES

The contents of this chapter were previously published in the Monthly Notices for the Royal Astronomical Society as Zahedy, F. S., Chen, H.-W., Gauthier, J.-R., & Rauch, M. 2017, MNRAS, 466, 1071. They are reproduced here in accordance with the copyright agreement and with permission from the Oxford University Press.

3.1 Introduction

The presence of chemically-enriched gas out to large projected distances $d \sim 100$ kpc from galaxies is commonly attributed to super-galactic winds in starburst galaxies (e.g., Murray et al. 2011; Booth et al. 2013, Borthakur et al. 2013). However, the presence of chemically-enriched cool gas around quiescent galaxies both in the local universe and at high redshifts (e.g., Young et al. 2011; Gauthier & Chen 2011; Zhu et al. 2014; Huang et al. 2016) is difficult to reconcile on the basis of a simple outflow model. Because of a lack of intense star formation for $\gtrsim 1$ Gyrs in these quiescent galaxies, additional mechanisms beyond super-galactic winds are clearly needed to explain the presence of chemically enriched gas around galaxies. While tidal interactions and ram pressure force can work to remove interstellar gas of satellite galaxies and fill the halo around the primary galaxy (e.g., Wang 1993; Agertz et al. 2009; Gauthier 2013), without a continuing feedback mechanism the gas is expected to cool and trigger new generations of star formation in the center of the galaxy (e.g., Conroy et al. 2015).

In Chapter 2, we investigated the cool gas content around three lensing galaxies at redshift $z \sim 0.5$, using multiply-lensed QSOs. These lensing galaxies are massive with total stellar masses of $\log M_{\rm star}/M_{\odot} \gtrsim 11$ and half-light radii of $r_e = 2.6 - 8$ kpc. Their spectral and photometric properties resemble nearby elliptical galaxies, showing no trace of on-going star

formation. The multiply-lensed images of the background QSOs occur at $d = 3 - 15$ kpc, corresponding to $1 - 2\,r_e$, and therefore provide a sensitive probe of both interstellar and circumgalactic gas in these quiescent, lensing galaxies. An interesting finding from this study is that wherever Mg II absorption transitions are detected, strong Fe II absorption features are also found with an observed column density ratio, $N(\mathrm{Fe\,II})/N(\mathrm{Mg\,II})$, exceeding the typical values seen along random QSO sightlines (e.g., Rigby et al. 2002; Narayanan et al. 2008). In addition, the absorption profiles reveal complex gas kinematics with $8 - 15$ individual components per sightline over a line-of-sight velocity interval of $\Delta\,v \approx 300 - 600$ km s^{-1}.

The observed relative abundance of singly-ionized iron and magnesium has two important utilities. First of all, because Mg^+ and Fe^+ share similar ionization potentials, the relative ionization correction is small in moderately ionized gas. As demonstrated in the previous chapter, in most conditions the observed ionic column density ratio $N(\mathrm{Fe\,II})/N(\mathrm{Mg\,II})$ places a lower limit on the underlying (Fe/Mg) elemental abundance ratio. Secondly, while iron is produced in both core collapse and Type Ia supernovae (SNe) (e.g., Tsujimoto et al. 1995), magnesium is an α element produced primarily in massive stars and core-collapse SNe (e.g., Nomoto et al. 2006). The lower limit of the underlying Fe/Mg elemental abundance ratio from the observed $N(\mathrm{Fe\,II})/N(\mathrm{Mg\,II})$ therefore provides a powerful means of distinguishing between different chemical enrichment sources. In Chapter 2, we found that the cool gas in the vicinities of massive lensing galaxies exhibits a uniformly super-solar (Fe/Mg) abundance pattern, and concluded that the Fe-rich gas is most likely located in the interstellar medium (ISM) of the lensing galaxies with a significant contribution ($\gtrsim 20\%$) of Type Ia supernovae (SNe Ia) to the ISM chemical enrichment history.

The findings of Chapter 2 illustrate the potential of applying the observed $N(\mathrm{Fe\,II})/N(\mathrm{Mg\,II})$ to gain new insights into the origin of chemically-enriched diffuse gas around distant galaxies. Specifically, recently accreted gas from the intergalactic medium (IGM) is expected to show α-element enhanced abundance pattern, reflecting its early enrichment history (e.g.,

Rauch et al. 1997), while stripped gas from the ISM of evolved satellites is expected to display a relatively more Fe-rich pattern owing to a longer lifetime over which more SNe Ia can occur and contribute a higher fraction of Fe-peak elements to the environment.

On the other hand, Chapter 2 also raises an interesting question regarding the extent of SNe Ia-dominated feedback in quiescent galaxies. It has been found that the radial distribution of the rate of Type Ia SNe in early-type galaxies appears to follow the same Sérsic profile describing the stellar light distribution of the galaxies (Förster & Schawinski 2008). If cool gas around passive galaxies is locally enriched by SNe Ia, then a radial dependence in Fe/α should be expected, with a higher fraction of Fe-rich absorbers observed at smaller d. In this chapter, we expand the lensing sample studied in the previous chapter, which probes the ISM of massive quiescent galaxies at $d < 15$ kpc, to include both quiescent and star-forming galaxies with measurements of $N(\mathrm{Fe\,II})$ and $N(\mathrm{Mg\,II})$ available out to $d \approx 200$ kpc. This expanded sample allows us to examine the radial profiles of the gas-phase Fe/α ratio in galaxy halos based on the observed $N(\mathrm{Fe\,II})/N(\mathrm{Mg\,II})$.

This chapter is organized as follows. Section 3.2 presents the QSO-galaxy pair sample, as well as the QSO spectroscopic data and corresponding data reduction. The absorption-line measurements are presented in Section 3.3, and the observed absorption-line properties as a function of projected distance from passive and star-forming galaxies are presented in Section 3.4. Finally, a discussion of the implications is presented in Section 3.5. Throughout this chapter, a Λ cosmology of $\Omega_{\mathrm{M}} = 0.3$ and $\Omega_{\Lambda} = 0.7$, with a Hubble constant of $H_0 = 70$ km s^{-1} Mpc^{-1} is adopted.

3.2 Observational Data

A sample of 27 intermediate-redshift galaxies is assembled for investigating the radial profiles of the gas-phase Fe/α ratio in galaxy halos. This galaxy sample comprises 13 passive galaxies at $z = 0.40 - 0.73$ and 14 star-forming galaxies at $z = 0.10 - 1.24$ from a combination of a literature search and our own observations. These galaxies are probed by background

QSO sightlines over a range of projected distances, from $d \approx 3$ kpc to $d \approx 400$ kpc for the subsample of passive galaxies and from $d \approx 8$ kpc to $d \approx 160$ kpc for the subsample of star-forming galaxies. Here we describe the assembly of the galaxy sample, and associated echelle spectroscopy of the background QSOs.

3.2.1 Absorbing Galaxy Sample

We first performed a literature search of intermediate-redshift galaxies that are associated with known Mg II absorbers and have high-resolution echelle absorption spectra of the background QSOs available in the public data archives. Our search resulted in 16 Mg II absorbing galaxies at redshifts $0.10 \leq z \leq 0.95$ in 10 QSO fields: PKS 0122−0021, PKS 0349−1438, PKS 0439−433, PKS 0454−2203, Q1148+387, Q1241+176, PKS 1354+1933, PKS 1424−1150, 3C 336, and Q2206−199. A number of studies have previously investigated the photometric and spectroscopic properties of these absorbing galaxies (e.g, Steidel et al. 1997, 2002; Chen et al. 1998, 2001, 2005, 2008; Kacprzak et al. 2010, 2011), based on high-resolution *Hubble Space Telescope* (*HST*) imaging and deep ground-based spectroscopic observations. We utilized these studies to classify the selected galaxies into two subsamples: star-forming and passive galaxies. Star-forming galaxies are classified based on an emission-line dominated spectrum or a disk-dominated light profile (disk-to-bulge light ratios > 3, e.g., Chen et al. 1998) when the galaxy spectrum is not available. Passive galaxies are classified based on an absorption-line dominated spectrum and a bulge-dominated light profile (disk-to-bulge light ratios of < 3). Following these criteria, 13 galaxies are classified as star-forming galaxies, whereas 3 galaxies are classified as passive galaxies. In addition to these previously known Mg II-absorbing galaxies, we included a newly identified $z_{\rm gal} = 1.2418$ star-forming galaxy at $d = 17$ kpc from the QSO SDSSJ 1430+0149, where an ultra-strong Mg II absorber of rest-frame absorption equivalent width $W_r(2796) \approx 2.8$ Å had been identified at the same redshift (e.g., Zych et al. 2009).

To increase the number of passive galaxies in our sample, we included Luminous Red

Galaxies (LRGs) at $z \sim 0.5$ with associated Mg II absorption features from Gauthier & Chen (2011). We further supplemented this passive galaxy subsample with new, unpublished Mg II-absorbing LRGs from our own survey. Together with two massive lensing galaxies with associated Mg II absorption from Zahedy et al. (2016), this process resulted in 10 additional passive galaxies probed by 11 QSO sightlines at $d = 3-398$ kpc. A summary of the properties of the final sample of 27 galaxies is presented in Columns 2 to 7 of Table 3.1, where we list for each galaxy its right ascension and declination, redshift $z_{\rm gal}$, galaxy projected distance from the QSO sightline d, and the B-band luminosity L_B in unit of L_*, calculated using the redshift-dependent absolute B-band magnitude measurements from Faber et al. (2007).

3.2.2 QSO Absorption Spectroscopy

High-resolution echelle spectra of the QSOs PKS 0349−1438, PKS 1424−1150, SDSS J1430+0149, 3C336, and Q2206−199 were obtained using the Ultraviolet and Visual Echelle Spectrograph (UVES; D'Odorico et al. 2000) on the VLT-UT2 telescope under multiple observing programs (PIDs 076.A-0860(A), 075.A-0841(A), 079.A-0656(A), 081.A-0478(A), 69.A-0371(A), and 65.O-0158(A), respectively). We retrieved the reduced and order-combined individual exposures from the ESO Advanced Data Products Archive. Following data retrieval, we performed vacuum and heliocentric corrections to the QSO spectra, co-added different exposures, and performed continuum fitting to the data. The resulting spectra typically have a high signal-to-noise ratio of $S/N > 15$ per resolution element of $7 - 8$ km s^{-1} in full-width-at-half-maximum (FWHM).

Echelle spectroscopic observations were obtained using the MIKE echelle spectrograph (Bernstein et al. 2003) on the Magellan Clay Telescope for the QSOs PKS 0122−0021, PKS 0349−1438, PKS 0454−2203, SDSSJ1144+0714, SDSSJ1422+0414, SDSSJ1506+0419, SDSSJ1025+0349, SDSSJ1146+0207, SDSSJ2116−0624, and SDSSJ2324−0951 during multiple observing runs between October 2007 and April 2015. A $1''$ slit and 2×2 binning were employed for the observations of PKS 0122−0021, PKS 0349−1438, PKS 0454−2203,

Table 3.1: Summary of galaxy and absorption properties

QSO	Galaxy						Absorption[a]				
Sightline	RA (J2000)	Dec (J2000)	$z_{\rm gal}$	Ref.[b]	L_B/L_*	d (kpc)	$W_r(2796)$ (Å)	log N_{tot}(Fe II)[c]	log N_{tot}(Mg II)[d]	log N_{tot}(Mg I)[c]	log $\langle \frac{N(\rm Fe\,II)}{N(\rm Mg\,II)} \rangle$
(1)	(2)	(3)	(4)	(5)	(6)	(7)	(8)	(9)	(10)	(11)	(12)
Passive galaxies											
HE 0047−1756 *A*	00:50:27.84	−17:40:09.6	0.408	Z16	0.9	5	4.46 ± 0.02	14.61	14.67	12.97	-0.06 ± 0.14
HE 0047−1756 *B*						3	3.69 ± 0.04	14.70	14.98	12.86	-0.28 ± 0.16
SDSSJ1025+0349	10:25:32.53	+03:49:25.0	0.4650	BOSS	1.7	166	2.38 ± 0.03	14.45	> 14.48	12.41	< -0.03
HE 1104−1805 *A*	11:06:33.45	−18:21:24.5	0.729	L00	3.5	8	0.64 ± 0.01	13.50	13.44	11.75	0.06 ± 0.04
SDSSJ1144+0714	11:44:45.30	+07:14:56.5	0.4906	GC11	2.1	100	0.74 ± 0.01	14.03	14.72	12.41	-0.69 ± 0.16
SDSSJ1146+0207	11:46:58.64	+02:07:16.8	0.5437	GC11	2.6	74	1.48 ± 0.05	14.45	> 14.23	12.34	< 0.22
Q1241+176[e]	12:44:09.17	+17:21:11.9	0.5591	BOSS	3.8	159	0.14 ± 0.01	< 11.80	12.50	< 10.61	< -0.70
	12:44:11.05	+17:21:04.9	0.5507	CSV96	0.5	21	0.48 ± 0.01	13.68	13.68	12.00	0.00 ± 0.05
SDSSJ1422+0414	14:22:42.63	+04:15:12.0	0.5512	GC11	2.6	211	0.28 ± 0.01	13.13	13.71	11.07	-0.58 ± 0.04
SDSSJ1506+0419	15:06:38.26	+04:19:06.9	0.6155	GC11	3.4	299	0.35 ± 0.02	13.23	13.69	< 11.28	-0.46 ± 0.08
3C 336	16:24:37.52	+23:45:06.0	0.3675	S97	1.2	113	0.25 ± 0.01	12.99	13.11	11.13	-0.12 ± 0.22
	16:24:38.59	+23:45:21.9	0.3181	S97	0.6	55	0.51 ± 0.01	13.39	13.66	11.33	-0.27 ± 0.19
SDSSJ2116−0624	21:16:25.96	−06:24:15.4	0.5237	GC11	2.3	144	0.55 ± 0.01	13.45	> 13.80	11.66	< -0.35
SDSSJ2324−0951	23:24:50.18	−09:50:48.5	0.5446	GC11	2.1	398	1.65 ± 0.03	13.79	> 14.12	12.28	< -0.33
Star-forming galaxies											
PKS 0122−0021	01:25:27.67	−00:05:31.4	0.3985	M15	1.8	163	0.34 ± 0.02	12.74	14.29	11.92	-1.55 ± 0.28
	01:25:28.21	−00:05:54.6	0.9541	M15	1.6	77	0.12 ± 0.01	12.00	12.91	< 10.89	-0.91 ± 0.12
PKS 0349−1438	03:51:27.80	−14:28:58.2	0.3567	C98	0.6	72	0.21 ± 0.01	13.07	13.97	11.04	-0.91 ± 0.11
PKS 0439−433	04:41:17.25	−43:13:40.1	0.1010	CKR05	1.0	8	...	14.92	15.51[f]	...	-0.59 ± 0.07[h]
PKS 0454−2203	04:56:08.82	−21:59:27.0	0.4838	K10	1.4	108	0.42 ± 0.01	13.49	13.66	11.83	-0.17 ± 0.08
Q 1148+387[e]	11:51:29.26	+38:25:56.4	0.5536	S02	1.0	23	0.64 ± 0.01	13.49	13.74	< 11.08	-0.25 ± 0.05
PKS 1354+1933	13:57:04.53	+19:19:15.1	0.4592	EGY91	0.5	44	0.85 ± 0.01	13.64	13.88	11.86	-0.24 ± 0.14
PKS 1424−1150	14:27:38.18	−12:03:32.9	0.3404	C01	0.6	85	0.15 ± 0.02	< 12.73	12.70	11.49	< 0.03
SDSSJ1430+0149	14:30:40.71	+01:49:40.8	1.2418	Z16b	0.8	17	2.86 ± 0.01	15.23	15.48[g]	13.04	-0.25 ± 0.09[i]
3C 336	16:24:38.19	+23:45:22.0	0.702	S97	0.5	113	0.040 ± 0.003	< 11.35	12.16	< 10.25	< -0.81
	16:24:38.42	+23:45:15.2	0.798	S97	0.4	71	0.45 ± 0.01	12.59	13.29	< 11.02	-0.70 ± 0.08
	16:24:38.77	+23:45:08.3	0.472	S97	0.2	34	0.81 ± 0.01	13.52	14.12	11.70	-0.59 ± 0.12
	16:24:39.30	+23:45:12.1	0.892	S97	0.7	23	1.55 ± 0.01	14.73	> 14.50	12.50	< 0.23
Q2206−199	22:08:51.55	−19:43:52.6	0.948	GB97	2.1	87	0.25 ± 0.01	12.48	13.37	10.87	-0.89 ± 0.15

Notes

[a] The typical uncertainty in total column densities of Fe II, Mg II, and Mg I absorption (Columns 9 through 11) is smaller than 0.05 dex for all absorption systems; see Section 3.3. The quoted uncertainty in $\log \langle N(\rm Fe\,II)/N(\rm Mg\,II) \rangle$ (Column 12) for each system is the dispersion from the weighted mean, which represents the scatter in $N(\rm Fe\,II)/N(\rm Mg\,II)$ among individual components of the corresponding absorber.

[b] References for galaxy redshifts: Ellingson, Green & Yee 1991 (EGY91); Churchill, Steidel & Vogt 1996 (CSV96); Steidel et al. 1997 (S97); Guillemin & Bergeron 1997 (GB97); Chen et al. 1998 (C98); Lidman et al. 2000 (L00); Chen et al. 2001 (C01); Steidel et al. 2002 (S02); Chen, Kennicutt & Rauch 2005 (CKR05); Kacprzak et al. 2010 (K10); Gauthier & Chen 2011 (GC11); Dawson et al. 2013 (BOSS); Muzahid et al. 2015 (M15); Zahedy et al. 2016 (Z16); This work (Z16b).

[c] The upper limits are 2-σ limits on the total column density for non detections, estimated using the error spectrum.

[d] The lower limits represent 2-σ limits on the total column density for saturated Mg II $\lambda\lambda$ 2796, 2803 absorption doublet.

[e] Absorption-line measurements for these fields are adopted from Churchill et al. (2000) and Churchill & Vogt (2001).

[f] Because the Mg II $\lambda\lambda$ 2796, 2803 absorption doublet falls outside the observable spectral window for this QSO sightline, the total N(Mg II) of the system was estimated from the total S II column density of the system, $\log N_{\rm tot}$(S II); see Section 3.3.

[g] Because the Mg II $\lambda\lambda$ 2796, 2803 absorption doublet is heavily saturated for this absorption system, $\log N_{\rm tot}$(Mg II) was estimated from the total Si II column density of this system, $\log N_{\rm tot}$(Si II); see Section 3.3.

[h] The error is estimated by propagating the statistical errors for $\log N_{tot}$ (Fe,II), $\log N_{tot}$(S II), and the uncertainty in the adopted (Mg/S) ratio from Asplund et al. 2009; see Section 3.3.

[i] The error is estimated by propagating the statistical errors for $\log N_{tot}$ (Fe,II), $\log N_{tot}$(Si II), and the uncertainty in the adopted (Mg/Si) ratio from Asplund et al. 2009; see Section 3.3.

Table 3.2: Journal of QSO echelle spectroscopy

QSO Image (1)	$z_{\rm em}$ (2)	Instrument (3)	Exp. time (s) (4)	Date (5)
3C336	0.927	UVES	9800	2002 Apr, May
HE 0047−1756*A*	1.676	MIKE	7200	2013 Nov
HE 0047−1756*B*	1.676	MIKE	5700	2013 Nov
HE 1104−1805*A*	2.305	HIRES	19300	1997 Feb
		UVES	19000	2001 Jun
PKS 0122−0021	1.077	MIKE	1200	2007 Oct
PKS 0349−1438	0.616	MIKE	1800	2007 Oct
PKS 0454−2203	0.533	MIKE	2700	2007 Oct
PKS 1354+1933	0.720	UVES	600	2001 Jun
PKS 1424−1150	0.806	UVES	720	2005 Jul
Q2206−199	2.558	UVES	17100	2000 May
SDSSJ1025+0349	1.325	MIKE	5400	2015 Apr
SDSSJ1144+0714	0.919	MIKE	6000	2010 May
SDSSJ1146+0207	1.137	MIKE	9000	2010 May
SDSSJ1422+0414	0.972	MIKE	6000	2010 May
SDSSJ1430+0149	2.119	UVES	12150	2007 May, Jun
		UVES	2930	2008 Aug
SDSSJ1506+0419	1.288	MIKE	9000	2010 May
SDSSJ2116−0624	1.042	MIKE	8000	2010 May
SDSSJ2324−0951	0.764	MIKE	9000	2010 Sep

SDSSJ1144+0714, SDSSJ1422+0414, SDSSJ1506+0419, SDSSJ2116−0624, and SDSSJ2324 −0951. A $0.7''$ slit and 2×2 binning were employed for the observations of SDSSJ1146+0207, and a $0.7''$ slit and 3×3 binning were employed for the observations of SDSSJ1025+0349. MIKE delivers spectral resolutions of FWHM ~ 12 km s^{-1} and 8 km s^{-1} for the $1.0''$ and $0.7''$ slits, respectively. The spectra were reduced using a custom data reduction pipeline previously described in Chen et al. (2014) and Zahedy et al. (2016). The final combined spectra are characterized by $S/N > 10$ per resolution element at $\lambda > 3500$ Å. Finally, details of the data reduction for the echelle spectra of the two lensed QSO systems HE 0047−1756 (MIKE) and HE 1104−1805 (UVES and Keck HIRES) have previously been described in Zahedy et al. (2016). A journal of the echelle spectroscopic observations of the QSO sightlines in our study is shown in Table 3.2.

3.3 Absorption Line Analysis

The high-resolution echelle spectra of the QSOs described in Section 3.2 enable accurate constraints on both the integrated rest-frame Mg II absorption equivalent width ($W_r(2796)$) and the ionic column densities of Fe^+, Mg^+, and Mg^0 for each galaxy in our sample. In particular, a component-by-component analysis allows us to examine how the relative abundance ratios between any two ions vary within individual galaxy halos and across the full sample (see Chapter 2). We employ a custom software, previously developed by and described in Zahedy et al. (2016), to perform a Voigt profile fitting analysis for constraining the Mg II, Mg I, and Fe II column densities of individual absorbing components. We perform a simultaneous fit to prominent absorption transitions, including the Mg II $\lambda\lambda\,2796, 2803$ doublet, Mg I $\lambda\,2852$, and a series of Fe II transitions. For all galaxies, Fe II $\lambda\,2600$ and Fe II $\lambda\,2586$ transitions are included in the Voigt profile analysis. For galaxies at $z \gtrsim 0.5$, additional Fe II $\lambda\,2382$, Fe II $\lambda\,2374$, and Fe II $\lambda\,2344$ transitions are included.

For individual Mg II absorbing components with no corresponding Fe II or Mg I absorption, we measure a 2-σ upper limit in the absorption equivalent width of the strongest transitions using the error spectrum. The upper limits are evaluated over a spectral window twice the FWHM of the corresponding Mg II component. The measured 2-σ equivalent width limits are then converted to 2-σ upper limits of the component column densities under an optically-thin assumption. For saturated Mg II absorbing components, we place 2-σ lower limits of the component column densities based on a grid search of the χ^2 values from the Voigt profile fitting results.

In five cases, we cannot measure the Mg II absorption strength directly either due to missing echelle spectra in the public archives or a lack of spectral coverage for the relevant transitions. Three of these systems are identified along QSO sightlines Q1241+176 and Q1148+387. The observed $W_r(2796)$ and total Fe II, Mg II, and Mg I column density measurements for these systems have been published in Churchill et al. (2000) and Churchill & Vogt (2001). We adopt these values for our subsequent analysis. In addition, the galaxy

at $z = 0.101$ in the field of PKS 0439−433 does not have Mg II absorption spectra available. The Mg II absorber associated with the galaxy at $z = 1.24$ in the field of SDSSJ 1430+0549 is heavily saturated, and no useful constraint for the Mg II absorption column density is available. Finally, two lensing galaxies have been published in Zahedy et al. (2016). Excluding these galaxies leads to 20 galaxies for which we can perform our own Voigt profile analysis. The results of the component-by-component Voigt profile analysis of Mg II, Mg I, and Fe II absorption for these 20 galaxies are presented in Figure 3.1.

For the galaxy at $z = 0.101$ and $d = 8$ kpc from PKS 0439−433, a damped Lyman Lyα (DLA) absorption feature is found in the QSO spectrum. Measurement of the total Fe II column density, $N_{\rm tot}$(Fe II), is based on far-ultraviolet transitions observed using the Cosmic Origins Spectrograph (COS; Green et al. 2012) on board *HST*. We adopt $\log N_{\rm tot}({\rm Fe\,II})/{\rm cm}^{-2} = 14.92 \pm 0.03$ from Som et al. (2015). Furthermore, because no Mg II column density measurement is available for this galaxy, we infer the total Mg II column density, $N_{\rm tot}$(Mg II), from the reported total column density of another α-element ion S^+, $N_{\rm tot}$(S II). For this DLA, Som et al. (2015) measured $\log N_{\rm tot}({\rm S\,II})/{\rm cm}^{-2} = 15.03 \pm 0.03$. We assume a solar elemental abundance pattern of $\log ({\rm Mg/S})_\odot = 0.5$ dex (Asplund et al. 2009) for this system, motivated by the observed near-solar metallicity of the DLA (e.g., Chen et al. 2005; Som et al. 2015). To investigate the ionization correction between the elemental ratio (Mg/S) and the observed ionic ratio $N_{\rm tot}({\rm Mg\,II})/N_{\rm tot}({\rm S\,II})$, we perform photoionization calculations using Cloudy (Ferland et al. 2013; v.13.03) for a $T = 10^4$ K cloud with neutral hydrogen column density and metallicity reported for this system ($\log N({\rm H\,I})/{\rm cm}^{-2} = 19.63$; [S/H]= 0.1). We assume a plane-parallel geometry for the gas cloud, which is illuminated with an updated Haardt & Madau (2001) ionizing radiation field (HM05 in Cloudy) at $z = 0.1$. Using the photoionization model and applying $N_{\rm tot}({\rm Fe\,II})/N_{\rm tot}({\rm Fe\,III})$ of the absorbing gas for constraining the mean ionization parameter, we find that the ionization correction is negligible between (Mg/S) and $N_{\rm tot}({\rm Mg\,II})/N_{\rm tot}({\rm S\,II})$. Based on the assumed $({\rm Mg/S})_\odot$, we infer $\log N_{\rm tot}({\rm Mg\,II})/{\rm cm}^{-2} = 15.51 \pm 0.06$, where the error is estimated by prop-

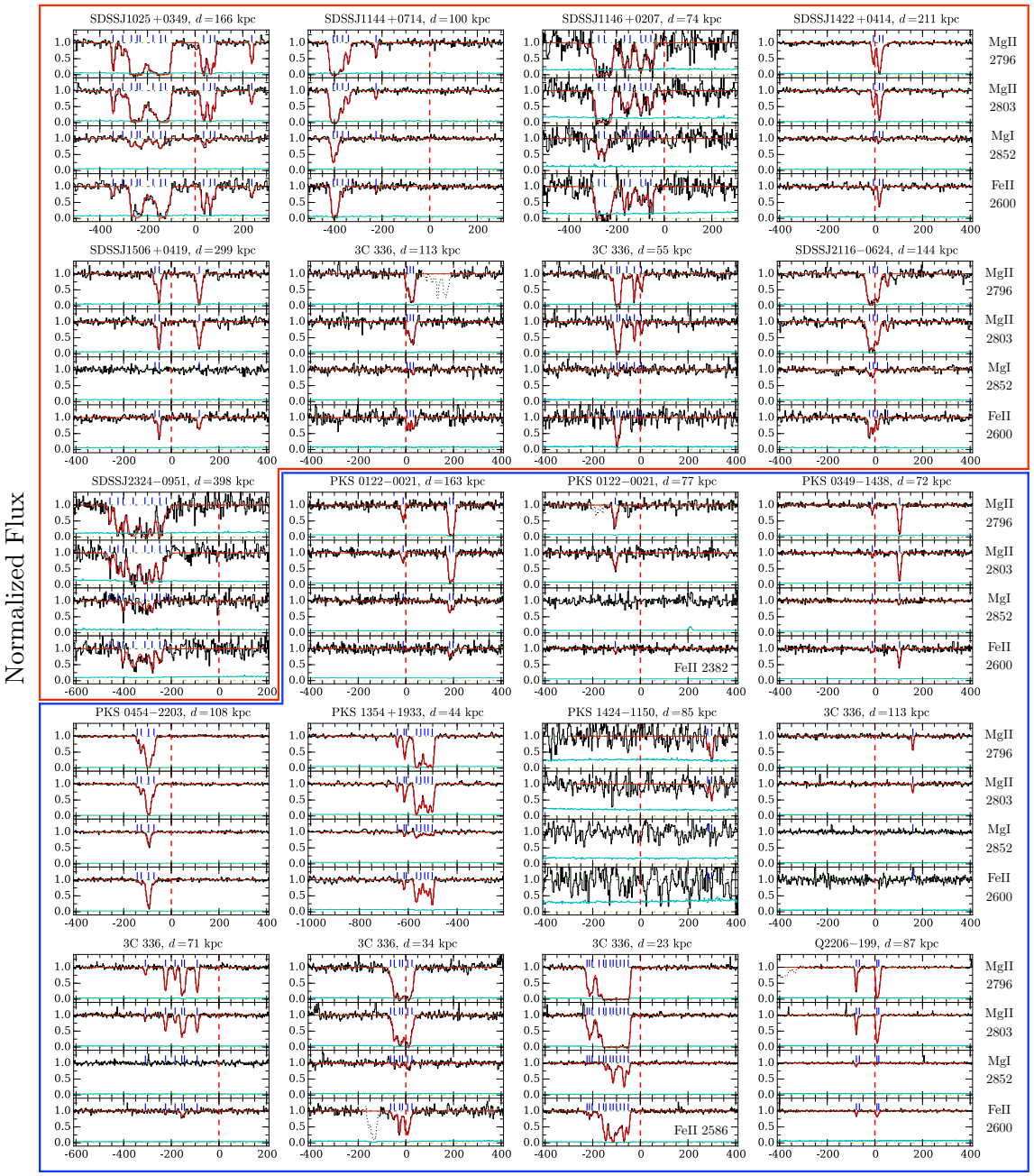

Figure 3.1: Summary of the component-by-component Voigt profile analysis of Mg II, Mg I, and Fe II absorption for 20 galaxies that have not been published previously. For each galaxy, the observed absorption files of the Mg II doublet, Mg I λ 2852, and Fe II λ 2600 are presented from top to bottom panels. In each panel, the absorption spectra and corresponding 1-σ error array are shown in black and cyan, respectively. The best-fit Voigt profile is shown in red. Contaminating features have been dotted out for clarity. The centroid of each absorbing component is marked by a blue tick mark at the top of each panel. Zero velocity corresponds to the systemic redshift of the absorbing galaxy. Galaxy projected distance is indicated at the top of each four-panel block. Finally, the red outlining box encloses passive galaxies and blue includes star-forming galaxies.

agating the statistical error for $\log N_{\rm tot}(\rm S\,II)$ and the uncertainty in the adopted (Mg/S) ratio from Asplund et al. 2009.

For the galaxy at $z = 1.2418$ and $d = 17$ kpc from SDSSJ1430+0149, the Mg II absorption line is heavily saturated. We infer $N_{\rm tot}(\rm Mg\,II)$ from the absorption strength of the weaker and non-saturated Si II λ1808 transition also recorded in the public UVES spectra. A Voigt profile analysis returns a best-fit integrated $\log N_{\rm tot}(\rm Si\,II)/cm^{-2} = 15.75 \pm 0.05$, which is consistent with the published value in Zych et al. (2009). We adopt a solar elemental abundance ratio of $\log (\rm Mg/Si)_{\odot} = 0.1$ dex for this system, which is consistent with what has been observed for a number of $z > 1$ DLAs (e.g., Dessauges-Zavadsky et al. 2006). The ionization correction between (Mg/Si) and ionic ratio $N_{\rm tot}(\rm Mg\,II)/N_{\rm tot}(\rm Si\,II)$ is estimated using a CLOUDY photoionization model for a plane-parallel cloud with 0.1 solar metallicity and $\log N(\rm H\,I)/cm^{-2} = 19.5$, which is illuminated with the HM05 radiation field at $z = 1.24$. Using the model output and the observed $N_{\rm tot}(\rm Mg\,I)/N_{\rm tot}(\rm Si\,II)$ ratio, we estimate $N_{\rm tot}(\rm Mg\,II)/N_{\rm tot}(\rm Si\,II) = 0.44 \times N(\rm Mg)/N(\rm Si)$ for this system and infer $\log N_{\rm tot}(\rm Mg\,II)/cm^{-2} = 15.48 \pm 0.07$, where the error is estimated by propagating the statistical error for $\log N_{\rm tot}(\rm Si\,II)$ and the uncertainty in the adopted (Mg/Si) ratio from Asplund et al. 2009.

The results of the absorption-line analysis are summarized in Columns 8 through 11 of Table 3.1, which present $W_r(2796)$ and the total column densities of Fe II, Mg II, and Mg I absorption, $\log N_{\rm tot}(\rm Fe\,II)$, $\log N_{\rm tot}(\rm Mg\,II)$, $\log N_{\rm tot}(\rm Mg\,I)$, summed over all individual components. Upper limits of the total column densities indicate non-detections, whereas lower limits indicate saturated absorption. The typical uncertainty in the total integrated column densities is smaller than 0.05 dex for all absorption systems.

The general absorption properties of the galaxy sample are summarized by the radial profile of Mg II absorption in Figure 3.2, which displays the observed $W_r(2796)$ versus projected distance d for all galaxies in the sample where $W_r(2796)$ measurements are available. The data points are color-coded according to the $N_{\rm tot}(\rm Fe\,II)$ associated with each galaxy.

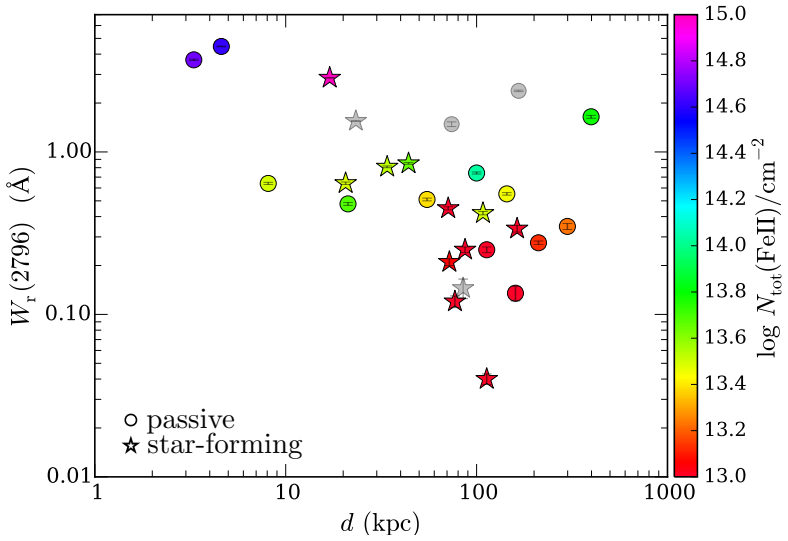

Figure 3.2: Rest-frame Mg II absorption equivalent width $W_r(2796)$ versus galaxy projected distance d for the galaxy sample in this study. Circles represent passive galaxies, while stars represent star-forming galaxies. The color of each data point represents the total Fe II column density, $N_{\rm tot}$(Fe II), of the absorption system associated with each galaxy. grayed out data points mark absorption systems with no constraints on the mean Fe II/Mg II ratio (see Figure 3.4 below) due to saturation (three galaxies) and poor signal-to-noise ratio (one galaxy). We note that the Mg II doublet falls outside the observable window for PKS 0439−433 and thus is not plotted here (see also Section 3.3 for a detailed discussion on this system).

Absorption systems with poor constraints on the N(Fe II)/N(Mg II) ratio due to either saturation or low signal-to-noise ratios are shown in gray (see below). With the exception of two passive galaxies at $d > 100$ kpc which exhibit saturated Mg II absorption features, the Mg II absorbing gas around the galaxies in our sample follow a similar declining trend of $W_r(2796)$ with increasing d as presented in Chen et al. (2010) and Nielsen et al. (2013). In addition, the observed N(Fe II) also appears to decline with increasing d.

To examine the relative Fe to Mg abundance pattern, we present in Figure 3.3 the Fe II to Mg II column density ratio, N(Fe II)/N(Mg II), versus Fe II column density, N(Fe II), for individual absorbing components associated with passive (circles in the top panel) and star-forming (star symbols in the bottom panel) galaxies. The data points are color-coded by the projected distances of the absorbing galaxies, and components associated with the two lensing galaxies (both passive) at $d < 10$ kpc are shown in pale red to be separated from absorbing components found at $d > 10$ kpc from non-lensing galaxies. When Fe II

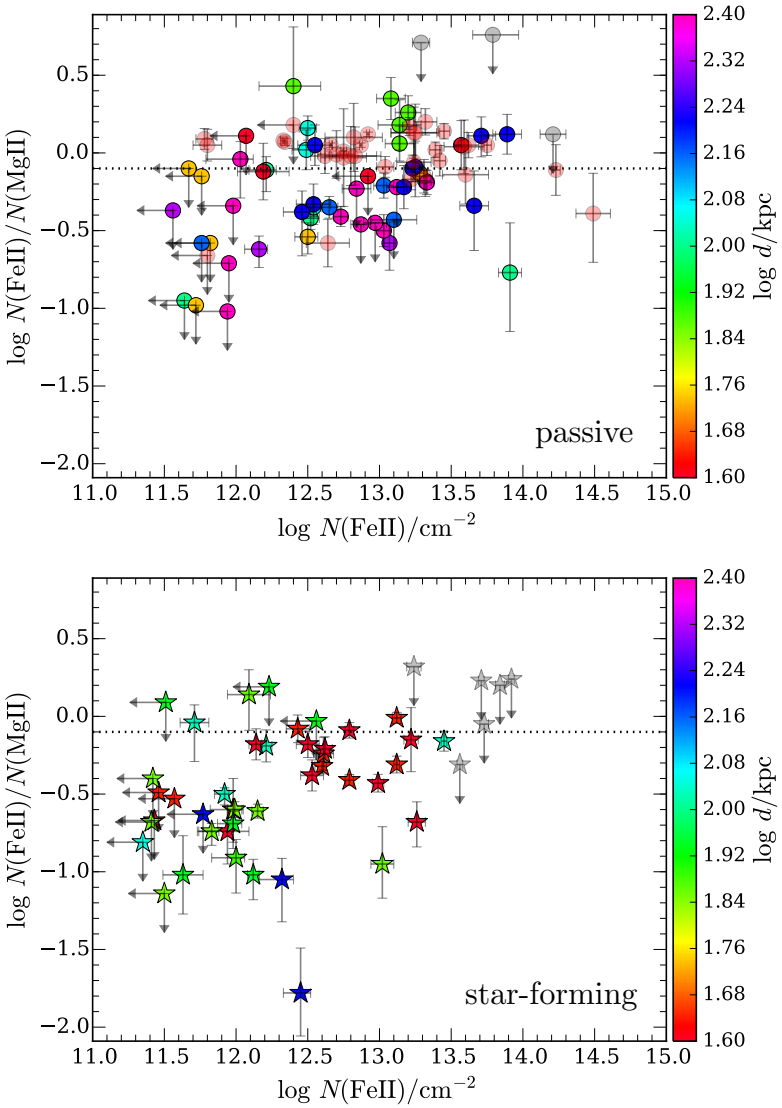

Figure 3.3: Observed Fe II to Mg II column density ratios versus Fe II column density for individual components associated with passive (circles in the top panel) and star-forming (star symbols in the bottom panel) galaxies in this study. Error bars associated with each data point show the measurement uncertainties. The color of each data point represents the projected distance d of the absorbing galaxy. Saturated components associated with galaxies with poor constraints on the mean Fe II/Mg II ratio (see Figure 3.4 below) are grayed out. Both lensing galaxies in the passive subsample exhibit strong Mg II absorption at $d < 10$ kpc. The absorbers are resolved into $8 - 15$ components and show pre-dominantly Fe-rich gas (Zahedy et al. 2016). Components associated with these lensing galaxies are shown in pale red to be separated from non-lensing galaxies at $d > 10$ kpc in the top panel. In both panels, when a Mg II absorbing component has no corresponding Fe II absorption detected, it is shown as downward and left-pointing arrows with the data point indicating the 2-σ upper limit of N(Fe II). In addition, when Mg II components are saturated, the inferred 2-σ lower limit on N(Mg II) directly translates to a 2-σ upper limit on N(Fe II)/N(Mg II). The dotted horizontal line indicates the solar (Fe/Mg) abundance pattern from Asplund et al. (2009), log $(\mathrm{Fe/Mg})_\odot = -0.10$, to guide visual comparisons.

absorption is not detected or when Mg II components are saturated, a 2-σ limit is placed on $N(\mathrm{Fe\,II})/N(\mathrm{Mg\,II})$. For heavily saturated Mg II components, no sensitive constraints can be obtained. These components are shown in gray.

Two interesting features are seen in Figure 3.3. First, passive galaxies (including both lensing and non-lensing galaxies) display a large fraction ($> 50\%$) of Fe II-rich gas at $d < 100$ kpc (data points with colors red through green) with $\log N(\mathrm{Fe\,II})/N(\mathrm{Mg\,II}) > -0.1$ dex. At larger distances, $d \gtrsim 100$ kpc, only five components associated with two passive galaxies show predominantly Fe II-rich content and the remaining 33 components are consistent with Mg II-rich gas with $\log N(\mathrm{Fe\,II})/N(\mathrm{Mg\,II}) \lesssim -0.1$ dex (data points with colors blue through magenta). Secondly, the majority of absorbing components associated with star-forming galaxies are consistent with an Mg II-rich content with $\log N(\mathrm{Fe\,II})/N(\mathrm{Mg\,II}) \lesssim -0.1$ dex over the full projected distance range probed by the sample. Only three out of 43 non-saturated components display $\log N(\mathrm{Fe\,II})/N(\mathrm{Mg\,II}) \gtrsim -0.1$ dex.

3.4 The Radial Profile of $N(\mathrm{Fe\,II})/N(\mathrm{Mg\,II})$ in Galaxy Halos

Figure 3.3 suggests that $N(\mathrm{Fe\,II})/N(\mathrm{Mg\,II})$ in galaxy halos depends on both the projected distance and star formation history of the absorbing galaxy. To better quantify how the observed $N(\mathrm{Fe\,II})/N(\mathrm{Mg\,II})$ ratio depends on galaxy properties, we compute a $N(\mathrm{Mg\,II})$-weighted mean Fe II to Mg II column density ratio for each absorption system according to the following equation,

$$\begin{aligned} \log \left\langle \frac{N(\mathrm{Fe\,II})}{N(\mathrm{Mg\,II})} \right\rangle &= \log \sum_i w_i \frac{N_i(\mathrm{Fe\,II})}{N_i(\mathrm{Mg\,II})} \\ &= \log N_{\mathrm{tot}}(\mathrm{Fe\,II}) - \log N_{\mathrm{tot}}(\mathrm{Mg\,II}), \end{aligned} \tag{3.1}$$

where $w_i = N_i(\mathrm{Mg\,II})/N_{\mathrm{tot}}(\mathrm{Mg\,II})$ for component i, and $\log N_{\mathrm{tot}}(\mathrm{Fe\,II})$ and $\log N_{\mathrm{tot}}(\mathrm{Mg\,II})$ are the total column densities of Fe II and Mg II, respectively, summed over all individual

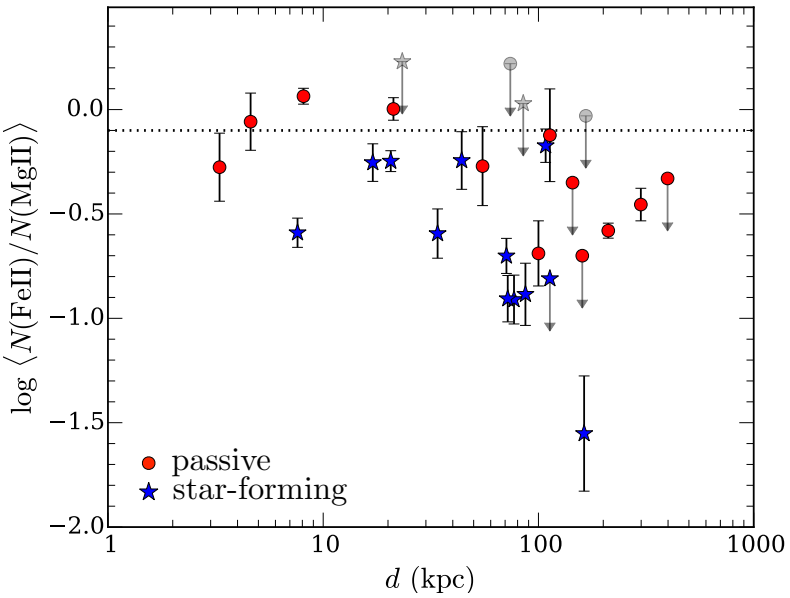

Figure 3.4: Mean Fe II to Mg II column density ratio, $\langle N(\mathrm{Fe\,II})/N(\mathrm{Mg\,II})\rangle$, from Equation (3.1) versus galaxy projected distance, d, for absorbers associated with passive galaxies (red circles) and for those associated with star-forming galaxies (blue stars). Error bars for each data point represent the dispersion among individual component Fe II to Mg II ratios of the corresponding absorber. As shown in Figure 3.3, only 2-σ upper limits can be placed on $N(\mathrm{Fe\,II})/N(\mathrm{Mg\,II})$, if Fe II absorption is not detected or if Mg II components are saturated. These upper limits are propagated into the estimates of $\langle N(\mathrm{Fe\,II})/N(\mathrm{Mg\,II})\rangle$ for each absorbing galaxy and are indicated as downward arrows. Four galaxies do not have sensitive constraints for $\langle N(\mathrm{Fe\,II})/N(\mathrm{Mg\,II})\rangle$, either due to heavily saturated Mg II absorbers or absence of a strong limit on the Fe II absorption. These data points are grayed out for clarity. Following Figure 3.3, the dotted horizontal line indicates the solar (Fe/Mg) abundance pattern, for visual comparisons. Two interesting features are evident: (1) passive galaxies exhibit on average higher $\langle N(\mathrm{Fe\,II})/N(\mathrm{Mg\,II})\rangle$ than star-forming galaxies; and (2) $\langle N(\mathrm{Fe\,II})/N(\mathrm{Mg\,II})\rangle$ appears to show a mild declining trend toward larger d for both passive and star-forming subsamples.

absorbing components in a given system. The mean $N(\mathrm{Fe\,II})/N(\mathrm{Mg\,II})$ ratio for each absorption system is presented in Column 11 of Table 1. The quoted uncertainty in $\log\langle N(\mathrm{Fe\,II})/N(\mathrm{Mg\,II})\rangle$ for each system is the dispersion from the weighted mean, which represents the scatter in Fe II to Mg II column density ratio among individual components of the corresponding absorber.

Figure 3.4 displays $\langle N(\mathrm{Fe\,II})/N(\mathrm{Mg\,II})\rangle$ versus d for passive (red circles) and star-forming (blue stars) galaxies. Three galaxies exhibit heavily saturated Mg II absorbers: (1) the passive galaxy at $z = 0.5437$ and at $d = 74$ kpc from SDSSJ 1146+0207; (2) the passive galaxy

at $z = 0.465$ and at $d = 166$ kpc from SDSSJ 1025+0349; and (3) the star-forming galaxy at $z = 0.892$ and at $d = 23$ kpc from 3C336. No meaningful constraints for $\langle N(\mathrm{Fe\,II})/N(\mathrm{Mg\,II})\rangle$ can be obtained for these absorbers. In addition, the star-forming galaxy at $z = 0.3404$ and at $d = 85$ kpc from PKS 1424−1150 exhibit only a weak Mg II absorber and Fe II absorption is not detected. The available absorption spectra do not place a sensitive constraint for $\langle N(\mathrm{Fe\,II})/N(\mathrm{Mg\,II})\rangle$. All four galaxies are grayed out in Figure 3.4 for clarity. Considering only galaxies for which measurements of (or strong constraints for) $\langle N(\mathrm{Fe\,II})/N(\mathrm{Mg\,II})\rangle$ are available, it is clear that passive galaxies exhibit on average higher $\langle N(\mathrm{Fe\,II})/N(\mathrm{Mg\,II})\rangle$ than star-forming galaxies. In addition, $\langle N(\mathrm{Fe\,II})/N(\mathrm{Mg\,II})\rangle$ appears to show a mild declining trend toward larger d for both passive and star-forming subsamples.

To further examine the dependence of $N(\mathrm{Fe\,II})/N(\mathrm{Mg\,II})$ ratio on galaxy projected distance d, we divide each of the passive and star-forming subsamples into low- and high-d subsamples. The adopted bin size in d is determined so that there are roughly equal number of galaxies (five to seven galaxies) in each subsample. We then compute the median value $\log\langle N(\mathrm{Fe\,II})/N(\mathrm{Mg\,II})\rangle_{\mathrm{med}}$ in each bin as well as the dispersion of each subsample around the median value. Saturated absorption systems are excluded from this exercise, because no constraints on $N(\mathrm{Fe\,II})/N(\mathrm{Mg\,II})$ can be derived either due to heavily saturated Mg II absorption or insufficient limits on $N(\mathrm{Fe\,II})/N(\mathrm{Mg\,II})$ (see Column 12 of Table 1). In addition, for passive galaxies at $d \gtrsim 100$ kpc two of the seven galaxies have only a relatively strong upper limit at $\log\langle N(\mathrm{Fe\,II})/N(\mathrm{Mg\,II})\rangle \approx -0.3$. For this subsample, we infer a 85% upper limit for the underlying distribution of $\log\langle N(\mathrm{Fe\,II})/N(\mathrm{Mg\,II})\rangle_{\mathrm{med}} < -0.3$. The results are presented in Figure 3.5 for passive galaxies (red circles) and star-forming galaxies (blue stars).

Figure 3.5 shows that $\log\langle N(\mathrm{Fe\,II})/N(\mathrm{Mg\,II})\rangle_{\mathrm{med}}$ declines with increasing d, from $\log\langle N(\mathrm{Fe\,II})/N(\mathrm{Mg\,II})\rangle_{\mathrm{med}} = -0.06 \pm 0.15$ at $d < 60$ kpc to $\log\langle N(\mathrm{Fe\,II})/N(\mathrm{Mg\,II})\rangle_{\mathrm{med}} < -0.3$ at $d > 100$ kpc. For star-forming galaxies, a similar declining trend is found with increasing projected distance, from $\log\langle N(\mathrm{Fe\,II})/N(\mathrm{Mg\,II})\rangle_{\mathrm{med}} = -0.25 \pm 0.21$ at $d < 44$

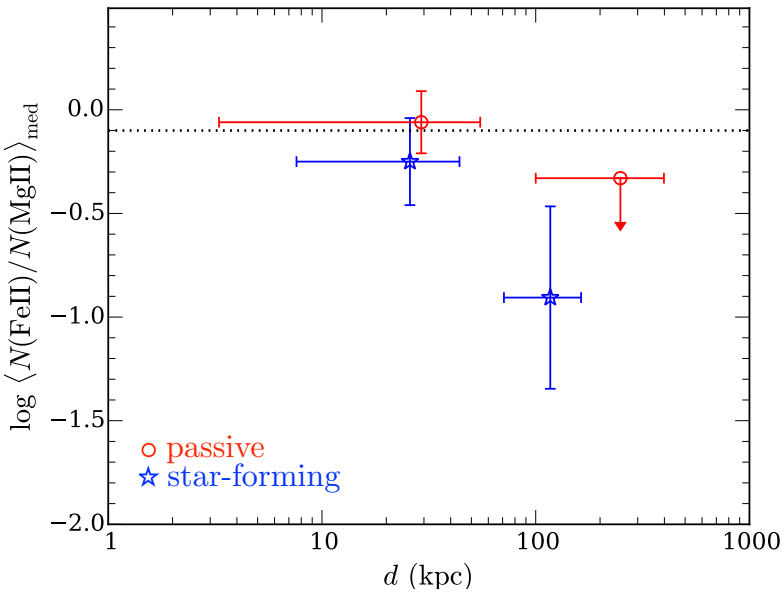

Figure 3.5: Dependence of median column density ratio, $\log \langle N(\mathrm{Fe\,II})/N(\mathrm{Mg\,II}) \rangle_{\mathrm{med}}$, on galaxy projected distance d for passive galaxies (red circles) and star-forming galaxies (blue stars). The horizontal error bars represent the full range of projected distances in each bin, whereas the vertical error bars show the dispersion from $\log \langle N(\mathrm{Fe\,II})/N(\mathrm{Mg\,II}) \rangle_{\mathrm{med}}$ in each bin. Two of the seven passive galaxies at $d \gtrsim 100$ kpc have only a relatively strong upper limit at $\log \langle N(\mathrm{Fe\,II})/N(\mathrm{Mg\,II}) \rangle \approx -0.3$ (Figure 3.4). For this subsample, we infer a 85% upper limit for the underlying distribution of $\log \langle N(\mathrm{Fe\,II})/N(\mathrm{Mg\,II}) \rangle_{\mathrm{med}} < -0.3$, which is shown as the downward arrow. Like Figure 3, the dotted horizontal line indicates the solar (Fe/Mg) abundance pattern.

kpc to $\log \langle N(\mathrm{Fe\,II})/N(\mathrm{Mg\,II}) \rangle_{\mathrm{med}} = -0.91 \pm 0.44$ at $d > 70$ kpc. Furthermore, while $\log \langle N(\mathrm{Fe\,II})/N(\mathrm{Mg\,II}) \rangle_{\mathrm{med}}$ is about 0.2 dex higher in the inner halos ($d \lesssim 60$ kpc) of passive galaxies than those around star-forming ones, both galaxy populations display a comparable $\log \langle N(\mathrm{Fe\,II})/N(\mathrm{Mg\,II}) \rangle_{\mathrm{med}}$ in the outer halos.

3.5 Discussion

A primary goal of our study is to determine the extent SNe Ia-dominated feedback in gas around galaxies. The analysis presented in Section 3.3 and 3.4 indicates that passive galaxies display on average a higher $N(\mathrm{Fe\,II})/N(\mathrm{Mg\,II})$ in their halos than star-forming galaxies. In addition, there appears to be a modest decline in the relative ionic ratio with increasing projected distance. To infer the underlying elemental abundance ratio between Fe and Mg

from the observed relative abundances of Fe^+ and Mg^+, it is necessary to first address the differential ionization fraction between the two ions. Furthermore, it is also necessary to quantify possible systematic biases due to differential dust depletion. Here we discuss both of these effects and the implications of our findings.

3.5.1 Differential Ionization Fraction

To determine the ionization state of the gas, measurements of $N(\mathrm{H\,I})$ and relative abundance ratios between multiple ions are often necessary. While the observed relative ionic ratios constrain the ionization parameters, knowledge of $N(\mathrm{H\,I})$ determines whether the gas is optically-thin or optically-thick to the background radiation field. However, $N(\mathrm{H\,I})$ is not known for all but one galaxy in our sample. As illustrated in Chapter 2, useful empirical constraints on the relative Fe/α abundances can be obtained in the absence of $N(\mathrm{H\,I})$. This is achieved by performing a series of photoionization calculations that explore a wide range of ionization conditions. Then, constraints for the ionization state of the gas are obtained based on comparisons of the predicted and observed column density ratios between Mg^0 and Mg^+ ions.

In Figure 3.6, we present the observed Mg I to Mg II column density ratio, $N(\mathrm{Mg\,I})/N(\mathrm{Mg\,II})$, versus Mg II column density, $N(\mathrm{Mg\,II})$, for individual absorbing components associated with passive (circle symbols) and star-forming (star symbols) galaxies. The data points are color-coded by the projected distances of the absorbing galaxies. gray data points represent 2-σ upper limit of $N(\mathrm{Mg\,I})/N(\mathrm{Mg\,II})$, due to either non-detection of Mg I or saturated Mg II absorption. Figure 3.6 shows that the majority ($> 90\%$) of absorbing components with $\log N(\mathrm{Mg\,II})/\mathrm{cm}^{-2} \lesssim 13.8$ occur in a range of $\log N(\mathrm{Mg\,I})/N(\mathrm{Mg\,II})$ values of $-2.2 \lesssim \log N(\mathrm{Mg\,I})/N(\mathrm{Mg\,II}) \lesssim -1.4$. On the other hand, for high column density absorbing components, $\log N(\mathrm{Mg\,II})/\mathrm{cm}^{-2} \gtrsim 14$, the ratios are lower with a typical $\log N(\mathrm{Mg\,I})/N(\mathrm{Mg\,II}) \sim -2.5$, albeit with larger uncertainties. The range of $N(\mathrm{Mg\,I})/N(\mathrm{Mg\,II})$ in Figure 3.6 is consistent with what has been found for randomly selected Mg II absorbers by Churchill et al.

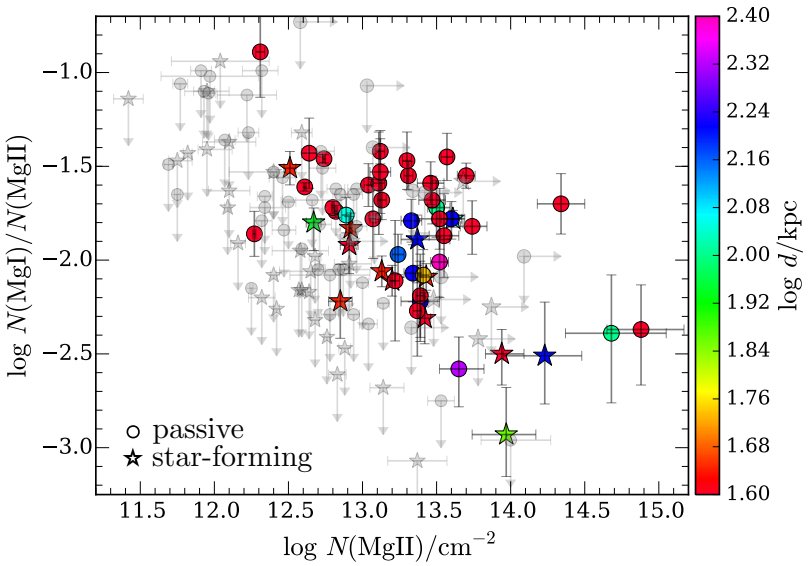

Figure 3.6: Observed Mg I to Mg II column density ratio, $N(\mathrm{Mg\,I})/N(\mathrm{Mg\,II})$, versus Mg II column density, $N(\mathrm{Mg\,II})$, for individual components identified in our Voigt profile analysis (Section 3). Absorption components associated with passive galaxies are plotted in circle symbols, whereas those associated with star-forming galaxies are plotted in star symbols. The error bars associated with each data point show the measurement uncertainties. The color of each data point represents the projected distance d of the absorbing galaxy to the background QSO sightline. When a Mg II absorbing component has no corresponding Mg I absorption detected, it is shown as a downward arrow, with the gray data point indicating the 2-σ upper limit of $N(\mathrm{Mg\,I})/N(\mathrm{Mg\,II})$.

(2003).

In Zahedy et al. (2016), we performed a series of photoionization calculations for a photoionized gas of temperature $T = 10^4$ K and a range of gas densities, metallicities, and $N(\mathrm{H\,I})$. A plane-parallel geometry was assumed for the gas, which was illuminated with the updated Haardt & Madau (2001) ionizing background radiation field (HM05 in Cloudy v.13.03; Ferland et al. 2013) at $z = 0.5$. For each model, the expected relative abundance ratio between Mg^0 and Mg^+ ions and the ionization fraction ratio between Fe^+ and Mg^+ were calculated for a gas that follows the solar abundance pattern. For absorption components with $\log N(\mathrm{Mg\,II})/\mathrm{cm}^{-2} \lesssim 13.8$ in the present study, comparing the observed $N(\mathrm{Mg\,I})/N(\mathrm{Mg\,II})$ and predictions from Zahedy et al. (2016) leads to constraints on the gas density of $3 \times 10^{-2}\,\mathrm{cm}^{-3} \lesssim n_{\mathrm{H}} \lesssim 2 \times 10^{-3}\,\mathrm{cm}^{-3}$. Over the range of allowed gas densities, we find that the ionization fraction of Fe^+ (f_{Fe^+}) remains roughly equal to that of Mg^+

($f_{\rm Mg^+}$) in the optically-thick regime and lower than $\rm Mg^+$ in optically-thin gas. As a result, $f_{\rm Fe^+}/f_{\rm Mg^+} < 1$ and $N({\rm Fe\,II})/N({\rm Mg\,II})$, which is equal to $(f_{\rm Fe^+}/f_{\rm Mg^+}) \times N({\rm Fe})/N({\rm Mg})$, marks a lower limit to the underlying $N({\rm Fe})/N({\rm Mg})$.

For strong Mg II components of $\log N({\rm Mg\,II})/{\rm cm}^{-2} \gtrsim 14$, however, the observed low $N({\rm Mg\,I})/N({\rm Mg\,II})$ ratios require a low density gas of $n_{\rm H} \approx 10^{-3}\,{\rm cm}^{-3}$ for the same HM05 ionizing radiation intensity. The inferred low gas density together with a large $N({\rm Mg\,II})$ implies a cloud size of > 10 kpc if the gas has a solar metallicity or > 100 kpc if the gas metallicity is 0.1 solar. The unphysically large cloud sizes inferred for the strongest Mg II absorbing components raise questions for the accuracy of the photoionization models.

Because the observed ionic ratios in photoionization models is dictated by the ionization parameter, which is the number of ionizing photons per atom, a natural explanation for the inferred low gas density is that the ionizing radiation intensity has been underestimated. To increase the ionizing radiation intensity from the standard HM05, we experiment with adding a local ionizing radiation field due to the absorbing galaxy. We first generate a synthetic galaxy spectrum using Starburst99 (Leitherer et al. 1999) and assuming a star formation rate of 1 $M_\odot\,{\rm yr}^{-1}$, an age of 10^7 yr, and an ionizing photon escape fraction of 2%. Then, we normalize the flux to match an L_* galaxy at $z = 0.5$. For a gas cloud located at 15 kpc from the galaxy, we find that the ionizing radiation from the galaxy provides a 20-fold increase to the number density of hydrogen-ionizing photons. With an increased ionizing radiation intensity, the inferred underlying gas density increases accordingly. We find that with this revised radiation field the observed low $N({\rm Mg\,I})/N({\rm Mg\,II})$ for strong Mg II components of $\log N({\rm Mg\,II})/{\rm cm}^{-2} \gtrsim 14$ can be reproduced for a gas density of $n_{\rm H} \sim 0.01\,{\rm cm}^{-3}$. At this gas density, we find that $\log f_{\rm Fe^+}/f_{\rm Mg^+} \approx -0.4$ and confirm that the observed $N({\rm Fe\,II})/N({\rm Mg\,II})$ represents a lower limit to the underlying $N({\rm Fe})/N({\rm Mg})$.

An alternative explanation for the observed low $N({\rm Mg\,I})/N({\rm Mg\,II})$ in strong Mg II absorbing components is the presence of additional heating sources that may increase the ionization of the gas in a warmer temperature regime. To explore this alternative scenario,

we repeat the photoionization calculations for a higher temperature of $T = 3 \times 10^4$ K, assuming the original HM05 radiation field. The adopted higher temperature is motivated by the observed Doppler parameters of individual Mg II, Mg I and Fe II absorption components. A median value of $b \sim 5$ km s^{-1} is found for each of the three transitions, placing an upper limit on the allowed gas temperature at $T \lesssim 3 \times 10^4$ K.

The resulting model predictions show that the observed $\log N(\mathrm{Mg\,I})/N(\mathrm{Mg\,II}) \sim -2.5$ in most $\log N(\mathrm{Mg\,II})/\mathrm{cm}^{-2} \gtrsim 14$ absorbing components can also be reproduced for a warm ($T = 3 \times 10^4$ K) optically-thick gas with $\log N(\mathrm{H\,I})/\mathrm{cm}^{-2} \gtrsim 19$ and 0.1 solar metallicity under a standard HM05 radiation field over a wide range of gas densities. For gas with lower-$N(\mathrm{H\,I})$, a still higher gas temperature is required, which then becomes incompatible with the observed b value. Imposing a maximum cloud size of $l \sim 10$ kpc based on observations of Galactic high-velocity clouds (e.g., Putman et al. 2012) constrains the gas density to be $n_\mathrm{H} \gtrsim 4 \times 10^{-3}\,\mathrm{cm}^{-3}$ for a gas with 0.1 solar metallicity. Over the range of allowed n_H, $\log f_{\mathrm{Fe}^+}/f_{\mathrm{Mg}^+} \approx -0.3$, indicating that the observed $N(\mathrm{Fe\,II})/N(\mathrm{Mg\,II})$ marks a lower limit to the underlying $N(\mathrm{Fe})/N(\mathrm{Mg})$.

In summary, the exercise described in this section demonstrates that *for both weak and strong Mg II absorption systems identified in this study, the observed* $N(\mathrm{Fe\,II})/N(\mathrm{Mg\,II})$ *ratio represents a lower limit to the underlying elemental* (Fe/Mg) *ratio of the gas for both optically-thin and thick gases*. Comparing the observed $N(\mathrm{Fe\,II})/N(\mathrm{Mg\,II})$ to the solar (Fe/Mg) abundance ratio from Asplund et al. (2009; dotted line in Figures 3.3 to 3.5), our analysis shows that $> 60\%$ of passive galaxies exhibit an enhanced Fe/α elemental abundance ratio at $d \lesssim 60$ kpc that exceeds what is observed in the solar neighborhood. At the same time, the majority of passive galaxies at $d \gtrsim 100$ kpc and all star-forming galaxies at $d \lesssim 150$ kpc exhibit chemical compositions consistent with α-element enhancement.

3.5.2 Differential Dust Depletion

It is known from observations of the Milky Way ISM that Fe is more readily incorporated into dust grains than Mg, showing in excess of 0.5 dex more depletion than Mg in cool ($T \sim 500$ K) ISM gas (e.g, Savage & Sembach 1996). Including such differential dust depletion, the inferred $N(\mathrm{Fe})/N(\mathrm{Mg})$ after accounting for possible differential ionization fraction correction may still represent a lower limit to the underlying elemental abundance ratio. At the same time, dust grains are expected to be easily destroyed in warmer environment (e.g., Draine & Salpeter 1979). Indeed, the observed differential depletion between Fe and Mg reduces to ≈ 0.35 dex in warm ($T \approx 6000$ K) ISM gas (e.g, Savage & Sembach 1996). For Mg II absorbing gas of $T \sim 10^4$ K, it is expected that dust destruction is still more effective (e.g., McKee et al. 1987) and that differential dust depletion is at its minimum. X-ray observations of the hot ISM gas in 19 local early-type galaxies from Humphrey & Buote (2006) have yielded a median Fe to Mg ratio of $\log(\mathrm{Fe/Mg}) = -0.01 \pm 0.18$ at $d \lesssim 10 - 60$ kpc from these galaxies. This median value is consistent with what we found for singly ionized Fe and Mg at $d < 60$ kpc from $z \sim 0.5$ passive galaxies, supporting the expectation that dust depletion is not significant in the cool ($T \sim 10^4$ K) halo clouds revealed by Mg II absorption transitions.

However, it is possible that the observed low $N(\mathrm{Fe\,II})/N(\mathrm{Mg\,II})$ ratio around star-forming galaxies is due to a larger amount of differential dust depletion around these galaxies, particularly for the Mg II absorbers detected at $d < 50$ kpc. These absorbers are all relatively strong with $W_r(2796) \gtrsim 0.6$ Å, and it has been shown that $\approx 30 - 40\%$ of these strong Mg II absorbers contain neutral gas of $N(\mathrm{H\,I}) \gtrsim 2 \times 10^{20}\,\mathrm{cm}^{-2}$ (e.g., Rao et al. 2006). Therefore, a large fraction of these absorbers are likely to arise in DLA gas. For DLAs at $z \sim 0.5 - 3$, Fe is found to be more depleted than Mg by ≈ 0.2 dex (e.g., Vladilo et al. 2011; De Cia et al. 2016). If dust is present in these strong Mg II absorbers around $z \sim 0.5$ star-forming galaxies, then adopting the mean differential dust depletion between Fe and Mg observed for DLAs would imply a median underlying (Fe/Mg) abundance ratio of $\log(\mathrm{Fe/Mg}) = -0.05$

at $d < 50$ kpc, comparable to both the solar value and what is observed at $d < 60$ kpc from passive galaxies. For weaker Mg II absorbers at $d > 50$ kpc, the dust content is expected to be significantly less and little correction for differential dust depletion is expected.

The differential dust depletion between Fe and Mg can be inferred directly for the absorption systems around two star-forming galaxies in the $d < 50$ kpc subsample, providing a comparison to the underlying (Fe/Mg) ratio implied from the subsample median. For the star-forming galaxy at $z = 0.101$ and $d = 8$ kpc from PKS 0439−433, the roughly solar metallicity known for the DLA gas associated with this galaxy (Chen et al. 2005; Som et al. 2015) allows us to estimate the dust depletion factors for Fe and Mg based on a known correlation between dust depletion and gas-phase metallicity. The differential dust depletion between Fe and Mg is expected to vary between +0.5 and +0.8 dex for a solar-metallicity gas, based on observations of Galactic absorbers (e.g., De Cia et al. 2016). If dust is present in this DLA, this range of differential dust depletion would imply an underlying (Fe/Mg) abundance ratio of $\log(\mathrm{Fe/Mg}) = -0.1$ to +0.2 for the gas. Similarly for the ultra-strong Mg II absorber associated with the $z = 1.24$ galaxy at $d = 17$ kpc from SDSSJ 1430+0149, although the metallicity is not known, the relative abundance ratio of Cr to Zn is estimated to be $[\mathrm{Cr/Zn}] = -0.51 \pm 0.06$ (Zych et al. 2009), indicating a modest level of dust depletion comparable to what is seen in the Galactic Halo (e.g., Savage & Sembach 1996). The expected differential depletion between Fe and Mg in such an environment is $\approx +0.2$ dex, which would imply an underlying (Fe/Mg) ratio of $\log(\mathrm{Fe/Mg}) = -0.05$ for this Mg II absorber. In both of these cases, applying the estimated dust depletion correction individually for each galaxy results in an implied underlying (Fe/Mg) abundance ratio that is comparable to solar value, consistent with what is found by applying the mean dust depletion correction for DLAs on the median value for the inner-d bin. This exercise lends strong support for the finding that solar-level (Fe/Mg) gas may not be uncommon at $d < 50$ kpc from intermediate-redshift, star-forming galaxies.

3.5.3 Implications on the Origin of Chemically Enriched Gas in Galaxy Halos

As previously mentioned in Section 3.1, iron is produced in both core collapse and Type Ia SNe, whereas magnesium is produced primarily in massive stars and core-collapse SNe. Specifically, a Type Ia supernova is expected to produce $\sim 0.7\,M_{\odot}$ of Fe while releasing no more than $0.02\,M_{\odot}$ of magnesium at the same time (e.g., Iwamoto et al. 1999). Different types of SNe originate in different progenitor stars of different stellar ages. The elemental (Fe/Mg) ratio therefore provides a measure of the relative contributions from different massive stars to the chemical enrichment history of a galaxy (e.g., de Plaa et al. 2007; Zahedy et al. 2016). Consequently, the inferred lower limit of the underlying (Fe/Mg) elemental abundance ratio from the observed $N(\mathrm{Fe\,II})/N(\mathrm{Mg\,II})$ provides a useful "clock" for timing the age of the stellar population. In addition, the spatial profiles of $N(\mathrm{Fe\,II})/N(\mathrm{Mg\,II})$ offers important constraints for the extent of SNe Ia-dominated chemical enrichment in galactic halos.

For quiescent galaxies in this study, the observed $N(\mathrm{Fe\,II})/N(\mathrm{Mg\,II})$ at $d \lesssim 60$ kpc is high with a median and dispersion of $\log \langle N(\mathrm{Fe\,II})/N(\mathrm{Mg\,II})\rangle_{\mathrm{med}} = -0.06 \pm 0.15$. The large column density ratio implies a lower limit to the underlying (Fe/Mg) ratio of the gas at $[\mathrm{Fe/Mg}] \equiv \log(\mathrm{Fe/Mg}) - \log(\mathrm{Fe/Mg})_{\odot} \gtrsim 0$. The implied fractional contribution from SNe Ia to the chemical enrichment of the gas is $f_{\mathrm{Ia}} \gtrsim 17\%$ based on the expected nucleosynthetic yields for Type Ia and core-collapse SNe from Iwamoto et al. (1999). This minimum value is comparable to what has been estimated for solar-abundance gas in the Milky Way (e.g., Tsujimoto et al. 1995). With such a significant contribution from SNe Ia, it can also be expected that cool gas at $d \lesssim 60$ kpc from passive galaxies has been enriched to a relatively high metallicity, reflecting the role of multiple generations of massive stars and SNe Ia in its chemical enrichment history. Indeed, this expectation is at least consistent with what has been found in the hot ISM of local elliptical galaxies, where near-solar mean metallicities are commonly observed at a similar range of d (e.g., Humphrey & Buote 2006; Loewenstein &

Davis 2010, 2012). Furthermore, we note that Fe/α radial profile measurements are available from X-ray observations of the hot ISM in several nearby massive quiescent galaxies (e.g, Nagino & Matsushita 2010; Loewenstein & Davis 2010, 2012), where it has been found that the Fe/α radial profile in these galaxies is consistent within measurement errors with being flat at [Fe/α] ~ 0 level at $d \lesssim 40$ kpc, comparable to what can be inferred from our observations at $d \lesssim 60$ kpc from $z \sim 0.5$ passive galaxies.

Our analysis also provides a quantitative constraint on the Fe/α ratio at $d \gtrsim 100$ kpc from passive galaxies, where the gas is typically too diffuse to be detected in emission even in the local universe. We find that at $d \gtrsim 100$ kpc the absorbing gas generally shows lower $N(\mathrm{Fe\,II})/N(\mathrm{Mg\,II})$ ratios than typically seen at $d \lesssim 60$ kpc. Specifically for passive galaxies, the $N(\mathrm{Fe\,II})/N(\mathrm{Mg\,II})$ ratios at $d \gtrsim 100$ kpc can be characterized by a 85% upper limit to the underlying distribution of $\log \langle N(\mathrm{Fe\,II})/N(\mathrm{Mg\,II})\rangle_{\mathrm{med}} < -0.3$. In at least three out of seven cases ($\approx 40\%$), the absorbing gas displays $\log \langle N(\mathrm{Fe\,II})/N(\mathrm{Mg\,II})\rangle_{\mathrm{med}} \lesssim -0.6$. Allowing a modest differential ionization fraction between Fe^+ and Mg^+ of up to $\log f_{\mathrm{Fe}^+}/f_{\mathrm{Mg}^+} \approx -0.3$ dex (assuming an optically thick gas, see Section 5.2), the implied underlying (Fe/Mg) relative abundance ratio is [Fe/Mg] $\lesssim -0.2$ for a $\log N(\mathrm{Fe\,II})/N(\mathrm{Mg\,II}) = -0.6$ gas. This range of [Fe/Mg] ratios is comparable to that of high-redshift DLAs, where the mean [Fe/α] has been found to be -0.26 ± 0.12 at $z \gtrsim 3$ (e.g., Rafelski et al. 2012). For [Fe/Mg] $\lesssim -0.2$, the expected maximum fractional contribution from SNe Ia to the chemical enrichment is $f_{\mathrm{Ia}} \lesssim 5\%$, based on supernova nucleosynthetic yields from Iwamoto et al. (1999). Our analysis therefore indicates that SNe Ia-driven chemical enrichment is relatively localized in inner halos at $d \lesssim 60$ kpc and that the chemical enrichment of the cool gas at $d \gtrsim 100$ kpc from $z = 0.5$ passive galaxies is consistent with an early enrichment driven by core-collapse SNe.

For star-forming galaxies, interpretations of our observations are more uncertain. As previously noted in Section 3.5.2, if differential dust depletion is important, then the absorbing gas at $d \lesssim 50$ kpc from these star-forming galaxies may also have a near solar-level (Fe/Mg)

ratio. Such a high level Fe/Mg ratio may not be surprising for a mature disk galaxy at low- to intermediate-redshifts. However, it is interesting to find that a strong Mg II absorber of $W_r(2796) = 2.86$ at $d = 17$ kpc from a star-forming galaxy at $z = 1.24$ could potentially have a solar Fe/Mg ratio after differential dust depletion corrections. The implication is that the galaxy contains a relatively evolved stellar population, while maintaining an active level of star formation when the universe was ≈ 5 Gyr old. Follow-up studies of the stellar populations and star formation history in this galaxy are necessary for a better understanding of the observed high Fe/Mg ratio in the absorber.

At $d > 70$ kpc from star-forming galaxies, the observed Fe II to Mg II column density ratios are generally low with a median and dispersion of $\log \langle N(\mathrm{Fe\,II})/N(\mathrm{Mg\,II})\rangle_{\mathrm{med}} = -0.91\pm0.44$. For a median $N(\mathrm{Mg\,I})/N(\mathrm{Mg\,II})$ ratio of $\log N(\mathrm{Mg\,I})/N(\mathrm{Mg\,II}) = -1.9$, the expected differential ionization fraction between Fe^+ and Mg^+ is $\log f_{\mathrm{Fe}^+}/f_{\mathrm{Mg}^+} \approx -0.6$ dex for an optically-thin gas (and negligible for an optically-thick gas). Applying this ionization correction leads to an implied underlying (Fe/Mg) relative abundance ratio of $[\mathrm{Fe/Mg}] \lesssim -0.2$ at $d = 70 - 160$ kpc. Similar to what is seen at $d > 100$ kpc from passive galaxies, cool gas at $d > 70$ kpc from star-forming galaxies also shows an α-element enhanced abundance pattern driven by core-collapse SNe.

In summary, our analysis suggests that Fe/α in galactic halos declines with increasing projected distance from both passive and star-forming galaxies. At $d \lesssim 60$ kpc, a significant contribution from SNe Ia ($f_{\mathrm{Ia}} \gtrsim 15\%$) is necessary to explain the observed Fe/Mg ratios, whereas at $d \gtrsim 70$ kpc, contributions from SNe Ia are limited to $f_{\mathrm{Ia}} \lesssim 5\%$ in both star-forming and quiescent halos. Together, our analysis shows that SNe Ia-driven chemical enrichment is relatively localized in inner halos at $d \lesssim 60$ kpc. Alternatively, inflowing gas from the IGM could also "dilute" an Fe-rich gas and produce a declining Fe/α radial profile in the halo, because accreted IGM gas is expected to show an α-enhanced abundance pattern which reflects the early enrichment history (e.g., Rauch et al. 1997). However, such dilution effect is likely minimal if the metallicity of an α-enhanced inflowing gas is significantly lower

than the Fe-rich gas.

It is clear that there is a significant scatter in the empirical measurements of $N(\mathrm{Fe\,II})/N(\mathrm{Mg\,II})$, while the inferred f_{Ia} depends sensitively on the input Fe/α elemental abundance ratio. We anticipate that future observations combining metallicity and relative abundance measurements in stars/ISM and in halo gas for a large sample of galaxies will provide the precision necessary to distinguish between different scenarios.

CHAPTER 4

HUBBLE SPACE TELESCOPE DETECTION OF EXTENDED NEUTRAL HYDROGEN IN A MASSIVE ELLIPTICAL AT $z = 0.4$

The contents of this chapter were previously published in the Astrophysical Journal Letters as Zahedy, F. S., Chen, H.-W., Rauch, M., & Zabludoff, A. 2017, ApJL, 846, L29. They are reproduced here in accordance with the copyright agreement and with permission from the American Astronomical Society.

4.1 Introduction

A large fraction of massive quiescent galaxies are not gas-poor. 21 cm surveys have revealed that $30 - 40\%$ of of nearby early-type galaxies contain a large amount of neutral hydrogen (H I) gas (e.g., Grossi et al. 2009; Oosterloo et al. 2010; Serra et al. 2012; Young et al. 2014). Beyond the local universe, QSO absorption-line surveys of Mg II $\lambda\lambda$ 2796, 2803 absorption features near luminous red galaxies (LRGs) reveal extended cool gas out to projected distances $d \gtrsim 100$ kpc, with a mean covering fraction of $> 15\%$ (e.g., Gauthier et al. 2009, 2010; Bowen & Chelouche 2011; Huang et al. 2016). Because Mg II absorption traces photoionized, cool $T \sim 10^4$ K gas (e.g., Bergeron & Stasińska 1986), the significant covering fraction of Mg II absorbers indicates not only that cool gas is present in these quiescent halos, but also that the gas has been enriched with heavy elements.

The finding that passive galaxies harbor a significant reservoir of chemically enriched cool gas remains a central puzzle in galaxy evolution, requiring some physical processes to prevent the gas from cooling and eventually forming stars (e.g., McNamara & Nulsen 2007; Johansson et al. 2009; Conroy et al. 2015). While feedback powered by central supermassive black holes (SMBH) is frequently invoked as an explanation (e.g., McNamara & Nulsen 2007), observationally it has been difficult to directly connect active galactic nuclei (AGN) activity

to the quenching of star formation. Alternatively, the stars themselves may be crucial in providing additional heating, which is consistent with the observed anticorrelation between stellar surface density and specific star formation rate in both low- and high-redshift galaxies (e.g., Kauffmann et al. 2003, 2006; Franx et al. 2008; Fang et al. 2013; Whitaker et al. 2017). Specifically, it has been suggested that old stellar populations can prevent continuing star-formation in passive galaxies through energy injection from Type Ia supernovae (SNe Ia) and winds from asymptotic giant branch (AGB) stars (see Conroy et al. 2015 and references therein).

In a pilot study, Zahedy et al. (2016, hereafter Z16; Chapter 2) employed high-resolution absorption-line spectroscopy of lensed background QSOs to examine the cool gas content in the inner halo ($d = 3 - 15$ kpc) of three massive quiescent lensing galaxies at $z = 0.4 - 0.7$. While the gas content varied significantly among lenses and different sightlines of the same lens, a supersolar Fe/Mg relative abundance pattern, [Fe/Mg] $\gtrsim 0.1$, was found in *every* sightline where cool gas was detected ($\sim 40\%$ of all sightlines). Such high [Fe/Mg] ratios indicate a significant contribution ($\gtrsim 20\%$) from SNe Ia to the chemical enrichment history of the gas, exceeding what have been observed in mature stellar populations such as the solar neighborhood (e.g., Tsujimoto et al. 1995). Z16 suggest that these absorbers reside in the interstellar medium (ISM), where the gas is likely to have been enriched and heated by SNe Ia ejecta. However, to facilitate a direct comparison with different chemical enrichment models, it is necessary to probe the bulk of the cool ISM, neutral hydrogen (H I), and constrain its column density, N(H I).

We have obtained UV absorption spectra of the doubly lensed QSO HE 0047−1756 at $z_{\rm QSO} = 1.676$, using the Space Telescope Imaging Spectrograph (STIS) on board the *Hubble Space Telescope* (*HST*). The lens of HE 0047−1756 at $z = 0.408$ is a massive elliptical galaxy with a total stellar mass of $M_{\rm star} \approx 10^{11}\,M_{\odot}$ and no ongoing star formation (Z16). Ultra-strong Mg II absorbers of rest-frame absorption equivalent width $W_r(2796) > 3.6$ Å are found along both lensed QSO sightlines probing opposite sides of this LRG lens at $d = 4.6$ kpc (1.8

half-light radii, r_e) and $d = 3.3$ kpc ($1.3\ r_e$). The STIS spectra allow us to measure the total integrated N(H I) at two locations separated by ≈ 8 kpc in this massive quiescent galaxy, thereby constraining the mean gas metallicity. In this chapter, we report a large column density of extended neutral hydrogen gas detected in the inner ISM of the HE 0047−1756 lens, the first such discovery in a quiescent galaxy beyond $z \sim 0$. Throughout the chapter, we adopt a flat cosmology of $\Omega_{\rm M} = 0.3$ and $\Omega_\Lambda = 0.7$, with a Hubble constant of $H_0 = 70$ km s^{-1} Mpc^{-1}.

4.2 Observations and Data Reduction

Long-slit FUV spectroscopy of the doubly lensed QSO HE 0047−1756 was obtained on 2016 December 5 using the FUV-MAMA detector in *HST*/STIS with the $52'' \times 0''.2$ long slit and the low-resolution G140L grating (PID: 14751; PI: Zahedy). This configuration provides a dispersion of ≈ 0.6 Å per pixel with a corresponding spectral resolution of ≈ 270 km s^{-1}. Because the two lensed images of HE 0047−1756 are separated by merely $1.4''$, the long-slit spectroscopic mode of STIS enabled observation of both QSO images in a single setup, which was achieved by orienting the slit at a position angle of $-9.51°$. At the redshift of the lensing galaxy, the broad wavelength coverage of the G140L grating ($1150 - 1720$ Å) includes the entire H I Lyman series. The total integration time of the observations was 7689 s, which was divided into six individual exposures of roughly equal durations.

Individual spectral images were initially processed using the automatic STIS calibration pipeline, CALSTIS (Hodge et al. 1998), which performed dark and bias subtractions, flat-fielding, and wavelength calibration, and produced a series of data products including a two-dimensional rectified spectral image for each science exposure. The pipeline-calibrated data products were retrieved from the *HST* archive for further processing. We developed a custom spectral extraction software to optimize signal-to-noise ratio (S/N) in the resulting spectra, especially that of the fainter lensed QSO image HE 0047−1756*B*. The custom software first constructed a model spatial profile along the cross dispersion direction for each QSO image

by averaging the two-dimensional rectified spectral image along the wavelength direction. Regions affected by strong sky emission lines were excluded from this exercise. Next, the software extracted individual QSO spectra by applying the mean spatial profile of each QSO image as optimal weights for the spatially resolved spectral signal at each wavelength. Finally, the optimally extracted one-dimensional spectra from individual exposures were coadded to form a single combined spectrum per QSO image, which is characterized by a mean S/N $\approx 20 - 25$ per resolution element for HE 0047−1756A, and S/N $\approx 10 - 13$ per resolution element for HE 0047−1756B, over the full wavelength range ($1150 - 1720$ Å).

4.3 Large Interstellar N(HI) in the Massive Quiescent Lens

The final coadded FUV spectra of the two lensed QSO images are presented in Figure 4.1. The absorption features along sightline B (black) are redshifted by ≈ 1.8 Å relative to those along sightline A (red), consistent with the kinematic offset of ≈ 360 km s^{-1} seen in Mg II, Fe II, and Mg I. Strong absorption features are detected along both sightlines, which can be attributed to the H I Lyman series as well as various low- to high-ionization metal transitions at the redshift of the lensing galaxy.

For both sightlines, the FUV spectra exhibit a lack of continuum flux blueward of the Lyman limit (at ≈ 1280 Å in observed wavelength) expected for the lens galaxy. The mean flux averaged over a finite spectral window below the Lyman limit is consistent with zero to within the 1σ associated uncertainty, indicating that the absorbing gas at $d \sim r_e$ from the lens galaxy of HE 0047−1756 is optically thick to hydrogen-ionizing photons. We estimate a 2σ upper limit to the Lyman-continuum flux using the mean value of the error spectrum between 870 and 900 Å in the rest frame of the lens galaxy, which we then convert to a 2σ lower limit to the continuum opacity by calculating its ratio to the mean continuum level redward of the Lyman limit at rest-frame $955 - 965$ Å. Given that the H I photoionization cross-section varies as $\sigma(\lambda) = 6.30 \times 10^{-18}\,(911.8\,\text{Å}/\lambda)^{-3}\,\text{cm}^2$ (Osterbrock & Ferland 2006), we estimate 2σ lower limits of $\log N(\text{HI})/\text{cm}^{-2} > 17.8$ for HE 0047−1756A and $\log N(\text{HI})\text{cm}^{-2} > 17.6$

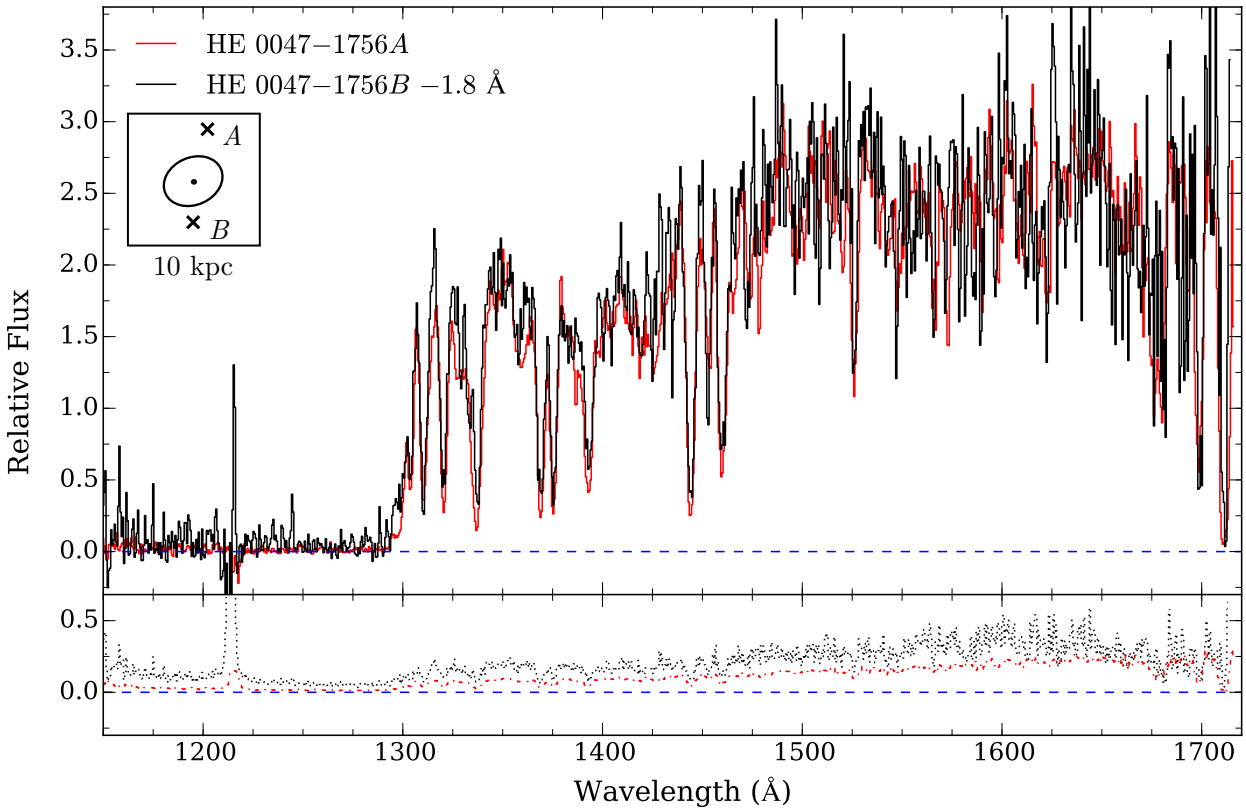

Figure 4.1: *HST*/STIS FUV spectra of the doubly lensed QSO HE 0047−1756. The spectrum of HE 0047−1756B (red) has been shifted blueward by 1.8 Å to align the absorption features with those seen in HE 0047−1756A (black). The corresponding 1-σ error spectra are shown as dotted lines in the bottom panel. The zero flux level is indicated with the blue dashed line. Inset: the configuration of the two lensed QSO sightlines (shown with crosses) in a 10×10 kpc region around the lensing galaxy (shown with an ellipse). The size and orientation of the ellipse correspond to the half-right radius and position angle of the semi-major axis of the lens galaxy as described in Z16 (see Chapter 2).

for HE 0047−1756B at the lens redshift.

Including the entire Lyman series lines allows us to better constrain N(HI). We perform a Voigt-profile analysis using a custom program previously developed by and described in Z16. For each sightline, the combined spectrum is first continuum normalized using a low-order polynomial function. Then, a simultaneous Voigt-profile fit is performed on the following Lyman series lines: Lyα λ1215, Lyβ λ1025, Lyγ λ972, Lyϵ λ937, and Lyζ λ930. The Lyδ λ949 line is excluded from the fit because it is blended with the Galactic C II λ1334 absorption. Higher-order Lyman series lines (Ly-7 and onward) are also excluded due to contaminations by the [O I] $\lambda\lambda$ 1302,1306 airglow emission-line doublet.

The Voigt-profile analysis results in a best-fit log N(H I)/cm^{-2} $= 19.7 \pm 0.1$ for the absorber along HE 0047−1756A, and log N(H I)/cm^{-2} $= 19.6^{+0.2}_{-0.3}$ for the absorber along HE 0047−1756B. The quoted uncertainties represent the estimated 95% confidence level of the best-fit log N(H I), marginalized over the Doppler parameter b. The best-fit Voigt profiles of the Lyman series lines are presented in Figure 4.2 (in red) along with the data (in black). A lower N(HI) value fails to reproduce the damping wing of the Lyα line, demonstrating that strong constraints can be obtained for N(H I) based on the low-resolution STIS spectra. We also perform a curve-of-growth (COG) analysis for estimating N(H I) along each sightline and find consistent results with the Voigt-profile analysis, with log N(H I)/cm^{-2} $= 19.6 \pm 0.2$ for A and log N(H I)/cm^{-2} $= 19.5^{+0.2}_{-0.4}$ for$B$, and an effective b value of 135 ± 10 km s^{-1} for A and 125 ± 15 km s^{-1} for B. The large effective b values are understood to be driven by gas kinematics rather than the actual thermal width of the gas. To quantify the uncertainties in N(H I) and b as a result of uncertainties in the STIS line-spread function (LSF), we repeat the Voigt-profile analysis by varying the width of the STIS LSF, and find that a 10% change in the LSF results in less than a 5% change in the best-fit b and less than a 10% change in N(H I).

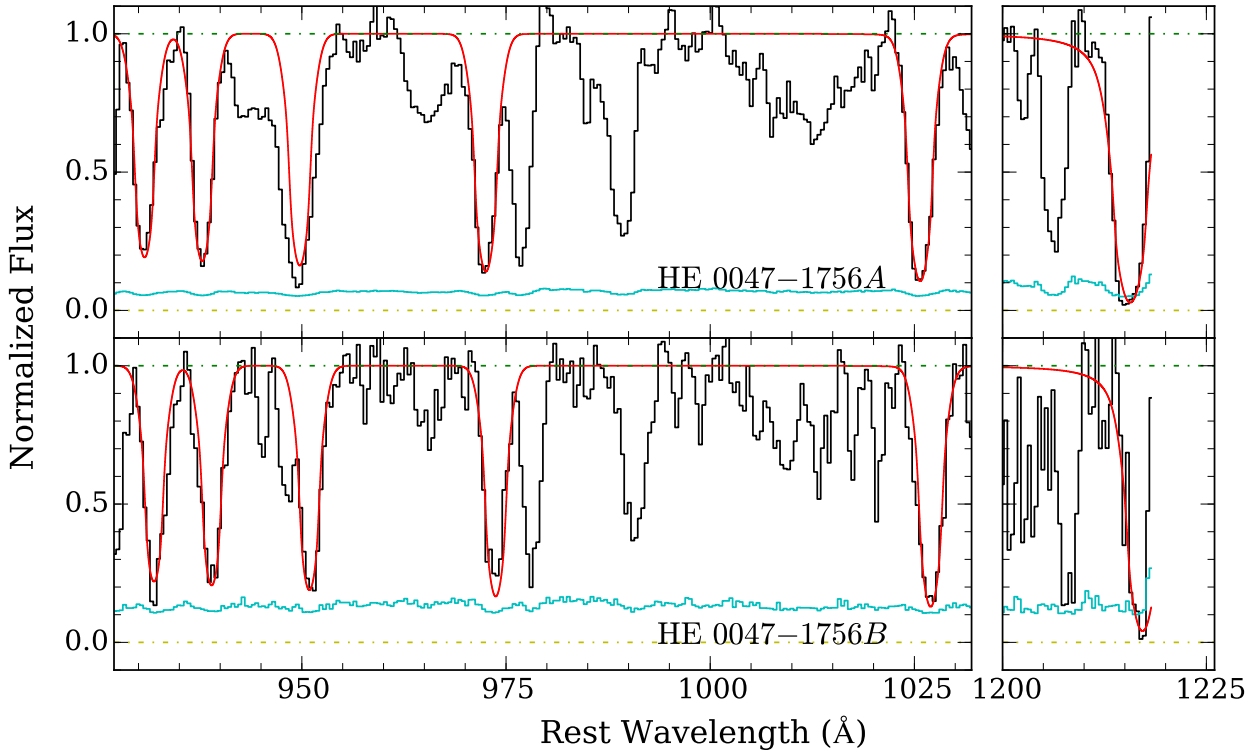

Figure 4.2: Continuum-normalized absorption profile of H I Lyman series transitions along the doubly lensed QSO sightlines HE 0047−1756A (top) at d= 4.6 kpc (or 1.8 r_e) and HE 0047−1756B (bottom) at d= 3.3 kpc (or 1.3 r_e) from the HE 0047−1756 lens galaxy. The x-axis corresponds to the rest-frame wavelength of the galaxy at $z = 0.408$. The 1σ error spectra are plotted in cyan histograms. The best-fit Voigt-profile models for the H I Lyman series, convolved with the STIS LSF, are included in red, with $\log N(\mathrm{H\,I}) = 19.7^{+0.1}_{-0.1}$ for the absorber along HE 0047−1756A and $\log N(\mathrm{H\,I}) = 19.6^{+0.2}_{-0.3}$ for the absorber along HE 0047−1756B. Note that the Lyδ λ949 line is contaminated by C II λ1334 absorption from the Milky Way ISM.

4.4 Discussion and Implications

Our analysis of the STIS spectra of the doubly lensed QSO HE 0047−1756 has yielded, for the first time, constraints on the neutral gas content at two locations separated by ≈ 8 kpc in a massive quiescent galaxy beyond $z \sim 0$. The range of observed $N(\mathrm{H\,I})$ along both lensed sightlines, $\log N(\mathrm{H\,I})/\mathrm{cm}^{-2} = 19.6 - 19.7$, is comparable to what is commonly seen in 21cm maps of the ISM in nearby early-type galaxies ($\log N(\mathrm{H\,I})/\mathrm{cm}^{-2} \approx 19.3 - 20.3$, e.g., Oosterloo et al. 2010; Serra et al. 2012), but is high among previous single-sightline surveys of more distant passive galaxies (e.g., Thom et al. 2012; Prochaska et al. 2017). Detections of high-$N(\mathrm{H\,I})$ absorbers at two different locations suggest the presence of extended interstellar H I. Here, we discuss the implications of this finding.

4.4.1 Chemical Enrichment Level in the Cool ISM of the Lens

While the detailed gas kinematics are not resolved in the low-resolution spectra, the line centroids can be determined to high accuracy. The H I gas kinematics are found to match well with the kinematics of the Fe II absorption complex revealed in ground-based echelle data. Both H I and metal absorption lines display a large velocity shear of $v_B - v_A = +360\,\mathrm{km\ s}^{-1}$ over a projected distance of ≈ 8 kpc across the quiescent galaxy, flanking the systemic redshift of the lens.

We estimate a mean gas metallicity averaged across all components by combining the newly available $N(\mathrm{H\,I})$ and previously published total Fe II column densities from Zahedy et al. (2017). The Fe abundance of the gas, (Fe/H), is related to the observed column density ratio of Fe II and H I corrected for the expected ionization fractions, following $\log(\mathrm{Fe/H}) = \log N(\mathrm{Fe\,II})/N(\mathrm{H\,I}) - \log(f_{\mathrm{Fe}^+}/f_{\mathrm{H}^0})$. In the absence of a large *relative* ionization fraction correction, with $\log(f_{\mathrm{Fe}^+}/f_{\mathrm{H}^0}) \sim 0$, the observed column density ratio translates directly into the Fe abundance, $\log N(\mathrm{Fe\,II})/N(\mathrm{H\,I}) \approx \log(\mathrm{Fe/H})$.

We perform a series of photoionization calculations using Cloudy v.13.03 (Ferland et al.

2013) to estimate the necessary ionization fraction corrections for a wide range of gas densities and metallicities in a photoionized gas of temperature $T = 10^4$ K and $\log N(\mathrm{H\,I})/\mathrm{cm}^{-2} = 19.6 - 19.7$. We assume a plane-parallel slab, illuminated on both sides with the updated Haardt & Madau (2001) ionizing background radiation field (HM05 in CLOUDY) at $z = 0.4$. Adopting a maximum cloud size leads to a lower limit on the allowed gas density for a given $N(\mathrm{H\,I})$. We adopt a maximum cloud size of 1 kpc, consistent with observations of Galactic high-velocity clouds (e.g., Putman et al. 2012), and find $n_{\mathrm{H}} \gtrsim 10^{-1.6}$ cm^{-3} for the absorbers along the two lensed QSO sightlines. Over this allowed gas density range, the calculations show that the gas is mostly neutral with $f_{\mathrm{H}^0} > 0.6$ and the relative ionization fraction correction between Fe^+ and H^0 is $(f_{\mathrm{Fe}^+}/f_{\mathrm{H}^0}) \approx 1$. Therefore, to a good approximation, the gas metallicity can be estimated directly from $\log N(\mathrm{Fe\,II})/N(\mathrm{H\,I})$, following $[\mathrm{Fe/H}] \approx \log N(\mathrm{Fe\,II})/N(\mathrm{H\,I}) - \log(\mathrm{Fe/H})_\odot$[1].

The total Fe II column density is $\log N(\mathrm{Fe\,II})/\mathrm{cm}^{-2} = 14.61 \pm 0.02$ for the absorber along HE 0047−1756A and $\log N(\mathrm{Fe\,II})/\mathrm{cm}^{-2} = 14.70 \pm 0.08$ for the absorber along HE 0047−1756B (Z16; Zahedy et al. 2017). Adopting the solar chemical abundance pattern from Asplund et al. (2009), where $\log(\mathrm{Fe/H})_\odot = -4.50 \pm 0.04$, we find that the estimated Fe abundance is $[\mathrm{Fe/H}] = -0.6 \pm 0.1$ for the absorber along HE 0047−1756A, and $[\mathrm{Fe/H}] = -0.4 \pm 0.3$ for the absorber along HE 0047−1756B.

4.4.2 Effects of Dust Depletion

Dust depletion, when unaccounted for, can lead to underestimated chemical abundances, particularly in high-metallicity gas. For the HE 0047−1756 lens, Ca II $\lambda\lambda$ 3934,3969 absorption has also been observed along both sightlines (Z16). It has been shown that the strength of Ca II absorption correlates with both reddening (Murga et al. 2015) and the [Cr/Zn] relative abundance (e.g., Zych et al. 2009), two common diagnostics of the dust con-

1. If the intrinsic $N(\mathrm{H\,I})$ of the Fe II absorbing gas is lower than observed (namely, only part of the observed $N(\mathrm{H\,I})$ is cospatial with the Fe II gas), then the gas metallicity would be higher still.

tent. Z16 previously reported $W_r(3934) = 0.3\,\text{Å}$ and $W_r(3934) = 0.1\,\text{Å}$ for the absorption systems along sightlines A and B, respectively. For moderately strong Ca II absorbers of $W_r(3934) = 0.1 - 0.5\,\text{Å}$, the range of observed [Cr/Zn] is [Cr/Zn] $\sim -0.4 \pm 0.2$ (e.g., Zych et al. 2009 and references therein). The inferred [Cr/Zn] level indicates a modest amount of dust depletion similar to that seen in the Galactic halo, where the expected amount of Fe depletion is $0.5-0.6$ dex (e.g., Savage & Sembach 1996; De Cia et al. 2016). For both sightlines, applying the expected dust depletion leads to still higher gas metallicities, reaching solar or supersolar values, [Fe/H] $\gtrsim 0$, and comparable to the typical mean metallicities in the hot ISM of nearby ellipticals, [Fe/H] $\gtrsim 0 - 0.3$ (e.g., Humphrey & Buote 2006; Loewenstein & Davis 2010, 2012).

4.4.3 Fe Mass Budget

In Z16, we reported a supersolar [Fe/Mg] abundance pattern in the lensing galaxy and suggested that the gas has been enriched by the Fe-rich ejecta from SNe Ia. Now that we have estimated the gas metallicity, we can estimate the total Fe mass observed in the cool ISM and compare it with the expected contribution from SNe Ia.

The Fe mass in the cool ISM of the lens is estimated based on the observed $N(\text{H I})$, the inferred solar gas metallicity, and the ionization state of the gas from the CLOUDY models in Section 4.4.1. We find a total Fe mass within $d = 5$ kpc ($\approx 2\,r_e$; the region probed by the doubly lensed QSO) of $M_{\rm cool}(\text{Fe}) \sim (5-8) \times 10^4\,(f_{\rm cov})\,M_\odot$ in the cool ISM of the lens, where $f_{\rm cov}$ is the cool gas covering fraction.

Next, we estimate the expected SNe Ia contribution based on the observed rate and expected yields of SNe Ia. The observed radial distribution of SNe Ia in elliptical galaxies follows the stellar light distribution (Förster & Schawinski 2008). The mean SNe Ia rate per unit stellar mass is found to be 0.044 SNe per century per $10^{10}\,M_\odot$ in nearby ellipticals (Mannucci et al. 2005). Combining these findings, we estimate that the integrated SNe Ia rate within $d \sim 5$ kpc of the lens is ~ 0.3 per century. Given a minimum stellar population

age of $\approx$ 1 Gyr for this galaxy (Z16) and assuming a constant SNe Ia rate, a total of 3×10^6 SNe Ia should have occurred in this volume. Because SN Ia is expected to produce $\approx 0.6 - 0.7\,M_\odot$ in Fe (e.g., Iwamoto et al. 1999), the estimated total number of SNe Ia leads to an expected total Fe mass of $M_{\rm Fe_{Ia}} \sim 2 \times 10^6\,M_\odot$ over the 1 Gyr time interval. Note that if the SNe Ia rate were higher in the past, then this estimate should be considered as a lower limit. Comparing $M_{\rm cool}$(Fe) to $M_{\rm Fe_{Ia}}$, we conclude that the Fe uncovered in the absorbers accounts for at most $\sim 5\%$ of all Fe produced by SNe Ia over the lifetime of a massive elliptical galaxy. As a result, the majority of Fe must reside in a hot ISM phase.

Although no direct observations of the hot ISM are available for this quiescent galaxy, we could use nearby massive ellipticals as a reference. X-ray observations have shown that their hot ISM has a typical mean [Fe/H] ~ 0 and a mean central density of $n_{\rm H} \sim 0.1\,{\rm cm}^{-3}$ (e.g., Mathews & Brighenti 2003). Adopting these numbers, we infer a total hot-phase Fe mass within $2\,r_e$ of $M_{\rm hot}({\rm Fe}) \sim 2.5 \times 10^6\,M_\odot$, in good agreement with the expected contribution from SNe Ia. Therefore, the implication that the majority of Fe produced in SNe Ia resides in the hot phase is at least consistent with the empirical understanding of nearby massive ellipticals.

4.5 Conclusions

Using *HST*/STIS UV spectra of the doubly lensed images of QSO HE 0047−1756, we have discovered a high column density of neutral hydrogen gas at $3 < d < 5$ kpc (or $r_e < d < 2\,r_e$) from a massive ($M_{\rm star} \approx 10^{11}\,M_\odot$) elliptical lens galaxy at $z = 0.408$. The new STIS spectra not only allow direct measurements of the ISM N(HI) and metallicity, but also constrain the Fe mass budget in this distant elliptical. We find an ISM N(H I) of log $N({\rm H\,I})/{\rm cm}^{-2} = 19.6 - 19.7$ at two locations separated by ≈ 8 kpc on opposite sides of the galaxy. This large N(H I) is comparable to the range of N(H I) in nearby ellipticals. The Fe abundance is $0.3 - 0.4$ solar along both sightlines, which increases to solar or supersolar after accounting for likely dust depletions. Together, the observed N(H I) and Fe abundance

constrain the Fe mass budget. For a 100% gas covering fraction, we infer a total Fe mass of $M_{\rm cool}({\rm Fe}) \sim (5-8) \times 10^4\ M_\odot$ in the cool ISM of the lens. Including previous findings that SNe Ia contribute significantly to the chemical enrichment in massive quiescent halos (e.g., Mernier et al. 2017), we find that the majority ($\approx 95\%$) of Fe produced by SNe Ia resides in the hot phase. Future studies probing warm ($T \sim 10^{5-6}$ K) gas in the halos of luminous red galaxies using high-ionization metal absorption (e.g., O VI, likely tracing cooling gas) will provide new insights into SNe Ia heating and assess its relative importance to other forms of late-time feedback in the halos of massive quiescent galaxies.

CHAPTER 5

CHARACTERIZING CIRCUMGALACTIC GAS AROUND MASSIVE ELLIPTICALS AT $z \sim 0.4$: PHYSICAL PROPERTIES AND ELEMENTAL ABUNDANCES

The contents of this chapter were previously published in the Monthly Notices for the Royal Astronomical Society as Zahedy, F. S., Chen, H.-W.,Johnson, S. D., Pierce, R. M., Rauch, M., Huang, Y.-H., Weiner, B. J., & Gauthier, J.-R. 2019, MNRAS, 484, 2019. They are reproduced here in accordance with the copyright agreement and with permission from the Oxford University Press.

5.1 Introduction

Substantial efforts have been made in the last two decades to identify and characterize the physical processes which are at play in the gaseous halo surrounding galaxies, known as the circumgalactic medium (CGM; see recent reviews by Chen 2017 and Tumlinson et al. 2017 and references therein). The CGM is situated between the intergalactic medium (IGM), where most baryons in the Universe reside, and galaxies, where star formation occurs and heavy metals are synthesized. This unique characteristic makes the CGM a prime location to investigate the intricate interplay between gas accretion from the IGM and feedback processes originating in galaxies, in order to understand the baryon cycles that regulate galaxy evolution over cosmic time.

Some of the major unanswered questions in the study of galaxy evolution concern the origin and nature of cool ($T \sim 10^{4-5}$ K) gas in and around massive quiescent galaxies. Among the most massive galaxies in the Universe, they consist of predominantly old ($\gtrsim$ 1 Gyr) stars and do not show any recent star formation (e.g., Eisenstein et al. 2003; Roseboom et al. 2006; Gauthier & Chen 2011). While it is tempting to attribute the "red and dead" nature of quiescent galaxies as due to the absence of cool gas needed to fuel star formation,

successive QSO absorption-line studies probing the CGM of luminous red galaxies (LRGs) have established that a significant fraction of these $z \sim 0.5$ massive elliptical galaxies host chemically enriched cool gas (e.g., Gauthier et al. 2009, 2010; Lundgren et al. 2009; Bowen & Chelouche 2011; Gauthier & Chen 2011; Thom et al. 2012; Zhu et al. 2014; Huang et al. 2016; Chen et al. 2018). These findings at intermediate redshifts are consistent with observations in the local Universe, where H I and CO surveys found that at least a third of nearby ellipticals contain abundant atomic or even molecular gas (e.g., Serra et al. 2012; Young et al. 2014; 2018). The high incidence of cool gas in massive quiescent halos is puzzling, and it presents a challenge to our current understanding of galaxy formation.

First, how does cool gas survive in massive halos? The strong clustering of LRGs indicates that these galaxies reside inside massive dark matter halos with $M_{\rm h} \gtrsim 10^{13}\,{\rm M}_{\odot}$, where gas accreted from the IGM is expected to be shock-heated to the virial temperature of the halo, $T \sim 10^{6.5-7}\,{\rm K}$ (see Faucher-Giguère 2017 for a recent review). Recent cosmological simulations predict that massive galaxies at high redshifts can still acquire cool gas via dense and narrow filaments that penetrate deep into the halo (e.g., Dekel et al. 2009; Kereš et al. 2009; van de Voort et al. 2012; Nelson et al. 2013; Shen et al. 2013), but they also show that this mechanism may not be effective for massive dark matter halos hosting LRGs at $z < 1$ (e.g., Kereš et al. 2009). Alternatively, thermal instabilities may cause cool clumps to condense from the hot halo and fall toward the galaxy (e.g., Mo & Miralda Escude 1996; Maller & Bullock 2004; Sharma et al. 2012; Voit et al. 2015). Although some observational results suggest this mechanism as a promising explanation (Huang et al. 2016), infalling cool clumps of gas are subject to disruption from ram pressure drag and thermal conduction with the hot medium. For that reason, it is still unclear whether cool clumps in the gaseous halo of LRGs will survive their journey to the center of the halo. The detection of high-column density cool gas within projected distances $d < 10$ kpc from $z \sim 0.5$ massive quiescent galaxies (Zahedy et al. 2016; 2017a) indicates that some cool gas may survive, but *to address this question quantitatively requires knowledge of the density and size distributions of cool clumps*

in LRG halos.

Secondly, what are the dominant feedback mechanisms in massive quiescent halos? The quiescent nature of both local and intermediate-redshift massive ellipticals indicates that some form of energetic feedback is effective at preventing the cooling of the hot halo over cosmic time, which would otherwise trigger continuing star formation. At the same time, the absence of young stellar populations and strong active galactic nuclei (AGNs) in typical LRGs (e.g., Roseboom et al. 2006; Sadler et al. 2007; Hodge et al. 2009; Gauthier & Chen 2011; Huang et al. 2016) makes it difficult to invoke starburst-driven outflows or AGN feedback to explain the high incidence of chemically enriched cool gas in and around massive quiescent galaxies. On the other hand, recent observational and theoretical studies have emphasized the importance of the old stellar population themselves in providing the necessary heating, through energy injection from Type Ia supernovae (SNe Ia) and/or winds from asymptotic giant branch (AGB) stars (e.g., Conroy et al. 2015; Zahedy et al. 2016, 2017b; Li et al. 2018; and references therein). Further insights into the dominant feedback mechanisms in LRGs can be obtained by directly comparing observations in the CGM with theoretical predictions for different feedback prescriptions. *Doing so requires knowledge of the ionization states and chemical abundances in the CGM of LRGs.*

A systematic study is necessary to characterize the physical properties and chemical abundances in the CGM of LRGs. This is a primary motivation behind our COS-LRG survey, a comprehensive survey of the gaseous halos of 16 LRGs at $z \sim 0.4$ using a combination of far-ultraviolet (FUV) spectra from the Cosmic Origins Spectrograph (COS) on board the *Hubble Space Telescope* (*HST*) and ground-based optical echelle spectra. *The COS-LRG sample was selected without any prior knowledge of the absorption properties of the LRGs.* In Chen et al. (2018, hereafter Paper I), we presented the initial results of our study, which we summarize here. First, high H I column density gas is common in the CGM of LRGs, with a median of $\langle \log N(\mathrm{H\,I})/\mathrm{cm}^{-2} \rangle = 16.6$ at $d < 160$ kpc. Secondly, we measured a high covering fraction of optically thick gas ($\log N(\mathrm{H\,I})/\mathrm{cm}^{-2} \gtrsim 17.2$) of $\langle \kappa \rangle_{\mathrm{LLS}} = 0.44^{+0.12}_{-0.11}$

at $d < 160$ kpc, which increases to $\langle\kappa\rangle_{\rm LLS} = 0.71^{+0.11}_{-0.20}$ at $d < 100$ kpc. Moreover, the CGM of LRGs contains widespread chemically enriched gas traced by low-, intermediate-, and high-ionization metals. The most prominent metal transitions in LRG halos are those of intermediate-ionization species such as C III and Si III, with a high covering fraction of $\langle\kappa({\rm C\,III})\rangle = 0.75^{+0.08}_{-0.13}$ within $d < 160$ kpc, comparable to what have been observed in the CGM of star-forming galaxies (e.g., Werk et al. 2013). In this chapter, we expand our investigation with absorption-line and ionization analyses of both metal and H I absorption in LRG halos, in order to characterize the physical properties and elemental abundances in the CGM of LRGs.

The chapter is organized as follows. In Section 5.2 we discuss the COS-LRG sample and the spectroscopic observations and data reduction of the background QSOs. We describe the absorption-line and ionization analyses in Section 5.3. In Section 5.4, we characterize the physical properties and elemental abundances in the gaseous halos of LRGs. Finally, we discuss the implications of our findings in Section 5.5 and present a summary of our results/conclusions in Section 5.6. In addition, we discuss the results of the analysis for each individual LRG halo in Appendix A. A standard Λ cosmology is adopted throughout the chapter, with $\Omega_M = 0.3$, Ω_Λ=0.7, and a Hubble constant of $H_0 = 70\,{\rm km\,s^{-1}\,Mpc^{-1}}$.

5.2 Sample and Data

In this section we summarize the COS-LRG sample and the observations of background QSOs. We refer the readers to Paper I for a more detailed discussion on the program design, sample selection, and data reduction of the far-ultraviolet COS spectra and optical echelle spectra of background QSOs in our sample.

The COS-LRG sample was established by cross-correlating spectroscopically identified LRGs in the Sloan Digital Sky Survey (SDSS; York et al. 2000) archive and the literature with all known UV-bright QSOs with FUV $\lesssim$ 18.5 mag.[1] No prior knowledge of the absorption

1. Because the FUV bandpass of GALEX has a minimum wavelength of $\approx$ 1350 Å, our FUV-bright

properties of the LRGs was used in selecting all the LRG-QSO pairs that make up our sample. The UV magnitude cut was chosen to ensure that high-quality and high-resolution spectra of the background QSOs could be obtained with the Cosmic Origins Spectrograph (COS; Green et al. 2012) onboard the *HST*. Furthermore, we imposed a lower limit on the LRG stellar mass of $\log M_{\rm star}/{\rm M}_{\odot} > 11$, and a maximum projected distance of $d = 160$ kpc from the QSO. Both choices were informed by the well-known finding of a significant incidence ($> 10\%$) of Mg II absorbers at $d < 120$ kpc from massive LRGs (e.g., Gauthier et al. 2010; Huang et al. 2016). These selection criteria resulted in a mass-limited sample of 16 quiescent galaxies at $0.21 < z < 0.56$, each probed by a background QSO at $d < 160$ kpc (which corresponds to roughly 1/3 of the virial radius, $R_{\rm h}$, of a $10^{13}\,M_{\odot}$ dark-matter halo).

All 16 QSOs in the COS-LRG sample were observed with COS, either during our own observing program (PID: 14145) or previously available from the *HST* data archive. *HST*/COS with the G130M and G160M gratings provides high-resolution (FWHM $\approx 17\,{\rm km\ s^{-1}}$) FUV spectra of the QSOs over a nearly contiguous wavelength coverage between $\lambda \approx 1150$ Å and $\lambda \approx 1780$ Å, allowing us to probe halo gas using observations of the full H I Lyman series and corresponding low-, intermediate-, and high-ionization metal absorption features at the LRG redshift, including C III $\lambda977$, the O VI $\lambda\lambda1031, 1037$ doublet, Si III $\lambda1206$, and Si II $\lambda1260$. The COS data were downloaded from the *HST* archive and processed using our custom software. The data reduction steps were previously described in detail in Paper I. To summarize, an important aspect of our custom data reduction software is a recalibration of the COS wavelength solution, which was done in two steps. First, relative wavelength offsets between different exposures of the same QSO were corrected using a low-order polynomial that best describes the offsets of common narrow absorption features found in different exposures. Next, different exposures were co-added and an absolute wavelength correction was performed on the combined spectrum by registering non-saturated, low-ionization Galac-

selection for the background QSOs does not bias against optically thick Lyman-limit systems at $z \lesssim 0.5$, which is coincident with the redshift range of COS-LRG galaxies.

Table 5.1: Summary of spectroscopy of background QSOs

QSO	Instrument	Spectral Window (Å)	S/N	Notes
SDSS J0246−0059	COS	1140 − 1790	10	PID: 14145
	MIKE	3350 − 9400	41	
SDSS J0803+4332	COS	1160 − 1800	9	PID: 11598
	HIRES	3150 − 5870	24	
SDSS J0910+1014	COS	1140 − 1790	7	PID: 11598
	HIRES	3150 − 5870	15	
SDSS J0925+4004	COS	1160 − 1800	6	PID: 11598
	HIRES	3240 − 5870	16	
SDSS J0946+5123	COS	1140 − 1780	7	PID: 14145
SDSS J0950+4831	COS	1070 − 1800	10	PID: 11598 & 13033
	HIRES	3100 − 5870	30	
SDSS J1111+5547	COS	1140 − 1800	15	PID: 12025
SDSS J1127+1154	COS	1140 − 1780	8	PID: 14145
	MIKE	3350 − 9400	17	
SDSS J1243+3539	COS	1140 − 1780	14	PID: 14145
SDSS J1244+1721	COS	1420 − 1780	7	PID: 12466
	MIKE	3350 − 9400	33	
SDSS J1259+4130	COS	1120 − 1790	13	PID: 13833
SDSS J1357+0435	COS	1130 − 1800	13	PID: 12264
	MIKE	3350 − 9400	25	
SDSS J1406+2509	COS	1140 − 1780	6	PID: 14145
	MIKE	3350 − 9400	10	
SDSS J1413+0920	COS	1130 − 1750	17	PID: 13833
SDSS J1550+4001	COS	1140 − 1790	8	PID: 11598
	HIRES	3100 − 5870	31	
SDSS J1553+3548	COS	1140 − 1790	8	PID: 11598
	HIRES	3100 − 5870	36	

tic absorption lines to their known vacuum wavelengths. The final wavelength solution for our FUV COS spectra is accurate to within $\pm 3\,\mathrm{km\ s^{-1}}$, based on a comparison with low-ionization absorption features seen in the ground-based optical echelle spectra.

Optical echelle spectra of COS-LRG QSOs are available for 11 out the 16 QSOs in the sample. The echelle observations were obtained using two high-resolution spectrographs, MIKE (Bernstein et al. 2003) on the Magellan Clay telescope and HIRES (Vogt et al. 1994) on the Keck I telescope. The MIKE observations were obtained during our own observing program, whereas the HIRES data were retrieved from the Keck Observatory Archive (KOA). The instrumental configuration chosen for our MIKE observations provides a spectral resolution of FWHM $\approx$ 10 km s^{-1} at wavelength $\lambda < 5100$ Å. The archival HIRES observations are characterized by a spectral resolution of FWHM ≈ 6.5 km s^{-1} at $\lambda < 5900$

Å. By extending the spectral coverage of the COS-LRG QSOs to optical wavelengths (from $\lambda \sim 3100$ Å to well over $\lambda \sim 5000$ Å), the echelle spectra of the QSOs allow access to additional prominent absorption features arising in low-ionization gas in LRG halos, especially the Mg II $\lambda\lambda 2796, 2803$ doublet, the Mg I $\lambda 2852$ transition, and a series of Fe II transitions including Fe II $\lambda 2586$ and Fe II $\lambda 2600$. A detailed description of the data reduction for the MIKE and HIRES spectra can be found in Paper I.

A summary of FUV and optical echelle spectroscopic observations is presented in Table 5.1, where we list for each background QSO the instrument used for the observations, the spectral coverage of the data, and the mean S/N per resolution element in final reduced spectrum.

5.3 Analysis

To promote a deeper understanding of the circumgalactic environment of massive halos, we assembled a mass-limited sample of 16 LRGs with $\log M_{\rm star}/{\rm M}_{\odot} > 11$. The LRGs were selected without prior knowledge of the presence or absence of CGM absorption features. This uniform sample of galaxies allows an unbiased and accurate characterization of the gaseous halo of intermediate-redshift, massive elliptical galaxies. The two main objectives of the COS-LRG program are: (1) to probe the bulk of cool gas in LRG halos by obtaining accurate measurements of N(H I); and (2) to constrain the physical properties and elemental abundances in massive quiescent halos by observing different ionic metal transitions that probe a wide range of ionization states.

In Paper I, we presented N(H I) measurements for the sample and reported significant incidences ($> 40\%$) of low-, intermediate-, and high-ionization metal absorptions at $d < 160$ kpc in massive quiescent halos. To investigate the physical properties of the CGM of LRGs and constrain the chemical abundance of the gas requires (1) accurate column density measurements for the observed metal absorption features, and (2) a detailed ionization modeling of the gas under different physical conditions (e.g., density, metallicity) to explain the ob-

servations. Here we describe the analysis to first measure the ionic column densities and subsequently constrain the physical properties and metallicities of the gas.

5.3.1 Voigt Profile Analysis

The available high-resolution FUV and optical echelle spectra of the QSOs enable us to resolve the component structures of different absorption transitions and measure the column densities of metal ions accurately. Utilizing a custom software previously developed by and described in Zahedy et al. (2016, see Chapter 2), we performed a forward modeling of Voigt profiles to constrain the ionic column densities of individual absorbing components in each LRG halo. The software was designed to analyze both well-sampled and under-sampled absorption spectra with known line-spread function (LSF), and to properly assess the confidence intervals of derived model parameters via a Markov Chain Monte Carlo (MCMC) analysis.

In summary, the Voigt profile of each absorption component is uniquely defined by three parameters: the column density N_c, the Doppler parameter b_c, and the velocity centroid $\mathrm{d}v_c$ relative to the redshift of the strongest H I component in the absorption system. To perform the fit, the program first generated a theoretical spectrum using the minimum number of components necessary to explain the observed absorption profile. Then, this model spectrum was convolved by the appropriate instrumental LSF of the spectrograph used to collect the data, and binned to match the spectral pixel width of the data. Finally, the simulated absorption profile was compared to the observed absorption profile, and the best-fit model was found by minimizing the χ^2 value.

To assess uncertainties in the model parameters, we performed a MCMC analysis using the EMCEE package (Foreman-Mackey et al. 2013). The MCMC analysis allows us to construct the marginalized posterior probability distribution for each model parameter. Each MCMC run consisted of 500 steps performed by an ensemble of 250 walkers. To speed up convergence, the walkers were seeded in a tiny region within the parameter space which is

centered at the minimum χ^2 solution.

The absorption transitions which were analyzed in a given absorption system include all observed transitions from the following list, ordered by increasing rest wavelength: O I λ971, C III λ977, O I λ988, N III λ989, the O VI $\lambda\lambda$1031, 1037 doublet, C II λ1036, N II λ1083, Fe III λ1122, Fe II λ1144, Si II λ1190, Si II λ1193, Si III λ1206, Si II λ1260, O I λ1302, C II λ1334, Si IV $\lambda\lambda$1393, 1402, Fe II λ2382, Fe II λ2586, Fe II λ2600, the Mg II $\lambda\lambda$2796, 2803 doublet, and Mg I λ2852. In our analysis, we required different transitions of the same species (e.g., Si II λ1190 and Si II λ1193) to have the same Voigt profile parameters. Furthermore, we imposed the same kinematic structure (i.e., number of components and velocity structure) among H I, low-ionization, and intermediate-ionization species. This choice was justified by the excellent kinematic agreement among the observed absorption profiles of various low- and intermediate-ionization species, including Mg II, Si II, Si III, and C III (Paper I). Excepted from this requirement was high-ionization O VI absorption, which is known to often exhibit distinct velocity profiles compared to lower-ionization gas (e.g., Savage et al. 2010; Werk et al. 2016). For that reason, we performed the Voigt profile analysis for the O VI doublet independently from the analysis for H I and lower-ionization metals.

The results of our Voigt profile analysis are presented in Appendix A for each LRG. In Figures A.1a to A.16a, we present the continuum-normalized absorption profiles of different transitions, the best-fit Voigt profiles for individual components, and the integrated Voigt profile summed over all components. These figures show the excellent agreement in velocity centroids among individual components of different ionic species, including the H I Lyman series, C II, Mg II, Si II, and C III, which demonstrates the high accuracy of our wavelength calibration. In Tables A.1a to A.16a, we report the best-fit Voigt profile parameters and the associated 68% confidence intervals for each component identified in the Voigt profile analysis. For saturated components, we report the 95% lower limits on the column density N_c and the corresponding 95% upper limits on Doppler parameter b_c. For non-detections, we report the 95% upper limits on N_c based on the error spectrum, calculated over a spectral

window that is twice the FWHM of a line with $b_c = 10\,\mathrm{km\ s^{-1}}$ for low- and intermediate-ionization species and $b_c = 30\,\mathrm{km\ s^{-1}}$ for highly ionized O VI. Finally, we also report in Table A.1a to Table A.16a the total $N(\mathrm{H\,I})$ and ionic metal column densities summed over all components in each system.

5.3.2 Ionization Analysis

To constrain the metallicity and other physical quantities of the CGM, it is necessary to determine the ionization state of the gas. The inferred cool temperature of the gas ($T \lesssim$ a few $\times 10^4$ K, see Section 5.4.2 and Appendix A) is consistent with a photoionized gas. The ionization state of the gas can be determined by comparing the observed column densities of different ionic species to predictions from photoionization calculations (e.g., Chen et al. 2017). An important physical quantity in photoionized gaseous environment is the ionization parameter U, defined as the number of incident ionizing photons per hydrogen atom. For a fixed radiation field characterized by a total flux of hydrogen-ionizing (≥ 1 Ryd) photons Φ, the U parameter is inversely proportional to the hydrogen number density n_{H}, according to $U \equiv \Phi / c\, n_{\mathrm{H}}$. Higher gas density results in lower U, which leads to a more neutral gas, and vice versa. Another physical quantity which affects the observed ionic column densities is the metallicity of the gas [M/H]. High-metallicity gas cools more efficiently than low-metallicity gas, shifting the photoionization equilibrium toward lower ionization (i.e., more neutral) states.

We performed a series of photoionization calculations using Cloudy v.13.03 (Ferland et al. 2013) package. We considered a plane-parallel column of gas with uniform volume density n_{H}, which was irradiated by an ultraviolet background (UVB) radiation field. To investigate how uncertainty on the UVB affects the derived gas density and metallicity (see Chen et al. 2017 for an extensive discussion), we performed two sets of calculations using two different UVBs: (1) the updated Haardt & Madau (2001) UVB, known as HM05 in Cloudy; and (2) the Haardt & Madau (2012) UVB, known as HM12 in Cloudy. The two radiation fields

differ in both their spectral slopes and overall intensities between $1 - 10$ Ryd. While the HM05 spectrum is softer than HM12 within this energy regime, the HM05 UVB has more $1 - 3$ Ryd photons which have large photoionization cross-sections for neutral hydrogen atoms as well as low- to intermediate-ionization metals. Furthermore, the HM05 UVB has about 2.5 times (0.4 dex) the total number of hydrogen-ionizing photons of the HM12 UVB. In our ionization calculations, both UVBs were adopted at $z = 0.4$, which is roughly the median redshift of the COS-LRG galaxies. At this fiducial redshift, the relationship between U and $n_{\rm H}$ is $\log U = -5.42 - \log n_{\rm H}$ for HM05, and $\log U = -5.83 - \log n_{\rm H}$ for HM12. For example, a typical CGM gas density of $n_{\rm H} = 0.01\,{\rm cm}^{-3}$ corresponds to $\log U \approx -3.4$ and $\log U \approx -3.8$ for the HM05 and HM12 UVBs, respectively.

For each UVB, we constructed a grid of CLOUDY models spanning a wide range of H I column densities ($14 \leq \log N({\rm H\,I})/{\rm cm}^{-2} \leq 20$ in 0.25 dex steps), gas densities ($-5 \leq \log n_{\rm H}/{\rm cm}^{-3} \leq 1$ in 0.25 dex steps), and metallicities ($-3 \leq [{\rm M/H}] \leq 1$ in 0.25 dex steps). For each point in the grid, CLOUDY calculated the expected column densities and ionization fractions of different ionic species assuming photoionization equilibrium. We assumed a solar abundance pattern for the gas, although when the predictions were compared to observations, we relaxed this assumption whenever necessary and allowed by the data (see Appendix A).

An example of CLOUDY calculations is presented in Figure 5.1, where the predicted column densities of different ions are plotted as a function of ionization parameter U. The column density curves are shown for a gas with $\log N({\rm H\,I})/{\rm cm}^{-2} = 16.5$ and $[{\rm M/H}] = -0.5$, which are typical values for individual components in our sample. The model predictions for a gas irradiated by the HM05 UVB are shown in solid lines, whereas predictions for a gas irradiated by the HM12 UVB are shown in dash-dotted lines. Comparing the model expectations under the two different UVBs, it is clear that at fixed ionization parameter, the predicted ionic abundances for neutral and singly ionized species (e.g., Mg I, Si II, and Mg II) are systematically lower under HM12 UVB than HM05 UVB. In addition, the decrements in HM12-predicted column densities relative to HM05 grow larger for higher U parameter (or

equivalently, lower $n_{\rm H}$). Similar, albeit more modest, trends are also predicted for doubly ionized species such as C III and Si III. These trends result from of the harder HM12 UVB spectrum, which has a higher fraction of > 3 Ryd photons that are needed to produce highly ionized (triply ionized or more) metal species compared to the HM05 UVB. As U increases, both low- and intermediate-ionization species are preferentially lost to higher ionization states under HM12 UVB than HM05 UVB. As a consequence of these intrinsic differences between HM05 and HM12 UVBs, HM05 models require a higher gas metallicity than HM12 models to reproduce the observed ionic abundances (see also Wotta et al. 2016).

To estimate the metallicity and density of the gas, we compared the resulting CLOUDY grid of predictions to the data and performed a statistical analysis which took into account measurements as well as upper limits (non-detections) and lower limits (saturation) in the data. Given a suite of observed ionic transitions $\{y_i\}$ for a kinematically matched absorbing component with n number of measurements, m upper limits, and l lower limits, the probability that the gas has a given density and metallicity is defined to be

$$\begin{aligned}\mathcal{P}(n_{\rm H}, [{\rm M/H}] \mid \{y_i\}) \propto & \left(\prod_{i=1}^{n} \exp\left\{-\frac{1}{2}\left[\frac{y_i - \bar{y_i}(n_{\rm H}, [{\rm M/H}])}{\sigma_i}\right]^2\right\}\right) \\ & \times \left(\prod_{i=1}^{m} \int_{-\infty}^{y_i} dy' \exp\left\{-\frac{1}{2}\left[\frac{y' - \bar{y_i}(n_{\rm H}, [{\rm M/H}])}{\sigma_i}\right]^2\right\}\right) \\ & \times \left(\prod_{i=1}^{l} \int_{y_i}^{+\infty} dy' \exp\left\{-\frac{1}{2}\left[\frac{y' - \bar{y_i}(n_{\rm H}, [{\rm M/H}])}{\sigma_i}\right]^2\right\}\right), \end{aligned} \tag{5.1}$$

where $y_i = \log N_i$ is the observed column density of the i-th ionic species, and σ_i is the measurement uncertainty of y_i, and $\bar{y_i} = \log \bar{N_i}$ is the corresponding model prediction. Note that in equation 5.1, the first product is equivalent to calculating $e^{-\frac{1}{2}\chi^2}$ for the n ionic column density measurements, whereas the second and third products extend the calculation over the m upper limits and l lower limits, respectively (see also Chen et al. 2010; Crighton et al. 2015; Stern et al. 2016).

The statistical analysis described above was performed for each absorbing component identified in our Voigt profile analysis (Section 5.3.1). For each component, all available

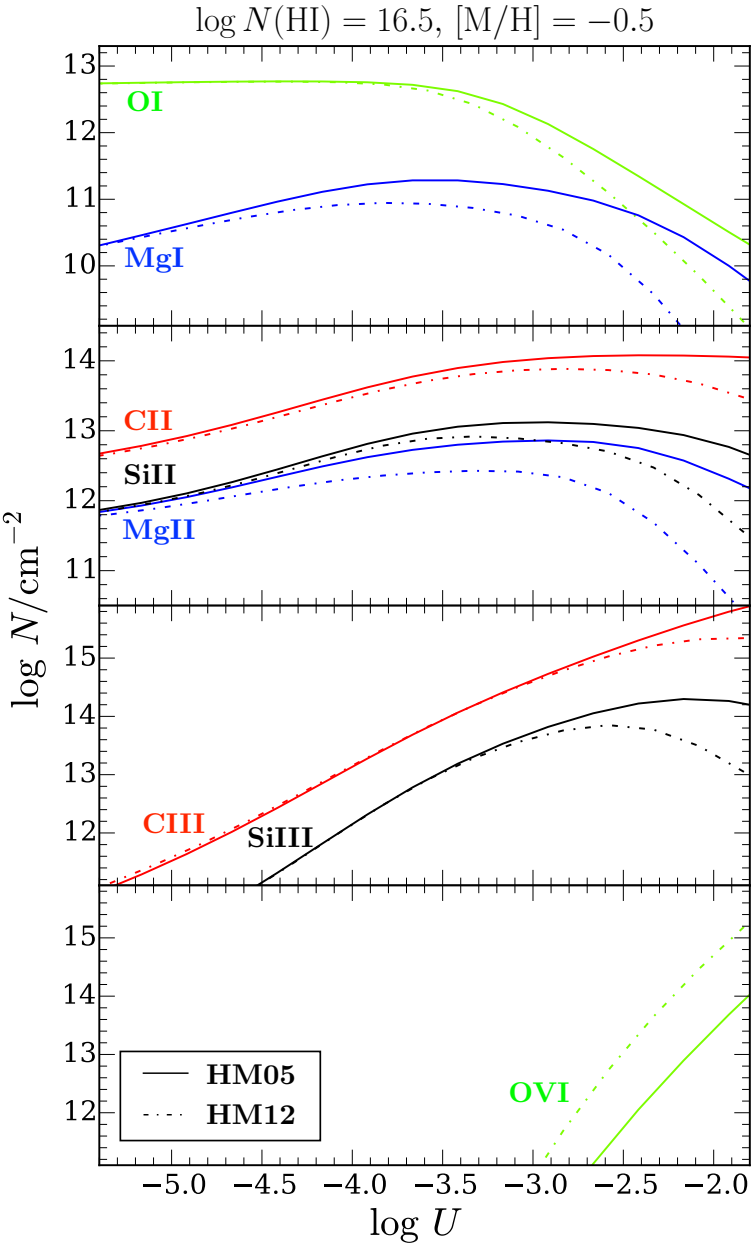

Figure 5.1: Example predictions of ionic column densities as a function of ionization parameter U from CLOUDY photoionization calculations. From top to bottom, the panels are ordered by increasing ionization state, shown here for common ionic species O I, Mg I, C II, Mg II, Si II, C III, Si III, and O VI. The prediction curves are shown for a gas with $\log N\,(\mathrm{H\,I}) = 16.5$ and a metallicity of $[\mathrm{M/H}] = -0.5$, which are typical values in our sample. In solid lines, we show the predicted column densities for a gas irradiated by an updated Haardt & Madau (2001) ionizing background radiation field (HM05 in CLOUDY) at $z = 0.4$. In dashed-dotted lines, we show the corresponding predictions under the Haardt & Madau (2012) background radiation field (HM12 in CLOUDY) at the same redshift. A solar abundance pattern is assumed for the model calculations shown here.

column density measurements, upper limits, and lower limits for low- and intermediate-ionization species were compared to an interpolated grid of CLOUDY models evaluated at the observed N(H I) of the data. We note that O VI measurements were excluded from this analysis, not only because of the the well-known uncertainty in the ionization mechanism of O VI absorbers, but also because of the observed kinematic misalignments between the absorption profiles of O VI and lower-ionization gas (H I and metal ions; see Section 5.4.2 and Appendix A). As discussed in Section 5.5.3, our observations indicate that contributions from higher ionization gas phase to the observed column densities of lower ionization species are negligible, so the exclusion of higher ionization gas from our ionization analysis should not bias the inferred ionization parameter of cool and lower-ionization gas phase considered here. We discuss the possible origins of the high-ionization gas traced by O VI absorbers in LRG halos in Section 5.5.3.

The results of the ionization analysis are presented in Tables A.1b to A.16b in Appendix A, where for each individual component we report the number of detected metal species which are used to constrain the model, $N_{\rm metal}$, the most probable gas metallicity [M/H] and density $n_{\rm H}$ under both the HM05 and HM12 UVBs, as well as the estimated 68% confidence intervals for [M/H] and $n_{\rm H}$. For components with $N_{\rm metal} < 2$, we find that the inferred [M/H] and $\log n_{\rm H}$ are subject to large uncertainties of > 0.5 dex, and in a number of cases there is no clear point of maximum probability within the parameter space of the models. For these components, we report in Tables A.1b to A.16b the estimated 95% upper or lower limits on the parameter values. In addition, we report in Tables A.1b to A.16b the inferred gas metallicity and density considering each absorber as a single clump. For the single-clump (SC) model, the aforementioned ionization analysis was performed using the integrated N(H I) and ionic column densities summed over all components in each system, to facilitate comparisons with existing CGM/IGM ionization studies in the literature (e.g., Werk et al. 2014; Prochaska et al. 2017; Muzahid et al. 2018). Finally, we present in Figures A.1b to A.16b the two-dimensional joint probability distribution of [M/H] and $n_{\rm H}$

for components with $N_{\rm metal} \geq 2$, under both the HM05 (black contours) and HM12 (blue contours) UVBs. The contours indicate the estimated 68% and 95% confidence levels for the model parameters.

5.4 Physical Properties and Metallicities in LRG halos

Our analysis of CGM absorption in the COS-LRG sample reveals a diversity of gas properties in massive quiescent halos $z \sim 0.4$. A detailed discussion on the absorption and gas properties in individual LRG halos is presented in Appendix A, which we summarize as follows. First, a combined Voigt profile analysis on H I and metal absorption lines shows that absorbers in LRG halos exhibit a multi-component structure that is distributed over up to ±a few ×100 km s^{-1} in line-of-sight velocity relative to the LRGs. Furthermore, the excellent kinematic alignments between H I, low ions (e.g., Mg II), and intermediate ions (e.g., C III) indicate a physical connection between these different species. In this section, we characterize the physical properties and chemical abundances in the gaseous halos of LRGs.

5.4.1 Column Density Profiles of H I and Heavy Ions

In Figure 5.2, we present the spatial distribution of absorption column densities for various ions observed in the gaseous halos of COS-LRG galaxies. From top to bottom panels, we show the integrated column densities versus projected distance d for neutral H I, low-ionization Mg II, intermediate-ionization C III and Si III, and high ionization O VI species. To facilitate comparisons with other surveys, we include a second horizontal axis showing the halo radius-normalized projected distance $d/R_{\rm h}$. Recall from Paper I that the COS-LRG sample of massive quiescent galaxies has a median stellar mass and dispersion of $\log \langle M_{\rm star}/{\rm M}_\odot \rangle = 11.2 \pm 0.2$, which corresponds to a typical halo mass of $M_{\rm h} \approx 10^{13}\,{\rm M}_\odot$ according to the Kravtsov et al. (2018) stellar-to-halo-mass relation, and a halo radius of $R_{\rm h} \approx 500$ kpc at

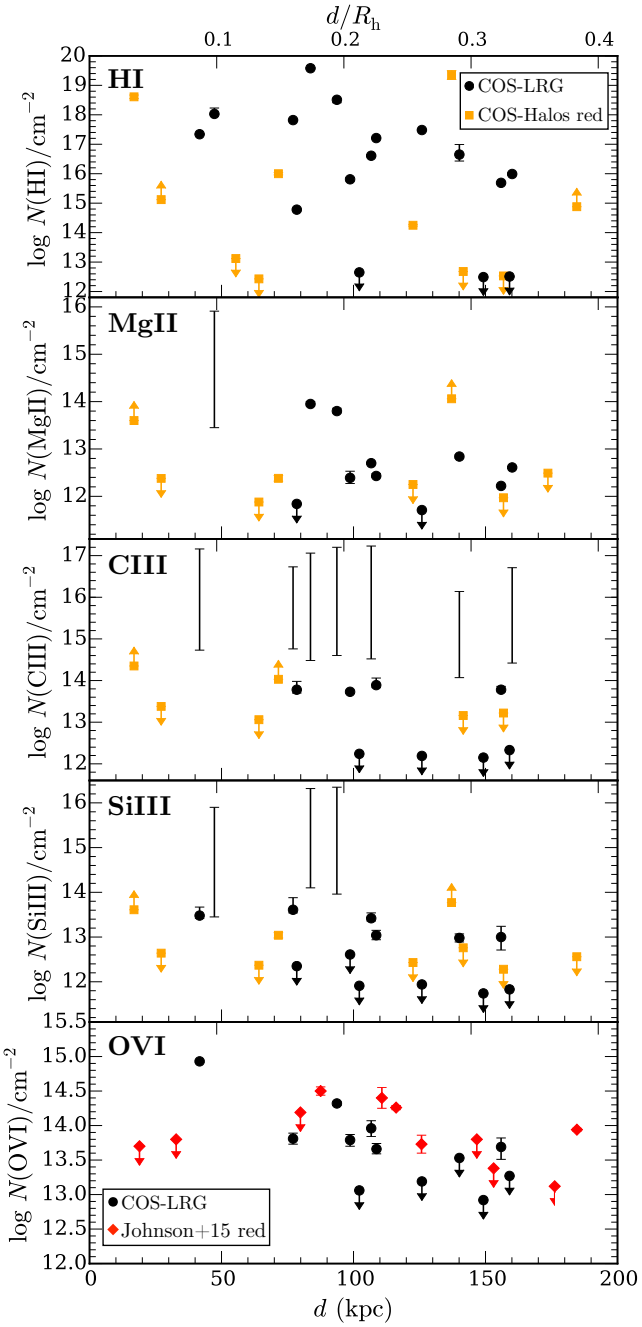

Figure 5.2: Radial profile of integrated absorption column densities in the CGM of quiescent galaxies, shown for H I, Mg II, C III, Si III, and O VI. COS-LRG measurements (black circles) are plotted versus projected distance d. For comparison, absorption measurements from passive galaxies in COS-Halos (Werk et al. 2013; orange squares) and Johnson et al. (2015; red diamonds) are plotted versus normalized projected distance $d/R_{\rm h}$. We have excluded five COS-Halos red galaxies which overlap with our LRG sample. Non-detections are shown as downward arrows which represent the 2σ upper limits on ionic column density. Meanwhile, the allowed column density range for saturated absorbers in COS-LRG are shown in empty vertical error bars. For COS-Halos red galaxies, saturated absorbers are represented by upward arrows, which show the lower limits on the absorption column density.

$z = 0.4$.[2] Given the narrow range in $M_{\rm star}$, we adopt this R_h for all COS-LRG galaxies plotted in Figure 5.2.

For comparison, Figure 5.2 shows absorption measurements for the COS-Halos red galaxy subsample (Werk et al. 2013; Prochaska et al. 2017) for H I, Mg II, C III, and Si III. For O VI, we also show measurements from the passive galaxy subsample of Johnson et al. (2015), which includes all COS-Halos red galaxies. Note that column density measurements from these studies are plotted versus the normalized projected distance of the galaxies, $d/R_{\rm h}$. Compared to COS-LRG, the COS-Halos subsample of red galaxies comprises predominantly lower mass galaxies, with a mass range of from $\log M_{\rm star}/{\rm M}_\odot = 10.3$ to $\log M_{\rm star}/{\rm M}_\odot = 11.3$, and a median of $\log \langle M_{\rm star}/{\rm M}_\odot \rangle = 10.8$.

Despite considerable scatter in the observed N(H I) radial profile, there is a general trend of declining N(H I) with increasing d in the COS-LRG sample (top panel of Figure 5.2). This trend is consistent with what is seen in COS-Halos red galaxies as well as previous CGM surveys of the general galaxy populations (e.g., Chen et al. 1998; Johnson et al. 2015). To further examine the decline of N(H I) with increasing distance, we divide our sample into two bins at $d = 100$ kpc, which is approximately the median projected distance. At $d < 100$ kpc from LRGs, the majority of H I absorbers are optically thick (LLSs with $\log N({\rm H\,I})/{\rm cm}^{-2} > 17.2$). In contrast, there is a significantly higher fraction of optically thin absorbers as well as sightlines with non-detections at $d > 100$ kpc. The mean covering fraction of optically thick H I gas is $\langle \kappa \rangle_{\rm LLS} = 0.71^{+0.19}_{-0.26}$ at $d < 100$ kpc, which declines to $\langle \kappa \rangle_{\rm LLS} = 0.22^{+0.22}_{-0.14}$ at $d = 100 - 160$ kpc.

A trend of declining column density with increasing d is also seen in low-ionization metal species such as Mg II. At $d < 100$ kpc, strong N(Mg II) absorbers with $\log N({\rm Mg\,II})/{\rm cm}^{-2} > 13$ are common in COS-LRG. In contrast, absorbers at $d \gtrsim 100$ kpc exhibit significantly lower N(Mg II), where $\log N({\rm Mg\,II})/{\rm cm}^{-2} < 13$ is seen in all cases. For strong Mg II absorbers in

2. We approximate $R_{\rm h}$ as the region with average density of 200 times above the mean matter density of the Universe at a given epoch.

COS-LRG, we estimate a mean covering fraction of $\langle\kappa(\mathrm{Mg\,II})\rangle_{13.0} = 0.60^{+0.25}_{-0.30}$ at $d < 100$ kpc. A caveat of this calculation is that two sightlines at $d < 100$ kpc do not have any Mg II constraints and consequently do not contribute to the covering fraction estimation. Including these two sightlines would lead to a mean Mg II covering fraction of $\langle\kappa(\mathrm{Mg\,II})\rangle_{13.0} \approx 0.4-0.7$ at $d < 100$ kpc, depending on whether these two absorbers satisfy the strong Mg II absorption criterion or not. In contrast, the lack of strong Mg II absorption At $d = 100 - 160$ kpc from LRGs in our sample constrains the mean covering fraction to $\langle\kappa(\mathrm{Mg\,II})\rangle_{13.0} \approx 0.0 - 0.2$, for $\log N(\mathrm{Mg\,II})/\mathrm{cm}^{-2} > 13$.

A surprising finding from Paper I is the high incidence of absorption from intermediate-ionization species C III and Si III, comparable to what have been observed around star-forming galaxies. While the high oscillator strength of the C III $\lambda977$ transition makes C III absorption easily detectable, it also means that C III absorption profiles are often saturated (see Appendix A). For that reason, it is difficult to draw a strong conclusion on possible radial trends in intermediate ionic column densities using C III absorption. For the comparatively weaker Si III absorption, it is clear that strong Si III absorption with $\log N(\mathrm{Si\,III})/\mathrm{cm}^{-2} > 13.0$ are more prevalent at smaller d. At $d < 100$ kpc from COS-LRG galaxies, absorbers with $\log N(\mathrm{Si\,III})/\mathrm{cm}^{-2} > 13.0$ are present in 5 out of 7 cases, which constraints the mean Si III covering fraction to $\langle\kappa(\mathrm{Si\,III})\rangle_{13.0} = 0.71^{+0.19}_{-0.26}$. In contrast, Si III absorption are generally weaker at $d = 100 - 160$ kpc, with a high fraction (50 percent) of non-detections. The estimated mean Si III covering fraction absorption at $d = 100 - 160$ kpc is $\langle\kappa(\mathrm{Si\,III})\rangle_{13.0} = 0.37^{+0.24}_{-0.19}$, for $\log N(\mathrm{Si\,III})/\mathrm{cm}^{-2} > 13.0$.

For high-ionization gas, measurements of O VI column density in LRG halos are available for 12 out of 16 COS-LRG galaxies. We detect O VI absorption in 7 sightlines at a detection threshold of $\log N(\mathrm{O\,VI})/\mathrm{cm}^{-2} > 13.5$, which translates to an estimated mean covering fraction of $\langle\kappa(\mathrm{O\,VI})\rangle_{13.5} = 0.58^{+0.17}_{-0.18}$ at $d < 160$ kpc ($\sim 0.3\,R_{\rm h}$). The mean O VI covering fraction for LRGs is comparable to what Johnson et al. (2015) found at $d \lesssim 0.3\,R_{\rm h}$ for their passive galaxy subsample, $\langle\kappa(\mathrm{O\,VI})\rangle_{\rm J15} = 0.62^{+0.13}_{-0.17}$ for $\log N(\mathrm{O\,VI})/\mathrm{cm}^{-2} > 13.5$. Note

that the red galaxies in Johnson et al. (2015) are predominantly less massive than COS-LRG galaxies, with a median stellar mass and dispersion of $\log \langle M_{\rm star}/{\rm M}_\odot \rangle = 10.7 \pm 0.5$. The comparable O VI covering fractions in massive quiescent halos spanning over an order of magnitude in halo mass (from $M_{\rm h} \sim 10^{12}\,{\rm M}_\odot$ to $M_{\rm h} \gtrsim 10^{13}\,{\rm M}_\odot$) suggest that O VI absorbers in all quiescent halos may share a similar physical origin. A two-sample Kolmogorov-Smirnov (K-S) test demonstrates that we cannot rule out at high statistical significance (> 99 percent) that the lower-mass (Johnson et al. 2015) and massive (COS-LRG) quiescent halo samples of O VI absorbers are drawn from the same parent population.

5.4.2 Kinematic and Thermal Properties

The line-of-sight kinematics of absorbing gas relay crucial information about the underlying motion of cool clumps within LRG halos. Our discussion of individual LRG halos in Appendix A highlights the fact that cool gas absorption profiles in the CGM of LRGs consist of multiple components that are distributed within $\pm$ a few hundred km s^{-1} in line-of-sight velocity relative to the systemic redshift of the galaxy. The distribution of line-of-sight velocities of individual H I components relative to the LRGs is shown in the left panel of Figure 5.3. The velocity distribution can be characterized by a mean and dispersion of $\langle \Delta v_{\rm gas-galaxy} \rangle = 17\,{\rm km\ s^{-1}}$and $\sigma_{\Delta v_{\rm gas-galaxy}} = 147\,{\rm km\ s^{-1}}$. The observed velocity dispersion is consistent with what have been reported for Mg II absorbers around large samples of Mg II absorbers around LRGs using low-resolution data (e.g., Zhu et al. 2014; Huang et al. 2016; Lan et al. 2018). To provide a physical context, the inferred mean mass of LRG halos is $M_{\rm h} \approx 10^{13.4}\,{\rm M}_\odot$ (e.g., Mandelbaum et al. 2008; Gauthier et al. 2009), and the expected line-of-sight velocity dispersion for virialized motion in LRG halos is $\sigma_{\rm h} \approx 260$ km s^{-1}. The observed line-of-sight velocity dispersion of the gas, $\sigma_{\Delta v_{\rm gas-galaxy}} = 147$ km s^{-1}, is merely ~ 60 percent of the expectation from virial motion. The narrow distribution of line-of-sight velocities indicates that an effective dissipative mechanism is at play to slow down the motion of cool gas in the halo (e.g., Huang et al. 2016).

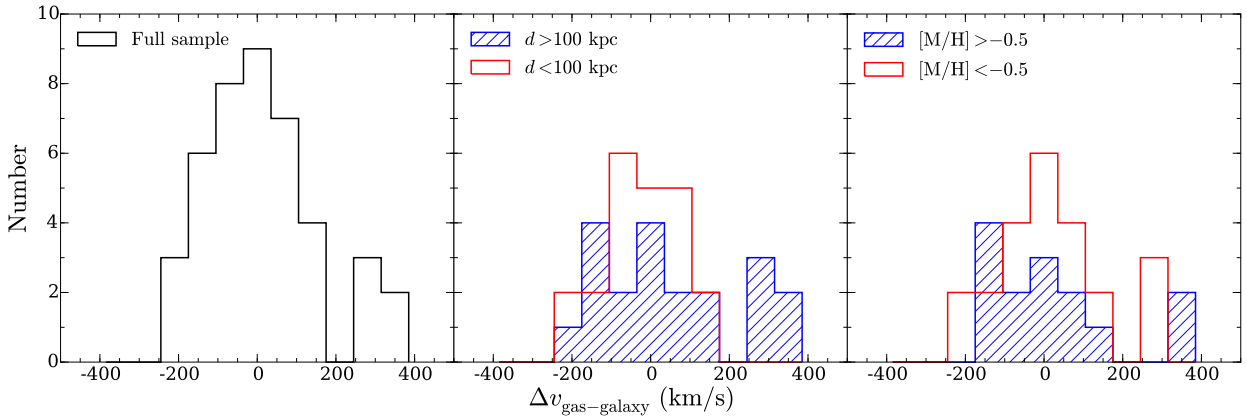

Figure 5.3: Line-of-sight velocity distributions of individual absorption components relative to the LRG systemic redshifts. For the full COS-LRG sample (left panel), we find a mean and dispersion of $\langle \Delta v_{\rm gas-galaxy} \rangle = 17$ km s^{-1}and $\sigma_{\Delta v_{\rm gas-galaxy}} = 147$ km s^{-1}. In the middle panel, the sample is bisected by projected distance d, whereas in the right panel the sample is divided by metallicity. We find no statistically significant distinction between the subsamples in either case.

To evaluate whether the observed velocity dispersion varies with projected distance, we divide the absorbing components into two subsamples on d, one for components at $d < 100$ kpc and another for those at $d > 100$ kpc. The resulting velocity distributions of the two subsamples are shown in the middle panel of Figure 5.3. While the velocity histograms are understandably noisy due to the smaller size of the two subsamples, no significant trend is detected between the line-of-sight velocity distributions at small and large d. Using a two-sided Kolmogorov-Smirnov (K-S) test, we cannot rule out that the two d subsamples come from the same parent distribution in $\Delta v_{\rm gas-galaxy}$ at > 50 percent confidence. We also bisect the sample of individual components into two groups based on their metallicities, a low-metallicity subsample with [M/H] < -0.5 and a high-metallicity subsample with [M/H] > -0.5. Again, no statistically significant distinction can be made between the low- and high-metallicity subsamples, with components from each subsample occupying the full range of velocities with respect to the LRGs (Figure 5.3, right panel). A K-S test cannot rule out that the two [M/H] subsamples come from the same parent distribution in $\Delta v_{\rm gas-galaxy}$ at > 68 percent confidence.

Our Voigt profile analysis also allows us to examine the thermal properties of cool clumps

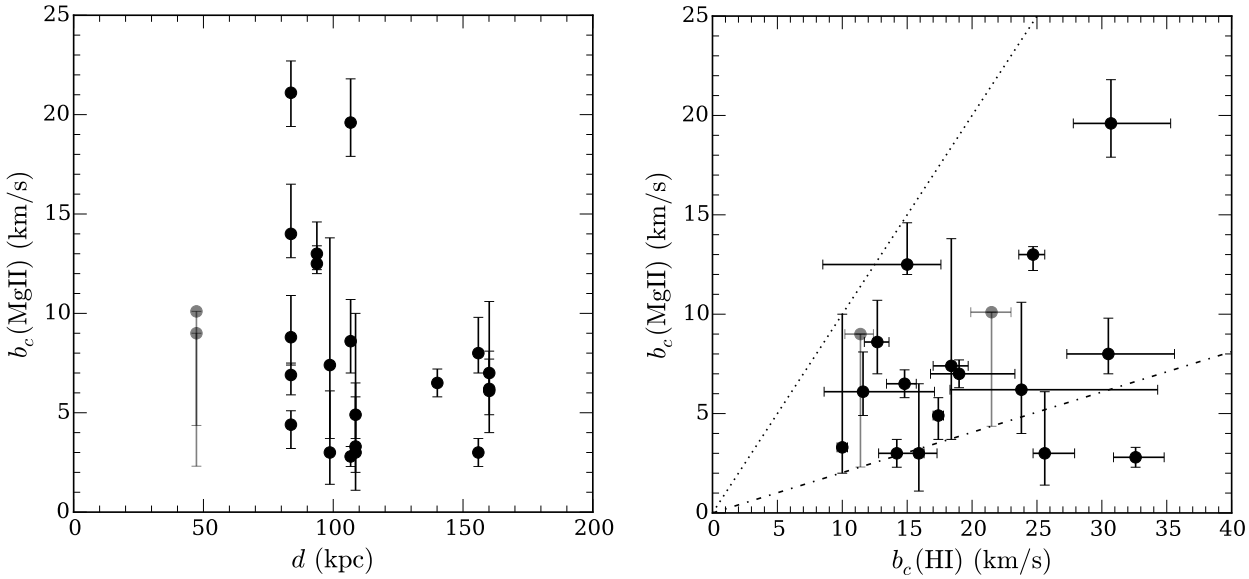

Figure 5.4: *Left*: Doppler parameter b_c plotted versus d for individual Mg II absorption components. Saturated components are represented by grayed out data points. *Right*: Distribution of Doppler linewidths for matched H I and Mg II components. The dashed-dotted line shows the expectation for a pure thermal broadening case, $b_c(\mathrm{Mg\,II}) \approx 0.2\,b_c(\mathrm{H\,I})$, whereas the dotted line shows the expected relationship when Mg II and H I linewidths are dominated by non-thermal broadening, $b_c(\mathrm{Mg\,II}) = b_c(\mathrm{H\,I})$. We find that cool CGM gas around LRGs has a mean temperature and dispersion of $\langle T \rangle = 2.0 \times 10^4\,\mathrm{K}$ and $\sigma_T = 1.4 \times 10^4\,\mathrm{K}$, with a modest non-thermal broadening of $\langle b_{\rm nt} \rangle = 7 \pm 5\,\mathrm{km\ s^{-1}}$.

in LRG halos. In the left panel of Figure 5.4, we plot the Doppler linewidths of Mg II components as a function of d. With the exception of a few broad components, most Mg II components in LRG halos are narrow with $b_c(\mathrm{Mg\,II}) < 10\ \mathrm{km\ s^{-1}}$. The narrow linewidths imply that the gas is both cool and kinematically quiescent. Furthermore, no trend in $b_c(\mathrm{Mg\,II})$ in seen versus d, indicating that cool gas at small and large projected distances from LRG have similar thermal properties.

Next, we show the distribution of Doppler linewidths for matched H I and Mg II absorption components in the right panel of Figure 5.4. Two straight lines are drawn to indicate two limiting cases. First, the dashed-dotted line in the bottom represents the expectation for a pure thermal-broadening case where the Mg II and H I linewidths are related by the square root of their mass ratio alone, giving $b_c(\mathrm{Mg\,II}) \approx 0.2\,b_c(\mathrm{H\,I})$. Secondly, the dotted line on top of the panel shows the expected relation when the Mg II and H I linewidths are

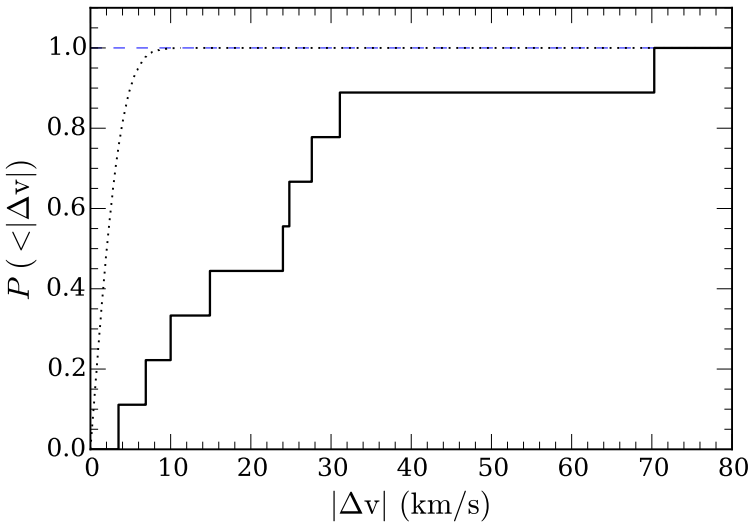

Figure 5.5: Cumulative fraction, P, of O VI absorption components with absolute centroid velocity difference less than $|\Delta v|$ from the nearest low-ionization metal and H I components (solid histogram). The mean/median value is $\langle|\Delta v|\rangle = 24$ km s^{-1}, with a full range of from $|\Delta v| = 4$ to $|\Delta v| = 71$ km s^{-1}. Note that the final wavelength solution for our FUV COS spectra is accurate to within ± 3 km s^{-1}, and the expected $P(|\Delta v|)$ for a normal distribution with a width of $\sigma = 3$ km s^{-1} is shown in dotted curve for comparison. The mismatched kinematics between high-ionization and low-ionization gas in COS-LRG suggest different physical origins between the high- and low-ionization gas.

dominated by non-thermal broadening, b_c(Mg II) $\approx b_c$(H I).[3] It is clear from the right panel of Figure 5.4 that a large majority data points are situated closer to the thermal-broadening line than to the non-thermal broadening line. This is consistent with a quiescent gas that is subject to little non-thermal broadening. The ratios of Doppler linewidths for matched H I and Mg II components in the COS-LRG sample show that the gas has a mean temperature and dispersion of $\langle T\rangle = 2.0 \times 10^4$ K and $\sigma_T = 1.4 \times 10^4$ K, with a modest mean non-thermal line broadening of $\langle b_{\rm nt}\rangle = 7 \pm 5$ km s^{-1}.

Finally, we find that O VI absorption profiles in COS-LRG show distinct kinematic structures from the absorption profiles of lower-ionization metal and H I (see Appendix A for a de-

3. While the parameter space outside the region bounded by the two limiting cases is unphysical, two components are found below the thermal-broadening line. One has a b_c(Mg II) that is consistent within 1-σ with thermal broadening. The other component has a broad b_c(H I) = 33 km s^{-1}, but its Mg II linewidth is only 3 km s^{-1}, which is narrower than expected from thermal broadening. The unphysical relationship between b_c(H I) and b_c(Mg II) for this component implies the presence of unresolved H I components that are not Mg II-bearing.

tailed description of individual absorbing systems). The mean/median absolute difference in centroid velocity between O VI absorption components and the nearest H I and low-ionization metal component is $\langle|\Delta v|\rangle = 24$ km s^{-1}, with a full range of from $|\Delta v| = 4$ to $|\Delta v| = 71$ km s^{-1} (Figure 5.5). Recall that the final wavelength solution for our FUV COS spectra is accurate to within ± 3 km s^{-1}. The kinematic misalignments between high-ionization and low-ionization gas in the COS-LRG sample suggest that different phases of the CGM gas of LRGs have different physical origins (a more in-depth discussion is presented in Section 5.5.2 and Section 5.5.3).

5.4.3 Metallicities and Densities

Our ionization analysis on matched absorption components reveals significant variations in gas metallicities and densities in the cool CGM of LRGs, both within individual halos and among different halos in the COS-LRG sample. We now discuss and investigate for trends in gas metallicities and densities in the COS-LRG ensemble of galaxies. We begin with a discussion on systematic errors in the ionization analysis.

Systematic Errors Arising from the Uncertain UVB

Metallicity and density estimates in CGM studies are based on comparing the absorption column densities of ionic metals and neutral hydrogen. Because the gas is highly ionized in all but the highest column density absorbers, substantial ionization fraction corrections are necessary to convert the observed ionic column density ratios to the desired elemental abundances. A complicating factor in the ionization analysis of CGM gas is the well-known uncertainties in the shape, intensity, and redshift evolution of the extragalactic UVB (e.g., Faucher-Giguère et al. 2008; Haardt & Madau 2012; Kollmeier et al. 2014; Shull et al.2015), which affect the expected ionization fraction corrections in the gas. Adopting different UVBs for the ionization analysis can propagate to order-of-magnitude discrepancies in the inferred gas metallicity (see Chen et al. 2017 for an extensive discussion on the subject).

To explore how the uncertain UVB spectrum affects the derived gas densities and metallicities, we performed our ionization analysis using two different photoionizing background radiation fields, the HM05 and HM12 UVBs (see the discussion in Section 5.3.2). In the top panel of Figure 5.6, the difference in gas densities derived under HM05 and HM12 UVBs is plotted versus component H I column density N_c(H I). Over almost 5 decades in N_c(H I), the gas densities inferred using HM05 UVB are systematically higher than gas densities inferred using the HM12 UVB, with a median difference and dispersion of $\langle \Delta \log n_{\rm H} \rangle = 0.34$ dex and $\sigma_{\Delta \log n_{\rm H}} = 0.10$ dex. The higher inferred gas density under HM05 can be understood as due to the higher intensity of HM05 UVB compared to the HM12 UVB. Recall from our discussion in Section 5.3.2 that the total flux of hydrogen-ionizing photons in HM05 UVB is ~ 0.4 dex higher than that of the HM12 UVB. Consequently, the higher-intensity HM05 UVB requires a higher underlying gas density than the HM12 UVB for fixed ionization parameter U, which describes the ionization state of the gas.

In the bottom panel of Figure 5.6, we plot the difference in metallicities derived under HM05 and HM12 UVBs versus N_c(H I). Over more than 5 decades in H I column density, not only is the [M/H] inferred under HM05 UVB systematically lower than inferred under HM12 UVB, but also the difference in metallicities depends on N_c(H I). For optically thick gas with $\log N_c({\rm H\,I})/{\rm cm}^{-2} \gtrsim 17$, the typical metallicity difference between HM05 and HM12 is modest, $\langle \Delta[{\rm M/H}] \rangle = -0.1 \pm 0.1$ dex. The median metallicity difference is larger for lower N_c(H I) gas, ranging from $\langle \Delta[{\rm M/H}] \rangle \sim -0.3$ dex for gas with $\log N_c({\rm H\,I})/{\rm cm}^{-2} \sim 16$ to $\langle \Delta[{\rm M/H}] \rangle \sim -0.7$ dex for optically thin gas with $\log N_c({\rm H\,I})/{\rm cm}^{-2} < 15$. To understand the origin of this trend, recall from Section 5.3.2 that not only does the HM12 UVB have a harder spectrum than the HM05 UVB, but also it has a higher fraction of > 3 Ryd photons which are required to produce high-ionization (triply ionized or more) metal species. As N_c(H I) decreases and the gas becomes more highly ionized, more low- and intermediate-ionization metals are preferentially lost to higher ionization states under HM12 UVB than under HM05 UVB. Because metallicity estimates of cool CGM gas often rely on suite of low-

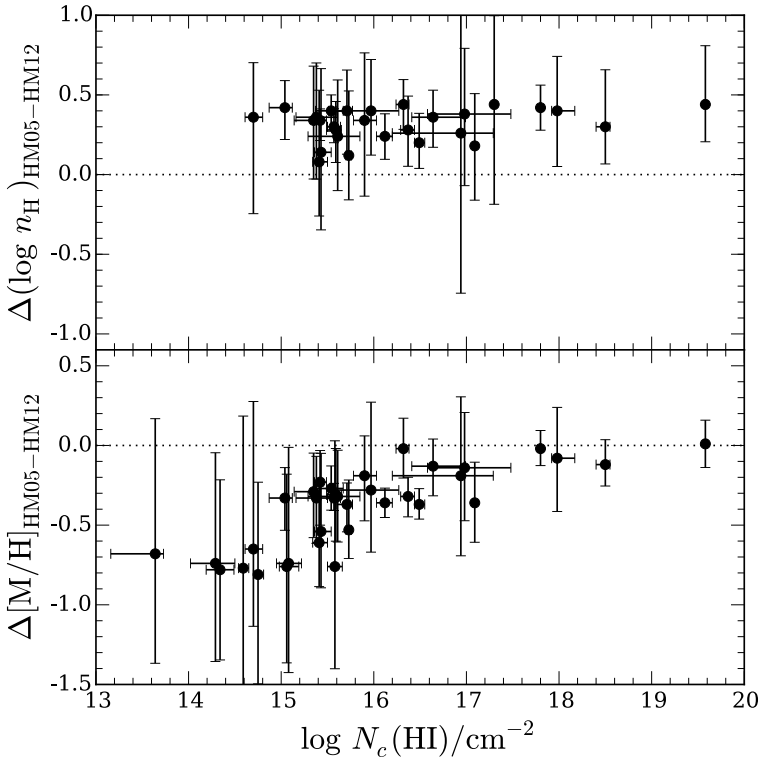

Figure 5.6: *Top*: Difference in gas densities derived under HM05 and HM12 UVBs, plotted versus N_c(H I). Compared to the HM12 UVB, the HM05 UVB leads to higher inferred $n_{\rm H}$ values, with a median difference and dispersion of $\langle \Delta \log n_{\rm H} \rangle = 0.34$ dex and $\sigma_{\Delta \log n_{\rm H}} = 0.10$ dex. *Bottom*: Difference in metallicities derived under HM05 and HM12 UVBs, plotted versus individual component H I column density, N_c(H I). The HM05 UVB leads to lower inferred [M/H] than the HM12 UVB, with a metallicity difference that range from $\langle \Delta[{\rm M/H}] \rangle = -0.1$ for LLSs to $\langle \Delta[{\rm M/H}] \rangle = -0.7$ for optically thin gas.

ionization and intermediate-ionization metal species, the difference in metallicities inferred under HM05 and HM12 UVBs naturally increases with decreasing $N(\mathrm{H\,I})$.

Finally, we note that in all ionization calculations performed in this work, both HM05 and HM12 UVBs were adopted at redshift $z = 0.4$, which is roughly the median redshift of COS-LRG galaxies. Changing the adopted UVB redshift to $z = 0.2$ or $z = 0.6$ would change the intensity of each UVB by no more than ± 0.2 dex. As a result, the inferred gas density n_{H} would change by less than ± 0.2 dex by changing the adopted UVB redshift, which is smaller than the median difference in n_{H} derived under HM05 and HM12 UVBs.

Using two different UVBs that are frequently utilized in CGM/IGM studies, we have quantified the systematic errors resulting from the uncertain shape and intensity of the extragalactic UVB radiation field. It must also be noted that a known issue with the HM12 UVB is that it over-predicts the amplitude of H I column density distribution function in low-redshift ($z < 1$) Lyα forest by a factor of $2 - 4$ (e.g., Kollmeier et al. 2014; Shull et al. 2015; Viel et al. 2017). The HM12 UVB does not match low-redshift IGM observations because of its low hydrogen photoionization rate (Γ_{H}), which is a result of the adopted negligible escape fraction of Ly-continuum photons from low-redshift galaxies (e.g., Shull et al. 2015). In contrast, the HM05 UVB assumes a higher escape fraction of ionizing photons from galaxies, which has been shown to provide better agreement with observations (e.g., Kollmeier et al. 2014; Khaire & Srianand 2015; Viel et al. 2017). For that reason, we adopt the gas metallicities and densities inferred using the HM05 UVB for subsequent analyses and discussions in this work.

Trends in Gas Metallicities and Densities

To illustrate the diversity of inferred gas metallicities and densities in the cool CGM of LRGs, we plot component [M/H] versus n_{H} in Figure 5.7. While no evidence is seen for any correlation between [M/H] and n_{H}, Figure 5.7 shows that cool gas in LRG halos occupy a wide range of metallicities (from less than 0.01 solar to solar and super-solar metallicities)

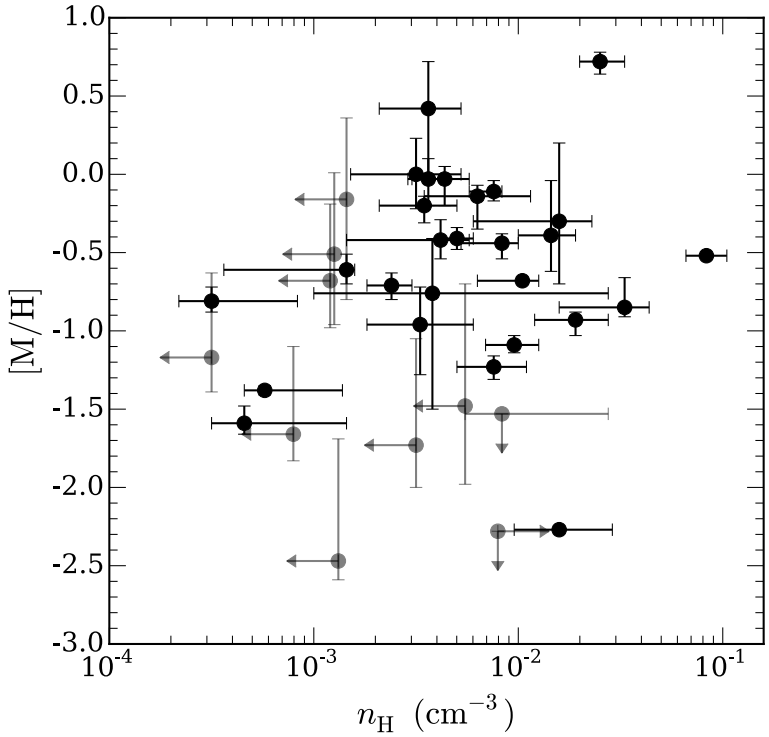

Figure 5.7: Inferred gas metallicity [M/H] versus hydrogen density $n_{\rm H}$ for individual absorbing components in the COS-LRG sample. The vertical and horizontal error bars associated with each data point show the 68 percent confidence intervals for [M/H] and $n_{\rm H}$, respectively. Grayed out data points show components for which only upper/lower limits on [M/H] and/or $n_{\rm H}$ are available, with arrows indicating the 95 percent upper/lower limits. We find no statistically significant correlation between [M/H] and $n_{\rm H}$.

and densities (from $n_{\rm H} \lesssim 0.001\,{\rm cm}^{-3}$ to $n_{\rm H} \sim 0.1\,{\rm cm}^{-3}$).

We present the spatial distribution of component metallicity as a function of d in the left panel of Figure 5.8. Two interesting features are revealed by this plot. First, [M/H] exhibits large variations among different components detected in the gaseous halo of an LRG, at small and large d alike. A majority of LRG halos ($\sim$ 60 percent) that exhibit multi-component absorption profiles show over a factor of 10 difference in [M/H] between the most metal-rich and metal-poor components. Such large variations in [M/H] within the gaseous halo indicate poor chemical mixing in the CGM of LRGs and underscore the importance of resolving the component structures of CGM absorbers, which is afforded by our high-resolution absorption spectra (see also e.g., Churchill et al. 2012; Rosenwasser et al. 2018). In contrast, any information on intra-halo variations is lost if one utilizes only

the integrated H I and metal column densities along individual sightlines in the ionization analysis.

Furthermore, while high-metallicity ([M/H] $\gtrsim -1.0$) components are observed in most LRG halos, metal-poor ([M/H] $\lesssim -1.0$) components are found in half of LRG halos, with a majority these low-metallicity components occuring at $d \gtrsim 100$ kpc. Over the full sample, the median metallicity of individual components is $\langle[\mathrm{M/H}]\rangle = -0.7 \pm 0.2$, where the uncertainty is calculated using a combined bootstrap and Monte-Carlo resampling. In addition, we estimate the 16-84 percentile range in [M/H] to be [M/H] $= (-1.6, -0.1)$ for the whole sample. Note that components with poor constraints on [M/H] (those with metallicity upper limits which are higher than solar metallicity) are excluded from these estimates.

In the right panel of Figure 5.8, we present a plot of [M/H] versus component H I column density. We find no significant trend in [M/H] versus N_c(H I). This lack of correlation in our data stands in contrast to the anti-correlation between metallicity and H I column density that were reported in a number of recent studies (e.g., Prochaska et al. 2017; Muzahid et al. 2018). Considering the known trend of declining N(H I) with d in the CGM (e.g., Chen et al. 1998; Johnson et al. 2015; see also Section 5.4.1), the reported anti-correlation implies that metallicity increases with distance from galaxies, which is difficult to explain. This discrepancy can be attributed as due to two systematic effects. First, the HM12 UVB, which was the adopted UVB in Prochaska et al. (2017), predicts progressively higher metallicities (up to 0.7 dex) with decreasing N(H I) compared to the HM05 UVB (see previous subsection). Secondly, the ionization analyses in these studies utilized integrated H I and metal column densities summed over all components in each absorption system. As we approach lower column density regime, the required data quality (S/N) is higher to detect the gas. Given a fixed S/N and a system with multiple components, weaker metal components is more challenging to uncover. Consequently, relatively more metal-poor gas goes undetected more easily. By treating resolved components separately, we find that several low-N(H I) components only have non-constraining metallicity upper limits. The combination of these

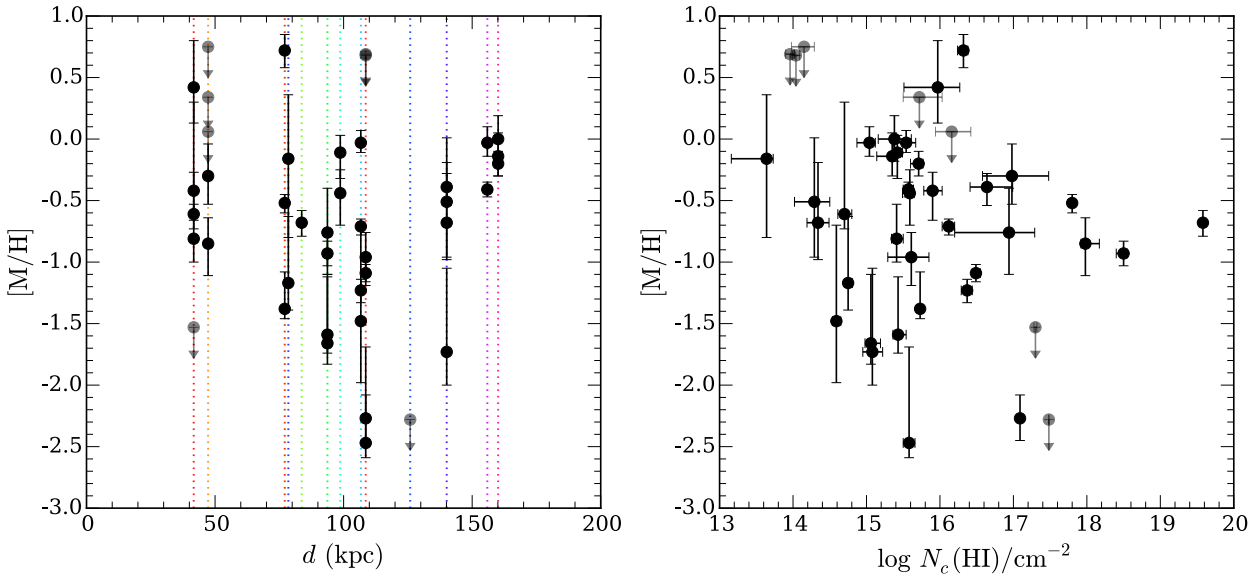

Figure 5.8: *Left*: Gas metallicity [M/H] versus d in the COS-LRG sample. Each vertical colored line connects different absorption components detected within the same LRG halo. The vertical error bar associated with each data point shows the 68 percent confidence interval for [M/H]. Grayed out data points are absorbing components with no metal ions detected, with downward arrows indicating the 95 percent upper limits on [M/H]. Large ($\gtrsim 1$ dex) variations in gas metallicities within the CGM are seen in a majority of LRGs that exhibit multi-component absorption profiles. *Right*: [M/H] versus component H I column density N_c(H I). There is no evidence for any metallicity trend with N_c(H I). The median metallicity of individual components is $\langle$[M/H]$\rangle = -0.7 \pm 0.2$, with an estimated 16-84 percentile range of [M/H] $= (-1.6, -0.1)$ for the whole sample.

two systematic effects explain the reported anti-correlation between [M/H] and N(H I).

A surprising finding from our analysis is the significant incidence of low-metallicity LLSs in the COS-LRG. The right panel of Figure 5.8 shows that three optically thick components (out of seven overall) with $\log N_c(\mathrm{H\,I})/\mathrm{cm}^{-2} \gtrsim 17$ have very low metallicities, [M/H] $\lesssim -1.5$ or less than 0.03 solar metallicity. Two of these components (component 2 along SDSS J0946+5123 and component 4 along SDSS J0246−0059, see Section A1 and Section A10 in the Appendix A, respectively) contain anomalously little ionic metals despite hosting the bulk of the total H I column density in their respective absorbers. The other component, a remarkable metal-free LLS along SDSS J1357+0435, has the lowest metallicity in the COS-LRG sample, with an estimated metallicity upper limit of [M/H] < -2.3 or lower than 0.5 percent of solar metallicity. Such low metallicities in low-redshift LLSs are consistent with

recently accreted gas from the IGM (e.g., Hafen et al. 2017). We estimate the rate of very-low-metallicity LLS (with [M/H] $\lesssim -1.5$) to be $0.43^{+0.25}_{-0.22}$ assuming binomial statistics (Gehrels 1986), which suggests that chemically pristine gas accreted from the IGM contributes to a substantial fraction of LLS population in LRG halos at $z \lesssim 0.5$. A more in-depth discussion on the possible origins of low-metallicity gas in LRG halos is presented in a companion paper on the galaxy environment of the chemically pristine LLS observed along SDSS J1357+0435 (Chen et al. 2018b).

Next, we present a plot of gas density $n_{\rm H}$ versus d in the left panel of Figure 5.9. Similar to what is seen with gas metallicities, the inferred $n_{\rm H}$ shows substantial variations among different components detected within the gaseous halo of a given LRG. In half of LRG halos (6/12) that exhibit multi-component absorption profiles, we find over a factor of 10 difference in $n_{\rm H}$ between the highest and lowest density components. These large intra-halo variations in $n_{\rm H}$ are observed at both $d < 100$ kpc and $d > 100$ kpc. The median gas density of individual components is $\log \langle n_{\rm H} \rangle / {\rm cm}^{-3} = -2.4 \pm 0.1$, where the uncertainty is calculated using a combined bootstrap and Monte-Carlo resampling. In addition, the estimated 16-84 percentile range in gas density is $\log n_{\rm H} / {\rm cm}^{-3} = (-3.0, -1.8)\,{\rm cm}^{-3}$.

To investigate whether gas density varies with H I column density, we plot $n_{\rm H}$ versus N_c(H I) in the right panel of Figure 5.9. The corresponding ionization parameter U for a given $n_{\rm H}$ is indicated on the right y-axis. The data points exhibit a clear trend of rising gas density with increasing H I column density. Because the ionizing background radiation is fixed, the observed correlation is consistent with what is expected from a photoionized gas: more optically thick gas has lower ionization parameter U and is therefore less ionized than optically thin gas. The inferred median U for our sample is $\log \langle U \rangle = -3.0 \pm 0.1$. For stronger absorption components with $\log N_c({\rm H\,I}) / {\rm cm}^{-2} \gtrsim 16$, the median ionization parameter is lower, $\log \langle U \rangle \approx -3.5$, which is comparable to what have been found in previous surveys of $z < 1$ pLLSs/LLSs (e.g., Lehner et al. 2013).

The strong correlation between $n_{\rm H}$ and N_c(H I) also suggests that cool clumps in the

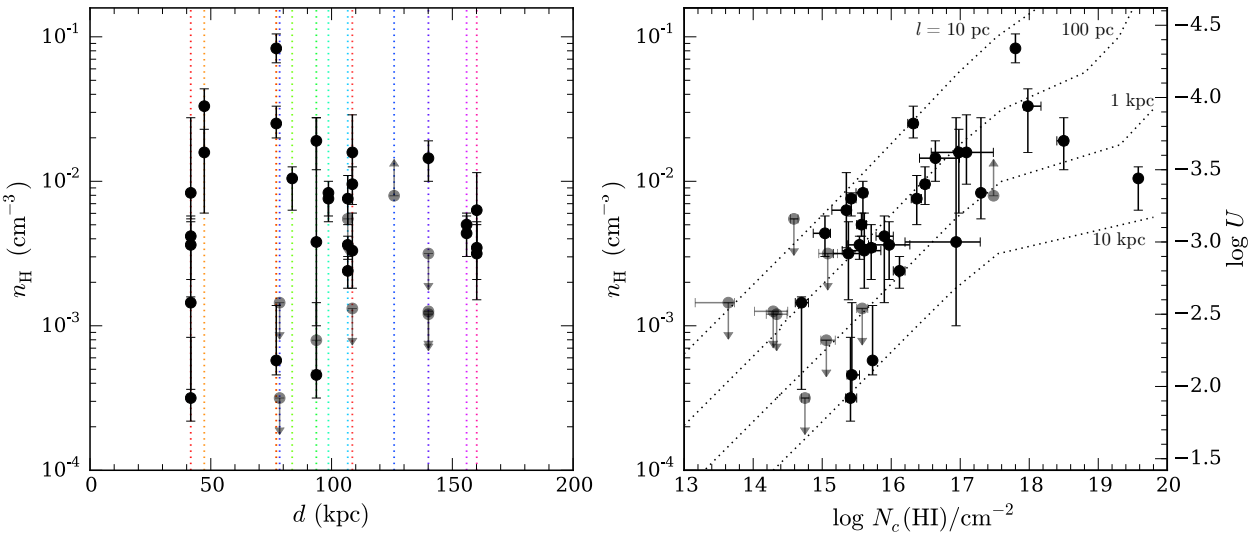

Figure 5.9: *Left*: Gas density $n_{\rm H}$ versus d in the COS-LRG sample. Each vertical colored line connects different absorption components detected within the same LRG halo. The vertical error bar associated with each data point shows the 68 percent confidence interval for $n_{\rm H}$. Grayed out data points show components for which only upper/lower limits on $n_{\rm H}$ are available, with upward/downward arrows indicating the 95 percent upper/lower limits on the underlying gas density. Large ($\gtrsim$ 1 dex) variations in $n_{\rm H}$ within the CGM are seen in half of COS-LRG galaxies that exhibit multi-component absorption profiles. The median gas density of individual components is $\log \langle n_{\rm H} \rangle / {\rm cm}^{-3} = -2.4 \pm 0.1$. *Right*: $n_{\rm H}$ versus component H I column density N_c(H I). The corresponding ionization parameter U for a given $n_{\rm H}$ is indicated on the right y-axis. The trend of rising gas density with increasing H I column density indicates that high N_c(H I) gas has lower ionization parameter U and is therefore less ionized than low N_c(H I) gas. The median U in the COS-LRG sample is $\log \langle {\rm U} \rangle \approx -3.0$. Finally, each dotted curve shows the expected $n_{\rm H}$-N_c(H I) relation for a cool cloud of a given line-of-sight thickness, from l = 10 pc to l = 10 kpc. The distribution of cool clump sizes shows a clear mode at $\sim$ 100 pc, with an estimated median of $\langle l \rangle = 120^{+80}_{-40}$ pc.

CGM of LRGs follow a well-defined distribution of clump sizes. In the right panel of Figure 5.9, we plot the expected relationship between $n_{\rm H}$ and $N_c({\rm H\,I})$ for cool clumps of different thicknesses, from $l = 10$ pc to $l = 10$ kpc. It is clear that a large majority of clumps are between ~ 10 pc and ~ 1 kpc thick, with a mode of ~ 100 pc. Furthermore, this characteristic clump thickness of $l \sim 100$ pc is shared by both optically thin and thick clumps, covering a range of nearly three orders of magnitude in $N({\rm H\,I})$. The median clump size estimated for the COS-LRG sample is $\langle l \rangle = 120^{+80}_{-40}$ pc, where the uncertainty is calculated using a combined bootstrap and Monte-Carlo resampling. In addition, we estimate that the range of l containing 68 percent of individual components is $l = (20, 800)$ pc. The range of inferred clump sizes in LRG halos is in excellent agreement with transverse clump sizes estimated directly from intervening low-ionization absorbers in the spectra of multiply lensed, high-redshift QSOs (e.g., Rauch et al. 1999; 2002).

To put the inferred gas densities of cool CGM clumps in a broader context, we compare the inferred $n_{\rm H}$ in the cool CGM with the expected gas densities in the hot CGM ($T \sim 10^6$ K) of LRGs in Figure 5.10. First, $n_{\rm H}$ is plotted versus d and shown in circles/triangles for optically thin/thick cool gas. We also show $n_{\rm H}$ derived for a single-clump model in hollow red squares, where different components within a given LRG halo are imposed to have the same density and metallicity.[4] For comparison, the solid line in Figure 5.10 represents $n_{\rm hot}(r)|_{r=d}$, the mean radial profile of mean hot gas density in LRG halos, evaluated at $r = d$. For $n_{\rm hot}(r)$, we chose a power-law model that describes the hot CGM of massive halos ($M_{\rm h} \sim 10^{13}\,{\rm M}_\odot$) from Singh et al. (2018), which is based on a combined analysis of X-ray and Sunyaev-Zel'dovich (SZ) signals from a stack of $\sim 10^5$ massive galaxies at $z \sim 0.1$. The dotted line in Figure 5.10 represents a boosted Singh et al. (2018) hot gas density profile which has been scaled up by a factor of 100, for visual comparison.

It is clear that the projected radial density profile of optically thick cool gas sits about

4. Note that the single-clump model results in a positive bias on the inferred distribution of $n_{\rm H}$, because the inferred density in the single-clump model is driven predominantly by the densest cool absorption component in each halo.

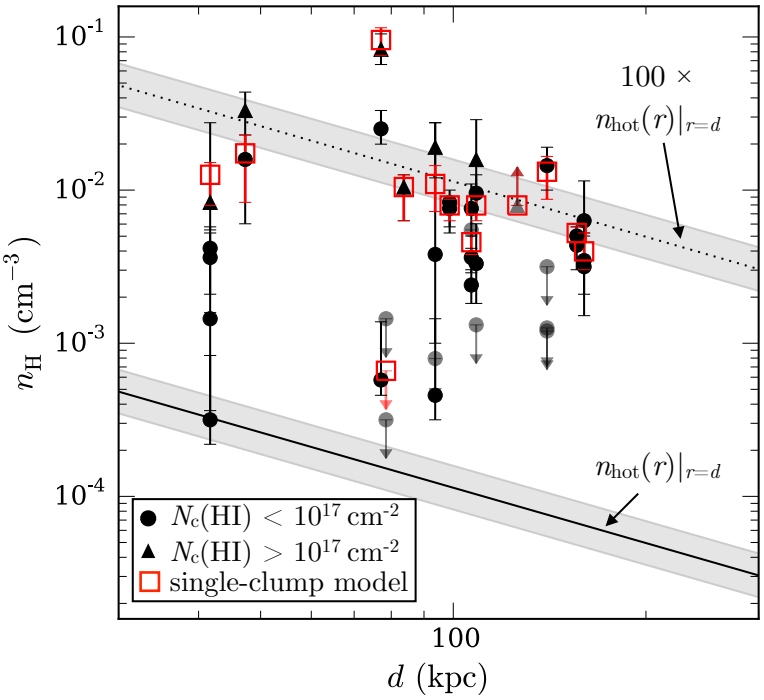

Figure 5.10: Spatial distribution of gas densities in the cool ($T \sim 10^4$ K) and hot ($T \sim 10^6$ K) CGM of LRGs. First, $n_{\rm H}$ is plotted versus d and shown in circles/triangles for optically thin/thick components. In hollow red squares we show $n_{\rm H}$ derived for a single-clump model, where a single density is assumed for different components within an individual halo. For comparison, the solid line shows $n_{\rm hot}(r)|_{r=d}$, the radial profile of mean hot gas density in massive halos ($M_{\rm h} \sim 10^{13}$ M$_\odot$; Singh et al. 2018) evaluated at $r = d$. The shaded gray area signifies the 68% confidence region of this power-law density profile. Finally, in dashed line we show the same hot CGM density profile which has been scaled up by a factor of 100.

100 times higher than $n_{\rm hot}(r)|_{r=d}$. Considering the two orders of magnitude of temperature difference between cool CGM gas ($T \sim 10^4$ K, see Section 5.4.2) and X-ray emitting hot gas ($T \sim 10^6$ K), the inferred density contrast of ~ 100 indicates that optically thick cool CGM gas occurs at $r \sim d$ and is close to being in pressure equilibrium with the hot halo (e.g., Mo & Miralda-Escudé 1996; Maller & Bullock 2004; see also a more in-depth discussion in Section 5.5.2). In contrast, Figure 5.10 shows only ~ 40 percent of optically thin components have densities consistent with being in thermal pressure equilibrium with the hot halo at $r \sim d$, which implies that a majority of optically thin absorbers likely occur at larger radii in the halo, $r > d$.

5.5 Discussion

The COS-LRG survey consists of a mass-limited sample of 16 LRGs with $\log M_{\rm star}/{\rm M}_\odot > 11$ and $d < 160$ kpc from a background QSO, chosen without any prior knowledge of the presence or absence of absorption features in the LRG halos. This mass-limited and absorption-blind sample enables an unbiased and accurate characterization of the physical properties and metallicities in the CGM of these intermediate-redshift massive ellipticals. Our survey demonstrates that despite their quiescent nature, LRGs are surrounded by widespread and chemically enriched cool gas. By carrying out a detailed ionization analysis on the absorbers, we discover large variations in gas metallicities and number densities in the cool gas, both within individual LRG halos and across the entire sample. When compared with the expected gas densities in the hot halo, the inferred densities of the cool gas imply that cool clumps in the CGM of LRGs are likely supported by thermal pressure. In addition, we find kinematic mismatches between high-ionization O VI gas and lower-ionization gas traced by H I and associated metal ions, which suggest different physical origins of the gas. We now discuss the implications of our study.

5.5.1 Total Mass in the Cool CGM of LRGs

The relative amounts of gas that reside in different phases of the CGM are governed by the interplay of accretion and feedback, as well as the detailed gas physics. Empirical constraints on the total mass of the gaseous halo around galaxies are therefore critical to test the validity of current theoretical models of galaxy formation. However, previous estimates of the total mass in the cool CGM of quiescent galaxies suffer from large uncertainties of up to two orders of magnitude, due to the unknown ionization state of the gas (e.g., Thom et al. 2012; Zhu et al. 2014).

Here, we leverage the results of our ionization analysis of the COS-LRG dataset in order to infer the surface mass density profile and estimate the total gas mass in the cool CGM of LRGs. For each absorption system, we first calculate the total hydrogen column density, $N_{\rm H}$, according to the following equation,

$$\log N_{\rm H} = \log \sum_i \frac{N_c({\rm H\,I})_i}{f_{{\rm H}^0{}_i}}, \tag{5.2}$$

where $f_{{\rm H}^0{}_i}$ is the hydrogen neutral fraction for component i determined by our ionization analysis, and the sum is evaluated over all components in the absorption system. For components with poorly constrained ionization state, the range of allowed ionization fraction correction is computed by imposing that the corresponding clump size is not larger than 1 kpc. Once $N_{\rm H}$ is calculated, the corresponding cool gas surface mass density can be computed using the relation $\Sigma_{\rm cool} = 1.4\, m_{\rm H}\, N_{\rm H}$, where $m_{\rm H}$ is the mass of the hydrogen atom and a factor of 1.4 is introduced to account for the contribution of helium to the total gas mass.

The spatial profile of cool gas surface mass density in the CGM is shown in Figure 5.11. It is clear that $\Sigma_{\rm cool}$ exhibits a declining trend with d. At $d < 100$ kpc, the mean $N_{\rm H}$ is $\log \langle N_{\rm H} \rangle / {\rm cm}^{-2} = 19.5 \pm 0.2$, which is equivalent to a mean cool gas surface density of $\langle \Sigma_{\rm cool} \rangle \approx 0.4^{+0.2}_{-0.1}\, {\rm M}_\odot\, {\rm pc}^{-2}$. The mean $\Sigma_{\rm cool}$ at $d < 100$ kpc is comparable to inferred surface

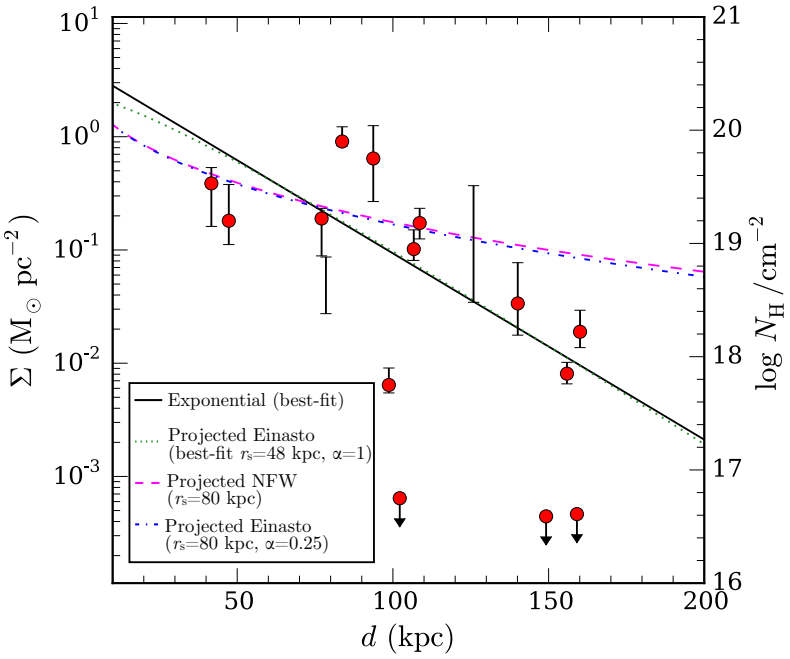

Figure 5.11: Surface mass density profile of the cool CGM of LRGs. The surface mass density, $\Sigma_{\rm cool}$, is estimated by calculating the total hydrogen column density along each sightline, $N_{\rm H}$, with the estimated ionization fraction corrections applied to the observed H I column densities according to equation (2). Downward arrows represent estimated upper limits on $\Sigma_{\rm cool}$ for LRG halos with non-detected H I . Empty vertical error bars show the range of allowed surface mass density for systems with weakly constrained $n_{\rm H}$, calculated by imposing that the corresponding clump size is $l \lesssim 1$ kpc. $\Sigma_{\rm cool}$ exhibits a steep decline with increasing d, which cannot be reproduced by a projected NFW profile or Einasto profile expected for $M_{\rm h} \approx 10^{13}\,{\rm M}_\odot$ dark-matter halos (dashed and dash-dotted curves). On the other hand, the radial profile of $\Sigma_{\rm cool}$ is best described by an exponential profile in either 2D (solid line) or 3D (a projected Einasto profile with $\alpha \approx 1$; dotted curve).

mass densities in the predominantly neutral ISM of an LRG lensing galaxy at $z = 0.4$ (Zahedy et al. 2017a). In contrast, the mean $N_{\rm H}$ and $\Sigma_{\rm cool}$ at $d = 100 - 160$ kpc are significantly lower, $\log \langle N_{\rm H} \rangle / {\rm cm}^{-2} = 18.7^{+0.2}_{-0.3}$ and $\langle \Sigma_{\rm cool} \rangle \approx (0.06 \pm 0.03)\,{\rm M}_\odot\,{\rm pc}^{-2}$.

To gain insights into the observed cool gas surface mass density profile in LRG halos, we compare the data with different analytic functions to obtain a best-fit model that characterizes the relationship between $\Sigma_{\rm cool}$ and d. We first consider a simple power-law in d, which has been used to describe the spatial distributions of H I and metal equivalent widths in the cool CGM (e.g., Chen et al. 2001, 2010), and find that it cannot reproduce the rapid decline of $\Sigma_{\rm cool}$ with increasing d. In contrast, we find that the steepness of the $\Sigma_{\rm cool}$ profile

is well-fitted by a exponential model in 2D, $\Sigma_{\rm cool} = \Sigma_0\, e^{-d/d_s}$, with best-fit parameters of $d_s = (27 \pm 4)\,{\rm kpc}$ and $\Sigma_0 = (4.1 \pm 1.4)\,{\rm M_\odot\,pc^{-2}}$ determined from a likelihood analysis (Figure 5.11, solid line).

Next, to investigate whether cool baryons follows the large-scale dark matter mass distribution in the halo, we compare the $\Sigma_{\rm cool}$ profile in Figure 5.11 to the projected surface density of spherically symmetric functions commonly used to describe dark-matter mass distributions, including the Einasto and NFW profiles. The Einasto profile (Einasto 1965) is defined by a power-law logarithmic slope, $\mathrm{d}\ln\rho/\mathrm{d}\ln r \equiv -2\,(r/r_s)^\alpha$, in which the scale radius r_s and shape parameter α are free parameters governing its shape. Relatively shallow Einasto profiles with $\alpha \lesssim 0.3$ have been found to produce good fits to the mass distribution of simulated dark-matter halos (e.g., Hayashi & White 2008; Gao et al. 2008; Dutton & Macciò 2014). By fitting a projected Einasto profile to our data, we find that $\Sigma_{\rm cool}$ requires a steep Einasto profile with $\alpha = 1.0^{+0.6}_{-0.2}$ and $r_s = 48^{+19}_{-8}\,{\rm kpc}$ (Figure 5.11, dotted curve). Note that α and r_s is degenerate in a way that models with larger r_s would require still higher values of α in order to fit the observations.

Because an Einasto profile with $\alpha = 1.0$ is equivalent to an exponential profile in 3D, this exercise demonstrates that reproducing the observed $\Sigma_{\rm cool}$ requires an underlying density profile that is exponentially declining with radius. In contrast, neither a projected NFW profile (Navarro et al. 1997) with $r_s = 80$ kpc (expected for $M_{\rm h} \approx 10^{13}\,{\rm M_\odot}$ halos at $z = 0.5$, e.g., Dutton & Macciò 2014) nor a shallow Einasto profile with $\alpha < 0.3$ produces a good fit to the the data. As illustrated in Figure 5.11 (dashed and dashed-dotted curves), these dark-matter-like profiles can be ruled out because they cannot reproduce the sharp decline of $\Sigma_{\rm cool}$ with d. Therefore, it appears that the mass distribution of cool gas in the CGM of LRGs is different from the expected mass distribution of the underlying dark matter halo.

The estimated total mass in cool CGM gas within $d = 160$ kpc ($\sim 0.3\,R_{\rm h}$) of LRGs is

$$M_{\rm cool}(< 160\,{\rm kpc}) = 1.5^{+0.7}_{-0.3} \times 10^{10}\,{\rm M_\odot}, \tag{5.3}$$

which is obtained by first multiplying the estimated $\langle\Sigma_{\rm cool}\rangle$ at $d < 100$ kpc and $d = 100-160$ kpc by their respective surface areas modulo the covering fraction inferred from Figure 11 (unity at $d < 100$ kpc and ~ 0.7 at $d = 100-160$ kpc), and then summing them. We obtain a similar estimate of $M_{\rm cool} = (1-2) \times 10^{10}\,{\rm M}_{\odot}$ by integrating the best-fit exponential model for $\Sigma_{\rm cool}$ from $d = 0$ to 160 kpc. Note that we choose to limit our mass estimate out to only $d = 160$ kpc in the CGM because it is the largest projected distance probed in the COS-LRG data set. Our estimate above should therefore be considered as a lower limit on the total mass of cool, photoionized gas in massive quiescent halos. However, note that if we naively adopted the estimated $\langle\Sigma_{\rm cool}\rangle$ and gas covering fraction at $d = 100-160$ kpc and extrapolated these values out to $d = 500$ kpc, which is the typical virial radius of $z \sim 0.4$ LRGs, the mass estimate in Equation (5.3) would increase by a factor of three, to $M_{\rm cool} \approx 4 \times 10^{10}\,{\rm M}_{\odot}$.

Our mass estimate demonstrates that despite their quiescent nature, LRGs at $z \sim 0.4$ still host a significant reservoir of cool gas in their circumgalactic space. Furthermore, the estimated cool CGM mass of $\sim 10^{10}\,{\rm M}_{\odot}$ is comparable to the inferred total mass in the cool CGM of lower-mass and predominantly star-forming L^* galaxies (e.g., Chen et al. 2010; Prochaska et al. 2011; Werk et al. 2014; Stern et al. 2016). At the same time, the total baryon mass budget of the typical LRG in our sample is $\approx 1.6 \times 10^{12}\,{\rm M}_{\odot}$ within the virial radius, which is estimated for the median halo mass in COS-LRG, $M_{\rm h} \approx 10^{13}\,{\rm M}_{\odot}$ and adopting a baryon-to-dark-matter mass ratio of $\Omega_b/\Omega_{\rm DM} = 0.16$. Thus, the inferred $M_{\rm cool}$ in the CGM is at most ≈ 3 percent of the total baryon budget for typical LRGs.

It is also interesting to compare the total mass contained in cool clumps to the expected total mass of the hot CGM. The dotted curve in Figure 5.12 represents $\Sigma_{\rm hot}$, the inferred hot gas surface mass density profile in massive $M_{\rm h} \sim 10^{13}\,{\rm M}_{\odot}$ halos. $\Sigma_{\rm hot}$ is computed from the hot gas density profile shown in Figure 5.10 (Singh et al. 2018), assuming a unity volume filling fraction for the hot gas. The expected spatial mass profile of hot gas is more spatially extended than the observed $\Sigma_{\rm cool}$ profile (see also Liang et al. 2016). Within $d = 160$ kpc

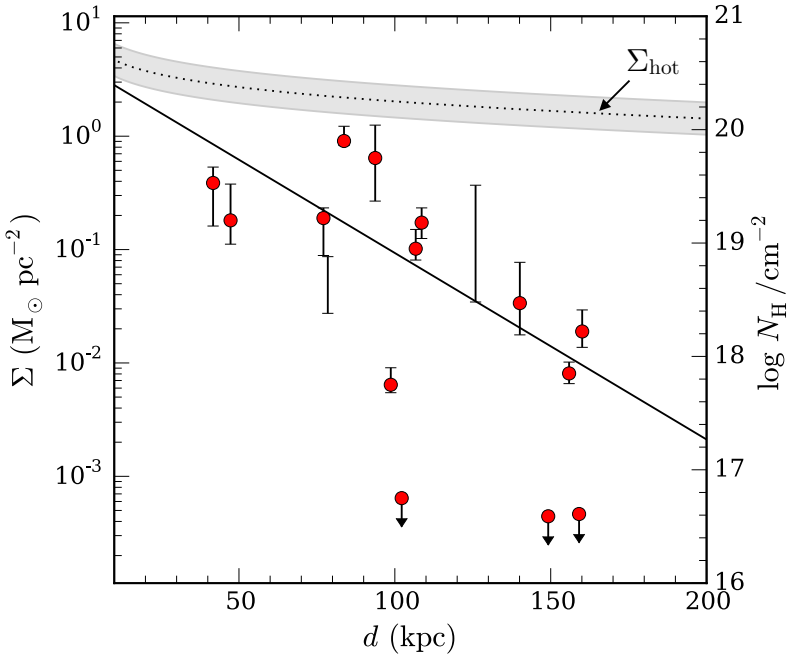

Figure 5.12: Comparison between the surface mass density profiles of the cool and hot CGM of LRGs. Symbols are the same as those in Figure 11, with the solid black line showing the best-fit exponential model describing the relationship of $\Sigma_{\rm cool}$ with d. In contrast, the dotted curve shows the inferred surface mass density profile in the hot CGM of LRG-sized halos ($M_{\rm h} \approx 10^{13}\,{\rm M}_\odot$), based on a combined X-ray and SZ analysis (Singh et al. 2018), with the 68% confidence region shaded in gray. Within $d < 160$ kpc from LRGs, we estimate a total cool gas mass of $M_{\rm cool} = 1.5^{+0.7}_{-0.3} \times 10^{10}\,{\rm M}_\odot$, which is $\sim 6-13$ percent of the expected total mass in the hot CGM.

from LRGs, we infer a total hot gas mass of $M_{\rm hot}(< 160\,{\rm kpc}) = (1.7 \pm 0.5) \times 10^{11}\,{\rm M}_\odot$. Comparing our estimate of $M_{\rm cool}$ with the inferred $M_{\rm hot}$, the cool-to-hot gas mass ratio in the CGM of LRGs is

$$X_{\rm cool} \equiv M_{\rm cool}/M_{\rm hot} \approx 0.06 - 0.13 \tag{5.4}$$

at $d < 160$ kpc, which is comparable to the inferred $X_{\rm cool}$ in the interstellar medium (ISM) of one of these massive ellipticals (Zahedy et al. 2017a).

Furthermore, our data also hint at a declining $X_{\rm cool}$ with increasing projected distance from LRGs, from $X_{\rm cool} \sim 0.1 - 0.2$ at $d < 100$ kpc, to no more than $X_{\rm cool} \sim 0.01 - 0.03$ at $d = 100 - 160$ kpc. The declining $X_{\rm cool}$ with increasing projected distance implies that the volume filling factor of cool gas is significantly lower in the outer CGM, at galacto-centric

radius $r \gtrsim 100$ kpc, than it is in the inner CGM, at $r \lesssim 100$ kpc. The mean volume filling factor of cool gas can be estimated using line-of-sight observables according to the following expression (e.g., McCourt et al. 2018),

$$\langle f_{\rm V} \rangle = \langle N_{\rm cl} \rangle \times \frac{l}{L}, \tag{5.5}$$

where $l \equiv N_{\rm H}/n_{\rm H}$ is the clump thickness along the line of sight, L is the path length through the CGM, and $\langle N_{\rm cl} \rangle$ is the mean number of clumps per line of sight. As shown in the right panel of Figure 9, the inferred clump sizes in COS-LRG range from 10 pc to 10 kpc, with a median value and mode of $l \sim 100$ pc. For the purpose of this calculation, we approximate $\langle N_{\rm cl} \rangle$ to be the average number of discrete components identified per sightline. Based on our data, there are on average $\langle N_{\rm cl} \rangle_{<100} = 3.7^{+0.6}_{-0.4}$ discrete components at $d < 100$ kpc, which subsequently declines to $\langle N_{\rm cl} \rangle_{>100} = 2.2^{+0.9}_{-0.5}$ at $d > 100$ kpc. Given that $\langle N_{\rm cl} \rangle_{<100}$ has contributions from both the inner and outer parts of the halo, we can solve for $\langle f_{\rm V} \rangle$ in the inner and outer CGM separately using the following approximations:

$$\langle f_{\rm V} \rangle_{\rm inner} \approx (\langle N_{\rm cl} \rangle_{<100} - \langle N_{\rm cl} \rangle_{>100}) \times \frac{l}{L_{\rm inner}} \tag{5.6}$$

$$\langle f_{\rm V} \rangle_{\rm outer} \approx \langle N_{\rm cl} \rangle_{>100} \times \frac{l}{L_{\rm outer}}. \tag{5.7}$$

By plugging the different quantities above to Equations (5.6) and (5.7) and adopting $L_{\rm inner} = 100$ kpc and $L_{\rm inner} = 500$ kpc, we estimate that the mean volume filling factor for typical clumps with $l = 100$ pc is $\langle f_{\rm V} \rangle_{\rm inner} \sim 2 \times 10^{-3}$ in the inner halo ($r \lesssim 100$ kpc), and $\langle f_{\rm V} \rangle_{\rm outer} \sim 4 \times 10^{-4}$ in the outer ($r \gtrsim 100$ kpc) halo of LRGs. This exercise illustrates that while the cool gas covering fraction in the CGM of LRGs is high, the volume filling factor can remain very low (for possible theoretical explanations, see e.g., McCourt et al. 2018; Liang & Remming 2018)

5.5.2 On the Origin and Fate of Cool Gas in LRG halos

In the previous section, we show that despite their "red and dead" nature, LRGs at $z \sim 0.4$ harbor as much as $\sim 10^{10}\,M_\odot$ of photoionized $T \sim 10^4$ K gas in their extended halos. This massive reservoir of cool gas appears to consist of compact clumps with a characteristic size of $\sim$ 100 pc (Section 5.4.3), which are pressure confined by the hot gaseous halo that is expected to be ubiquitous around LRGs.

To gain a better understanding of the nature of the cool gas around LRGs, we now consider our observational results in the larger context of a multiphase gaseous halo around LRGs.

The physical formalism for a two-phase CGM was first explored by Mo & Miralda Escude (1996), who argued that QSO absorption systems in the vicinity of galaxies originate in cool clouds which are in thermal pressure equilibrium with the hot halo. To explain the formation of cool clumps within an otherwise hot corona, Maller & Bullock (2004) elaborated on this simple model by incorporating multiphase cooling in the halo. In their analytic model, cool clumps originate from condensation in a hydrostatically stable hot halo, triggered by thermal instabilities which develop locally when the cooling time ($\tau_{\rm cool}$) is comparable to the the dynamical timescale ($\tau_{\rm ff}$) of the gas. Building on these earlier works, more recent numerical simulations have shown that a multiphase halo can form as soon as $\tau_{\rm cool}/\tau_{\rm ff} \lesssim 10$ (e.g., Sharma et al. 2012; McCourt et al. 2012), which is consistent with observations of multiphase gas in a number of nearby galaxy clusters and elliptical galaxies (e.g., Voit et al. 2015a, b).

Under the multiphase-cooling paradigm, cool clumps form within the cooling radius, R_c inside the halo, where thermal instability is prone to develop. For LRG-sized halos, R_c is estimated to be between 100 and 200 kpc (Maller & Bullock 2004, Equation 18), which is qualitatively consistent with a number of COS-LRG findings, including the observed decline in H I covering fraction with d (Paper I and Section 5.4.1) and the steep drop in inferred cool gas surface mass density and volume filling factor at $d \gtrsim 100$ kpc (Section 5.5.1).

In the absence of vigorous star formation activity capable of driving large scale outflows, circumgalactic cool gas is likely falling toward the center of the halo. The infall interpretation is supported by the observed line-of-sight velocity dispersion of individual absorbing components in the COS-LRG sample, $\sigma_{\rm gas} \approx 150$ km s^{-1}, which is merely ~ 60 percent of what is expected from virial motion (see also Huang et al. 2016; Lan et al. 2018). The observed narrow distribution of line-of-sight velocities indicates that dissipative processes are effective in slowing down cool clumps as they undergo orbital motions in the halo. By attributing the observed deceleration as due to ram pressure drag exerted by the hot halo, Huang et al. (2016) calculated an upper limit on the cool clump mass of $m_{\rm cl} \lesssim 10^4\,{\rm M}_\odot$ in LRG halos. This dissipative interaction with the hot gas would lead to orbital decay, causing cool clumps to fall toward the galaxy. *But does the cool gas survive this inward journey ?*

The survival of cool clumps depends on whether the infall time is sufficiently short compared to the timescales of cloud disruption processes acting on them. Cloud destruction is driven predominantly by thermal conduction between cool clumps and and the surrounding hot gas. If cool clumps are not sufficiently massive, they will not only decelerate due to ram pressure drag, but also evaporate due to thermal conduction before reaching the LRG at the center of the halo.

We expect cool clumps to eventually reach terminal speed when the ram pressure drag force exerted by the hot gas is balanced by the gravitational pull of the halo on the clump. By identifying this terminal speed with the observed $\sigma_{\rm gas} \sim 0.6\,\sigma_{\rm vir}$ in LRG absorbers, we can compute the typical cool clump mass (Maller & Bullock 2004, Equation 39),

$$m_{\rm cl} \approx 7.7 \times 10^2\, T_6^{-3/8} (\Lambda_Z\, t_8)^{1/2}\,{\rm M}_\odot, \tag{5.8}$$

where $T_6 = T/10^6\,{\rm K}$ is the temperature of the hot corona, Λ_Z is a cooling parameter which depends on the gas metallicity and $t_8 = t_f/8\,{\rm Gyr}$ is the halo formation timescale. For typical LRG halos in our sample, $T \sim 6 \times 10^6\,{\rm K}$ assuming an isothermal gas, and $t_f \sim 9\,{\rm Gyr}$

assuming t_f is comparable to the age of the Universe at $z \sim 0.4$. Using Equation (5.8), we find that $m_{\rm cl} = (2-8) \times 10^2\,{\rm M}_\odot$ for metallicities of between 0.01 solar and solar, respectively. This kinematics-based mass estimate can be compared to the cool clump mass independently constrained from our ionization analysis. Based on a combined bootstrap and Monte-Carlo resampling of the full range of inferred cool gas densities and characteristic clump sizes (Section 5.4.3), we estimate that the characteristic clump mass has a median value of $\langle m_{\rm cl} \rangle = 50 - 1000\,{\rm M}_\odot$, which is consistent with the mass range estimated using Equation (5.8).

Given a mass of cool clump $m_{\rm cl}$, the characteristic for cloud evaporation due to thermal conduction is given by (Maller & Bullock 2004, Equation 35),

$$\tau_{\rm evap} \approx 1.6\, m_{\rm cl}^{2/3}\, T_6^{-3/2} (\Lambda_Z\, t_8)^{-1/3}\,{\rm Myr}. \tag{5.9}$$

For typical $m_{\rm cl} \sim 10^2 - 10^3\,{\rm M}_\odot$ and a metallicity of between 0.01 solar and solar, we find that the evaporation timescale is $\tau_{\rm evap} \sim 1 - 20$ Myr. The expected evaporation time for typical cool clumps is vastly shorter than the minimum infall time of $\tau_{\rm infall} \sim 200 - 500$ Myr estimated for cool clumps which condense from the hot gas at $R_c \sim 100 - 200$ kpc. The evaporation time is still significantly less than infall time even for clumps as massive as $m_{\rm cl} \sim 10^4\,{\rm M}_\odot$ (Huang et al. 2016). This exercise suggests that cool clumps travel only a relatively small distance in the halo during their lifetimes, and a majority of clumps originating at large distances will evaporate before reaching the center of the halo.

The implication that a majority of cool clumps in the gaseous halo of LRGs never reaches the central galaxy could explain a number of observational findings that the cool ISM mass in massive quiescent galaxies remains low, $M_{\rm cool}({\rm ISM}) \sim 10^{8-9}\,{\rm M}_\odot$ (e.g., Serra et al. 2012; Zahedy et al. 2017a; Young et al. 2018), despite the existence of a much larger reservoir of cool gas in the halo, $M_{\rm cool}({\rm CGM}) \sim 10^{10}\,{\rm M}_\odot$. At the same time, the fact that cool gas is routinely observed in the gaseous halo of LRGs suggests that cool clumps are continuously

formed and destroyed in the predominantly hot gaseous halo. In this quasi steady state, $\sim 5-10$ percent of the CGM gas by mass reside in cool, $\sim 10^4$ K phase at any given time, a balance which is most likely determined by the amount of additional heating available to offset the increased cooling rate from the cool gas.

Finally, we note although our discussion above is based entirely on considering our observations in the context of thermal instability in a multiphase CGM, it does not exclude the possibility that cool gas in LRG halos is also generated by other physical processes. These additional mechanisms include cool gas recently accreted from the IGM along filaments (e.g., Churchill et al. 2012; Huang et al. 2016), gas originating in and/or stripped from the CGM or ISM of satellite galaxies (e.g. Gauthier et al. 2010; Huang et al. 2016), and gas ejected by SNe Ia (e.g., Zahedy et al. 2016; 2017b). Indeed, our finding that gas density and metallicity can vary by more than a factor of ten within individual LRG halos indicates that the CGM is a multiphase mixture of gas with different chemical enrichment histories, which hints at multiple origins of the cool gas. However, cool clumps in LRG halos are subject to the same interactions with the hot gas regardless of their physical origin. Therefore, our conclusion above can be applied generally on the nature of cool gas in massive quiescent halos.

5.5.3 The Nature of O VI Absorbers in the CGM: Insight from Massive Halos

A significant finding in CGM studies over the past decade is the ubiquitous presence of strong O VI absorption with $\log N(\mathrm{O\,VI})/\mathrm{cm}^{-2} \sim 14.5$ around $\sim L^*$ star-forming galaxies (e.g., Tumlinson et al. 2011). At the same time, O VI-bearing is found to be less prevalent in the gaseous halos of passive galaxies (e.g., Chen & Mulchaey 2009; Tumlinson et al. 2011; Johnson et al. 2015). The apparent dichotomy between O VI absorption properties around late-type and early-type galaxies is often ascribed to a direct link between star-formation and the observed warm gas properties: recent star formation drive powerful outflows that eject metals to large distances in the CGM. Alternatively, the lower incidence of strong O VI

absorption in passive galaxies has been attributed to further ionization of oxygen to higher states (e.g., O VII and O VIII) in the more massive and hotter halos of passive galaxies (e.g., Oppenheimer et al. 2016).

To gain new insights into the nature of O VI absorbers around galaxies, it is necessary to compare the observed O VI absorption properties around galaxies of different masses. In Figure 5.13, we present current observational constraints on circumgalactic O VI absorption spanning over more than three decades in galaxy stellar mass, from $\log M_{\rm star}/{\rm M}_{\odot} \sim 8$ to $\log M_{\rm star}/{\rm M}_{\odot} > 11$. O VI measurements for massive quiescent galaxies are from COS-LRG sample, whereas constraints for $\sim L^*$ star-forming galaxies are from Johnson et al. (2015) and those for star-forming dwarf galaxies are adopted from Johnson et al. (2017). The mean covering fraction of O VI at $d < 160$ kpc is plotted versus $M_{\rm star}$ in the top panel of Figure 5.13, for a column density threshold of $\log N({\rm O\,VI})/{\rm cm}^{-2} > 13.5$. In contrast to the near-unity covering fraction of O VI absorbers around L^* star-forming galaxies, passive LRGs and star-forming dwarf galaxies exhibit lower covering fraction of O VI gas, at $\sim 50-60$ percent. While star-formation driven winds is an attractive scenario to account for the ubiquity of O VI absorption around $\sim L^*$ star-forming galaxies, it does not explain the lower O VI covering fraction around star-forming dwarfs. Furthermore, despite the likely absence of strong outflows in LRGs, they still exhibit a significant incidence of O VI, not to mention comparable covering fractions of lower-ionization metals to what have been observed around star-forming galaxies (Paper I).

In the bottom panel of Figure 5.13, the mean and median $N({\rm O\,VI})$ at $d < 160$ kpc are plotted versus $M_{\rm star}$ for the three galaxy samples. It is clear that CGM O VI absorption strength peaks in $\sim L^*$ star-forming galaxies (where $M_{\rm h} = 10^{11.3-12.1}\,{\rm M}_{\odot}$). The mean $N({\rm O\,VI})$ declines toward both lower and higher-mass halos, where a majority of O VI absorbers around LRGs and star-forming dwarf galaxies have $N({\rm O\,VI})$ which are 0.5 to 1 dex lower than typical strong O VI absorbers around $\sim L^*$ galaxies. We note that a similar trend of $N({\rm O\,VI})$ with galaxy mass (or halo mass) is also present in simulated galaxies from

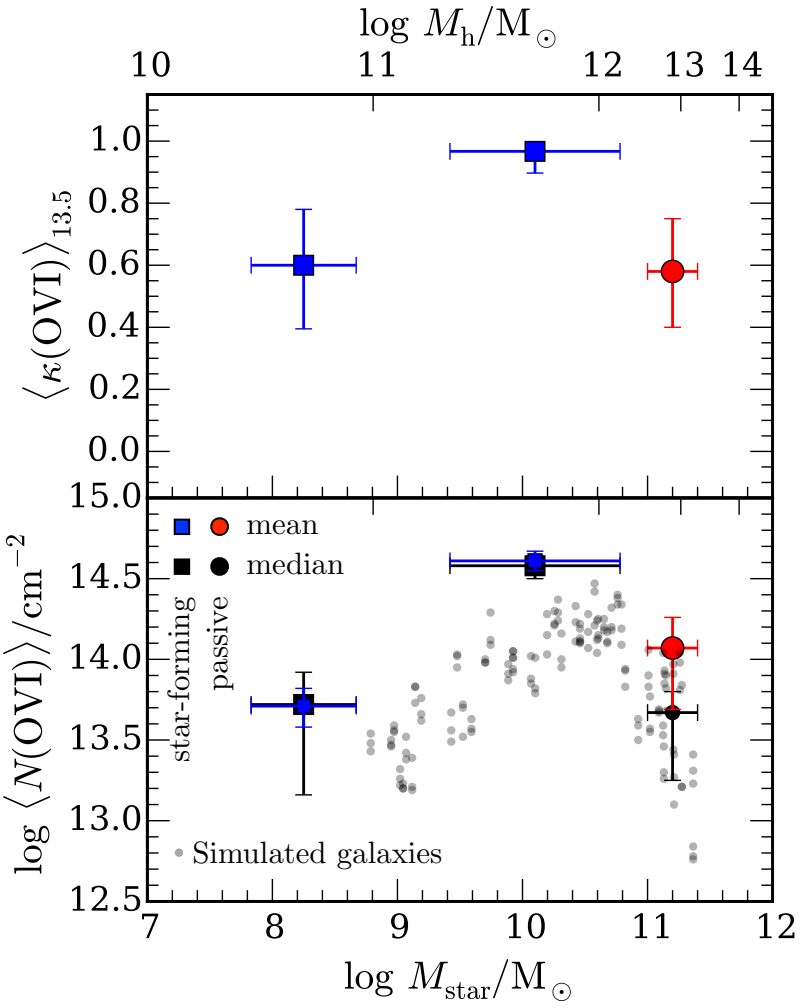

Figure 5.13: Observational constraints on CGM O VI absorption spanning more than three decades in galaxy stellar mass. Constraints for massive quiescent galaxies are from COS-LRG. Constraints for $\sim L^*$ star-forming galaxies are from Johnson et al. (2015), whereas those for star-forming dwarf galaxies are adopted from Johnson et al. (2017). *Top*: The mean covering fraction of O VI plotted versus $M_{\rm star}$ at $d < 160$ kpc, for a column density threshold of $\log N({\rm O\,VI})/{\rm cm}^{-2} > 13.5$. For each sample, the median stellar mass is plotted, with the horizontal error bars showing the sample dispersion. The corresponding halo mass for each point is indicated as well, based on the Kravtsov et al. (2018) stellar-to-halo-mass relation. The vertical error bars are calculated assuming binomial statistics. *Bottom*: the mean and median $N({\rm O\,VI})$ at $d < 160$ kpc plotted as a function of $M_{\rm star}$. The vertical error bars represent the 68% confidence intervals for the mean and median $N({\rm O\,VI})$, calculated using a combined bootstrap and Monte-Carlo resampling. For comparison, in gray circles we plot the mean $N({\rm O\,VI})$ within $d < 150$ kpc from simulated galaxies in EAGLE zoom simulations (Oppenheimer et al. 2017).

the EAGLE zoom simulations (gray points; Oppenheimer et al. 2017), despite the fact that the predicted $N(\mathrm{O\,VI})$ are systematically lower than observations over the range of galaxy masses considered (see also Nelson et al. 2018).

The strong dependence of circumgalactic $N(\mathrm{O\,VI})$ on stellar mass, which in turn correlates with the total halo mass including dark matter, hints at a connection between the dominant ionization state of oxygen and the virial temperature of the halo. In particular, the inferred halo virial temperature for the $\sim L^*$ star-forming galaxy sample is $T_{\rm vir} = 10^{5.3-5.8}\,\mathrm{K}$, which is coincident with the narrow range of temperatures where the fractional abundance of O VI is at a maximum in collisionally ionized gas (e.g., Heckman et al. 2002; Gnat & Sternberg 2007; Oppenheimer & Schaye 2013). In contrast, the expected virial temperatures for LRGs ($M_{\rm h} = 10^{12.6-13.5}\,\mathrm{M_\odot}$) and dwarf galaxies ($M_{\rm h} < 10^{11}\,\mathrm{M_\odot}$) are $T_{\rm vir} = 10^{6.5-7.0}\,\mathrm{K}$ and $T_{\rm vir} \lesssim 10^5\,\mathrm{K}$, respectively. At these temperatures, the expected O VI ionization fractions are very small (< 0.01) under collisional ionization models. The observed peak of $N(\mathrm{O\,VI})$ versus galaxy mass relation in $\sim L^*$ star-forming halos supports the interpretation that the high column of O VI around these galaxies originate in collisionally ionized gas at $T \sim T_{\rm vir}$ (e.g., Oppenheimer et al. 2016; Werk et al. 2016) or, perhaps more realistically, a gas that follows a temperature distribution centered at $T_{\rm vir}$ (McQuinn & Werk 2018).

For O VI absorbers originating in a radiatively cooling flow of coronal ($T \sim 10^{5.5}$ K) gas, $N(\mathrm{O\,VI})$ is expected to be related to the flow velocity (e.g., Edgar & Chevalier 1986; Heckman et al. 2002; Bordoloi et al. 2017). A cooling flow develops because as OVI-bearing gas cools in the halo, its density must increase to maintain pressure equilibrium. Consequently, the cooling gas sinks and flow inward. Because bulk motion in the gas broadens its line profile, the observed O VI linewidth is a combination of pure thermal broadening and additional broadening due to cooling-flow velocity. By investigating O VI absorbers in a wide range of environments (Galactic disk and high velocity clouds, the Large and Small Magellanic Clouds, nearby starburst galaxies, and the IGM), Heckman et al. (2002) found a correlation between O VI column density and linewidth that is consistent with the theoretical prediction

from the radiative cooling flow model. Later studies have also reported similar trends at both low and high redshifts (e.g., Tripp et al. 2008; Lehner et al. 2014; Werk et al. 2016).

To investigate whether O VI absorbers around LRGs can be explained by a radiatively cooling flow, we plot the observed Doppler linewidth versus column density for COS-LRG O VI absorbers in the left panel of Figure 5.14 (red circles). Additional O VI absorbers detected in the vicinity of massive quiescent galaxies ($\log M_{\rm star}/{\rm M}_\odot > 11$) in Johnson et al. (2015) are shown in black circles. For comparison, O VI measurements around $\sim L^*$ star-forming galaxies from Johnson et al. (2015) are shown in pale gray squares. Finally, the predicted relationship between O VI linewidth and column density for a radiatively cooling flow is shown in solid curve, for temperature $T_{\rm O\,VI} = 10^{5.5}\,{\rm K}$. We note that if the gas is radiatively cooling at a higher/lower temperature, the effect is to shift the prediction curve upward/downward in the parameter space (see e.g., Bordoloi et al. 2017).

It is apparent from the left panel of Figure 5.14 that O VI absorbers around $\sim L^*$ star-forming galaxies follow the trend predicted by the cooling flow model. This is consistent with the finding of Werk et al. (2016), who reported a statistically significant correlation between b_c(O VI) and N_c(O VI). For COS-LRG O VI absorbers, a Spearman test on the sample indicates a $2.3\,\sigma$ correlation between b_c(O VI) and N_c(O VI), with a coefficient of $r = 0.73$. While this marginal correlation is suggestive a cooling flow, note that most O VI absorbers around LRGs are situated above the prediction curve for a $T_{\rm O\,VI} = 10^{5.5}\,{\rm K}$ cooling flow. These vertical displacements imply that if O VI absorbers in LRG halos trace collisionally ionized gas in a radiatively cooling flow, the gas has to be significantly hotter with $T_{\rm O\,VI} \approx 10^6\,{\rm K}$ (Bordoloi et al. 2017).

On a superficial level, the existence of a $10^6\,{\rm K}$ cooling gas may not be that surprising given the expectation that LRGs are surrounded by a hot gaseous halo with $T \sim T_{\rm vir}$. However, the expected O VI ionization fraction in a $10^6\,{\rm K}$ gas is very low ($\sim 10^{-3}$) under collisional ionization models (e.g., Gnat & Sternberg 2007; Oppenheimer & Schaye 2013). For a solar metallicity gas at $T = 10^6\,{\rm K}$ and density of $\log n_{\rm H}/{\rm cm}^{-3} = -4$, the implied

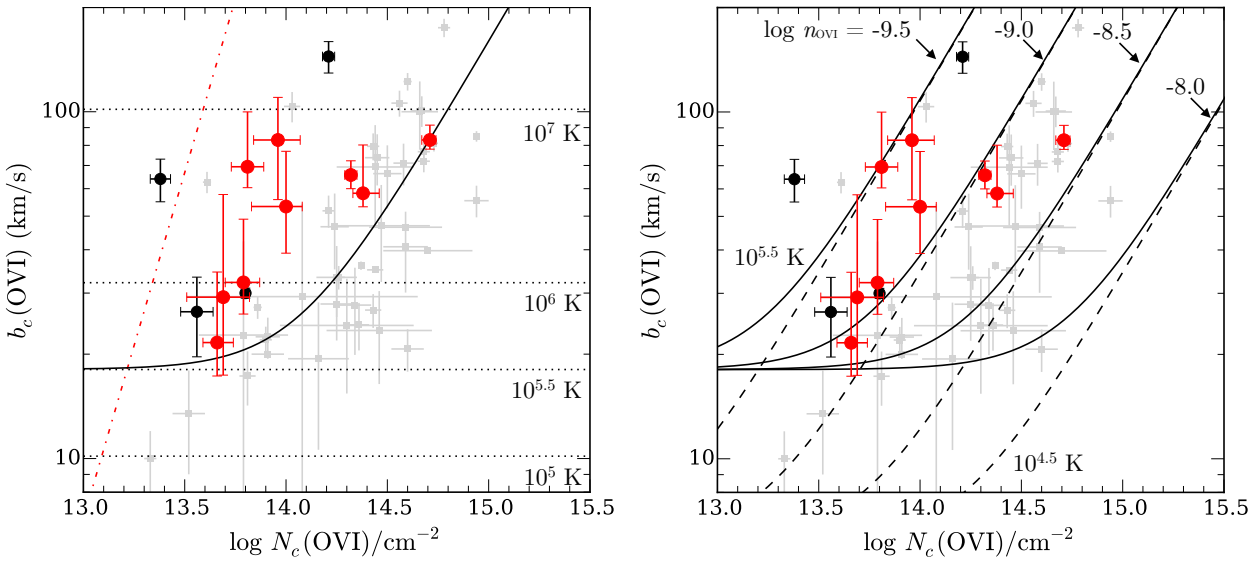

Figure 5.14: O VI component linewidth versus column density in the COS-LRG sample (red circles). The dashed-dotted line in the left panel represents the typical $3\,\sigma$ detection limit in the COS spectra for our sample. O VI absorbers detected in the vicinity of massive quiescent galaxies ($\log M_{\rm star}/{\rm M}_\odot > 11$) in Johnson et al. (2015) are shown in black circles, whereas absorbers around $\sim L^*$ star-forming galaxies in in Johnson et al. (2015) are shown in pale gray squares. The solid curve in the left panel shows the expected behavior for a radiatively cooling, collisionally ionized gas at $T = 10^{5.5}$ K (Heckman et al. 2002), whereas the dotted horizontal lines indicated the expected thermal broadening at different temperatures. In the right panel, the curves show expected behaviors for a gravitationally broadened O VI-bearing gas (Stern et al. 2018) at different O^{5+} volume densities, calculated for a $T = 10^{4.5}$ K gas in dashed curves and $T = 10^{5.5}$ K in solid curves.

cloud thickness for a $\log N(\mathrm{O\,VI})/\mathrm{cm}^{-2} = 14$ absorber is in excess of 200 kpc. The absorber size would be even larger for a lower metallicity and/or lower density gas, exceeding the size of typical LRG halos. For that reason, we consider it unlikely that O VI absorbers in LRG halos originate in a 10^6 K cooling gas.

Alternatively, we consider the possibility that O VI absorbers around LRGs trace cooler, photoionized gas. The expected O VI thermal linewidth for a $T \approx 10^{4.5}$ K gas is $6\,\mathrm{km\ s}^{-1}$, which is significantly smaller than the observed O VI linewidths in COS-LRG, $b_c\,(\mathrm{O\,VI}) = 20 - 100\,\mathrm{km\ s}^{-1}$(Figure 5.14). If these O VI absorbers originate in a photoionized gas, then their broad line profiles are predominantly due to non-thermal motions. At the same time, the implied non-thermal broadening of $b_{\mathrm{nt}} = 20 - 100\,\mathrm{km\ s}^{-1}$ for O VI gas is significantly higher than the modest non-thermal line broadening seen in lower-ionization gas around LRGs, $\langle b_{\mathrm{nt}} \rangle = 7 \pm 5\,\mathrm{km\ s}^{-1}$(Section 5.4.2). Because of this large discrepancy in the implied non-thermal motion *and* observed kinematic misalignments between O VI and H I as well as lower-ionization species (Section 5.4.2), we conclude that any photoionized O VI gas has a different physical origin from cool gas traced by H I and lower ions (Section 5.5.2).

In a recent study, Stern et al. (2018) considered the possibility that circumgalactic O VI absorbers trace infalling cool gas which has yet to be virially shocked by the halo. Assuming photoionization and thermal equilibrium with the UVB, the implied absorber size is $\sim$ a few$\times$ 10 kpc for a gas with $\log N(\mathrm{O\,VI})/\mathrm{cm}^{-2} = 14$ and a metallicity between $0.1 - 1$ solar (e.g, Oppenheimer & Schaye et al. 2013). Because of the substantial size of the absorber, bulk gravitational infall will produce a velocity shear which broadens the O VI line profile. This gravitational line broadening is expected to grow with increasing absorber size. Because absorber size is proportional to column density for a fixed gas density, a correlation between O VI linewidth and column density is naturally expected. In the right panel of Figure 5.14, we show the relationships between the two variables as predicted by Stern et al. (2018) for different densities of O^{+5} ions, $n_{\mathrm{O\,VI}}$.

Under the gravitational broadening scenario, the observed correlation between b_c(O VI)

and N_c(O VI) implies that O VI absorbers around L^* star-forming galaxies have densities of $-9 \lesssim \log n_{\rm O\,VI}/{\rm cm}^{-3} \lesssim -8.5$. In contrast, the implied O VI volume density is significantly lower for most O VI absorbers detected around massive quiescent galaxies in both COS-LRG (red circles) and Johnson et al. (2015, black circles) samples, $\log n_{\rm O\,VI}/{\rm cm}^{-3} \lesssim -9$.[5] For a photoionized O VI-bearing gas with a metallicity of [M/H] $= -0.7$, which is the median metallicity of lower-ionization gas in COS-LRG, the implied upper limit on $n_{\rm O\,VI}$ corresponds to an upper limit on gas density of $\log n_{\rm H}/{\rm cm}^{-3} \lesssim -4.3$. If one assumes that gas density monotonically declines with increasing galacto-centric distance, the lower O VI volume densities around LRGs suggest that these absorbers trace gas which resides at larger distances than typical O VI absorbers around L^* star-forming galaxies. This interpretation is consistent with our understanding that LRG halos are roughly twice the size of L^* star-forming halos, and that stable accretion shocks in LRG halos are expected to be situated further out from the galaxies than accretion shocks in lower-mass halos.

The inferred low density of O VI-bearing gas is also consistent with the lack of detection of N V absorption associated with O VI absorbers in COS-LRG. Coverage of the N V doublet is available for seven out of nine high-ionization absorption components detected in O VI. We do not detect N V absorption associated with any of these O VI absorbers. The typical upper limit on the N V to O VI column density ratio in COS-LRG is $\log N_c({\rm N\,V})/N_c({\rm O\,VI}) < -0.4$, estimated from the error array by assuming that N V has the same linewidth as O VI. For a photoionized gas with solar N/O elemental abundance ratio, this upper limit constrains the gas density of O VI-bearing gas to $\log n_{\rm H}/{\rm cm}^{-3} < -4.1$ under the HM05 UVB.[6] At these

5. It is possible that some of the broad O VI absorbers shown in Figure 5.14 are the result of unresolved blending of multiple, narrow O VI components. If unresolved components were present, they would naturally have narrower b_c and lower N_c(O VI) than the measurements shown, and as a consequence the data points in Figure 5.14 would move downward and leftward.

6. Zahedy et al. (2017b) reported that the outer CGM of quiescent galaxies exhibit α-element enhanced abundance pattern that is similar to what have been observed in the high-redshift IGM and damped Lyα absorbers (DLAs). Sub-solar N/O values of [N/O] $\lesssim -1$ have been reported in high-redshift DLAs (e.g., Petitjean et al. 2008). Therefore, it is possible that the outskirts of LRG halos have similarly sub-solar N/O ratios. If O VI absorbers in COS-LRG arise in gas with low [N/O] ≈ -1, the resulting constraint on gas density from the lack of N V would be less sensitive, $\log n_{\rm H}/{\rm cm}^{-3} \lesssim -3$.

low densities, the gas is highly ionized and little associated absorption is expected from low-ionization states. For instance, in a photoionized gas with $\log n_{\rm H}/{\rm cm}^{-3} \approx -5$ and a typical O VI column of of $\log N({\rm O\,VI})/{\rm cm}^{-2} = 14$, the expected column densities in C III and Si III are very low, $\log N/{\rm cm}^{-2} < 12$, which is consistent with the lack of lower ionization gas observed to be associated with O VI absorbers in COS-LRG. Therefore, while the current sample of O VI absorbers around LRGs is still small, our observations are suggestive of a physical picture where O VI absorbers around LRGs trace photoionized and low-density gas at large distances from the galaxy (see also Voit et al. in prep).

5.6 Summary and Conclusions

We carried out a systematic investigation of the physical conditions and elemental abundances in the CGM within $d < 160$ kpc from LRGs. The COS-LRG sample comprises 16 LRGs with $\log M_{\rm star}/{\rm M}_\odot > 11$ at $z = 0.21 - 0.55$, which were selected without prior knowledge of the presence or absence of any CGM absorption features. The primary objectives of the COS-LRG program are: (1) to probe the bulk of cool gas in LRG halos by obtaining accurate measurements of N(H I); and (2) to constrain the physical properties and chemical enrichment in massive quiescent halos by observing different ionic metal transitions that probe a wide range of ionization states. In Paper I, we presented the N(H I) measurements for the sample and reported that LRGs contains widespread chemically enriched gas traced by various metal ions. In this paper, we expanded our investigation with a detailed ionization analysis based on resolved component structures of a suite of absorption transitions, including the full H I Lyman series and multiple low-, intermediate-, and high-ionization metal transitions. Resolving the component structures of the various absorption lines was made possible by the high-resolution *HST* /COS FUV spectra and ground-based echelle optical spectra of the background QSOs. Our main findings are summarized below.

1. LRGs exhibit enhanced absorption in H I, low-ionization (Mg II), and intermediate-ionization (Si III and C III) metals at projected distances $d \lesssim 100$ kpc, compared to absorption at larger d (Figure 5.2).

2. H I-bearing gas detected around LRGs is predominantly cool, with temperatures of $T < 10^5$ K inferred from the H I linewidths. Using the ratios of Doppler linewidths for matched H I and Mg II components, we find that the gas has a mean temperature and dispersion of $\langle T \rangle = 2.0 \times 10^4$ K and $\sigma_T = 1.4 \times 10^4$ K, with a modest inferred non-thermal broadening of $\langle b_{\rm nt} \rangle = 7 \pm 5$ km s^{-1}(Figure 5.4).

3. The line-of-sight velocity distribution of individual absorption components relative to the systemic redshift of LRGs can be characterized by a mean and dispersion of $\langle \Delta v_{\rm gas-galaxy} \rangle = 17$ km s^{-1}and $\sigma_{\Delta v_{\rm gas-galaxy}} = 147$ km s^{-1}(Figure 5.3). The observed radial velocity dispersion is consistent with what have been observed in Mg II absorbers around LRGs using low-resolution data (e.g., Huang et al. 2016), but it is only ~ 60 percent of what is expected from virial motion.

4. By considering matched absorbing components and comparing the relative abundances of different ions for each component, we find that the underlying gas density and metallicity can vary by more than a factor of 10 within the gaseous halo of an LRG (left panels of Figures 5.8 and 5.9). Such large variations in gas density and metallicity within individual sightlines highlight a complex multiphase structure and poor chemical mixing in the gaseous halos of LRGs. Moreover, they underscore the importance of resolving the component structures of CGM absorbers using high-resolution absorption spectra, because any information on variations in gas metallicity and density within individual halos is lost in ionization studies utilizing only the integrated H I and metal column densities along individual sightlines.

5. Over the full sample, the median metallicity of absorbing components is $\langle [{\rm M/H}] \rangle = -0.7 \pm 0.2$, with an estimated 16-84 percentile range of $[{\rm M/H}] = (-1.6, -0.1)$. Metal-

poor components with $< 1/10$ solar metallicity are seen in 50% of the LRG halos, while gas with near-solar and super-solar metallicity is also common (Figure 5.8). Furthermore, we find a significant incidence of optically thick components with very low metallicities: 43^{+25}_{-22} percent of LLSs in the gaseous halos of LRGs have metallicities lower than a few percent solar.

6. The median gas density for individual components in COS-LRG is $\log \langle n_{\rm H} \rangle / {\rm cm}^{-3} = -2.4 \pm 0.1$, with an estimated 16-84 percentile range of $\log n_{\rm H} / {\rm cm}^{-3} = (-3.0, -1.8)\,{\rm cm}^{-3}$. The inferred median gas density implies a median ionization parameter of $\log \langle U \rangle = -3.0 \pm 0.1$ under the HM05 UVB. The data points exhibit a trend of rising gas density with increasing H I column density (Figure 5.9, right panel).

7. We infer a density contrast of ~ 100 between optically thick components and the expected gas densities in the hot CGM (Figure 5.10). The inferred density contrast indicates that optically thick gas in the CGM of LRGs is roughly in thermal pressure equilibrium with the hot halo at galactocentric radius $r \sim d$. In contrast, only ~ 40 percent of optically thin components have densities consistent with thermal pressure equilibrium with the hot halo at $r \sim d$, which implies that a majority of optically thin absorbers occur at larger radii, $r > d$.

8. Cool clumps in LRG halos are compact. The inferred clump sizes are between 10 pc and ~ 1 kpc thick, with a mode of ~ 100 pc (Figure 5.9, right panel). The estimated median clump size for the sample is $\langle l \rangle = 120^{+80}_{-40}$ pc.

9. We find that high-ionization O VI and low-ionization species (low-ionization metals and H I) exhibit distinct kinematic structures. The median absolute difference in centroid velocity between O VI components and the nearest low-ionization metal and H I components is 24 km s^{-1}, with a full range of from $|\Delta v| = 4$ to $|\Delta v| = 71$ km s^{-1}(Figure 5.5). Furthermore, the implied non-thermal line broadening for O VI gas is high, $b_{\rm nt} = 20 - 100\,{\rm km\ s}^{-1}$, significantly higher than the modest non-thermal broadening

inferred for lower-ionization gas. Such kinematic mismatches highlight different physical origins between high-ionization gas traced by O VI and lower-ionization gas traced by other metal ions. Based on the observed relation between O VI column density and linewidth, our data suggest that O VI absorbers around LRGs trace photoionized, low-density gas at large distances from the galaxy (Figure 5.14).

10. We calculate the total surface mass density of cool ($T \sim 10^4$ K) gas in the LRG halos, $\Sigma_{\rm cool}$, by applying estimated ionization fraction corrections to the observed H I column densities. The spatial profile of $\Sigma_{\rm cool}$ is equally well-described by an exponential profile in 2D, $\Sigma_{\rm cool} = (4.1 \pm 1.4)\, e^{-(d/27 \pm 4\,{\rm kpc})}\, {\rm M}_\odot\, {\rm pc}^{-2}$, and a steep projected Einasto profile with shape parameter $\alpha = 1.0^{+0.6}_{-0.2}$ and scale radius $r_s = 48^{+19}_{-8}$ kpc, consistent with a true exponential profile in 3D (Figure 5.11). On the other hand, a projected NFW profile or shallow Einasto profile with $\alpha < 0.3$ are ruled out because they cannot reproduce the steep decline of $\Sigma_{\rm cool}$ with d. We conclude that the mass distribution of cool gas in the CGM of LRGs is different from the expected mass distribution of the underlying dark matter halo.

11. We estimate that typical LRGs at $z \sim 0.4$ harbor at least $M_{\rm cool} = (1-2) \times 10^{10}\, {\rm M}_\odot$ of photoionized $T \sim 10^4$ K gas at $d < 160$ kpc in their halos (or as much as $M_{\rm cool} \approx 4 \times 10^{10}$ ${\rm M}_\odot$ at $d < 500$ kpc), which is comparable to the estimated cool CGM mass of star-forming L^* galaxies. The inferred cool CGM mass is about $\sim 6-13$ percent of the expected gas mass in the hot phase of the CGM (Figure 5.12).

Considering our observations in the context of a multiphase gaseous halo surrounding LRGs, our findings are consistent with a scenario in which cool clumps condense from the hot halo due to local thermal instabilities. The observed distribution of line-of-sight velocities indicates that ram pressure drag exerted by the hot halo is effective at dissipating the kinetic energy of cool clumps, causing them to fall toward the galaxy. It is likely that a large

majority of cool clumps in the CGM of LRGs are destroyed before reaching the central galaxy, thereby explaining the continuing lack of star-formation activity in these galaxies despite the existence of a large reservoir of cool gas in the CGM. Interactions with the hot gas (such as thermal conduction) and/or some form of energetic feedback from the galaxy itself (e.g., heating from stellar winds, SNe Ia, or an active nucleus) likely play an active role in preventing an accumulation of cool gas in the ISM the LRG. Moving forward, a systematic study of the incidence and physical properties of the cool ISM ($d \lesssim 10\,\mathrm{kpc}$; see e.g., Zahedy et al. 2017a) of LRGs is necessary to connect the observed plethora of cool gas at $d \sim 100$ kpc scales in the CGM with the continuing "red and dead" nature of LRGs over cosmic time.

CHAPTER 6

PROBING IGM ACCRETION ONTO FAINT LYα EMITTERS AT $z \sim 2.8$

The contents of this chapter were previously published in the Monthly Notices for the Royal Astronomical Society as Zahedy, F. S., Rauch, M., Chen, H.-W., Carswell, R. F., Stalder, B., & Stark, A. A. 2019, MNRAS, 486, 1392. They are reproduced here in accordance with the copyright agreement and with permission from the Oxford University Press.

6.1 Introduction

The presence of heavy elements in the intergalactic medium (IGM) can be used to probe the relationship between galaxies and the IGM. Absorption lines caused by common metals in the spectra of background QSOs, when observed in sightlines close to foreground galaxies, and, occasionally, supplemented by observations of nebular emission from the gas, can shed light on how galaxies accrete gas and smaller building blocks from the ambient IGM to fuel star formation, and subsequently eject metals and radiation to their environment.

Adding metals ab-initio to a cosmological hydro-simulation of the IGM, Haehnelt et al. (1996) showed that typical QSO metal absorbers can arise during the inflow of pre-enriched gas ($Z \lesssim -2.5\,Z_{\odot}$) into $z \sim 3$ galactic potential wells of progenitors ($M_{\rm baryon} \sim 10^{9-10} M_{\odot}$) of galaxies like the Milky Way. The close agreement between the properties of the simulated and observed $z \sim 3$ metal absorption lines, even in the absence of any local metal enrichment or galactic feedback (Rauch et al. 1997), suggest that metal absorption systems (e.g., C IV) may provide our earliest observational glimpses of the *accretion of gas* onto high redshift galaxies.

The early-enrichment or infall scenario for QSO metal absorbers can be contrasted with a more local origin for the heavy metals, where feedback from recent star formation activity enriches the gaseous environment of a galaxy with metals (the circumgalactic medium, CGM;

e.g. Adelberger et al. 2003; Steidel et al. 2010). However, the existence of long-range outflows able to explain the widespread metal enrichment through local feedback has been questioned (e.g., Kawata & Rauch 2007; Gauthier & Chen 2012). Furthermore, the observed low levels of turbulence and spatial small-scale structure in the IGM seen in multiple lines-of-sight to lensed QSOs broadly support the idea that most metal absorbers are seen in stages of inflow as part of the general IGM, unaffected by recent feedback (e.g., Rauch et al. 2001a,b). A study of the CGM of Lyman break galaxies has confirmed that the redshift distortions in the velocity field of H I, Si IV and C IV absorption at $z = 2 - 3$ are in fact due to infall, not outflows (Turner et al. 2017).

The formation of QSO metal absorbers from infalling IGM gas requires an earlier epoch of widespread metal enrichment in the IGM, the existence of which has been established by detections of ionic metal species at high redshifts currently up to $z \sim 6.8$ (e.g., Songaila 2001; Schaye et al 2003; Simcoe et al. 2004, 2011; Ryan-Weber et al. 2009; Becker et al. 2011; Chen et al. 2017; Cooper et al. 2019). Theoretical and empirical arguments also support the idea that the IGM was likely polluted by more widely distributed, low-mass galaxies at earlier times. Gas escapes the shallow potential well of low-mass objects more easily and high-redshift dwarf galaxies occur at high number densities, favoring a widespread pollution of the IGM at early times, aided by the Hubble expansion (e.g., Scannapieco 2005; Porciani & Madau 2005; Wiersma et al. 2010).

Recent advances in cosmological hydrodynamic simulations have refined predictions for galactic accretion and emphasized the importance of small scale structure embodied by cold accretion streams (e.g., Kereš et al. 2005; Goerdt et al. 2010; Faucher-Giguere & Kereš 2011; Fumagalli et al. 2011; Rosdahl & Blaizot 2012; Van de Voort et al. 2012; Shen et al. 2013). Comparisons between observations and the expected accretion features in these cosmological simulations need to rely on statistical arguments, focusing on a subset of properties like column density or metallicity distributions (e.g., Cooper et al, 2015; Hafen et al. 2017).

In contrast, direct detections of accretion onto individual high-redshift galaxies have re-

mained rare, as they must rely on multiple strands of evidence, essentially requiring two- or three-dimensional information that can only be provided by simultaneous observations of gas and stars in emission. Evidence for gaseous accretion onto galaxies may include kinematic signatures of gas streams attached to and/or moving towards a galaxy, gaseous filaments converging on starburst regions fueled by the inflow, and tidal tails from the simultaneous infall of small halos. One candidate system for filamentary infall onto a high-redshift galaxy was reported by Rauch et al. (2011, 2016). That particular system owes its discovery to fluorescent radiation from gaseous features which have exposed to ionizing photons escaping from the starbursting region. However, such a situation may be atypical of galaxies undergoing the cold accretion process, most of which will have too low star-formation rates and presumably masses required to illuminate their gaseous environment.

Observing more typical forms of galactic accretion requires the ability to simultaneously detect fainter galaxies and fainter nebular emission features. In this chapter we will study such a putative accretion environment, by paying a closer look at a grouping of $z \sim 2.8$ Lyα emitters (LAEs) previously discovered through a blind spectroscopic long-slit search (Rauch et al. 2008, hereafter R08). As shown in Figure 6.1, this grouping is unique because the LAEs are coincident in redshift with a number of Lyα absorption complexes seen in the sightline of a nearby background QSO, DMS 2139−0405. The underlying galaxies of the LAEs are faint, with low inferred star formation rates of SFR $< 1\,\mathrm{M}_\odot\,\mathrm{yr}^{-1}$. In particular, one of the gas complexes, Complex A, occurs in a structure spanned by a pair of Lyα-emitting galaxies which are situated at projected distances $d = 87$ and 161 kpc on opposite sides of the QSO sightline. One of the LAEs shows a relatively rare Lyα emission profile with a dominant blue peak (R08), which is commonly associated with infalling gas (e.g., Verhamme et al. 2006).

The positional information about the LAEs derived from the two-dimensional low resolution spectra of the field, and the high-resolution absorption spectra of neutral hydrogen and metal species along the QSO sightline, allow us to study the physical association between the galaxies and the gas, and to test the predictions of the infall scenario for metal

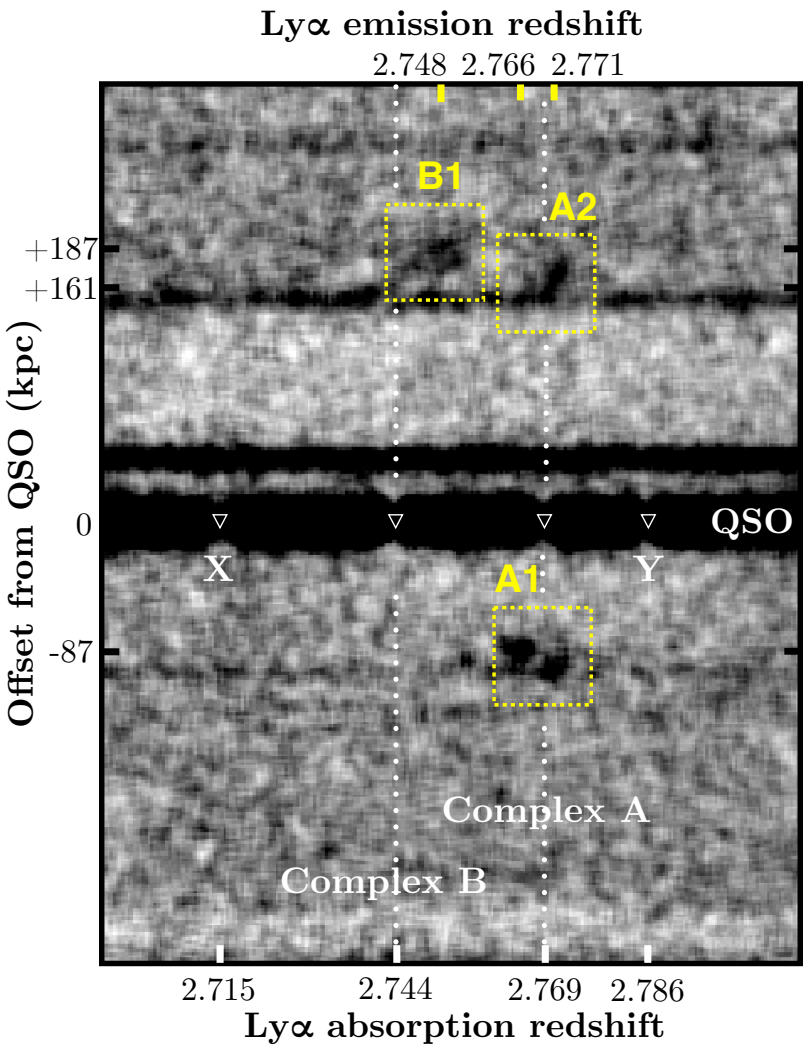

Figure 6.1: Two-dimensional long-slit spectrum centered at QSO DMS 2139−0405. The dispersion axis is in the horizontal direction, covering roughly 4480 − 4640 Å in observed wavelength, which corresponds to the location of Lyα transition at $z = 2.7-2.8$. The spatial axis is in the vertical direction and covers 75 arcsec from top to bottom, approximately 600 kpc in projected distance. The strong continuum at the center is the QSO, whereas featureless and fainter continua above it are likely lower-redshift objects. Three foreground Lyα emitters (LAEs) are detected at $d < 300$ kpc from the QSO (dotted squares; see Rauch et al. 2008), with their Lyα emission redshifts indicated on the upper horizontal axis. In addition, the locations of strong Lyα absorption in the QSO continuum are shown with inverted triangles, with their absorption redshifts indicated on the lower horizontal axis. LAEs A1 and A2 are situated at $d = 87$ and 161 kpc on opposite sides of the QSO, where a strong Lyα absorption is coincident with both LAEs in redshift space (Complex A, see Figure 3). Another Lyα absorption system (Complex B, see Figure 4) is detected at $d = 187$ kpc and a velocity separation $|\Delta v| < 500$ km s^{-1} from LAE B1. Two additional Lyα absorption complexes (X and Y) are also found at $z = 2.7 - 2.8$ (see discussion of these systems in Appendix B and its associated tables and figures).

absorption systems against the observed gas column density, chemical abundance, ionization state, and kinematics. The low luminosities and likely low masses of the LAEs also enable us to examine the validity of the late-time outflow scenario and the CGM paradigm in a more typical environment of the cosmic web far from massive starburst galaxies.

This chapter is organized as follows. Section 6.2 presents the observational dataset and corresponding data reduction. We describe the properties of the foreground LAEs in Section 6.3. In Section 6.4, we present the absorption-line measurements, describe the absorption line complexes near the LAEs, and investigate the ionization and chemical properties of the gas. Finally, we discuss the interpretations of our findings in Section 6.5 and summarize our study in Section 6.6. Throughout this chapter, we adopt a Λ cosmology of $\Omega_{\rm M} = 0.3$ and $\Omega_\Lambda = 0.7$, with a Hubble constant of $H_0 = 70$ km s^{-1} Mpc^{-1}. All magnitudes are reported in the AB system.

6.2 Observations

To characterize the properties of the absorbing gas and investigate its connection to the unique grouping of $z \sim 2.8$ LAEs, we carried out high-resolution echelle spectroscopy of the background QSO DMS 2139−0405 ($z_{\rm QSO} = 3.32$). In addition, we obtained new optical and near-infrared broadband imaging data of the field around the QSO in order to search for continuum counterparts to the LAEs. Here we describe the observations and data reduction procedures.

6.2.1 QSO Echelle Spectroscopy

We obtained high-resolution echelle spectra of QSO DMS 2139−0405 (right ascension $21^{\rm h}41^{\rm m}39.1^{\rm s}$, declination $-03°51'42.57''$ in the J2000 epoch) with the MIKE echelle spectrograph (Bernstein et al. 2003) on the Magellan Clay Telescope over two nights in 2016 September. A 1-arcsec slit and 3×3 binning during readout was chosen for the observations, delivering

a spectral resolution of FWHM $\approx 10 - 12$ km s^{-1} over a continuous wavelength coverage from 3350 Å to 9300 Å. The mean seeing over the observing period was $0.5 - 0.7$ arcsec. The total integration time of the MIKE observations was 26400 s, comprising eight individual exposures of equal duration. We reduced the MIKE spectra using an IDL-based custom data reduction software. For each individual exposure, the software performed optimal extraction of the QSO spectrum in each echelle order, using a Gaussian weighting scheme that matched the observed QSO spatial profile. Observations of a spectrophotometric standard star taken during the same night as the observations were utilized to determine the response function, which was then used to perform relative flux calibrations of the QSO spectrum. The individual echelle orders were combined for each exposure, and the different exposures were added to form a single spectrum, which was then continuum normalized using a low-order polynomial function that excluded regions of strong absorption. The final reduced spectrum of DMS 2139−0405 is characterized by a signal-to-noise ratio of S/N $\approx 10 - 15$ per resolution element at $\lambda > 4000$ Å.

6.2.2 Imaging Observations

Optical imaging data of the field around DMS 2139−0405 were obtained using the Parallel Imager for Southern Cosmology Observations (PISCO; Stalder et al. 2014) on the Magellan Clay Telescope in 2016 October. PISCO is a multi-band imager which provides simultaneous broadband coverage in g-, r-, i-, and z-bands. The observations consisted of a series of exposures 300 s in length, with a total integration time of 3300 s taken under a mean seeing of $0.9 - 1.0$ arcsec. The raw PISCO data were reduced using standard IRAF-based routines. The photometric zero points of the PISCO imaging data were determined using field stars observed in the Sloan Digital Sky Survey (SDSS; York et al. 2000). We supplement our PISCO imaging data with archival V- and I-band images of the field taken with LRIS (Oke et al. 1995) on the Keck-I Telescope, which were previously described in R08. The LRIS V- and I-band images are characterized by a mean seeing of $0.7 - 0.9$ arcsec.

Table 6.1: Journal of imaging observations of the field around QSO DMS 2139−0405

Telescope	Instrument	Filter	Exp. Time (s)	Date	5σ Limiting Mag. (AB)
Magellan Clay	PISCO	g	3300	2016 Nov	27.6
	PISCO	r	3300	2016 Nov	27.2
	PISCO	i	3300	2016 Nov	26.7
	PISCO	z	3300	2016 Nov	25.9
Magellan Baade	FourStar	K_s	14120	2016 Aug	25.1
Keck I	LRIS	V	1680	1998 Jun	27.1
	LRIS	I	4050	1998 Aug	26.2

In addition to the optical images, we obtained near-infrared (NIR) K_s-band observations of the field with FourStar (Persson et al. 2008) on the Magellan Baade Telescope in 2016 August. The field was observed for a total of 14120 s, under excellent seeing conditions of $0.5 - 0.8$ arcsec. To prevent saturation due to high sky and thermal backgrounds in the image, the observations consisted of a sequence of short 20 s exposures with a 10-arcsec random dither applied between successive exposures. The FourStar data were reduced using an IRAF-based routine which performed sky subtraction and flat-fielding using super sky frames created on a rolling basis. We used field stars observed with the Two Micron All Sky Survey (2MASS; Skrutskie 2006) to determine the photometric zero point of the K_s-band image.

We summarize the available imaging data of the field around QSO DMS 2139−0405 in Table 6.1, where we also show the mean 5σ limiting magnitudes measured over a 1 arcsec sky aperture for each bandpass. The limiting magnitudes range from 25.1 mag for NIR K_s band to deeper than 27 mag for the optical g-, V-, and r-bands. In Figure 6.2, we present a false-color composite image of the field around QSO DMS 2139−0405. The composite image was created using the V-, I-, and K_s-band images for blue, green, and red, respectively.

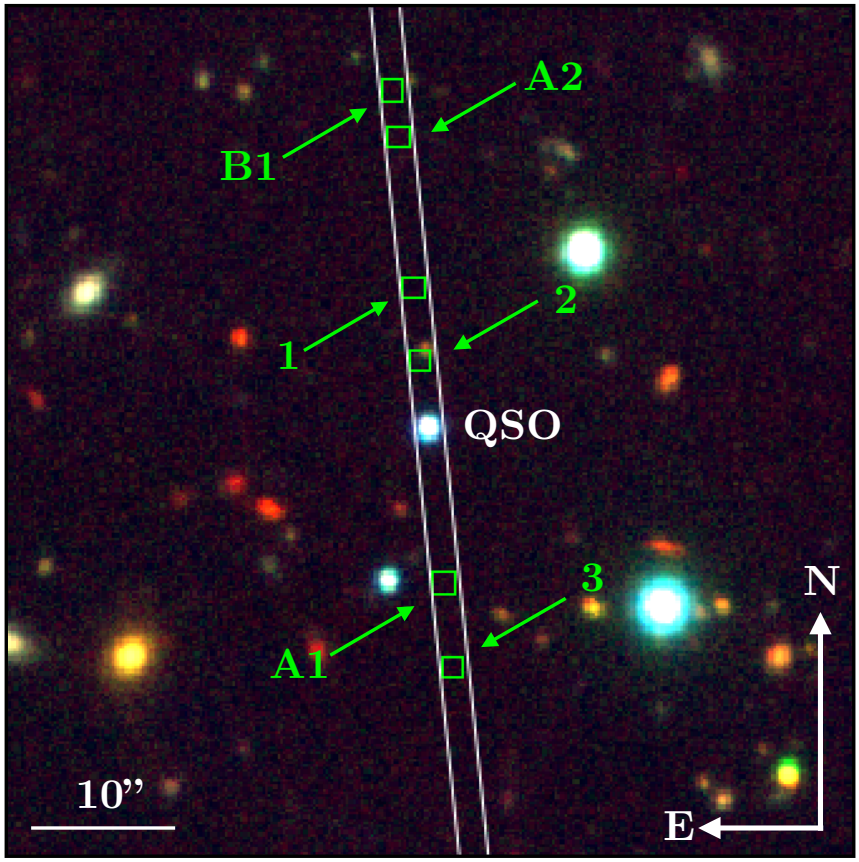

Figure 6.2: False-color composite image of the field around QSO DMS 2139−0405, created using the V-, I-, and K_s-band images for blue, green, and red, respectively. The QSO is the blue point source at the center of the image. The slit position and orientation of the deep spectroscopic observations reported in R08 are shown. The position of LAEs detected along the slit at $d < 300$ kpc from the QSO is shown with green squares and labeled by their IDs in Table 6.2.

6.3 Foreground LAEs at $d < 300$ kpc from DMS 2139−0405

To study the gaseous environment of high-redshift LAEs, we focus on foreground LAEs within $d < 300$ kpc from the sightline of background QSO DMS 2139−0405. Systematic surveys of gas absorption around $z = 2 - 3$ galaxies have shown enhanced gas absorption at $d \lesssim 300$ kpc (e.g., Rudie et al. 2012). As shown in Figure 6.2, six LAEs from the R08 study are detected within $d < 300$ kpc from the background sightline. To avoid confusion with possible outflows from the background QSO (e.g., Wild et al. 2008), we further limit our study to LAEs that are situated at a line-of-sight velocity difference of $\Delta v < -10000$ km s^{-1} from the background QSO. Three Lyα-emitting objects, LAEs 1, 2, and 3, which are located at $z \sim 3.3$ or less than a few $\times\, 1000$ km s^{-1} in velocity separation from the QSO, are excluded due to this requirement.

There are three foreground LAEs at $d < 300$ kpc from the QSO sightline. Two of these objects, LAE A1 at peak redshift $z_{\rm peak} = 2.7659$ and LAE A2 at $z_{\rm peak} = 2.7713$, are closely situated in redshift space with their Lyα emission peaks separated by merely $\Delta v \approx 400$ km s^{-1}. In addition, both LAEs are situated on opposite sides of the QSO at a projected separation of 248 kpc, with the QSO sightline probing the LAE A1 at $d = 87$ kpc and LAE A2 at $d = 161$ kpc (top-left panel of Figure 6.3). A third emitter, LAE B1, occurs at $z_{\rm peak} = 2.7483$, and is probed by the background QSO at $d = 187$ kpc (top-left panel of Figure 6.4).

Because the shape of Lyα emission line is highly sensitive to details of the radiative transfer (e.g., Verhamme et al. 2006), it is likely that the systemic redshifts of the LAEs, $z_{\rm sys}$, are different from their measured Lyα peak redshifts, $z_{\rm peak}$. Previous studies found that a large majority of Lyα-selected galaxies at $z \sim 2 - 3$ exhibit asymmetric Lyα emission line profiles, with a main peak that is typically redshifted from the systemic redshift by greater than 100 km s^{-1} (e.g., Erb et al. 2014; Hashimoto et al. 2015; Trainor et al. 2015). Using a sample of faint LAEs, Hashimoto et al. (2015) found a mean offset of $\Delta v_{\rm red} = +174$ km s^{-1} for the main red peak relative to systemic. To estimate the systemic redshifts of the LAEs,

we adopt the mean offset from Hashimoto et al. (2015) and apply it to the peak redshifts of LAEs A2 and B1. For LAE A1, which exhibits a dominant *blue* peak in its Lyα emission profile (R08), we estimate its systemic redshift by adopting an offset of $\Delta v_{\rm blue} = -316$ km s^{-1}, which is the mean offset Hashimoto et al. (2015) found for blueshifted Lyα emission line peaks.

The observed Lyα line fluxes of the three LAEs are $F_{\rm Ly\alpha} = (2.7 \pm 0.4) \times 10^{-18}, (3.3 \pm 0.6) \times 10^{-18}$, and $(3.5 \pm 0.5) \times 10^{-18}\,{\rm erg\,s^{-1}\,cm^{-2}}$ for LAEs A1, A2, and B1 (R08). These observed line fluxes correspond to Lyα luminosities of $L_{\rm Ly\alpha} = (1.7 - 2.2) \times 10^{41}\,{\rm erg\,s^{-1}}$. The inferred Ly$\alpha$ luminosities of the three LAEs are a factor of $20 - 30$ lower than the characteristic luminosity of the LAE luminosity function at $z \sim 3$ (e.g., Cassata et al. 2011; Konno et al. 2016; Drake et al. 2017), which indicate that these LAEs are intrinsically faint compared to the general LAE population at the same epoch.[1]

The available multi-band imaging data of the field around DMS 2139−0405 allows us to search for continuum light counterparts of these faint LAEs. We infer the positions of the LAEs on the sky based on the reported long-slit position and orientation for the R08 observations as well as the spatial position of the Lyα emissions in the long-slit spectrum from R08. For each bandpass, we then measure the total flux contained within a 3-arcsec diameter aperture centered at the inferred position of each LAE. The choice of aperture size is guided by the width of the long slit used in R08. We find that none of the three LAEs is detected in continuum light at 3σ or higher significance level, in all broadband filters. The lack of significant detection in any broadband image persists if a smaller (2 arcsec) or larger (5 arcsec) aperture is adopted instead.

The lack of detection of continuum light from all three LAEs ($r > 26.6$, $K_s > 24.5$) indicates that these LAEs are faint and low-mass galaxies. At $z = 2.7 - 2.8$, the upper limit on r-band flux corresponds to a rest-frame FUV absolute magnitude of $M(1700\,{\rm \AA}) \gtrsim -18.7$,

1. This conclusion would stand even if the observations were subject to significant slit losses of ∼50% (e.g., R08; Cassata et al. 2011).

Table 6.2: Properties of LAEs at $d < 300$ kpc from QSO DMS 2139−0405 ($z_{\rm QSO} = 3.32$)

ID	Alt. ID[a]	ΔRA[b]	ΔDec[b]	$z^{c}_{\rm peak}$	$z^{d}_{\rm sys}$	d^{e}	$F_{\rm Ly\alpha}$	Photometry[f]							$\rm SFR_{UV}$[g]	$\rm SFR_{Ly\alpha}$[h]
		(arcsec)	(arcsec)			(kpc)	($10^{-18}\,\rm erg\,s^{-1}\,cm^{-2}$)	AB(g)	AB(V)	AB(r)	AB(i)	AB(I)	AB(z)	AB(K_s)	($\rm M_\odot\,yr^{-1}$)	($\rm M_\odot\,yr^{-1}$)
A1	15	−1.1	−10.9	2.7659	2.7699	87	2.67 ± 0.41	> 27.1	> 26.3	> 26.6	> 26.0	> 25.5	> 25.3	> 24.5	< 3.2	0.1
A2	37	+2.1	+20.4	2.7713	2.7691	161	3.27 ± 0.57	> 27.1	> 26.3	> 26.6	> 26.1	> 25.5	> 25.4	> 24.5	< 3.0	0.1
B1	36	+2.5	+23.6	2.7483	2.7461	187	3.46 ± 0.52	> 27.1	> 26.3	> 26.6	> 26.1	> 25.5	> 25.4	> 24.5	< 3.0	0.1
1	12	+1.0	+9.8	3.3300	3.3275	73	3.36 ± 0.35	> 27.0	> 26.3	> 26.6	> 26.1	> 25.5	> 25.3	> 24.5	< 4.1	0.2
2	33	+0.6	+4.7	3.2646	3.2621	36	3.50 ± 0.34	> 26.9	> 26.3	> 26.5	> 26.0	> 25.5	> 25.3	> 24.4	< 4.4	0.2
3	16	−1.7	−16.9	3.3189	3.3164	127	3.06 ± 0.37	> 27.2	> 26.3	> 26.6	> 26.1	> 25.5	> 25.3	> 24.5	< 4.1	0.2

Notes

[a] Original ID from R08.

[b] Offset from the QSO position in J2000, (RA, Dec.)=($21^{\rm h}41^{\rm m}39.1^{\rm s}$, $-03^\circ51'42.57''$).

[c] Peak emission redshift of the LAE, from R08.

[d] The adopted LAE systemic redshift, calculated by applying an offset of $-174\,(+316)$ km s^{-1} to $z_{\rm peak}$ for redshifted (blueshifted) Lyα line peak, based on Hashimoto et al. (2015; see Section 6.3).

[e] Projected distance from the QSO. Note that LAEs 1, 2, and 3 are excluded from this study because they are situated at $\Delta v > -10000$ km s^{-1} from the QSO redshift, $z_{\rm QSO} = 3.32$ (see Section 6.3).

[f] Measured in a 3 arcsec aperture centered at the nominal sky coordinates of the object. The upper limits are 3σ.

[g] Calculated from the upper limit on the $i-$band flux, using the near-ultraviolet (NUV) star-formation rate (SFR) calibrator from Kennicutt & Evans (2012).

[h] Calculated from the Lyα line luminosity of the LAE, by converting the local Hα SFR calibrator from Kennicutt & Evans (2012) to one for Lyα, assuming case B recombination (see Section 6.3).

which is equivalent to $L \lesssim 0.1\,L^*$ (e.g., Reddy et al. 2008). Using this limit on FUV absolute magnitude, we constrain the total stellar masses of the LAEs to $M_{\rm star} \lesssim 10^9\,\rm M_\odot$, based on the inferred mean mass-to-light ratio and stellar mass function as this epoch (e.g., Reddy et al. 2012; Marchesini et al. 2009). The inferred low masses of the three LAEs are consistent with the low mean dark matter halo mass ($M_{\rm h} \sim 10^{11}\,\rm M_\odot$) of $z \sim 3$ LAEs inferred from clustering analyses (e.g., Bielby et al. 2016).

Next, we estimate the star-formation rate (SFR) of the LAEs. At $z \approx 2.8$, the effective wavelength of the i-band filter corresponds to a rest-frame wavelength of ≈ 2050 Å in the near-ultraviolet (NUV). By converting the i-band flux limits of the LAEs to their corresponding upper limits on specific luminosity in the NUV, and then adopting the local NUV star-formation rate relation from Kennicutt & Evans (2012, Equation 12), we estimate upper limits on unobscured SFR of $\rm SFR_{UV} \lesssim 3.0\,M_\odot\,yr^{-1}$ for the three LAEs.

An independent estimate of the star-formation rate of the LAEs can also be obtained by assuming that the observed Lyα emission is powered by underlying star formation activity in the galaxies. If we also assume case-B recombination (Brocklehurst 1971), the Kennicutt & Evans (2012) SFR relation for Hα can be converted into one for Lyα, following $\rm SFR_{Ly\alpha}\,(M_\odot\,yr^{-1}) = 6.2 \times 10^{-43}\,L_{Ly\alpha}\,(erg\,s^{-1})$. Applying this relation to the observed Lyα luminosities gives unobscured SFRs of $\rm SFR_{Ly\alpha} \approx 0.1\,M_\odot\,yr^{-1}$ for the three LAEs.

In Table 6.2, we summarize the photometric and spectroscopic properties of LAEs A1, A2, and B1. For each object, we report its angular offset from the QSO, observed peak Lyα redshift, estimated systemic redshift, total Lyα line flux, projected distance from the QSO sightline, 3σ upper limits on the broadband fluxes, and the inferred SFRs. For completeness, we also include the same information in Table 6.2 for LAEs 1, 2, and 3, which are located at $z \sim 3.3$ or less than a few $\times\, 1000\,\mathrm{km\ s^{-1}}$ in velocity separation from the QSO.

6.4 Analysis and Results

The high-resolution echelle spectrum of DMS 2139−0405 enables a detailed study of gas in proximity to the three foreground LAEs. As previously mentioned in Section 6.1, a number of Lyα absorption complexes at $z = 2.7 - 2.8$ are found in the low-resolution spectrum of the QSO (Figure 6.1). In particular, Complex A and Complex B are coincident in redshift space with the three foreground LAEs situated at $d < 300$ kpc (see Figure 6.1 and Section 6.3). In this section, we describe the observed gas properties in the vicinity of these $z = 2.7 - 2.8$ LAEs, based on our analysis of the high-resolution echelle spectrum of DMS 2139−0405.

6.4.1 Absorption Analysis

At the LAE redshifts, our MIKE spectrum of DMS 2139−0405 provides coverage of the H I Lyα λ1215 line and prominent ionic metal transitions C IV $\lambda\lambda$1548,1550 and Si IV $\lambda\lambda$1393,1402 doublets.[2] To characterize the absorbers, we first measure the total rest-frame equivalent widths for transitions H I Lyα λ1215, Si IV $\lambda\lambda$1548,1550, and Si IV $\lambda\lambda$1393,1402 absorption lines. When a given ionic transition is not detected, we use the error array to estimate the 2σ upper limit on the absorption equivalent width, integrated over a spectral window that is twice the FWHM of the corresponding C IV line. The equivalent width mea-

2. Note that while the MIKE data cover all higher order Lyman transitions, the presence of a higher-redshift Lyman-limit system results in low transmitted flux for rest wavelengths $\lambda_{\mathrm{rest}} \lesssim 1050\,\mathrm{\AA}$ at the LAE redshifts. Consequently, only Lyα λ1215 has sufficient data quality for analysis.

Table 6.3: Properties of $z = 2.7 - 2.8$ absorption complexes along DMS 2139−0405

Complex	$z_{\rm abs}$	H I λ1215		Si IV λ1393		Si IV λ1402		C IV λ1548		C IV λ1550	
		W_r (Å)	$[v_{\rm min}, v_{\rm max}]$ (km s^{-1})	W_r (Å)	$[v_{\rm min}, v_{\rm max}]$ (km s^{-1})	W_r (Å)	$[v_{\rm min}, v_{\rm max}]$ (km s^{-1})	W_r (Å)	$[v_{\rm min}, v_{\rm max}]$ (km s^{-1})	W_r (Å)	$[v_{\rm min}, v_{\rm max}]$ (km s^{-1})
A	2.7691	1.24 ± 0.02	$[-225, +225]$	0.05 ± 0.01	$[-100, +100]$	0.03 ± 0.01	$[-100, +100]$	0.35 ± 0.02	$[-100, +100]$	0.26 ± 0.02	$[-100, +100]$
B	2.7440	1.99 ± 0.03	$[-255, +645]$	...	...	< 0.02	$[-75, +65]$	0.09 ± 0.02	$[-75, +65]$	0.07 ± 0.02	$[-75, +65]$

surements are summarized in Table 6.3, where for each transition we present the absorption redshift $z_{\rm abs}$, the rest-frame equivalent width W_r, and the velocity interval over which the absorption equivalent width is integrated.

To further investigate the gas properties, we perform a Voigt profile fitting analysis using the VPFIT package (Carswell & Webb 2014), in order to constrain the centroid redshift, z_c, gas column density, log N_c, and Doppler parameter, b_c, of individual absorbing components. We report the results of the Voigt profile fitting in Table 6.4, and present the best-fit model absorption profiles for both absorption complexes along with the data in Figure 6.3 and Figure 6.4. Uncertainties in Table 6.4 represent the estimated 1σ (68%) confidence level from the fitting analysis. When no C IV or Si IV absorption is detected, we estimate the 2σ upper limit on the absorption equivalent width of the strongest available transition of the species, which is calculated over a velocity window twice the full-width-at-half-maximum (FWHM) of the corresponding Lyα component. Then, we calculate the corresponding 2σ upper limit on that component's column density assuming the gas is optically thin. For saturated Lyα components, we also estimate the range of allowed $\log N_c$ and b_c at the 95 percent confidence level, based on a likelihood contour constructed from a grid of χ^2 values from comparing Voigt profile models and observations.

6.4.2 Gaseous Environment of Three $z = 2.7 - 2.8$ LAEs

As discussed in Section 6.3, three LAEs occur at $d < 300$ kpc from the background QSO sightline (Figure 6.1). We now describe two Lyα absorption complexes which are coincident with these emitters in velocity space (see Figure 6.1). Each absorption system is found

Table 6.4: Voigt profile fitting results for $z \sim 2.8$ absorption complexes associated with LAEs

Species	z_c	$\log N_c/\mathrm{cm}^{-2}$	b_c ($\mathrm{km\,s}^{-1}$)
Complex A at $z = 2.7691$			
Si IV	2.76883 ± 0.00008	12.11 ± 0.24	7.9 ± 8.6
C IV	2.76893 ± 0.00001	13.70 ± 0.04	12.5 ± 1.6
H I	2.76914 ± 0.00001	17.1 ± 0.3	57 ± 3
Si IV	2.76926 ± 0.00004	12.11 ± 0.21	4.7 ± 8.9
C IV	2.76933 ± 0.00002	13.10 ± 0.24	3.4 ± 4.6
C IV	2.76959 ± 0.00001	13.81 ± 0.13	6.3 ± 1.6
Si IV	2.76962 ± 0.00002	12.47 ± 0.11	6.5 ± 4.3
C IV	2.77002 ± 0.00002	13.53 ± 0.05	12.8 ± 2.2
Si IV	2.77014 ± 0.00005	12.15 ± 0.20	6.0 ± 7.3
Complex B at $z = 2.7440$			
H I	2.7418 ± 0.0002	12.98 ± 0.29	25.9 ± 16.6
C IV	...	< 12.8	...
Si IV	...	< 12.5	...
C IV	2.74398 ± 0.00006	13.53 ± 0.07	40.4 ± 7.2
H I	2.74400 ± 0.00002	$17.3^{+0.3}_{-0.5}$	52^{+5}_{-2}
Si IV	...	< 12.7	...
H I	2.74755 ± 0.00003	13.36 ± 0.06	21.8 ± 3.0
C IV	...	< 12.8	...
Si IV	...	< 12.5	...
H I	2.74915 ± 0.00002	14.56 ± 0.06	51.5 ± 3.1
C IV	...	< 12.9	...
Si IV	...	< 12.7	...
H I	2.75127 ± 0.00004	13.37 ± 0.11	36.7 ± 6.5
C IV	...	< 12.9	...
Si IV	...	< 12.3	...

within a line-of-sight velocity difference of $|\Delta v| < 500$ km s^{-1} from the LAEs.

Complex A is found near the redshifts of LAE A1 and LAE A2 (see absorption spectra in the right panels of Figure 6.3). Our MIKE echelle spectrum of DMS 2139−0405 reveals strong H I Lyα absorption with a total rest-frame equivalent width of $W_r(1215) = 1.24 \pm 0.02$ Å. Corresponding strong C IV and modest Si IV metal absorptions are also detected. The metal absorption profiles exhibit a multi-component structure that kinematically flank the systematic redshifts of the two LAEs. By fitting a single absorption component to the observed Lyα absorption, our Voigt profile fitting procedure returns a best-fit $\log N(\mathrm{H\,I})/\mathrm{cm}^{-2} = 17.1 \pm 0.3$ for this system. The large uncertainty in N (H I) is understood as due to the saturated Lyα λ1215 profile and the fact that no higher-order H I transition is available in the MIKE data. Based on χ^2 values from the fitting analysis, we estimate that the range of allowed H I column density is $\log N(\mathrm{H\,I})/\mathrm{cm}^{-2} = 16.5 - 17.7$ at the 95 percent confidence level, with a corresponding Doppler parameter range of $b = 52 - 64$ km s^{-1}. The range of allowed total N (H I) does not change significantly if we instead impose a multi-component H I profile that match the kinematic structure of the observed C IV complex.

The C IV and Si IV absorption profiles in Complex A can each be separated into a minimum of four discrete components which are spread over almost 100 km s^{-1}in line-of-sight velocity. We measure a total ionic column density of $\log N(\mathrm{C\,IV})/\mathrm{cm}^{-2} = 14.21 \pm 0.06$ for C IV and $\log N(\mathrm{Si\,IV})/\mathrm{cm}^{-2} = 12.84 \pm 0.09$ for Si IV, integrated over all components.

Complex B is found at the redshift of LAE B1. In contrast to the more kinematically compact absorption profile of Complex A, the Lyα profile of Complex B consists of multiple components spread over nearly 900 km s^{-1} in line-of-sight velocity (see absorption spectra in the right panels of Figure 6.4). The integrated rest-frame equivalent width of the Lyα absorption is $W_r(1215) = 1.99 \pm 0.03$ Å. Our Voigt profile analysis shows that the total N (H I) in Complex B is dominated by a saturated Lyα component centered at $\Delta v = -170$ km s^{-1} blueward of the redshift of LAE B1. While the fitting procedure yields a best-fit $\log N(\mathrm{H\,I})/\mathrm{cm}^{-2} = 17.3^{+0.3}_{-0.5}$ for this component, a full χ^2 analysis indicates that the range

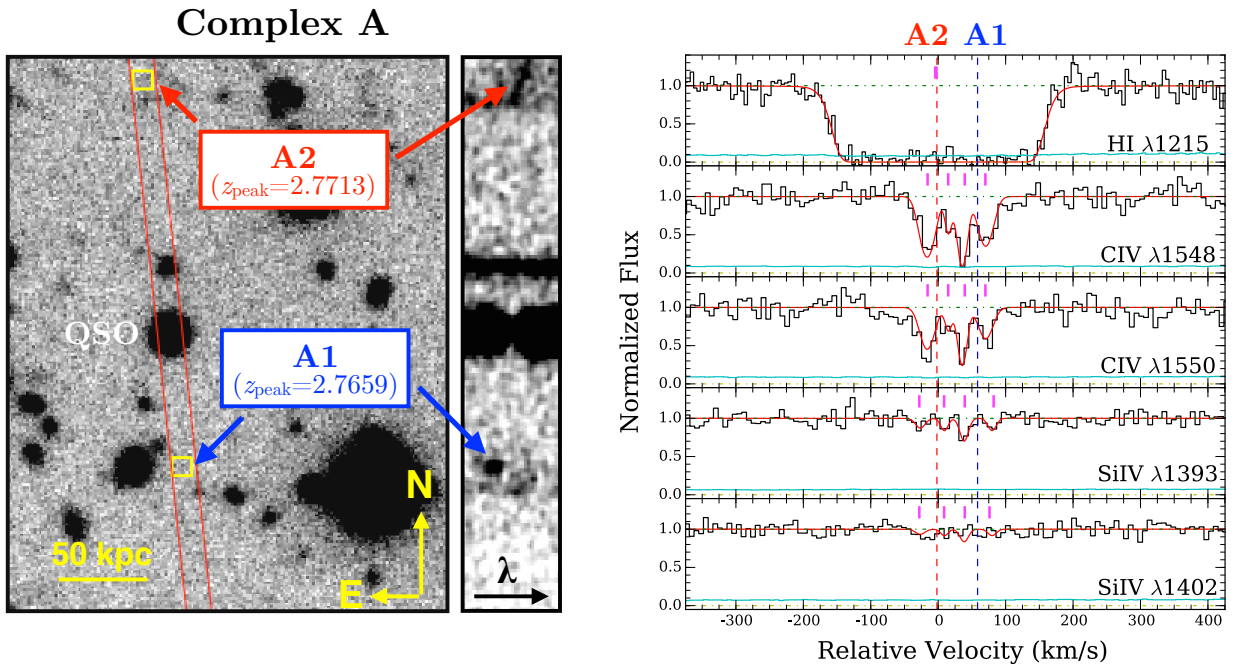

Figure 6.3: *Left*: White-light image of the field around QSO DMS 2139−0405. The slit orientation of the R08 long-slit observations is shown in parallel red lines. The positions of foreground LAEs A1 and A2 are indicated in yellow squares. The LAEs are situated on opposite sides of the QSO, with LAE A1 at $d = 87$ kpc and LAE A2 at $d = 161$ kpc. *Middle*: A cutout of the two-dimensional long-slit spectrum, centered in spectral (horizontal) and spatial (vertical) directions at the Lyα absorption from absorption complex A. The red (blue) arrow points to the location of Lyα emission from LAE A1 (LAE A2). *Right*: Continuum-normalized absorption profiles for various ionic transitions detected in absorption complex A. Zero velocity corresponds to the redshift of the Lyα absorption, $z = 2.7691$. The absorption spectra and corresponding 1σ error arrays are presented in black and cyan histograms. The dashed blue (red) line marks the adopted systemic redshift of LAE A1 (LAE A2). The best-fitting Voigt profile models are presented in red curves, with magenta tick marks indicating the centroid of individual components. For the saturated Lyα line, we estimate that the range of allowed $N\,(\mathrm{H\,I})$ is $\log N\,(\mathrm{H\,I})/\mathrm{cm}^{-2} = 16.5 - 17.7$ at 95 percent confidence level, with a corresponding Doppler parameter range of $b = 52 - 64$ km s^{-1}.

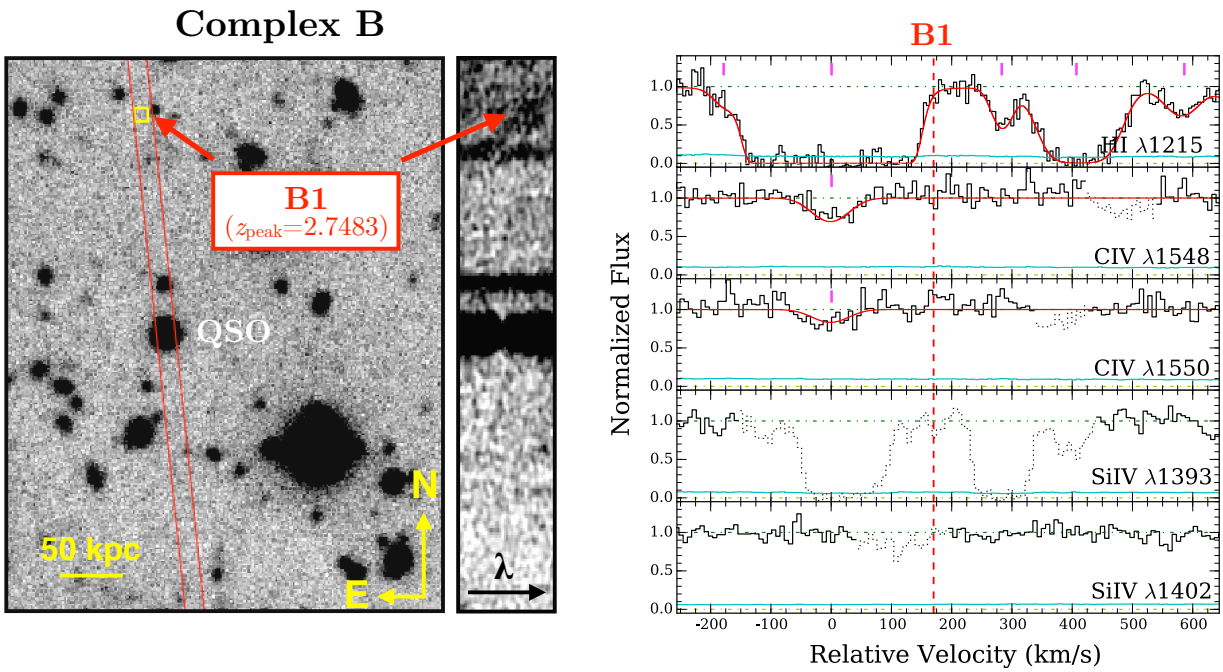

Figure 6.4: *Left*: White-light image of the field around QSO DMS 2139−0405. The yellow square indicates the position of foreground LAE B1 at $d = 187$ kpc. The slit orientation of the R08 long-slit observations is shown in two parallel red lines. *Middle*: A cutout of the two-dimensional spectrum, centered in spectral (horizontal) and spatial (vertical) directions at the Lyα absorption from absorption complex B. The red arrow points to the location of Lyα emission from LAE B1. *Right*: Continuum-normalized absorption profiles of ionic transitions in absorption complex B. Zero velocity corresponds to the redshift of the strongest Lyα absorption component at $z = 2.7440$. The absorption spectra and their corresponding 1σ error array are shown in black and cyan histograms in each panel. Contaminating features are dotted out for clarity. The dashed red line marks the adopted systemic redshift of LAE 7. The best-fitting Voigt profile models are shown in red curves, whereas magenta tick marks indicate the location of individual absorption components. The strong Lyα line at 0 km s^{-1} is saturated. The estimated range of allowed N(H I) is $\log N(\mathrm{H\,I})/\mathrm{cm}^{-2} = 16.5 - 17.8$ at 95 percent confidence level , with a corresponding Doppler linewidth range of $b = 48 - 61$ km s^{-1}.

of allowed column density is $\log N(\mathrm{H\,I})/\mathrm{cm}^{-2} = 16.5 - 17.8$ at the 95 percent confidence level, with a corresponding Doppler linewidth of $b = 48 - 61$ km s^{-1}. In addition to H I, we detect modest C IV absorption in this complex, at a location that matches the strongest Lyα component in velocity space. The best-fitting Voigt profile model for the C IV absorption is given by a single-component with $\log N(\mathrm{C\,IV})/\mathrm{cm}^{-2} = 13.53 \pm 0.07$. No Si IV absorption is detected for the strongest Lyα component, for which we compute a 2σ upper limit of $\log N\,(\mathrm{Si\,IV}) < 12.7$.

6.4.3 The Metallicity and Ionization Properties of the Gas

While our $N(\mathrm{H\,I})$ measurements of the two gas absorption complexes are subject to large uncertainties because of the saturated Lyα absorption, the range of allowed $N(\mathrm{H\,I})$ for each system is constrained to be $\log N(\mathrm{H\,I})/\mathrm{cm}^{-2} \sim 16 - 18$. Constraining H I column density enables us to subsequently constrain the chemical enrichment level of the gas, based on the observed measurements or limits on the column density of ionic metals. Specifically, the mean elemental abundance of the gas, averaged across all components, is related to the column density ratio of the metal ions C^{+3} and Si^{+3} to H^0, following an ionization fraction correction, $\log(\mathrm{C/H}) = \log N(\mathrm{C\,IV})/N(\mathrm{H\,I}) - \log(f_{\mathrm{C}^{+3}}/f_{\mathrm{H}^0})$, and $\log(\mathrm{Si/H}) = \log N(\mathrm{Si\,IV})/N(\mathrm{H\,I}) - \log(f_{\mathrm{Si}^{+3}}/f_{\mathrm{H}^0})$, where f_{H^0}, $f_{\mathrm{C}^{+3}}$, and $f_{\mathrm{Si}^{+3}}$ are the ionization fractions of H^0, C^{+3}, and Si^{+3} ions, respectively.

For a photoionized gas, the ionization fractions of different species can be predicted given constraints on the ionization parameter of the gas, U, which is defined as the number of incident ionizing photon per hydrogen atom. To estimate the necessary ionization fraction corrections, we perform a series of photoionization calculations using Cloudy v.13.03 (Ferland et al. 2013). We consider a plane parallel slab of gas which is irradiated with the updated Haardt & Madau (2001) ionizing background radiation field (HM05 in Cloudy) at $z = 2.7$. We assume a solar chemical abundance pattern for the gas, and that the gas is at ionization equilibrium. Cloudy then calculates the expected ionization fractions and column densities

for H^0, C^{+3}, and Si^{+3} ions over a wide range of gas densities and metallicities. Because the radiation field is fixed, changing the gas density leads to a change in the U parameter.

To estimate the metallicity of the gas, we perform two sets of CLOUDY calculations for each absorber: one for an optically thin gas ($\log N(\mathrm{H\,I})/\mathrm{cm}^{-2} < 17.2$) and another for a gas that is optically thick ($\log N(\mathrm{H\,I})/\mathrm{cm}^{-2} > 17.2$) to ionizing photons. The adopted $N(\mathrm{H\,I})$ for these two sets of calculations are matched to the allowed minimum and maximum $N\,(\mathrm{H\,I})$ value of each absorber (see Section 4.2). We present an example of CLOUDY predictions in Figure 6.5, where in the top panels we plot the expected $N(\mathrm{C\,IV})/N(\mathrm{Si\,IV})$ ratio plotted versus U for a range of gas metallicities (from 0.001 to 0.1 solar metallicity). In this example, the calculation are performed for an optically thin gas with $\log N(\mathrm{H\,I})/\mathrm{cm}^{-2} = 16.5$ and optically thick gas with $\log N(\mathrm{H\,I})/\mathrm{cm}^{-2} = 17.7$, bracketing the range of allowed $N\,(\mathrm{H\,I})$ for Complex A.

It is clear from the top two panels of Figure 6.5 that the predicted column density ratio of C IV to Si IV are insensitive to gas metallicity over the wide range of U and metallicities probed, for optically thin and thick gases alike. Therefore, the ionization parameter of the gas can be constrained if the $N(\mathrm{C\,IV})/N(\mathrm{Si\,IV})$ ratio is known. Constraining U then enables us to constrain the expected ionization fractions of C^{+3} and Si^{+3} relative to H^0, as shown in the bottom panels of Figure 6.5.

For absorption complex A near LAEs A1 and A2, our Voigt profile fitting analysis yields a column density ratio of $\log N(\mathrm{C\,IV})/N(\mathrm{Si\,IV}) = 1.37 \pm 0.11$. Comparing the measured $N(\mathrm{C\,IV})/N(\mathrm{Si\,IV})$ to CLOUDY predictions, we find that the estimated U parameter of the gas ranges from as low as $\log U = -1.8 \pm 0.1$ for the minimum allowed $N\,(\mathrm{H\,I})$, $\log N(\mathrm{H\,I})/\mathrm{cm}^{-2} = 16.5$, to possibly as high as $\log U = -1.2 \pm 0.1$ for the maximum allowed H I column density of $\log N(\mathrm{H\,I})/\mathrm{cm}^{-2} = 17.7$. Adopting the range of allowed U allows us to determine the relative ionization fractions of C^{+3} and Si^{+3} to H^0. Adopting the solar chemical abundance pattern from Asplund et al. (2009), we estimate that the metallicity of the gas ranges from as low as $[\mathrm{M/H}] = -3.7 \pm 0.2$ for $\log N(\mathrm{H\,I})/\mathrm{cm}^{-2} = 17.7$, to no higher

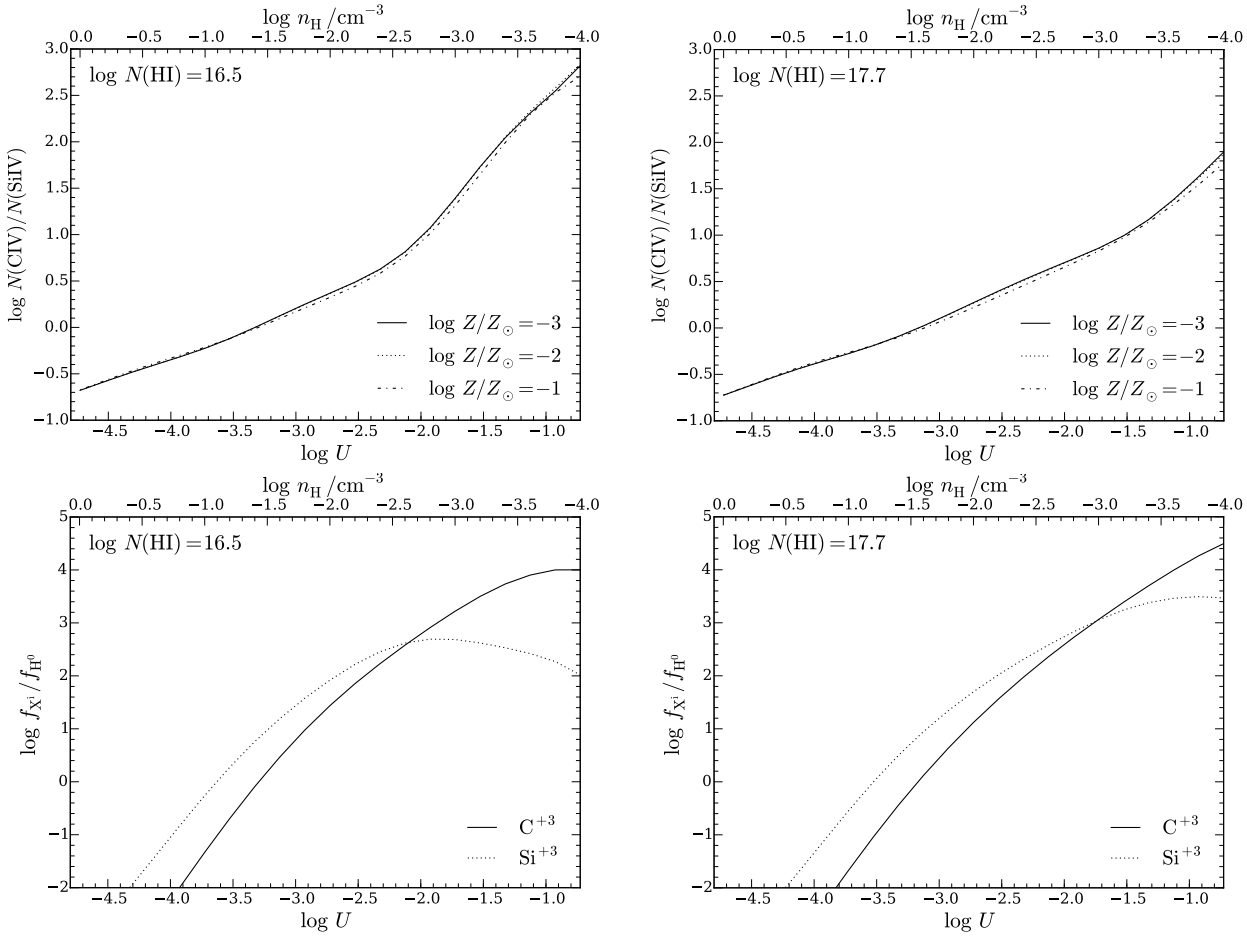

Figure 6.5: Example of predictions from CLOUDY photoionization calculations. The top two panels show the ionic column density ratio log N(C IV)/N(Si IV) as a function of ionization parameter U. The calculations are performed for for an optically thin gas ($\log N(\mathrm{H\,I})/\mathrm{cm}^{-2} = 16.5$) on the left and optically thick gas ($\log N(\mathrm{H\,I})/\mathrm{cm}^{-2} = 17.7$) on the right, matching the allowed minimum and maximum N (H I) of the absorption complex A (see Section 6.4.1). In the bottom two panels, the ionization fractions of C^{+3} and Si^{+3} relative to H^0 are plotted versus U for both optically thin and thick cases.

than $[\mathrm{M/H}] = -1.8 \pm 0.2$ for $\log N(\mathrm{H\,I})/\mathrm{cm}^{-2} = 16.5$.

For absorption complex B near LAE B1, the non-detection of Si II absorption implies a lower limit of $\log N(\mathrm{C\,IV})/N(\mathrm{Si\,IV}) > 0.83 \pm 0.07$. Based on our Cloudy calculations, the observed column density ratio requires $\log U > -2.1$, which in turn constrains the gas metallicity to $[\mathrm{M/H}] < -1.9$ for the allowed H I column density range of $\log N(\mathrm{H\,I})/\mathrm{cm}^{-2} = 16.5 - 17.8$.

It is instructive to compare the properties of these absorbers to similar H I absorption systems observed at $z = 2 - 3$. For both absorption complexes A and B, the the ionization parameter of the gas is constrained to $\log U \gtrsim -2$. This lower limit on U is consistent with the observed ionization states of Lyman limit systems (LLSs; $\log N(\mathrm{H\,I})/\mathrm{cm}^{-2} > 17.2$) at $z = 2-3$, for which $\log U \gtrsim -3$ is common (e.g., Fumagalli et al. 2016a; Lehner et al. 2016). Furthermore, the allowed metallicities of the gas, which range from as low as ~ 0.001 solar if the absorbers are optically thick, to no higher than ~ 0.02 solar if the absorbers are in the optically thin regime, are similar to the the range of metallicities seen in $z = 2 - 3$ LLSs (e.g., Fumagalli et al. 2016a; Lehner et al. 2016).[3]

6.5 Discussion

In the previous section, we characterize strong H I absorption systems at $d < 300$ kpc and $|\Delta v| < 500$ km s^{-1} from the three faint LAEs. It is also interesting to explore whether the gas is likely to be physically associated with these faint galaxies, and whether the galaxies themselves could be responsible for the origin of the gas. Because of the low completeness of the R08 spectroscopic observations of the field around DMS 2139−0405, it is challenging to link the absorption to a particular galaxy unambiguously, considering that it is possible

3. For our metallicity estimates, all the C IV and Si IV absorption are attributed to the total observed H I absorption. It is possible that these ionic metals originate in only a small but metal-rich portion of the H I-bearing gas complex. If such metal-rich pockets exist, the implication is that the large majority of the H I-bearing gas would be even more metal-poor than inferred here, and the conclusion that the observed gas complex is predominantly metal-poor ($\lesssim 0.01$ solar) would remain valid. In that regard, the metallicity constraints obtained in this section should be viewed as conservative upper limits to the mean chemical enrichment level in the bulk of the gas.

other faint galaxies occur at smaller d from the QSO than the nearest (in projection) LAE identified in our study (LAE A1 for Complex A and LAE B1 for Complex B). For the sake of argument, however, we begin our discussion under the assumption that the absorption is associated with the CGM of the LAE that is closest to it in projected distance. We will put this assumption under a closer examination in the next subsection.

6.5.1 Are the Observed Metals Due to Local Outflows?

We first investigate whether the gas can originate in a starburst-driven wind originating in the LAEs. Here we focus our discussion on Complex A, which is found closest to LAE A1 at $d = 87$ kpc. For a wind traveling with a velocity of $v_{\rm out} = 200$ km s^{-1}, which is typical of $z \sim 2.5$ LAEs (e.g., Trainor et al. 2015), a minimum of ~ 0.4 Gyr is required for outflowing material to reach a distance of ~ 90 kpc. This simple timing argument rests on the assumption that the outflow velocity can be maintained over cosmic time. In principle, if the galaxy had experienced a starburst episode at around $z \sim 3.3$ or earlier, enough time would have elapsed for the outflowing material to reach the QSO sightline at the epoch of the observations.

However, energetically it is a non trivial problem to propel gas to large distances from galaxies at high velocity (e.g., Gauthier & Chen 2012). Moreover, while down-the-barrel spectroscopic observations of $z > 2$ Lyman Break Galaxies (LBGs) and LAEs at have established the ubiquity of galactic-scale winds at high redshifts (e.g., Steidel et al. 2010; Hashimoto et al. 2013; Shibuya et al. 2014; Trainor et al. 2015), a primary caveat of the down-the-barrel method is that the galacto-centric distance of the gas is not well constrained. In the nearby universe, galactic-scale outflows have yet to be directly detected at $d \gtrsim 10$ kpc from starburst galaxies.

In spite of the lack of direct observation of outflowing gas far from galaxies, kinematic and chemical arguments have been put forward to link outflows with absorbing gas at $d \gtrsim 50$ kpc from both low- and high-redshift galaxies (e.g., Borthakur et al. 2013; Crighton et al.

2015; Muzahid et al. 2015). In particular, outflowing gas is expected to exhibit a large velocity width and a high chemical enrichment level, due to the supernova origin of a super-galactic wind. Observations of blue-shifted ISM absorption lines in lensed LBGs at $z \sim 2$ demonstrate that a high metallicity of $0.4 - 0.8$ solar is common in outflows (e.g., Pettini et al. 2002; Dessauges-Zavadsky et al. 2010).

While no direct chemical abundance measurement is available for LAE A1, the lack of continuum counterpart of this LAE ($r > 26.6$, $K_s > 24.5$) implies that the host galaxy is intrinsically faint and low-mass ($L \lesssim 0.1L^*$, $M_{\rm star} \lesssim 10^9\,{\rm M}_\odot$). Based on the mass-metallicity relation at $z \sim 2$, the expected gas-phase metallicity in the ISM of a $M_{\rm star} \sim 10^8\,{\rm M}_\odot$ galaxy is $0.1 - 0.2$ solar (e.g., Steidel et al. 2014; Sanders et al. 2015). The expected ISM abundance is similar to the mean metallicity of 0.2 ± 0.1 solar estimated from nebular emission lines in stacked spectra of faint $z \sim 2.5$ LAEs (Trainor et al. 2016).

In contrast, the inferred metallicity of Complex A is < 0.02 solar, which is at least an order of magnitude lower than both the observed metallicities in high-redshift outflows and the inferred chemical abundance in the ISM of faint LAEs. The stark difference between the chemical enrichment level of the gas and those expected in outflowing material and ISM gas indicates that a starburst-driven wind is unlikely to be the origin of the observed gas.

Next, we examine whether the observed gas in Complex A is likely to be situated in the CGM of LAE A1. The total carbon mass enclosed within a projected distance d in the CGM is $M_{\rm C} = \pi d^2 \langle N({\rm C\,IV})\rangle\, 12 m_{\rm H} f_{\rm cov}/f_{\rm C^{+3}}$, where $\langle N({\rm C\,IV})\rangle$ is the mean C IV column density, $f_{\rm cov}$ is the mean gas covering fraction and $f_{\rm C^{+3}}$ is the ionization fraction of triply ionized carbon. Assuming that that the radial profile of C IV absorption within $d \sim 90$ kpc has a mean column of $\langle N({\rm C\,IV})\rangle = 10^{14.2}{\rm cm}^{-2}$ (which is the measured total C IV column density in Complex A), and adopting $f_{\rm C^{+3}} = 0.2$ based on our CLOUDY calculations, we estimate a total CGM carbon mass of $M_{\rm C} \sim 2 \times 10^6\,{\rm M}_\odot\,(f_{\rm cov})$. In a similar fashion, the observed $N({\rm Si\,IV})$ implies a total silicon mass of $M_{\rm Si} \sim 3 \times 10^5\,{\rm M}_\odot\,(f_{\rm cov})$. For $f_{\rm cov} = 0.5$, which is typical at similar d from both low-redshift dwarf/sub-L^* galaxies and high-redshift LBGs

(e.g., Bordoloi et al. 2014; Liang & Chen 2014; Rudie et al. 2019), the estimated total carbon and silicon masses in the CGM are $\sim 1 \times 10^6\,M_\odot$ and $\sim 1.5 \times 10^5\,M_\odot$, respectively.

Can the galaxy produce the estimated amount of CGM metals? Assuming the galaxy has maintained a constant star-formation rate of $0.1\,M_\odot\,yr^{-1}$ (see Section 6.3) over time, and adopting a supernova carbon yield of 0.0088 $M_\odot$ per solar mass of star formation (Peeples et al. 2014), we estimate that a total mass of $\sim 9 \times 10^4\,M_\odot$ in carbon is produced over a ~ 0.1 Gyr timescale. The recent metal production budget in the galaxy is far below the estimated total carbon mass to explain the observed metal enrichment of the surrounding IGM through local galactic feedback. This exercise suggests that the absorbing gas is unlikely to originate in any form of CGM around the individual LAEs.

6.5.2 Evidence for Accretion from a Cosmic Web Filament?

In Figure 6.6, we present gas-phase metallicity measurements versus d for $z > 2$ galaxies, including LAEs in our study. For comparison, we indicate the range of metallicities seen in the $z \sim 2.5$ IGM in the shaded gray area (Simcoe et al. 2004).The inferred low metallicities of absorbers in our study (no higher than 0.02 solar and possibly lower than 0.001 solar metallicity) indicate that the gas originates in the more metal-poor IGM. Indeed, chemical enrichment level in the IGM at $z \sim 2.5$ is characterized by a median metallicity of [M/H] $= -2.8$ (or 0.002 solar) and a dispersion of 0.75 dex (e.g., Schaye et al. 2003; Simcoe et al. 2004), in excellent agreement with the metallicity constraints for absorbers in our study.

Furthermore, the presence of multiple LAEs within a close proximity from each other along the slit implies that the emitters may be situated in a coherent structure. Using the field LAE luminosity function at $z \sim 3$ from Drake et al. (2017), we expect to detect only ~ 0.3 LAEs above the detection limit in the observations of R08, within a cosmological volume of ~ 30 Mpc^3 defined by a slit width of 2 arcsec, a slit length of 453 arcsec, and a redshift range of $z = 2.74 - 2.78$ (≈ 3200 km s^{-1} in velocity space, bracketing the redshifts of the Complex A and Complex B). Within this volume, the probability that three LAEs

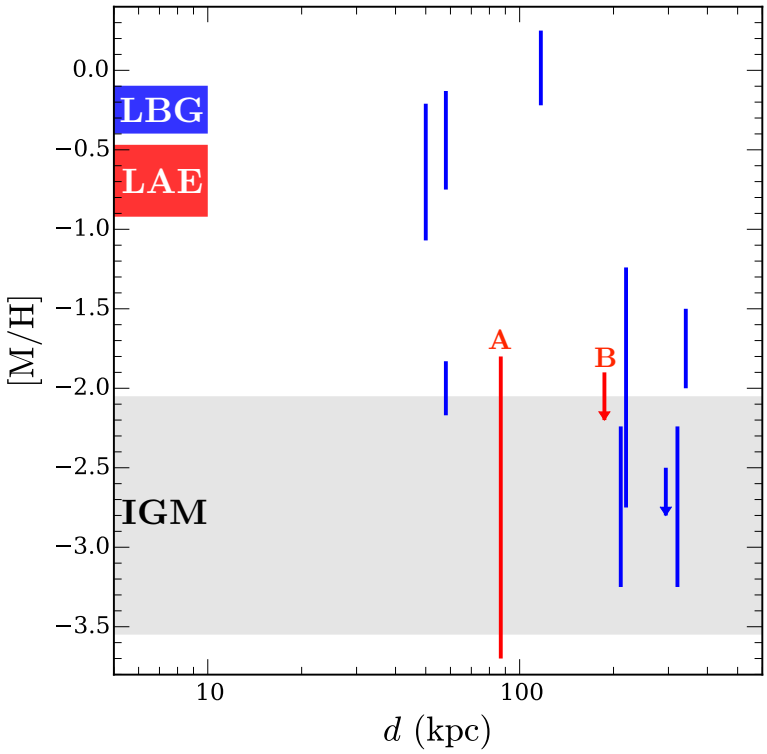

Figure 6.6: Gas-phase metallicity measurements versus projected distance for $z > 2$ galaxies. Constraints for gas metallicity in the vicinity of LAEs in our study are shown in vertical red bar and downward arrow, labeled by the absorption complex. Note that while Complex A is shown here at $d = 87$ kpc from LAE A1, another emitter LAE A2 is situated at $d = 161$ kpc from the sightline. Meanwhile, the red rectangle at $d < 10$ kpc marks the mean metallicity in the ISM of LAEs (Trainor et al. 2016), whereas the blue rectangle shows the typical ISM abundance level seen in LBGs (e.g., Pettini et al. 2002; Dessauges-Zavadsky et al. 2010; Strom et al. 2018). The range of metallicities seen in the $z \sim 2.5$ IGM is shown in the shaded gray area (Simcoe et al. 2004). Other absorption line measurements at $d > 10$ kpc from $z > 2$ galaxies are shown in vertical blue bars (Simcoe et al. 2006; Crighton et al. 2013, 2015). The low metallicities seen at $d \sim 100 - 200$ kpc from faint LAEs in our study are consistent with the chemical enrichment level seen in the IGM at the same epoch.

occur by random chance is very low, $\sim 3 \times 10^{-3}$. The probability that the grouping of three LAEs should occur within projected $\pm$300 kpc from each other is even lower, $\sim 1 \times 10^{-4}$, thereby suggesting that the LAEs are part of a spatially coherent structure.

The most plausible explanation for the unique arrangement of Lyα emitters and absorbers in our study (Figure 6.1) is that the spectrograph slit in R08 was serendipitously aligned (at least partially) with a cosmic web filament at $z \sim 2.8$, thereby explaining the presence of multiple LAEs and Lyα absorbers along a narrow line extending more than 200 kpc in projection (see also Fumagalli et al. 2016b). Several features of the absorbing gas in Complex A near LAEs A1 and A2 provide further support for this scenario.

First, the observed line-of-sight velocity spread of the multi-component C IV absorption in Complex A is low, with a statistical dispersion of $\sigma = 32$ km s^{-1}(see bottom panel of Figure 6.3). This velocity width is significantly smaller than those observed in down-the-barrel outflows from $z = 2 - 3$ galaxies ($\gtrsim 100$ km s^{-1}, e.g., Trainor et al. 2015; Jones et al. 2018) and expected from dynamical motion in the CGM (the line-of-sight velocity dispersion for virialized motion is $\sigma_{\rm h} \approx 60 - 130$ km s^{-1} in a $M_{\rm h} = 10^{11-12}\,{\rm M}_{\odot}$ halo). However, the observed narrow C IV width is consistent with the expected velocity spread for a quiescent, ~ 100 kpc scale gaseous filament that is simply moving with the Hubble flow at this redshift.[4] Secondly, the absorption is flanked on opposite sides of the slit by the two LAEs (top panel of Figure 6.3), which are separated by a projected 248 kpc and are consistent within uncertainties with having zero systemic velocity offset from each other. Furthermore, the mean Doppler parameter for the C IV absorption components in Complex A is $\langle b \rangle = 9.8 \pm 1.0$ km s^{-1}, which is very similar to the mode of the C IV Doppler parameter distribution predicted by simulations of gas accretion in cosmic filaments (e.g., Rauch et al. 1997). Together, these kinematic and morphological features suggest that the absorbing gas originates in a large and dynamically cold structure, such as that of a gaseous filament.

Recent hydrodynamical simulations of galaxy formation predict that cosmological accre-

4. The Hubble parameter is $H = 287\,{\rm km\ s^{-1}\ Mpc^{-1}}$ at $z = 2.77$, for the adopted cosmology in this work.

tion from the IGM onto high-redshift galaxies proceed along filaments that often manifest as low-metallicity LLSs (e.g., Fumagalli et al. 2011; van de Voort et al. 2012; Faucher-Giguère et al. 2015), in agreement with the observed properties of the absorption complexes in our study. In this physical picture, infalling streams of gas can proceed along such filamentary structure and fuel star-formation activity in the LAEs. This feeding scenario is further supported by the prominent blue peak that is observed in the Lyα emission line profile of LAE A1 (R08), an indication that the Lyα-emitting gas is flowing onto the galaxy (e.g., Verhamme et al. 2006). In conclusion, the observed properties of the absorbers and the unique orientation of faint LAEs and the background sightline are in good agreement with the predictions of infalling IGM gas along cosmic filaments.

6.6 Conclusions

Using high-resolution optical echelle spectrum of QSO DMS 2139−0405 we studied the gaseous environment of three faint LAEs ($L_{\mathrm{Ly}\alpha} \approx 2 \times 10^{41}$ erg s^{-1}) at $z = 2.7 - 2.8$. Strong H I absorption systems are found at d < 300 kpc and $|\Delta v| < 500$ km s^{-1} from the LAEs, allowing us to investigate the connection between faint, low-mass galaxies ($L \lesssim 0.1\,L^*$, $M_{\mathrm{star}} \lesssim 10^9\,\mathrm{M}_\odot$) and the IGM at this redshift. Our findings are summarized below.

1. We find that the absorbers have H I column densities which are consistent with being partial or full LLSs, $\log N(\mathrm{H\,I})/\mathrm{cm}^{-2} = 16 - 18$. The observed metal abundances of the gas are low, no higher than 0.02 solar metallicity if the absorbers are optically thin and possibly as low or lower than ~ 0.001 solar metallicity if the absorbers are optically thick LLSs. The inferred metallicities and ionization states of the gas are comparable to what have been observed in $z = 2 - 3$ LLSs.

2. Focusing on Complex A, which is found at $d = 87$ and 161 kpc from LAEs A1 and A2, we examined the possibility that the gas originates in a locally enriched CGM around one of the galaxies. While a galactic wind with a constant velocity of 200 km s^{-1} may

be formally able to cover a distance of ~ 90 kpc and reach the QSO sightline in ~ 0.4 Gyr, direct evidence for the existence of outflows at large distances remains elusive (see Section 6.1). Furthermore, given the inferred low SFR of the LAE, the expected metal production budget is insufficient to explain the observed metals as having been produced and expelled by these galaxies within the last ~ 0.1 Gyr.

3. The low metallicities of the gas are consistent with the gas originating in the general IGM. The spatial alignment of the LAEs along the slit, and the alignment of said LAEs and the absorbers in velocity space, suggest that we may be looking perpendicularly at a filamentary structure spanned by the galaxies over at least ~ 250 kpc in projection. The range of $N(\mathrm{H\,I})$ of the gas, its low metallicity and line-of-sight velocity dispersion, together with the observed mean C IV Doppler parameter values and presence of faint galaxies in the vicinity of the absorbers, are all in good agreement with the predictions for infalling gas along cosmic filaments (Rauch, Haehnelt & Steinmetz 1997; Fumagalli et al 2011, van de Voort et al 2012). The prominence of a blue Lyα emission peak in one of the LAEs (R08) is consistent with radiative transfer through infalling gas, making this a rare occasion where we can observe an accretion stream together with its final destination.

We expect that future spectroscopic surveys of QSO fields in search of faint line emitters, taking advantage of wide-field integral field spectrographs and coupled with very deep imaging of these fields, will provide new insights into the gaseous environment of low-mass galaxies at high redshifts and offer critical information on the relative importance and roles of feeding and feedback during the cosmic high noon.

CHAPTER 7

EPILOGUE

7.1 Concluding Thoughts

The work presented in this dissertation has resulted in significant insights into the physical connection between galaxies and and their gaseous halos, by specifically focusing on halos of massive galaxies showing no sign of recent star-formation activity. We began our journey in Chapter 2, which investigated the inner halos of three massive elliptical lens galaxies at $z = 0.4 - 0.7$. Despite the similarities among the three galaxies, dramatic differences are observed in the gas absorption properties, which implies that cool gas in the inner halos of massive elliptical galaxies is clumpy with partial covering fraction, consistent with the observed trend at larger scales ($d \sim 100$ kpc) in the halo. More importantly, whenever detected the gas exhibits a super-solar Fe/α abundance pattern, indicating that the gas originates in-situ in the galaxy's ISM due to the required high contribution ($\gtrsim 20\%$) from SNe Ia to its enrichment history. This conclusion is strengthened by UV spectroscopic observations of one of these lens systems (Chapter 4), which demonstrate that this Fe-rich gas is primarily neutral, with inferred high metallicity and density which are consistent with an ISM origin.

The discovery of Fe-rich cool gas at small projected distances from massive ellipticals underscores the important role that old stellar populations within these galaxies may play in heating the halos with SNe Ia. At the same time, this finding also raises an interesting question regarding the extent of SNe Ia-driven feedback in these quiescent halos. In Chapter 3, we investigated spatial variations in the chemical composition of the gaseous halos of distant galaxies and found that that the Fe/α ratio declines with increasing distance from quiescent galaxies. Specifically, our analysis shows that SNe Ia-driven chemical enrichment is relatively localized in inner halos at $d \lesssim 50$ kpc. In contrast, gas in the outer halos ($d \gtrsim 100$ kpc) of quiescent galaxies exhibits an α-enhanced enrichment pattern that is consistent with

more chemically primitive gas originating in the IGM (see also Chapter 6 for a high-redshift example). The multiple physical origins of heavy metals in the CGM are also highlighted by large variations (a factor of ten or more) in the inferred gas metallicities within individual halos of massive elliptical galaxies as well as the observed kinematic mismatches between low- and high-ionization gas (Chapter 5).

Chapter 5 presented a detailed ionization analysis of the gaseous halos of massive ellipticals, which allowed us to calculate the total surface mass density of cool gas in the CGM. A particularly surprising finding from this analysis is that the typical massive elliptical galaxy at $z \sim 0.5$ is surrounded by $M_{\rm cool} \sim 10^{10}\,{\rm M}_{\odot}$ of cool gas within the virial radius of its halo, an amount comparable to the cool CGM mass of L^* star-forming galaxies. At the same time, the observed radial velocity dispersion of the cool gas clumps is only $\approx 60\%$ of what is expected from virial motion. Our findings in Chapter 5 paint a physical picture in which cool clumps in massive quiescent halos condense from the hot halo due to local thermal instabilities, and are subject to dissipative interactions which cause them to fall toward the galaxy. Because the expected cloud evaporation timescale is significantly shorter than the typical infall time in these massive halos (Section 5.5.2), the implication is that cool clumps travel only a relatively small distance within the halo before they are destroyed.

The findings presented in preceding chapters, when considered together, provide a plausible explanation for the continuing quiescence of massive elliptical galaxies despite their abundant gas reservoirs. While abundant cool gas reservoirs exist in the outer CGM and the IGM, interactions with the hot halos prevent most of cool clouds formed at large distances from successfully accreting into the galaxy. Meanwhile, cool clouds originating closer to the galaxy such as in the inner halo/ISM are subject to energetic feedback from the galaxy itself, including SNe Ia, thereby preventing excessive cooling that would otherwise trigger star formation.

At the same time, there is much yet to be learned about the relationship between massive quiescent galaxies and their gas reservoirs. To illustrate the prospects for future progress in

the subject, I will briefly discuss two possible research directions to which we can go beyond the work presented in this dissertation.

First, while the presence of Fe-rich gas in the cool ISM of massive ellipticals indicates a significant contribution from SNe Ia to its chemical enrichment, it is not yet clear whether SNe Ia themselves are the dominant feedback mechanism in these massive galaxies. The importance of SNe Ia-driven feedback can be gauged by searching for a relationship between gas-phase chemical abundance pattern *and* the thermal state and ionization state of the ISM. If SNe Ia heating is dominant, gas exhibiting higher Fe/α ratios should also be hotter, more turbulent, and more highly ionized. Such investigation requires a larger sample of massive elliptical galaxies probed by background QSOs at small projected distances. The latest generation of wide-field imaging surveys have resulted in a large number of newly discovered gravitationally lensed QSO systems, making it feasible for the first time to construct a large sample of massive elliptical galaxies for this purpose.

Secondly, the role that galaxy environment plays in shaping the properties of the gaseous halos of massive elliptical galaxies is largely unexplored. While recent observations of local ellipticals suggest that recent gas-rich mergers may provide massive quiescent galaxies with a new supply of cool gas (Davis et al. 2019), it remains to be seen whether galaxy interaction is the primary mechanism for gas acquisition. The advent of deep and highly complete galaxy surveys in the vicinities of high-redshift QSOs, such as that being carried out by the COS Ultraviolet Baryon Survey (CUBS) collaboration that I am a part of, will result in a large sample passive galaxies with well-characterized environmental properties. In the near future, we will be able to ascertain the impact of galaxy environment on the gaseous halos of massive galaxies on both small and large scales.

In the remainder of this chapter, I present my current work to better understand the physical properties in the ISM of distant massive elliptical galaxies.

7.2 An Investigation of the Multiphase Interstellar Medium in a Massive Elliptical Galaxy at $z = 0.4$

To provide additional insights into the nature of diffuse gas detected at small projected distances from distant massive elliptical galaxies, I have embarked on a new observational campaign of one of the lensed QSO systems previously studied in Chapters 2 and 4 of this dissertation, HE 0047−1756. To summarize our previous findings of this system, the QSO HE 0047−1756 is doubly lensed by a massive elliptical galaxy at $z = 0.408$ (Figure 2.2, top panel). At the same time, ultra-strong Mg II absorptions ($W_r(2796) > 3.6$ Å) are found along two lensed QSO sightlines probing opposite sides of the galaxy at $d = 4.6$ kpc (or 1.8 r_e) and $d = 3.3$ kpc (or 1.3 r_e), each resolved into $11 - 15$ distinct components spanning a large velocity spread of $\Delta\, v \approx 600 - 700$ km s^{-1}. A particularly striking feature of the absorbing gas is the uniform, super-solar (Fe/Mg) abundance pattern, [Fe/Mg] $\gtrsim 0.1$, across the entire Δv of the absorbing gas in each sightline. Such high Fe/Mg ratios indicate a significant contribution ($\gtrsim 20\%$) from Type Ia supernovae (SNe Ia) to the chemical enrichment history. Furthermore, it suggests that the absorbing gas originates in the ISM of the massive elliptical lens galaxy, where the gas has been highly enriched and heated by SNe Ia ejecta (Chapter 2).

In Chapter 4, we reported longslit UV spectroscopic observations of both lensed QSO images. Based on the observed hydrogen Lyman series lines along the two lensed sightlines at the redshift of the elliptical lens galaxy, we measured H I column densities of $\log(\mathrm{H\,I}) = 19.6 - 19.7$ at both locations separated by 8 projected kpc, comparable to what is seen in 21-cm observations of nearby ellipticals. Furthermore, these measurements allowed us to constrain the gas metallicity to be $\gtrsim 1/3$ solar at both locations.

The low-resolution FUV spectra presented in Chapter 4 also revealed numerous additional strong absorption features at the redshift of the lens galaxy (Figure 4.1), likely arising from various ionic species probing a wide range of ionization states in the ISM of the lens. However,

the low spectral resolution of the data prevented a more detailed investigation of the line profiles, which is necessary to gain further insights into the physical conditions, thermal state, and ionization state of the gas (as demonstrated in Chapter 5 for CGM gas around massive ellipticals). In order to constrain the physical conditions of the gas and investigate the possible multi-phase nature of the ISM of this unique system, we recently obtained high-resolution FUV spectra of the brighter lensed QSO image of HE 0047−1756 using the *Hubble Space Telescope (HST)*.

7.2.1 Observations and Data Reduction

New FUV spectra of the brighter lensed image of the doubly lensed QSO HE 0047−1756 were obtained with the Cosmic Origins Spectrograph (Green et al. 2012) onboard *HST* during our own observing program (PID: 15250) in December 2018. *HST*/COS with the G130M and G160M gratings provided a moderately high resolution (FWHM $\approx 20\,\mathrm{km\ s^{-1}}$) over a contiguous wavelength coverage between $\lambda \approx 1130$ Å and $\lambda \approx 1790$ Å. The total integration time of the observations was 27.1 ks, divided into 22 individual exposures spread over three separate *HST* visits. The COS data were downloaded from the *HST* archive and processed further using our custom software. These additional data reduction steps involved a recalibration of the COS wavelength solution, which were previously described in Chapter 5 and Chen et al. (2018). To summarize, the first step was to correct the relative offsets between different exposures, using a low-order polynomial function that describes the offsets of common narrow absorption features found in all exposures. Next, different exposures were combined and an absolute wavelength correction was performed on the combined spectrum by registering non-saturated, low-ionization Galactic absorption lines to their known laboratory wavelengths in vacuum. The final COS spectrum of HE 0047−1756*A* has a mean S/N $\approx 10-15$ per resolution element over the full wavelength range of the spectrum ($1130-1790$ Å).

7.2.2 Detection of Molecular Hydrogen at $d = 4.6$ kpc from the Lens

A large number of absorption features consistent with the Lyman- and Werner-bands of molecular hydrogen (H_2) are detected in the COS spectrum of HE 0047−1756A at $z = 0.406$ or ≈ 430 km s^{-1} blueward of the systemic redshift of the lens galaxy. The H_2 absorption coincides in velocity space with the strongest absorption component identified in low-ionization metal species Mg II, Mg I, Fe II, and Ca II in Chapter 2 (Table 2.6). We show the H_2 absorption profiles in Figure 7.1, where we plot all detected H_2 lines which are not blended or contaminated by unrelated lines, grouped by their rotational J levels. The observed H_2 absorption lines arise from multiple rotational levels, from $J = 0$ to $J = 5$.

Preliminary H_2 Absorption Analysis

To constrain the H_2 column densities of the different rotational levels, we performed a forward modeling of the full Lyman and Werner bands of molecular hydrogen using a custom software. We adopted the H_2 line list compiled by Patrick Petitjean (private communication), which incorporate molecular data for H_2 Lyman- and Werner-band transitions reported in a number different studies (Bailly et al. 2010; Ubachs et al. 2007; Abgrall et al. 1993). We included all uncontaminated absorption transitions from the different rotational levels of H_2 in the absorption analysis, as shown in Figure 7.1. We first generated a model absorption spectrum of the Lyman and Werner bands using the minimum number of components necessary to achieve a satisfactory fit. For each absorption component, the Voigt profile is uniquely defined by three free parameters: the velocity shift of the line centroid from the systemic redshift of the lens, dv_c, the absorption column density log N_c, and the Doppler parameter, b_c. To reduce the number of free parameters, we tied the velocity centroid dv_c and Doppler parameter b for all H_2 transitions that were included in the fit. Furthermore, different transitions from a given rotational J level were constrained to have the same gas column density. Next, the H_2 model absorption spectrum was convolved with the published COS line spread function that is relevant to the epoch of observations (lifetime position 4),

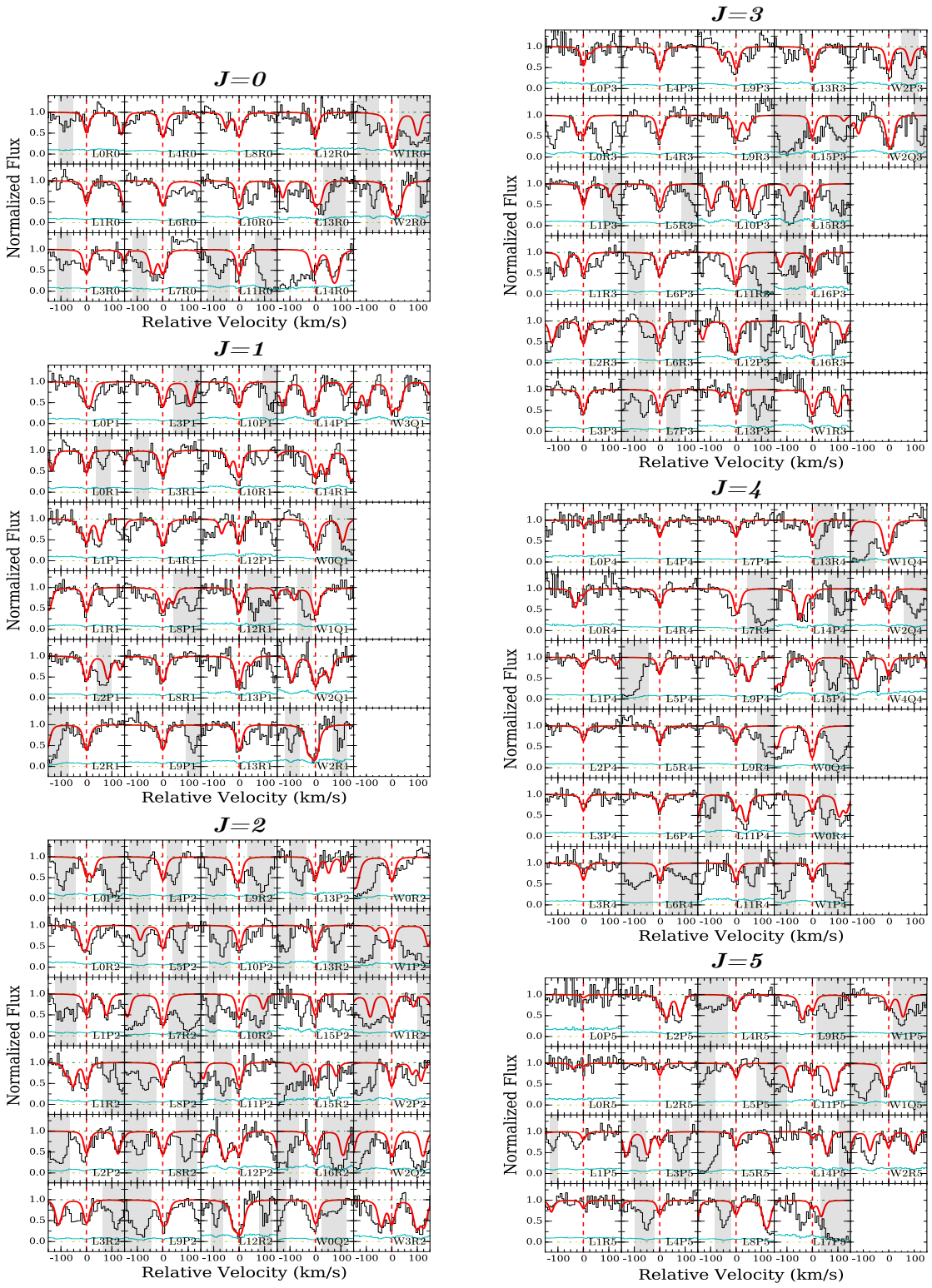

Figure 7.1: Continuum-normalized absorption profiles of H_2 absorption transitions, grouped by different rotational J levels, arising in image A of HE 0047−1756 at $d = 4.6$ kpc from the massive elliptical lens. Zero velocity marks the redshift of the H_2 absorption component identified in the Voigt profile analysis, $z_{\rm abs} = 0.40599$. The 1-σ error spectrum is included in cyan, above the zero-flux level. Contaminating features have been grayed out for clarity. The best-fit Voigt profiles for the full H_2 Lyman and Werner series are plotted in red curves.

Table 7.1: Voigt profile fitting results for the H_2 absorption detected at $d = 4.6$ kpc from the massive elliptical lens galaxy of HE 0047−1756

Component	J	dv_c[a] (km s^{-1})	$\log N_c/\mathrm{cm}^{-2}$	b_c (km s^{-1})
1	total	-429 ± 1	17.1 ± 0.4	4 ± 1
	0	-429	16.3 ± 0.4	4
	1	-429	16.9 ± 0.4	4
	2	-429	16.3 ± 0.3	4
	3	-429	16.3 ± 0.3	4
	4	-429	15.0 ± 0.3	4
	5	-429	14.7 ± 0.3	4
	6	-429	< 14.2[b]	4

[a] Velocity shift from the systemic redshift of the lens galaxy at $z = 0.408$.
[b] 2-σ upper limit.

and subsequently binned to the pixel resolution of the COS data. Finally, this theoretical spectrum was compared to the continuum-normalized COS spectrum, and the best-fitting model was found via χ^2 minimization.

Our analysis indicates that the best-fit model is achieved for a single-component H_2 absorption profile centered at $dv_{\rm abs} = -429 \pm 1$ or $z_{\rm abs} = 0.405985 \pm 0.000005$, with a narrow Doppler linewidth of $b = 4 \pm 1$ km s^{-1} and a total H_2 column density of $\log N(H_2)/\mathrm{cm}^{-2} = 17.1 \pm 0.4$. We summarize the results of the Voigt profile analysis for the H_2 absorption in Table 7.1, where we also present the best-fit column densities for each individual rotational J levels, from $J = 0$ to $J = 5$. For rotational level $J = 6$, which does not exhibit any significant absorption, we estimated the 2-σ upper limit on the gas column density for a $b = 4$ km s^{-1} absorption profile, based on the upper limit on the rest-frame equivalent width of the strongest $J = 6$ transition covered by the COS data. In addition, we present in Figure 7.1 the continuum-normalized absorption profiles of different H_2 transitions grouped by rotational J levels, over-plotted with the combined best-fit model for the Lyman- and Werner-band absorption.

Molecular Gas Fraction

The molecular gas mass fraction can be estimated by the following equation,

$$f_{\rm H_2} = \frac{2\,N({\rm H_2})}{2\,N({\rm H_2}) + N({\rm H\,I})}. \tag{7.1}$$

In Chapter 4, we reported a total $N(\mathrm{H\,I})$ of $\log N(\mathrm{H\,I})/\mathrm{cm}^{-2} = 19.7 \pm 0.2$ for the absorber along HE 0047−1756A, based on a full Lyman series fit and an independent curve-of-growth analysis on the low-resolution STIS FUV spectrum of the lensed QSO image. Using the higher-resolution COS spectrum of the QSO image, we have revisited the Lyman series analysis and obtained a revised total H I column density of $\log N(\mathrm{H\,I})/\mathrm{cm}^{-2} = 19.8 \pm 0.1$.

The strong low-ionization absorber found along HE 0047−1756A are resolved into 15 individual kinematic components, as observed in low-ionization metal absorption profiles in the high-resolution MIKE spectrum of the QSO sightline (the left panels of Figure 2.4 in Chapter 2). In principle, different components can have different $f_{\rm H_2}$ values. However, while the total H I column density of the system can be robustly measured due to the strong damping wing of the Lyα profile, it is not possible to constrain the H I column densities of the individual components directly because the H I Lyman series are heavily saturated.

To calculate a conservative lower bound on $f_{\rm H_2}$, we assume that all the H I gas is associated with all the H_2 in the system. This assumption yields a lower bound on the molecular gas mass fraction of $\log\,(f_{\rm H_2})_{\rm lower} = -2.4 \pm 0.4$. To estimate the upper bound on $f_{\rm H_2}$, note from Table 2.6 that component 1, which coincides in velocity space with the observed H_2 absorption, contains 40 − 45% of the total column densities of the low-ionization metals Mg I, Mg II, and Fe II. If we assume that different components have similar metallicities and dust content, which is not entirely unjustified considering the relatively uniform Fe/Mg relative abundance ratio across the 15 components (Figure 2.10, top panel), then the inferred H I column density of component 1 is $\log N(\mathrm{H\,I})/\mathrm{cm}^{-2} \approx 19.4$. Consequently, this estimate would imply an upper bound on $f_{\rm H_2}$ of $\log\,(f_{\rm H_2})_{\rm upper} = -2.0 \pm 0.4$.

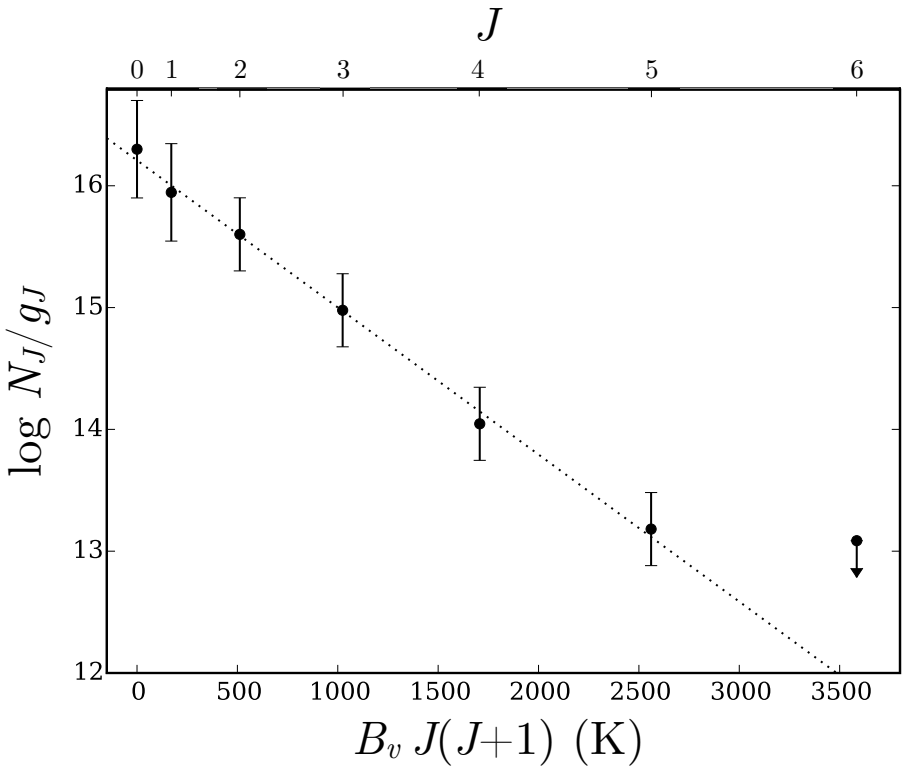

Figure 7.2: Excitation diagram for the different rotational levels of H_2 gas detected in absorption along HE 0047−1756*A* at $d = 4.6$ kpc from the massive elliptical lens. Assuming that the populations of H_2 molecules in different rotational levels follow a Boltzmann distribution, the observed ratios are well-described by a single excitation temperature of $T_{\rm ex} = 360 \pm 15$ K (shown in dotted line).

Excitation Temperature of the H_2-Bearing Gas

The relative populations of different rotational levels of H_2 can be described by a Boltzmann distribution (e.g., Draine 2011),

$$\frac{N_{\rm J}}{N_{\rm J=0}} = \frac{g_{\rm J}}{g_{\rm J=0}} \exp\Big(- \frac{B_v\, J(J+1)}{T_{\rm ex}} \Big), \tag{7.2}$$

where $N_{\rm J}$ is the H_2 column density for the rotational level J, $T_{\rm ex}$ is the excitation temperature of the molecular gas, and $B_v = 85.4$ K. The statistical weight $g_{\rm J}$ is $(2J{+}1)$ for even-numbered J levels or $3(2J+1)$ for odd-numbered J levels.

Figure 7.2 shows the H_2 excitation diagram for this system, shown for rotational states $J = 0$ to $J = 5$. By comparing the observed column densities of different J levels with

the expectations from a Boltzmann distribution, we find that the data are consistent with a single excitation temperature of $T_{\rm ex} = 360 \pm 15$ K (dotted line). The fact that a single excitation temperature describes all the observed rotational levels well in this system suggests that the level populations are thermalized, and that the gas is at a sufficiently high density that collisions are the dominant excitation and de-excitation mechanism for the different rotational energy levels of H_2. In this case, the excitation temperature likely represents the kinetic temperature of the H_2-bearing gas.

7.2.3 Highly Ionized Metals at $d = 4.6$ kpc from the Lens

In Section 4.3, we noted the presence of possible absorption features from of high-ionization metal lines in the FUV STIS spectrum of HE 0047−1756*A*. The presence of highly ionized gas within projected 5 kpc from the galaxy, together with the presence of low-ionization, neutral, and molecular gas phases (e.g., Fe II, H I, and H_2), would indicate a multiphase nature of the ISM in this massive elliptical galaxy. However, the low resolution of the STIS spectrum ($R \sim 1100$ or $\delta v \sim 270$ km s^{-1}) prevented a more detailed investigation into the nature of the supposed high-ionization gas, due to the unresolved kinematics of individual absorption profiles and the possibility of blending with neighboring absorption lines. In contrast, the high-resolution COS spectrum ($R \sim 18000$ or $\delta v \sim 17$ km s^{-1}) of HE 0047−1756*A* reveal the kinematic structure of the gas by resolving individual absorption profiles, allowing precise measurements of the kinematics and column densities of the highly ionized gas.

As shown in the top three panels of Figure 7.3, the new COS spectrum confirms the presence of highly ionized gas in the ISM of the massive elliptical lens galaxy, as traced by prominent high-ionization metal species O VI and N V. We performed a combined Voigt profile analysis of the O VI λ1031 transition and the N V $\lambda\lambda$1239, 1243 doublet, tying both the velocity structures and Doppler linewidths of the two ionic species. Our analysis identified a complex kinematic structure comprising a minimum of 5 broad components ($b \approx 25 -$

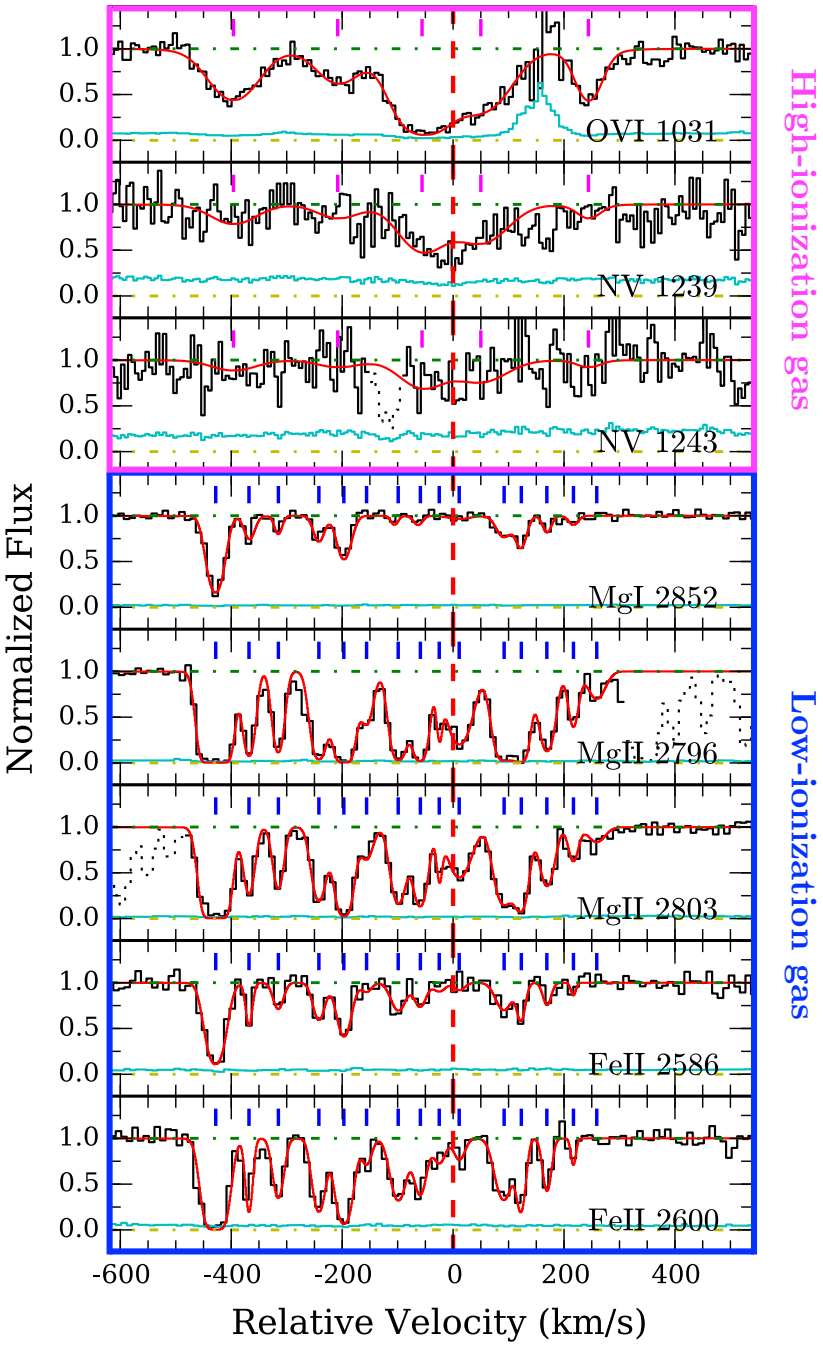

Figure 7.3: Continuum normalized absorption profiles of different high- and low-ionization metal transitions along HE 0047−1756A at d = 4.6 kpc from the massive elliptical lens. Zero velocity corresponds to the systemic redshift of the lens galaxy, z = 0.408. The 1-σ error spectrum is included in cyan. Contaminating features have been dotted out for clarity. The magenta tick marks at the top of the first three panels indicate the location of individual components for the high-ionization gas identified in the Voigt profile analysis (see Section 7.1.3), with the best-fit Voigt profile models included in red. For comparison, individual components of the low-ionization gas is shown marked with the blue tick marks in the bottom five panels (Section 2.4.1).

Table 7.2: Voigt profile fitting results for highly ionized gas detected at $d = 4.6$ kpc from the massive elliptical lens

Component	Species	dv_c (km s^{-1})	$\log N_c$	b_c (km s^{-1})
1	O VI	-396.4 ± 3.5	14.38 ± 0.03	51.4 ± 4.9
	N V	-396.4	13.75 ± 0.12	51.4
2	O VI	-208.3 ± 5.5	14.08 ± 0.06	46.1 ± 8.7
	N V	-208.3	13.53 ± 0.18	46.1
3	O VI	-56.1 ± 5.4	14.94 ± 0.05	50.0 ± 5.0
	N V	-56.1	14.20 ± 0.05	50.0
4	O VI	50.0 ± 12.7	14.57 ± 0.10	58.5 ± 11.8
	N V	50.0	14.14 ± 0.05	58.5
5	O VI	243.9 ± 3.0	14.18 ± 0.06	25.4 ± 4.6
	N V	243.9	13.33 ± 0.22	25.4

60 km s^{-1}) and spanning ≈ 640 km s^{-1} in line-of-sight velocity.[1] The observed total column densities of these highly ionized metal species are $\log N(\mathrm{O\,VI})/\mathrm{cm}^{-2} = 15.2 \pm 0.1$ and $\log N(\mathrm{N\,V})/\mathrm{cm}^{-2} = 14.6 \pm 0.1$ for O VI and N V, respectively.

The results of our Voigt profile analysis of the high-ionization absorption system are presented in Table 7.2. In addition, we present the continuum-normalized absorption profiles and the best-fit models for the O VI and N V absorption in the top three panels of Figure 7.3. For comparison, we also present the observed and modeled absorption profiles of select low-ionization metal species in the bottom panels of Figure 7.3, based on a Voigt profile analysis of these lines previously reported in Chapter 2 (Section 2.4.1).

While detailed analysis is still underway, a number of interesting features can already be noted in this system. As shown in Figure 7.3, the high-ionization absorption is strongest near the systemic redshift of the galaxy, where the low-ionization absorption is weak. Such

1. Note that the second member of the O VI doublet, O VI λ1037, was excluded from the Voigt profile analysis due to blending with neighboring low-ionization transitions C II λ1036 and O Iλ1039. The O VI λ1031 profile is also contaminated by a higher-redshift Lyϵ line at $z = 0.55003$, but in this case the absorption profile of the contaminating Lyϵ line was well-constrained by various other Lyman series lines observed in our COS spectrum. To remove the contamination from the observed O VI λ1031 absorption, we had divided the O VI λ1031 profile by the best-fit model of the Lyϵ absorption at $z = 0.55003$ prior to the analysis.

contrast suggests that there is a strong spatial variation on the ionization state of the ISM. At the same time, while the high- and low-ionization absorption species exhibit distinct velocity profiles, they both span similar range of line-of-sight velocities relative to the galaxy. One possible explanation for the observed absorption features is that both gas phases originate in the same large-scale gas flow or are located at similar distances from the galaxy, in which the low-ionization absorption is produced primarily in high-density clumps, whereas high-ionization gas originate in a smoother, lower-density, and possibly more volume-filling gas.

APPENDIX A

SUPPLEMENTARY INFORMATION FOR CHAPTER 5: DESCRIPTION OF INDIVIDUAL LRG HALOS

Here we describe the observed absorption properties and discuss the physical conditions (density and temperature) and chemical abundances of individual halos in the COS-LRG sample. The 16 QSO sightlines in COS-LRG are ordered by increasing projected distance from each LRG.

A.1 SDSS J0946+5123 at $d = 42$ kpc

This LRG is at redshift $z_{\rm LRG} = 0.4076$. A LLS with a total N(H I) of $\log N({\rm H\,I})/{\rm cm}^{-2} = 17.34 \pm 0.01$ is present near the redshift of the galaxy (Figure A.1a). In addition, the following ionic metal species are also detected: C II, C III, N II, O VI, Si II, and Si III.

Based on a combined Voigt profile analysis of H I and the corresponding metal absorption profiles, we identify five components in the absorption system (Figure A.1a and Table A.1a). The observed velocity spread of the absorber is $\Delta v \approx 200$ km s^{-1} from the bluest to the reddest component. Most (90 percent) of the H I column density is in component 2 at $z_{\rm abs} = 0.40701$, or 126 km s^{-1} blueward of the LRG. Two other components have $\log N_c({\rm H\,I})/{\rm cm}^{-2} \sim 16$, components 3 and 4 at $dv_c = +22$ and $+61$ km s^{-1} from the strongest component, respectively. While the bulk of the neutral hydrogen content is in component 2, little metal absorption is associated with it. In contrast, both low-ionization (e.g., C II and Si II) and intermediate-ionization (e.g., C III) absorption are very prominent in components 3 and 4. This particular characteristic of the absorber suggests a large variation in chemical abundances across different components.

The observed Doppler linewidths of individual H I components ($b_c({\rm H\,I}) \lesssim 25\,{\rm km\ s}^{-1}$ for all but one components) impose a temperature upper limit of $T \lesssim 4 \times 10^4$ K for the gas, under a purely thermal broadening assumption. The other component, component 5, has a

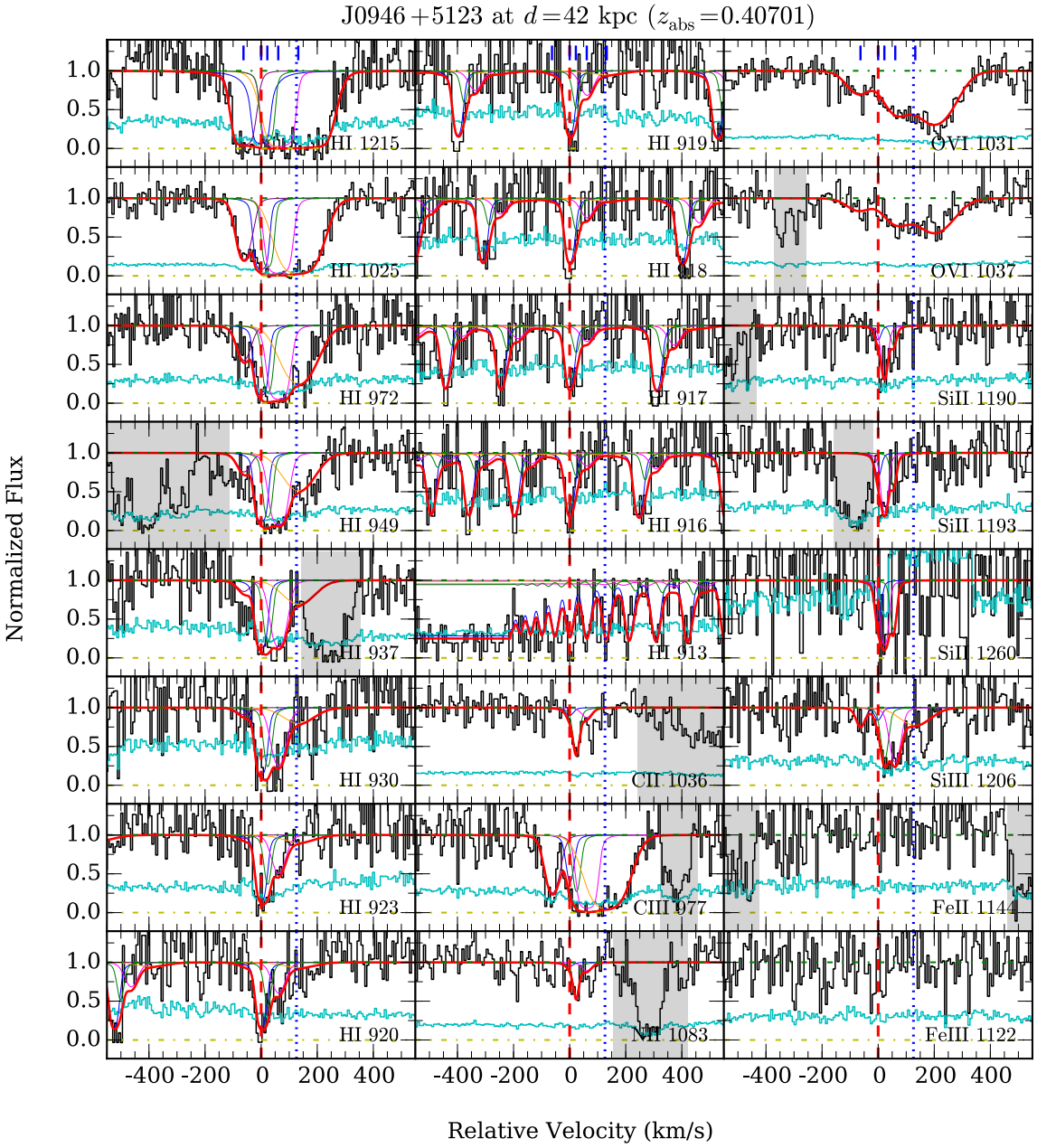

Figure A.1a: Continuum normalized absorption profiles of different transitions along QSO sightline SDSS J0946+5123 at $d = 42$ kpc from the LRG. The absorption transition is identified in the bottom-right corner of each panel. Zero velocity marks the redshift of the strongest H I absorption component identified in the Voigt profile analysis, $z_{\rm abs} = 0.40701$. The systemic redshift of the LRG is indicated with a blue dotted line. The 1-σ error spectrum is included in cyan, above the zero-flux level. Contaminating features have been grayed out for clarity. The best-fit Voigt profiles for each individual transition detected are plotted, both for the sum of all components (red curve) and for individual components (different-colored curves). The centroid of each absorption component is marked by a blue tick mark at the top of panels in the first row.

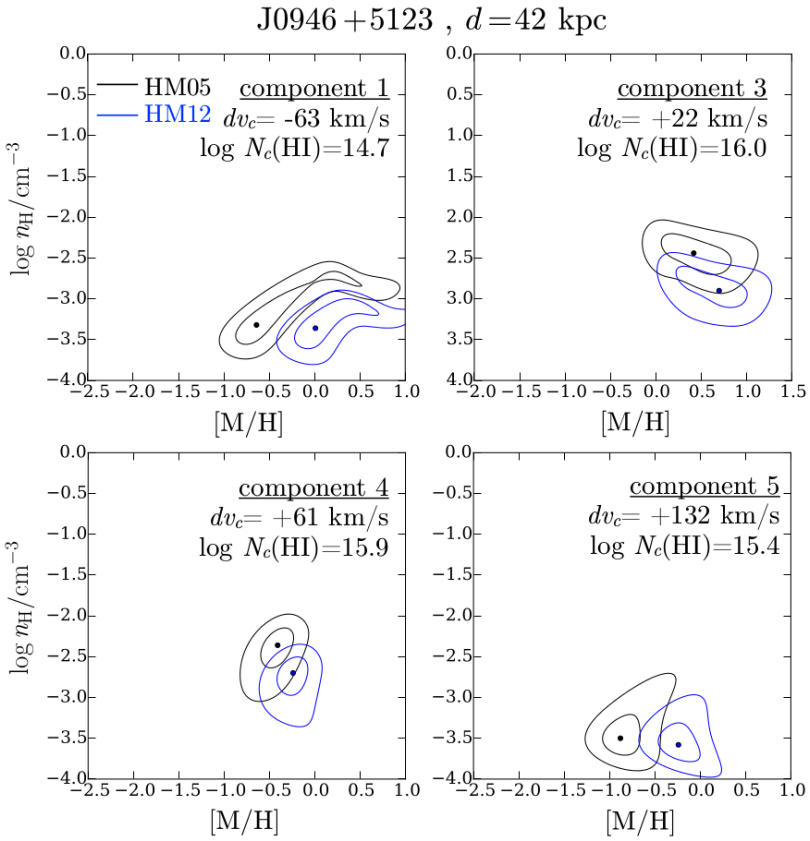

Figure A.1b: Probability distribution of gas metallicity and density for the individual absorption components detected along QSO sightline SDSS J0946+5123, at $d = 42$ kpc from the LRG. Each component shown here has at least two ionic metal species detected in absorption. The contour levels indicate areas enclosing estimated 68% and 95% probabilities of the model parameters, shown in black for models assuming the HM05 UVB and in blue for the HM12 UVB (see Section 3.2). Not shown here is component 2 at $dv_c = 0\,\mathrm{km\ s^{-1}}$, which has the strongest H I absorption in the absorber, with $\log N_c(\mathrm{H\,I})/\mathrm{cm}^{-2} = 17.3$, yet shows little metal absorption. The weak C III absorption seen in component 2, along with upper limits on the column density of other ions still allow us to constrain the gas metallicity to $[\mathrm{M/H}] \lesssim -1.5$.

very broad H I linewidth of $b_c(\mathrm{H\,I}) = 71$ km s^{-1}. However, similar linewidths are observed for the corresponding Si III and C III absorption in component, which implies that the gas is cool ($T \sim 10^4$ K) and the broad line profile is primarily due to non-thermal motion (e.g., turbulence) or the presence of blended narrow components.

As shown in Figure A.1b and Table A.1b, our ionization analysis separates the absorbing gas into two different regimes of gas density. For components 2, 3, and 4, which have $\log N_c(\mathrm{H\,I})/\mathrm{cm}^{-2} \sim 16$, good agreements between observations and models are achieved for a gas density range of from $\log n_\mathrm{H}/\mathrm{cm}^{-3} \approx -2.4$ to $\log n_\mathrm{H}/\mathrm{cm}^{-3} \approx -2.1$ under HM05, and from $\log n_\mathrm{H}/\mathrm{cm}^{-3} \approx -2.7$ to $\log n_\mathrm{H}/\mathrm{cm}^{-3} \approx -2.5$ under HM12. On the other hand, models for lower $N_c(\mathrm{H\,I})$ components 1 and 5 require lower gas densities to match the data: between $\log n_\mathrm{H}/\mathrm{cm}^{-3} \approx -3.6$ and $\log n_\mathrm{H}/\mathrm{cm}^{-3} \approx -3.0$ under both HM05 and HM12 UVBs.

Similarly, the Cloudy photoionization models indicate a large variation in metallicities (> 1 dex) across different components. For component 2 at $dv_c = 0$ km s^{-1}, which has the highest H I column density in the absorber ($\log N_c(\mathrm{H\,I})/\mathrm{cm}^{-2} = 17.3$) but exhibits little associated metals, the inferred metallicity is very low with an upper limit of $[\mathrm{M/H}] \lesssim -1.5$ under both HM05 and HM12 UVBs. In contrast, the observed ionic column densities in components 1,4, and 5 are consistent with the gas having sub-solar metallicities of between $[\mathrm{M/H}] \approx -0.8$ and $[\mathrm{M/H}] \approx -0.4$ under HM05, and between $[\mathrm{M/H}] \approx -0.3$ and $[\mathrm{M/H}] \approx 0$ under HM05. Finally, for component 3, which has $\log N(\mathrm{H\,I})/\mathrm{cm}^{-2} \approx 16$ yet shows the strongest metal absorption, solar or super-solar metallicities are required to match the data, $[\mathrm{M/H}] = 0.4 \pm 0.4$ under HM05 and $[\mathrm{M/H}] = 0.7 \pm 0.4$ under HM12.

This absorption system is also noteworthy because it is the strongest O VI absorber in the COS-LRG sample. The O VI absorption profile is kinematically complex, comprising three components that extend over ~ 300 km s^{-1} in line-of-sight velocity. The measured total O VI column density is $\log N(\mathrm{O\,VI})/\mathrm{cm}^{-2} = 14.93 \pm 0.02$, which is the highest yet detected in the vicinity of a passive galaxy (cf., Tumlinson et al. 2011; Johnson et al. 2015), and among the highest $N(\mathrm{O\,VI})$ seen in both star-forming and passive galaxies. The broad and

Table A.1a: Absorption properties along QSO sightline SDSS J0946+5123 at $d = 42$ kpc from the LRG

Component	Species	$\mathrm{d}v_c$ ($\mathrm{km\,s^{-1}}$)	$\log N_c$	b_c ($\mathrm{km\,s^{-1}}$)
all	H I	...	17.34 ± 0.01	...
	C II	...	14.11 ± 0.16	...
	C III	...	> 14.73	...
	N II	...	13.90 ± 0.22	...
	N V	...	< 13.97	...
	O VI	...	14.93 ± 0.02	...
	Si II	...	$13.87^{+0.21}_{-0.14}$	...
	Si III	...	$13.48^{+0.19}_{-0.06}$	...
	Fe II	...	< 14.04	...
	Fe III	...	< 14.14	...
1	H I	$-62.8^{+2.8}_{-3.0}$	$14.70^{+0.10}_{-0.09}$	18.2 ± 1.7
	C II	-62.8	< 13.24	10
	C III	-62.8	$13.67^{+0.13}_{-0.11}$	27.3 ± 8.9
	N II	-62.8	< 13.29	10
	Si II	-62.8	< 12.88	10
	Si III	-62.8	$12.35^{+0.20}_{-0.23}$	$17.3^{+8.6}_{-6.1}$
	Fe II	-62.8	< 13.48	10
	Fe III	-62.8	< 13.50	10
2	H I	0.0 ± 0.2	17.30 ± 0.02	$10.6^{+0.7}_{-0.6}$
	C II	0.0	< 13.22	10
	C III	0.0	$13.20^{+0.28}_{-0.26}$	$13.4^{+5.6}_{-2.0}$
	N II	0.0	< 13.40	10
	Si II	0.0	< 12.92	10
	Si III	0.0	< 12.08	10
	Fe II	0.0	< 13.47	10
	Fe III	0.0	< 13.55	10
3	H I	$+22.1^{+2.2}_{-2.8}$	$15.97^{+0.30}_{-0.46}$	$10.8^{+1.0}_{-0.9}$
	C II	$+22.1$	14.11 ± 0.16	$10.4^{+5.0}_{-2.5}$
	C III	$+22.1$	> 13.60	< 22.5
	N II	$+22.1$	13.90 ± 0.22	$9.1^{+5.8}_{-2.4}$
	Si II	$+22.1$	$13.80^{+0.22}_{-0.20}$	9.9 ± 4.7
	Si III	$+22.1$	$12.97^{+0.32}_{-0.26}$	$12.0^{+9.5}_{-2.3}$
	Fe II	$+22.1$	< 13.52	10
	Fe III	$+22.1$	< 13.49	10
4	H I	$+60.8^{+3.9}_{-4.9}$	$15.90^{+0.13}_{-0.12}$	$26.9^{+2.6}_{-1.9}$
	C II	$+60.8$	< 13.31	10
	C III	$+60.8$	> 13.68	< 35.7
	N II	$+60.8$	< 13.27	10
	Si II	$+60.8$	$13.07^{+0.20}_{-0.31}$	$9.7^{+6.4}_{-3.1}$
	Si III	$+60.8$	$13.09^{+0.29}_{-0.19}$	$20.0^{+8.3}_{-4.4}$
	Fe II	$+60.8$	< 13.51	10
	Fe III	$+60.8$	< 13.61	10
5	H I	$+132.3^{+5.2}_{-6.6}$	$15.41^{+0.09}_{-0.07}$	$71.3^{+3.7}_{-3.1}$
	C II	$+132.3$	< 13.16	10
	C III	$+132.3$	$14.34^{+0.22}_{-0.07}$	$69.8^{+5.3}_{-11.8}$
	N II	$+132.3$	< 13.37	10
	Si II	$+132.3$	< 12.73	10
	Si III	$+132.3$	12.81 ± 0.23	$70.0^{+35.1}_{-19.1}$
	Fe II	$+132.3$	< 13.49	10
	Fe III	$+132.3$	< 13.59	10
high-1	O VI	-69.7 ± 12.7	$14.00^{+0.08}_{-0.17}$	$53.3^{+23.6}_{-14.2}$
	N V	-69.7	< 13.67	
high-2	O VI	$+64.3 \pm 11.0$	$14.38^{+0.08}_{-0.05}$	$58.2^{+22.0}_{-5.0}$
	N V	$+64.3$	< 13.67	
high-3	O VI	$+202.6 \pm 11.0$	$14.71^{+0.03}_{-0.04}$	$82.9^{+8.6}_{-4.9}$
	N V	$+202.6$	< 13.82	

Table A.1b: Ionization modeling results for the absorber along SDSS J0946+5123 at $d = 42$ kpc from the LRG

Component	$N_{\rm metal}$	[M/H]		$\log n_{\rm H}/{\rm cm}^{-3}$	
		HM05	HM12	HM05	HM12
SC	5	-0.84 ± 0.16	$-0.73^{+0.16}_{-0.13}$	$-1.90^{+0.08}_{-0.20}$	$-2.28^{+0.10}_{-0.18}$
1	2	$-0.61^{+0.91}_{-0.12}$	$0.04^{+0.47}_{-0.17}$	$-2.84^{+0.04}_{-0.60}$	$-3.20^{+0.08}_{-0.34}$
2	1	< -1.53	< -1.41	$-2.08^{+0.52}_{-0.18}$	$-2.52^{+0.60}_{-0.20}$
3	5	$0.42^{+0.38}_{-0.29}$	$0.70^{+0.26}_{-0.40}$	$-2.44^{+0.16}_{-0.24}$	$-2.84^{+0.14}_{-0.28}$
4	3	$-0.42^{+0.15}_{-0.24}$	$-0.23^{+0.15}_{-0.20}$	$-2.38^{+0.14}_{-0.46}$	$-2.72^{+0.12}_{-0.40}$
5	2	$-0.81^{+0.28}_{-0.19}$	$-0.20^{+0.20}_{-0.22}$	$-3.50^{+0.42}_{-0.16}$	$-3.58^{+0.30}_{-0.16}$

asymmetric O VI absorption profile is in stark contrast to the narrower absorption profiles the lower-ionization metals, which indicates different physical origins between the low- and high-ionization species.

A.2 SDSS J1406+2509 at $d = 47$ kpc

This LRG occurs at $z_{\rm LRG} = 0.4004$. As shown in Figure A.2a, a strong LLS is present at the LRG redshift, with a total N(H I) of $\log N({\rm H\,I})/{\rm cm}^{-2} = 18.03^{+0.20}_{-0.03}$. The HI absorption is accompanied by associated detections of the following metal species: C II, C III, N II, Mg I Mg II, Si II, Si III, and Fe II. We note that two intervening absorbers at higher redshifts, a LLS at $z = 0.578$ and a pLLS at $z = 0.516$, absorb a majority of the QSO continuum flux below rest-frame $\lambda \approx 990$ Å for the LRG absorber. Because of the significantly reduced S/N in this spectral regime, we cannot reliably constrain the absorption properties of C III λ977 transition, and we chose to exclude C III from our subsequent analysis of the absorber.

We identify five distinct components in the absorption system, based on the Voigt profile analysis (Figure A.2a and Table A.2a). The observed velocity spread of the absorber is $\Delta v \approx 210$ km s^{-1} from the bluest to the reddest component. Two components are optically thick with $\log N_c({\rm H\,I})/{\rm cm}^{-2} \gtrsim 17$. The strongest H I absorption occurs in component 4 at $z_{\rm abs} = 0.40047$, or 16 km s^{-1} redward of the LRG. Component 4 comprises most (90 percent)

of the total $N(\mathrm{H\,I})$ of the absorption system. Most of the remaining neutral hydrogen is found in component 3, which is at $dv_c = -22$ km s^{-1} from the strongest component. These two strong components are also where all of the ionic metals in the absorber are detected. In contrast, the remaining components (components 1 to 3) are optically thin with $\log N_c(\mathrm{H\,I})/\mathrm{cm}^{-2} < 16$, and are not detected in associated metal absorption lines.

We find a consistent velocity structure in optically thick H I components (components 3 and 4) and metal species (e.g., Mg II and Mg I, see Figure A.2a). Based on the observed linewidths of H I and Mg I, the implied temperatures of the absorbing gas for components 3 and 4 are $T \approx 2.5 \times 10^4$ K and 10^4 K, respectively. The observed linewidths also indicate little non-thermal broadening in the optically thick gas, with $b_{\rm nt} \approx 3 - 4\,\mathrm{km\ s^{-1}}$. For optically thin components 1 to 3, the observed H I linewidths place an upper limit on the gas temperature of $T \lesssim 5 \times 10^4$ K.

Our ionization analysis finds a modest difference (~ 0.3 dex) in gas densities between the two optically thick components 3 and 4 (Figure A.2b and Table A.2b). For both components, the observed absorption profile can be reproduced by the models over a gas density range of from $\log n_{\rm H}/\mathrm{cm}^{-3} \approx -1.8$ to $\log n_{\rm H}/\mathrm{cm}^{-3} \approx -1.5$ under the HM05 UVB, and from $\log n_{\rm H}/\mathrm{cm}^{-3} \approx -2.1$ to $\log n_{\rm H}/\mathrm{cm}^{-3} \approx -1.8$ under the HM12 ionizing spectrum. The inferred metallicities are sub-solar, ranging from $[\mathrm{M/H}] = -0.9^{+0.2}_{-0.3}$ (component 4) to $[\mathrm{M/H}] = -0.3^{+0.3}_{-0.2}$ (component 3) under HM05, and from $[\mathrm{M/H}] = -0.8 \pm 0.2$ (component 4) to $[\mathrm{M/H}] = -0.2 \pm 0.2$ (component 3) under HM12. Finally, we note that the inferred Fe and Mg abundance ratio of the gas is consistent with solar value, $[\mathrm{Fe}/\alpha] \sim 0$, to within uncertainties.

A.3 SDSS J1111+5547 at $d = 77$ kpc

The LRG is located at $z_{\rm LRG} = 0.4629$. A LLS with a total $N(\mathrm{H\,I})$ of $\log N(\mathrm{H\,I})/\mathrm{cm}^{-2} = 17.82 \pm 0.01$ is found near the galaxy redshift (Figure A.3a). In addition, the following ionic metal species are detected: C II, C III, N II, N III, O I, O VI, Si II, and Si III.

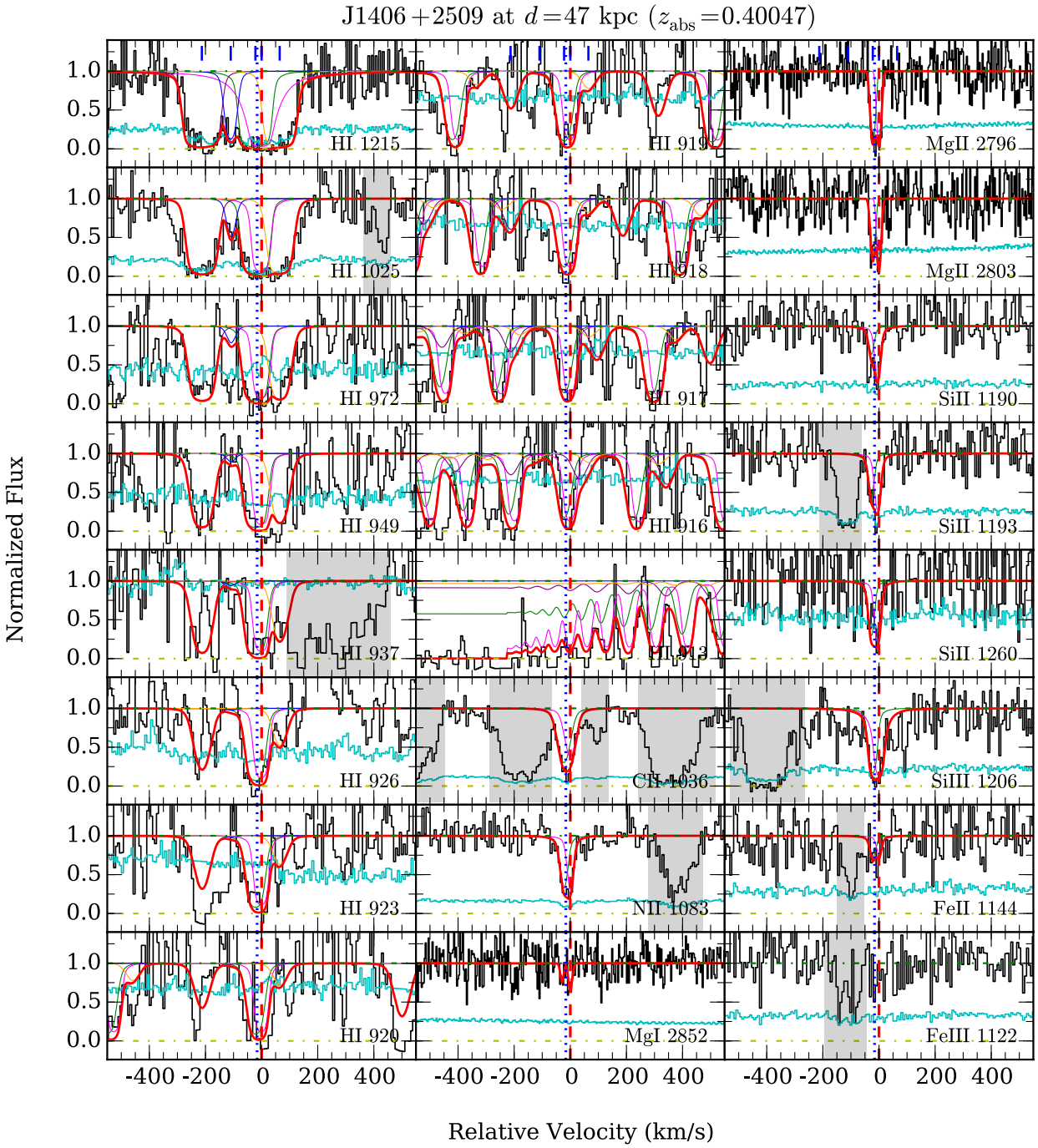

Figure A.2a: Similar to Figure A.1a, but for SDSS J1406+2509 at $d = 47$ kpc from the LRG.

Table A.2a: Absorption properties along QSO sightline SDSS J1406+2509 at $d = 47$ kpc from the LRG

Component	Species	$\mathrm{d}v_c$ ($\mathrm{km\,s^{-1}}$)	$\log N_c$	b_c ($\mathrm{km\,s^{-1}}$)
all	H I	...	$18.03^{+0.20}_{-0.03}$	...
	C II	...	$14.58^{+0.16}_{-0.04}$	...
	N II	...	> 14.47	...
	Mg I	...	$11.92^{+0.22}_{-0.17}$	...
	Mg II	...	> 13.45	...
	Si II	...	$14.29^{+0.47}_{-0.44}$	...
	Si III	...	> 13.45	...
	Fe II	...	$13.81^{+0.27}_{-0.24}$	...
	Fe III	...	< 14.18	...
1	H I	$-212.9^{+3.2}_{-3.0}$	$16.16^{+0.26}_{-0.22}$	$28.5^{+1.9}_{-2.0}$
	N II	-212.9	< 13.25	10
	Mg I	-212.9	< 11.61	10
	Mg II	-212.9	< 12.14	10
	Si II	-212.9	< 12.97	10
	Si III	-212.9	< 12.11	10
	Fe II	-212.9	< 13.43	10
	Fe III	-212.9	< 13.63	10
2	H I	$-109.9^{+5.1}_{-4.7}$	$14.15^{+0.14}_{-0.17}$	$16.7^{+1.6}_{-1.2}$
	N II	-109.9	< 13.22	10
	Mg I	-109.9	< 11.58	10
	Mg II	-109.9	< 12.13	10
	Si II	-109.9	< 12.96	10
	Si III	-109.9	< 12.05	10
3	H I	-22.1 ± 0.7	$16.98^{+0.50}_{-0.40}$	$21.5^{+1.5}_{-1.6}$
	C II	-22.1	$14.34^{+0.18}_{-0.06}$	$22.1^{+7.5}_{-4.6}$
	N II	-22.1	> 14.01	< 18.4
	Mg I	-29.7 ± 4.2	$11.47^{+0.25}_{-0.29}$	$4.8^{+3.7}_{-1.8}$
	Mg II	-22.1 ± 2.5	> 12.96	< 10.1
	Si II	-22.1	13.27 ± 0.36	$11.6^{+4.7}_{-5.1}$
	Si III	-22.1	> 12.90	< 26.9
	Fe II	-22.1	$13.55^{+0.32}_{-0.21}$	$12.7^{+5.0}_{-5.6}$
	Fe III	-22.1	< 13.58	10
4	H I	$0.0^{+1.0}_{-1.3}$	$17.98^{+0.19}_{-0.06}$	$11.4^{+1.0}_{-1.2}$
	C II	0.0	$14.20^{+0.19}_{-0.12}$	$19.7^{+5.0}_{-7.0}$
	N II	0.0	> 13.98	< 17.6
	Mg I	-2.2 ± 2.6	$11.73^{+0.25}_{-0.28}$	$5.1^{+3.3}_{-2.3}$
	Mg II	0.0 ± 2.2	> 13.08	< 9.0
	Si II	0.0	$14.25^{+0.49}_{-0.58}$	$6.0^{+3.9}_{-0.5}$
	Si III	0.0	> 12.92	< 25.8
	Fe II	0.0	13.46 ± 0.31	$11.0^{+2.4}_{-4.7}$
	Fe III	0.0	< 13.55	10
5	H I	$+64.5^{+5.9}_{-8.2}$	$15.72^{+0.31}_{-0.22}$	$27.5^{+2.8}_{-2.2}$
	N II	$+64.5$	< 13.16	10
	Mg I	$+64.5$	< 11.57	10
	Mg II	$+64.5$	< 12.11	10
	Si II	$+64.5$	< 12.71	10
	Si III	$+64.5$	< 12.04	10
	Fe II	$+64.5$	< 13.43	10
	Fe III	$+64.5$	< 13.52	10

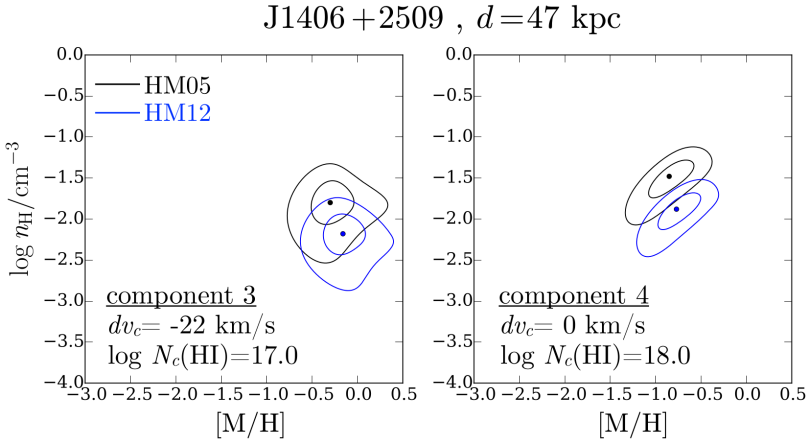

Figure A.2b: Probability distribution contours of gas metallicity and density for optically thick individual absorption components identified along SDSS J1406+2509, at d = 47 kpc from the LRG. Contour levels are the same as in Figure A.1b. Note that optically thin components 1,2 and 5 ($\log N_c(\mathrm{H\,I})/\mathrm{cm}^{-2} < 16$) are not shown here, because the absence of metal detections for these three components result in a lack of strong constraints on the metallicity and density of the gas (see Table A.2b).

Table A.2b: Ionization modeling results for the absorber along SDSS J1406+2509 at d = 47 kpc from the LRG

Component	N_{metal}	[M/H]		$\log n_{\mathrm{H}}/\mathrm{cm}^{-3}$	
		HM05	HM12	HM05	HM12
SC	7	$-0.64^{+0.17}_{-0.21}$	$-0.54^{+0.16}_{-0.19}$	$-1.76^{+0.12}_{-0.32}$	$-2.14^{+0.12}_{-0.34}$
1	0	< 0.06	< 0.14	> -4.84	> -4.82
2	0	< 0.75	< 0.78	> -4.72	> -4.72
3	7	$-0.30^{+0.26}_{-0.23}$	$-0.16^{+0.24}_{-0.23}$	$-1.80^{+0.16}_{-0.42}$	$-2.18^{+0.16}_{-0.38}$
4	7	$-0.85^{+0.21}_{-0.26}$	$-0.77^{+0.21}_{-0.24}$	$-1.48^{+0.12}_{-0.32}$	$-1.88^{+0.14}_{-0.32}$
5	0	< 0.34	< 0.43	> 4.82	> -4.80

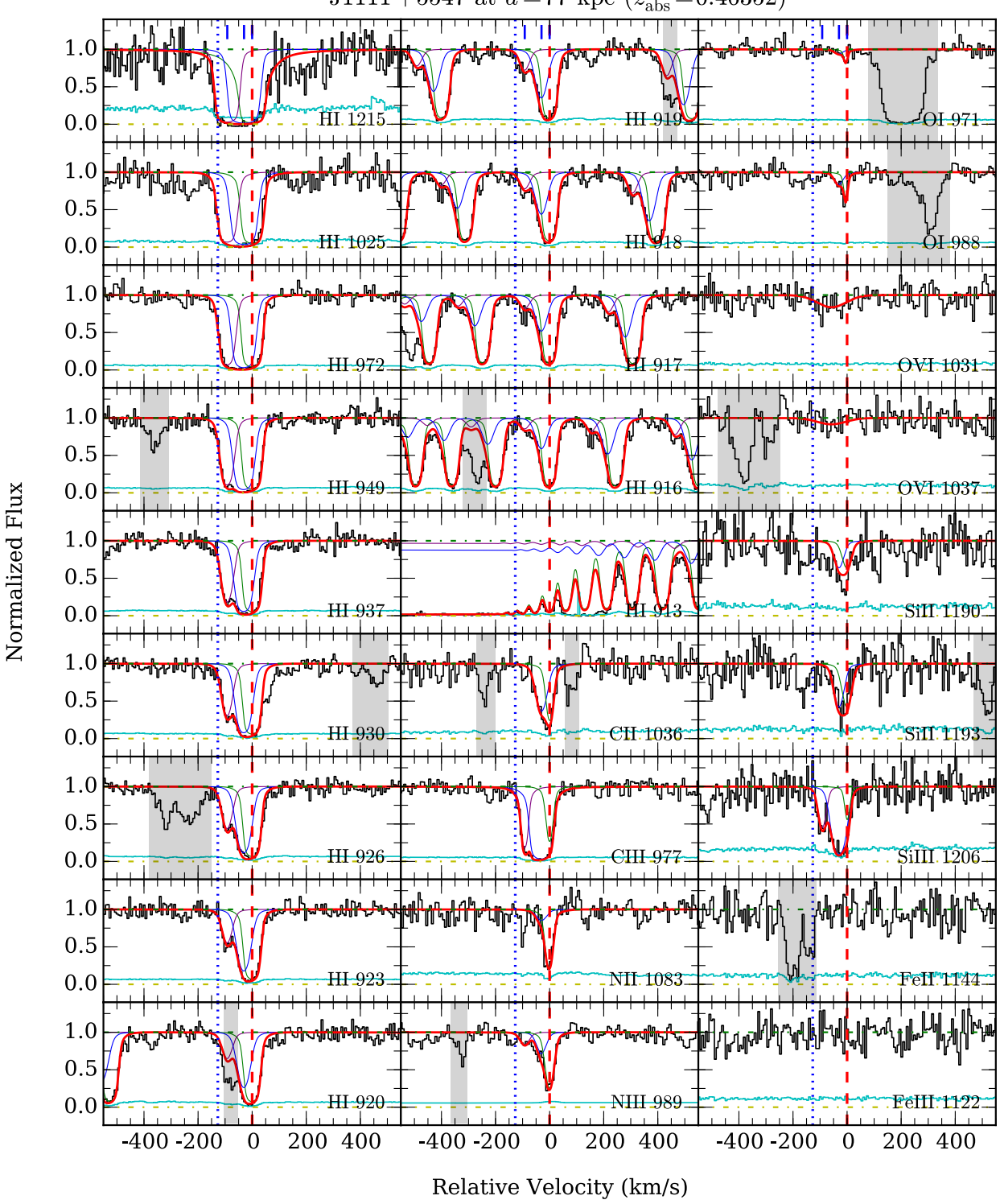

Figure A.3a: Similar to Figure A.1a, but for SDSS J1111+5547 at d = 77 kpc from the LRG. For the N III λ989 transition, contamination from the adjacent Si II λ989 line has been removed by dividing the observed absorption profile by a model profile of Si II λ989 line, which is constrained by fitting other Si II transitions in the spectrum.

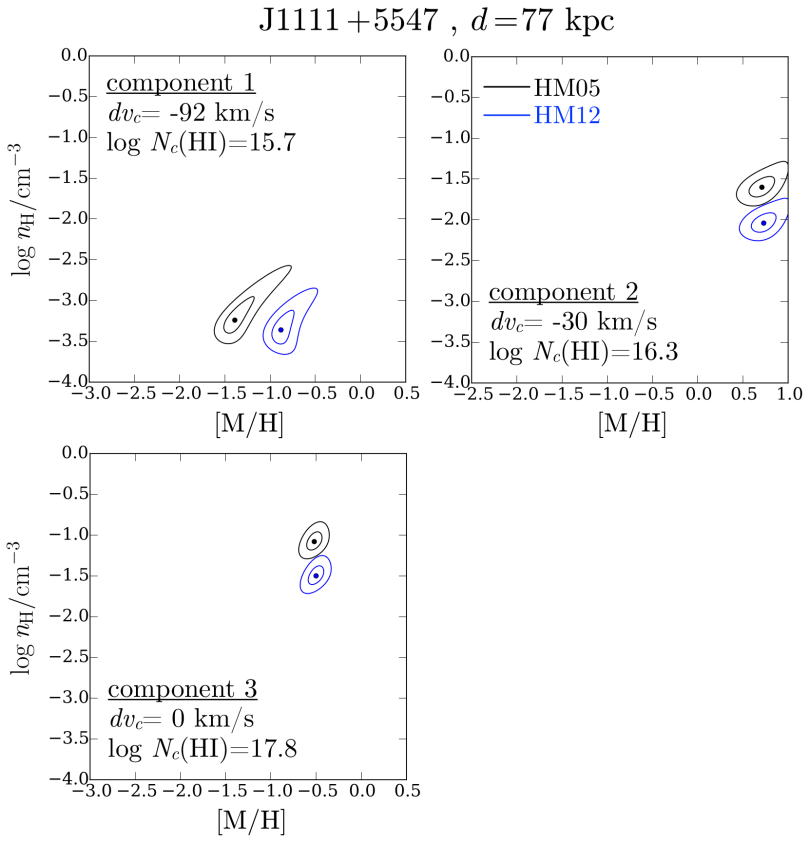

Figure A.3b: Probability distribution contours of gas metallicity and density for individual absorption components identified along SDSS J1111+5547, at $d = 77$ kpc from the LRG. Contour levels are the same as in Figure A.1b.

We identify three components in this absorber based on a combined Voigt profile analysis of H I and the metal absorption profiles (Figure A.3a and Table A.3a). The observed velocity spread is $\Delta v \approx 90$ km s^{-1} from the bluest to the reddest component. The bulk (95 percent) of the H I column density is concentrated in component 3 at $z_{\rm abs} = 0.46352$, or 127 km s^{-1} redward of the LRG. One other component has $\log N_c({\rm H\,I})/{\rm cm}^{-2} > 16$, component 2 at $dv_c = -30$ km s^{-1}. The observed H I linewidths for all three components constrain the gas temperature to $T \lesssim 3 \times 10^4$ K, consistent with the expectation for a photoionized gas.

Our ionization analysis finds a large variation in densities and metallicities among different components (Figure A.3b and Table A.3b). For component 1, the observed metal column densities are well-reproduced by a low density and metal-poor gas, with a density between $\log n_{\rm H}/{\rm cm}^{-3} \approx -3.4$ (HM12) and $\log n_{\rm H}/{\rm cm}^{-3} \approx -3.2$ (HM05), and a metallicity between ${\rm [M/H]} = -1.4^{+0.3}_{-0.1}$ (HM05) and ${\rm [M/H]} = -0.9^{+0.2}_{-0.1}$ (HM12).

In contrast, component 3, which contains most of the neutral hydrogen in the system, has an inferred density of between $\log n_{\rm H}/{\rm cm}^{-3} \approx -1.5$ (HM12) and $\log n_{\rm H}/{\rm cm}^{-3} \approx -1.1$ (HM05), and a sub-solar metallicity of ${\rm [M/H]} = -0.5 \pm 0.1$ under both HM05 and HM12. The close agreement in the derived metallicities between HM05 and HM12 for component 3 is due to the well-constrained O I column density, which scales proportionally with metallicity but is insensitive to different ionizing radiation fields. We note that the non-detection of Fe II in this component is consistent with the gas having an $\alpha-$element enhanced abundance pattern, with ${\rm [Fe/}\alpha{\rm]} \lesssim -0.3$.

For component 2, the presence of O I absorption in a component with a relatively low $N({\rm H\,I})$ of $\log N({\rm H\,I})/{\rm cm}^{-2} = 16.3$ indicates that the gas has been highly enriched by heavy elements. Indeed, our ionization analysis finds a super-solar metallicity of 0.7 ± 0.2 under both HM05 and HM12 UVBs. The gas density is found to be between $\log n_{\rm H}/{\rm cm}^{-3} \approx -2.0$ (HM12) and $\log n_{\rm H}/{\rm cm}^{-3} \approx -1.6$ (HM05). At the adopted metallicity, the non-detection of Fe II in component 2 is consistent with the gas having an $\alpha-$element enhanced abundance pattern, with ${\rm [Fe/}\alpha{\rm]} \lesssim -0.2$. Finally, we note that over the entire range of allowed gas

Table A.3a: Absorption properties along QSO sightline SDSS J1111+5547 at $d = 77$ kpc from the LRG

Component	Species	$\mathrm{d}v_c$ ($\mathrm{km\,s^{-1}}$)	$\log N_c$	b_c ($\mathrm{km\,s^{-1}}$)
all	H I	...	17.82 ± 0.01	...
	C II	...	$14.64^{+0.15}_{-0.10}$	...
	C III	...	> 14.76	...
	N II	...	$14.55^{+0.26}_{-0.18}$	...
	N III	...	$14.51^{+0.09}_{-0.05}$	...
	O I	...	$14.27^{+0.04}_{-0.06}$	...
	O VI	...	13.81 ± 0.08	...
	Si II	...	$13.71^{+0.06}_{-0.03}$	...
	Si III	...	$13.61^{+0.27}_{-0.07}$	...
	Fe II	...	< 13.46	...
	Fe III	...	< 14.57	...
1	H I	$-92.1^{+1.6}_{-1.3}$	15.73 ± 0.03	$20.1^{+1.1}_{-1.0}$
	C II	-92.1	< 12.97	10
	C III	-92.1	> 13.55	< 13.9
	N III	-92.1	13.48 ± 0.12	$20.0^{+7.7}_{-5.3}$
	O I	-92.1	< 13.18	10
	Si II	-92.1	< 12.35	10
	Si III	-92.1	12.78 ± 0.13	$15.7^{+5.3}_{-5.4}$
	Fe II	-92.1	< 13.07	10
	Fe III	-92.1	< 13.19	10
2	H I	$-30.4^{+2.5}_{-3.0}$	$16.32^{+0.06}_{-0.08}$	$23.9^{+1.7}_{-2.0}$
	C II	-30.4	$14.22^{+0.07}_{-0.06}$	$21.7^{+4.0}_{-3.3}$
	C III	-30.4	> 14.72	< 25.8
	N II	-30.4	$13.44^{+0.20}_{-0.31}$	$22.0^{+13.4}_{-7.7}$
	N III	-30.4	13.75 ± 0.11	$19.9^{+9.2}_{-3.9}$
	O I	-30.4	$13.83^{+0.09}_{-0.14}$	$18.3^{+9.8}_{-3.6}$
	Si II	-30.4	13.42 ± 0.09	$19.9^{+8.2}_{-5.2}$
	Si III	-30.4	$13.50^{+0.31}_{-0.11}$	$25.1^{+4.5}_{-4.8}$
	Fe II	-30.4	< 13.05	10
	Fe III	-30.4	< 13.18	10
3	H I	0.0 ± 0.1	17.80 ± 0.01	$12.8^{+0.4}_{-0.3}$
	C II	0.0	$14.43^{+0.22}_{-0.17}$	$11.2^{+2.8}_{-1.9}$
	C III	0.0	$13.50^{+0.41}_{-1.26}$	$11.2^{+15.1}_{-4.8}$
	N II	0.0	$14.52^{+0.28}_{-0.20}$	$11.5^{+3.7}_{-2.0}$
	N III	0.0	$14.37^{+0.13}_{-0.07}$	$15.3^{+1.6}_{-2.5}$
	O I	0.0	$14.08^{+0.07}_{-0.10}$	$5.0^{+3.0}_{-0.5}$
	Si II	0.0	$13.40^{+0.14}_{-0.07}$	$18.9^{+5.0}_{-9.9}$
	Si III	0.0	$12.51^{+0.35}_{-0.33}$	$8.0^{+6.5}_{-1.9}$
	Fe II	0.0	< 13.48	10
	Fe III	0.0	< 13.50	10
high-1	O VI	-58.0 ± 12.6	13.81 ± 0.08	$69.4^{+30.5}_{-9.0}$

Table A.3b: Ionization modeling results for the absorber along SDSS J1111+5547 at $d = 77$ kpc from the LRG

Component	$N_{\rm metal}$	[M/H]		$\log n_{\rm H}/{\rm cm}^{-3}$	
		HM05	HM12	HM05	HM12
SC	6	-0.33 ± 0.06	$-0.32^{+0.05}_{-0.07}$	$-1.02^{+0.08}_{-0.10}$	-1.48 ± 0.10
1	3	$-1.38^{+0.30}_{-0.08}$	$-0.85^{+0.16}_{-0.09}$	$-3.24^{+0.38}_{-0.10}$	$-3.36^{+0.26}_{-0.14}$
2	4	$0.72^{+0.13}_{-0.14}$	$0.74^{+0.12}_{-0.14}$	$-1.60^{+0.12}_{-0.10}$	$-2.04^{+0.12}_{-0.10}$
3	6	$-0.52^{+0.07}_{-0.08}$	$-0.50^{+0.07}_{-0.09}$	-1.08 ± 0.10	-1.50 ± 0.10

densities and metallicities, CLOUDY under-predicts the column densities of all intermediate ions (C III, N III, and Si III) in component 2 by ≈ 1 dex, which implies that most of the absorption from intermediate ions arises from a lower density phase.

A weak O VI absorption is present in this system, centered at $dv_c = -58$ km s^{-1}. The O VI absorption consists of a single component with $\log N({\rm O\,VI})/{\rm cm}^{-2} = 14.0 \pm 0.1$ and a broad Doppler b linewidth of of 69 km s^{-1}. No low- or intermediate-ionization metal or H I component is found to match the O VI absorption (Figure A.3a) in velocity space, which occurs at $\Delta v = -28$ km s^{-1} from the nearest low-ionization component.

A.4 SDSS J0803+4332 at $d = 79$ kpc

This LRG occurs at $z_{\rm LRG} = 0.2535$. As shown in Figure A.4a, an H I absorber is present near the LRG redshift, with a total N(H I) of $\log N({\rm H\,I})/{\rm cm}^{-2} = 14.78 \pm 0.05$. The only metal species detected is C III, which exhibits excellent kinematic alignment with HI.

Our Voigt profile analysis shows that the H I and C III absorption profile can be decomposed into two individual components (Figure A.4a and Table A.4a). The velocity spread of the absorbing gas is $\Delta v \approx 50$ km s^{-1} between the two components. The stronger of the two components (component 1) occurs at -48 km s^{-1} from the LRG, at $z_{\rm abs} = 0.25330$, whereas the weaker component occurs at the systemic redshift of the LRG. For both components, the measured ratios of H I and C III linewidths are consistent with expectations from pure thermal broadening. The inferred temperature of the gas is $T \sim (8-9) \times 10^4$ K for both

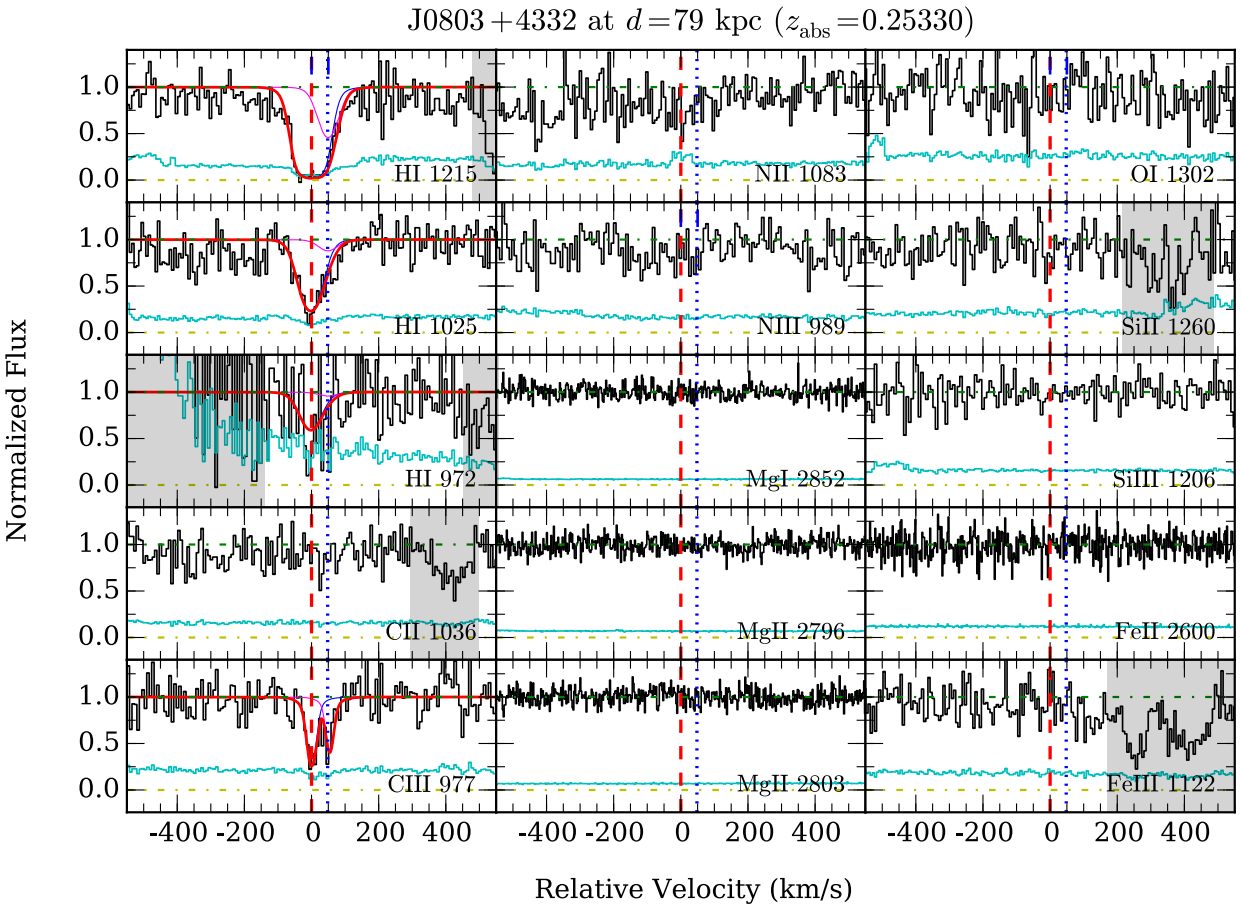

Figure A.4a: Similar to Figure A.1a, but for SDSS J0803+4332 at $d = 79$ kpc from the LRG.

components.

For both components, the observed N_c(C III) and upper limits on other ionic column densities constrain the gas to be low density, $\log n_{\rm H}/{\rm cm}^{-3} \lesssim -3$, under both HM05 and HM12 UVBs (Table A.4b). Because C III is the only metal species detected, the inferred chemical abundance of the gas is subject to large uncertainties. For the stronger component 1, the inferred metallicity is [M/H] $= -1.2^{+0.5}_{-0.2}$ under HM05, and [M/H] $= -0.4^{+0.7}_{-0.2}$ under HM12. For component 2, which has comparable N_c(C III) to component 1 despite a much lower N_c(H I), a higher metallicity is required to match the data, ranging from a sub-solar [M/H] $= -0.2^{+0.5}_{-0.6}$ under HM05, to possibly super-solar [M/H] $= 0.5^{+0.3}_{-0.7}$ under HM12.

This absorber was also studied in the COS-Halos survey. A major difference between our analysis and that of the COS-Halos survey (Werk et al. 2014; Prochaska et al. 2017) is that the COS-Halos ionization analysis utilized only the integrated H I and metal column densities summed over all components in each system, which is the same as imposing a single-clump model (see Section 5.3.2) where different components have the same density and metallicity. Using the Haardt & Madau (2001) UVB (which is similar of the HM05 UVB at energies $\lesssim 2$ Ryd), Werk et al. (2014) inferred a mean metallicity of [M/H] $= -0.9^{+0.9}_{-0.8}$ and density of $\log n_{\rm H}/{\rm cm}^{-3} < -3.7$ under the Haardt & Madau (2001) UVB. In an updated analysis using the HM12 UVB, Prochaska et al. (2017) found a mean metallicity of [M/H] $= 0.1^{+0.7}_{-0.6}$ and density of $\log n_{\rm H}/{\rm cm}^{-3} = -3.0^{+0.3}_{-0.8}$. The [M/H] and $n_{\rm H}$ values from COS-Halos are consistent what we find in our analysis assuming the single-clump model (Table A.4b).

A.5 SDSS J0925+4004 at $d = 84$ kpc

This LRG occurs at $z_{\rm LRG} = 0.2475$. As shown in Figure A.5a, a sub-damped Lyα absorber (sub-DLA) with a total N(H I) of $\log N({\rm H\,I})/{\rm cm}^{-2} = 19.58 \pm 0.02$ is present at $z_{\rm abs} = 0.24769$, or 46 km s^{-1} redward of the LRG. This absorber has the highest H I column density in the COS-LRG sample. In addition, the following ionic metal species are also detected: C II, C III, N II, O I, Mg I, Mg II, Si II, Si III, Si IV, and Fe II.

Table A.4a: Absorption properties along QSO sightline SDSS J0803+4332, $d = 79$ kpc from the LRG

Component	Species	$\mathrm{d}v_c$ ($\mathrm{km\,s^{-1}}$)	$\log N_c$	b_c ($\mathrm{km\,s^{-1}}$)
all	H I	...	14.78 ± 0.05	...
	C II	...	< 13.54	...
	C III	...	$13.78^{+0.20}_{-0.08}$	...
	N II	...	< 13.70	...
	N III	...	< 13.65	...
	N V	...	< 13.28	...
	O I	...	< 14.07	...
	Mg I	...	< 11.31	...
	Mg II	...	< 11.84	...
	Si II	...	< 12.68	...
	Si III	...	< 12.35	...
	Si IV	...	< 12.82	...
	Fe II	...	< 12.57	...
	Fe III	...	< 13.84	...
1	H I	$0.0^{+2.9}_{-2.3}$	$14.75^{+0.06}_{-0.05}$	$38.7^{+6.0}_{-1.7}$
	C II	0.0	< 13.16	10
	C III	-1.2 ± 2.9	$13.61^{+0.23}_{-0.15}$	$11.9^{+7.3}_{-2.1}$
	N II	0.0	< 13.41	10
	N III	0.0	< 13.27	10
	O I	0.0	< 13.67	10
	Mg I	0.0	< 10.91	10
	Mg II	0.0	< 11.44	10
	Si II	0.0	< 12.26	10
	Si III	0.0	< 11.93	10
	Si IV	0.0	< 12.42	10
	Fe II	0.0	< 12.17	10
	Fe III	0.0	< 13.47	10
2	H I	$+50.3^{+7.2}_{-6.4}$	$13.64^{+0.09}_{-0.48}$	$35.0^{+11.0}_{-6.2}$
	C II	+50.3	< 13.14	10
	C III	$+50.2 \pm 3.5$	$13.30^{+0.26}_{-0.09}$	$10.0^{+6.3}_{-3.5}$
	N II	+50.3	< 13.23	10
	N III	+50.3	< 13.26	10
	O I	+50.3	< 13.69	10
	Mg I	+50.3	< 10.92	10
	Mg II	+50.3	< 11.45	10
	Si II	+50.3	< 12.25	10
	Si III	+50.3	< 11.98	10
	Si IV	+50.3	< 12.41	10
	Fe II	+50.3	< 12.18	10
	Fe III	+50.3	< 13.44	10

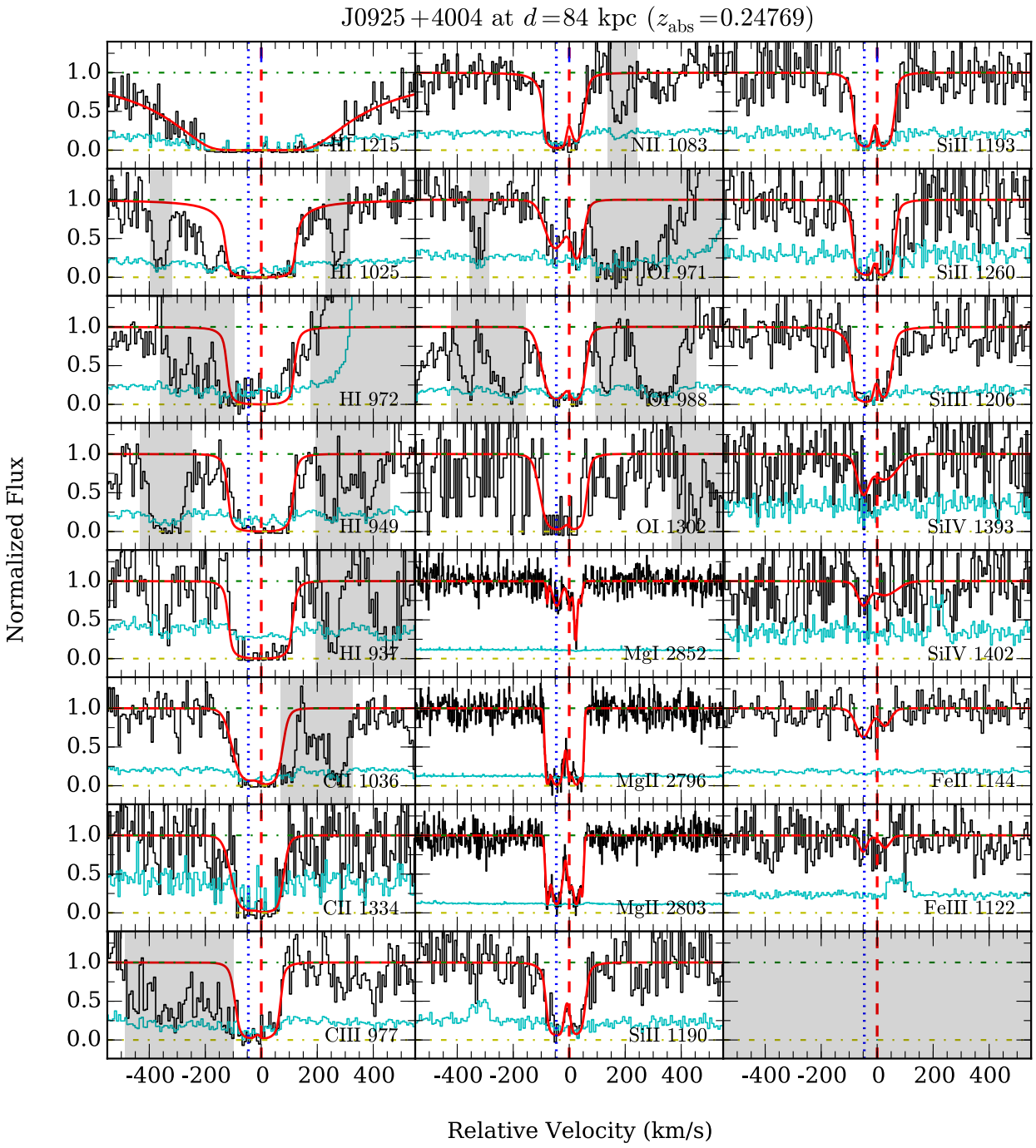

Figure A.5a: Similar to Figure A.1a, but for SDSS J0925+4004 at $d = 84$ kpc from the LRG. Note that while the saturated C III λ977 transition is partially contaminated on the blue side, we can still robustly constrain a lower limit on the C III column density.

Table A.4b: Ionization modeling results for the absorber along SDSS J0803+4332, at $d = 79$ kpc from the LRG

Component	$N_{\rm metal}$	[M/H]		$\log n_{\rm H}/{\rm cm}^{-3}$	
		HM05	HM12	HM05	HM12
SC	1	$-0.91^{+0.48}_{-0.23}$	$-0.10^{+0.52}_{-0.22}$	< -3.18	< -3.16
1	1	$-1.17^{+0.54}_{-0.22}$	$-0.36^{+0.65}_{-0.21}$	< -3.50	< -3.58
2	1	$-0.16^{+0.52}_{-0.64}$	$+0.52^{+0.25}_{-0.67}$	< -2.84	< -3.08

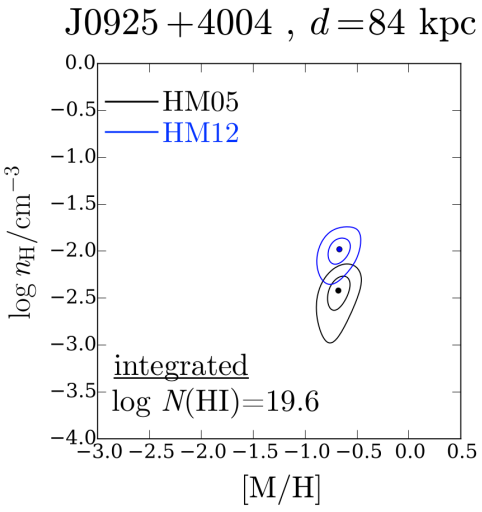

Figure A.5b: Probability distribution contours of gas metallicity and density for the integrated absorption near the LRG redshift, seen at $d = 84$ kpc from the LRG along sightline SDSS J0925+4004. Contour levels are the same as in Figure A.1b. Note the close agreement between the metallicities derived using the HM05 and HM12 UVBs, which can be attributed to the well-constrained O I column density in this system (see Section A.5).

Our Voigt profile analysis of the echelle spectrum of the Mg I and Mg II metal absorption has identified five absorption components which are tightly separated ($\lesssim$ 20 km s^{-1}) in velocity space. However, because of the lower resolution of the FUV COS spectrum and the fact that all H I and many metal transitions are saturated, we cannot reliably constrain the H I and metal column densities of individual components in this system. For that reason, we forgo component-by-component ionization analysis for this absorber and proceed by modeling the mean physical properties of the gas using the integrated column densities of H I and metal species (Table A.5a).

Our ionization analysis constrains the gas to a density of between $\log n_{\rm H}/{\rm cm}^{-3} = -2.0^{+0.1}_{-0.2}$ under HM05 and $\log n_{\rm H}/{\rm cm}^{-3} = -2.4^{+0.1}_{-0.4}$ under HM12 (Figure A.5b and Table A.5b). The gas density is well-constrained due to a combination of lower limits on the column density for saturated C III and Si III absorption, which set an upper bound on gas density, and the upper limit on Fe III column density, which imposes a lower bound on gas density. At the adopted gas density, CLOUDY under-predicts the observed Si IV column density by almost 0.5 dex, suggesting that some of the observed Si IV absorption likely arises from a lower-density gas phase.

The inferred gas metallicity is [M/H] $= -0.7 \pm 0.1$ under both HM05 and HM12 UVBs (Figure A.5b and Table A.5b). The close agreement in the derived metallicities between HM05 and HM12 is due to the well-constrained O I column density, which is insensitive to different ionizing background radiation fields in high N(H I) regimes (Section 4.3.1). We note that at this metallicity, the models over-predict the observed Fe II and Mg II column densities by 0.4 to 0.5 dex. The inferred depletions in *both* the observed Fe and Mg abundances are comparable to what have been observed in the Galactic halo (e.g., Savage & Sembach 1996; de Cia et al. 2016), and indicate the likely presence of dust grains in the gas (see also Zahedy et al. 2017).

This absorber was also studied in the COS-Halos survey. Using the Haardt & Madau (2001) UVB (which is similar of the HM05 UVB at energies $\lesssim$ 2 Ryd), Werk et al. (2014)

Table A.5a: Absorption properties along QSO sightline SDSS J0925+4004 at $d = 84$ kpc from the LRG

Component	Species	$\mathrm{d}v_c$ ($\mathrm{km\,s^{-1}}$)	$\log N_c$	b_c ($\mathrm{km\,s^{-1}}$)
all	H I	0.0 ± 1.7	19.58 ± 0.02	$36.2^{+0.7}_{-1.6}$
	C II	...	> 15.17	...
	C III	...	> 14.48	...
	N II	...	> 15.15	...
	N V	...	< 13.31	...
	O I	...	$15.63^{+0.11}_{-0.07}$	...
	Mg I	...	$12.51^{+0.05}_{-0.04}$	...
	Mg II	...	$13.95^{+0.05}_{-0.04}$	...
	Si II	...	> 14.60	...
	Si III	...	> 14.10	...
	Si IV	...	$13.61^{+0.07}_{-0.12}$	...
	Fe II	...	$14.12^{+0.08}_{-0.10}$	...
	Fe III	...	< 14.05	...

Table A.5b: Ionization modeling results for the absorber along SDSS J0925+4004 at $d = 84$ kpc from the LRG

Component	N_{metal}	[M/H]		$\log n_{\mathrm{H}}/\mathrm{cm^{-3}}$	
		HM05	HM12	HM05	HM12
SC	10	$-0.68^{+0.10}_{-0.11}$	$-0.69^{+0.10}_{-0.11}$	$-1.98^{+0.08}_{-0.22}$	$-2.42^{+0.08}_{-0.36}$

inferred a mean metallicity of [M/H] = -0.7 ± 0.2 under the Haardt & Madau (2001) UVB. In an updated analysis using the HM12 UVB, Prochaska et al. (2017) found a mean metallicity of [M/H] = $-0.81^{+0.15}_{-0.14}$. The chemical abundance estimated from these COS-Halos studies is consistent with what we find in our analysis.

A.6 SDSS J0950+4831 at $d = 94$ kpc

This LRG is at redshift $z_{\rm LRG} = 0.2119$. A strong LLS with a total N(H I) of $\log N({\rm H\,I})/{\rm cm}^{-2} = 18.51^{+0.05}_{-0.10}$ is present near the galaxy redshift (Figure A.6a). In addition, the following ionic metal species are detected: C II, C III, N II, O I, O VI, Mg I, Mg II, Si II, Si III, Si IV, Fe II, and Fe III.

We identify four components in the absorber, based on a combined Voigt profile analysis of H I and the corresponding metal absorption profiles (Figure A.6a and Table A.6a). The H I component structure is in very good agreement with those of the low- and intermediate-ionization metals. The observed velocity spread is $\Delta v \approx 200$ km s^{-1} from the bluest to the reddest component. Most (98 percent) of the H I column density is concentrated in component 3 at $z_{\rm abs} = 0.21166$, or 59 km s^{-1} blueward of the LRG. One other component has $\log N_c({\rm H\,I})/{\rm cm}^{-2} > 16$, component 2 at $dv_c = -32$ km s^{-1} . These two high N(H I) components exhibit associated absorption of multiple metal species, whereas optically thin components 1 and 4 at $dv_c = +22$ and $+61$ km s^{-1} show metal absorption only in intermediate ions (e.g., C III).

Comparing the H I and Mg II linewidths of the optically thick components 2 and 3, the implied gas temperature is $T \approx (1-3)\times10^4$ K for both components, with $b_{\rm nt} \approx 10-12\,{\rm km\ s}^{-1}$ of non-thermal line broadening. For components 1 and 4, the observed H I linewidths constrain the gas temperature to $T \lesssim 4\times10^4$ K, consistent with those of the optically thick components.

Our ionization analysis shows that the absorbing gas separates into two different regimes of gas density, as shown in Figure A.6b and Table A.6b. The inferred densities for the lower

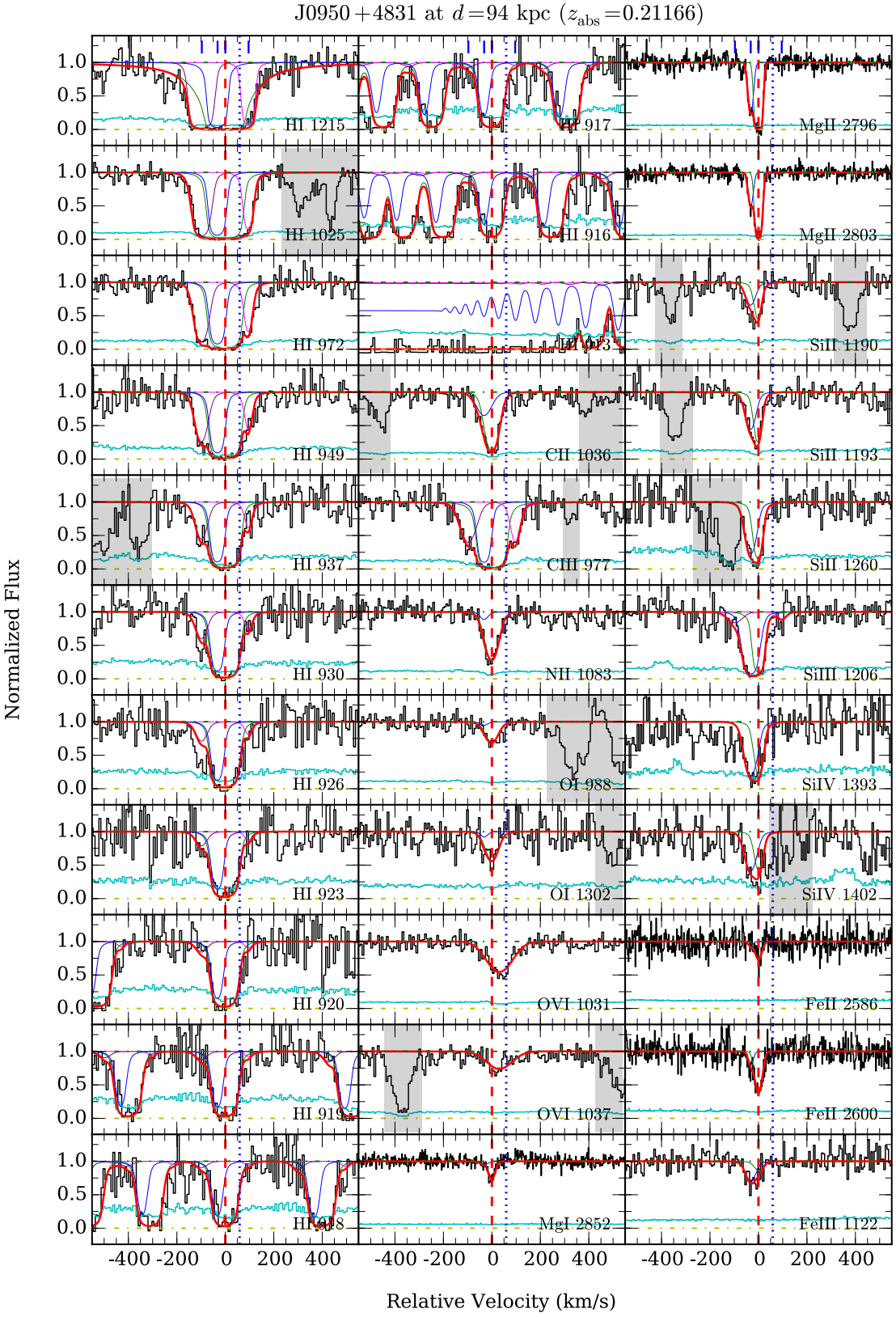

Figure A.6a: Similar to Figure A.1a, but for SDSS J0950+4831 at $d = 94$ kpc from the LRG.

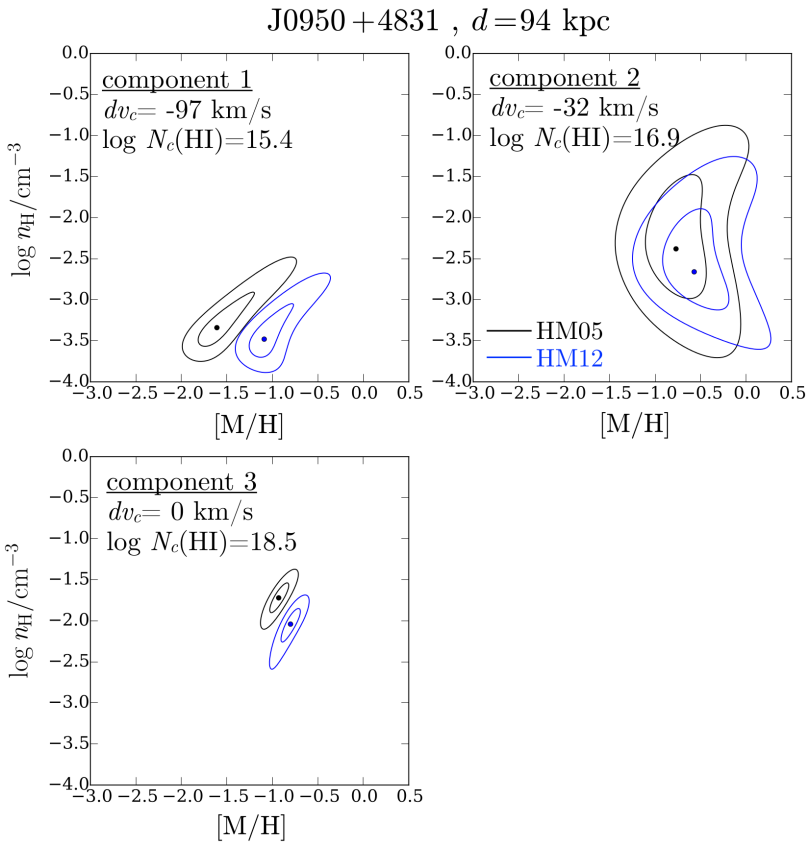

Figure A.6b: Probability distribution contours of gas metallicity and density for individual absorption components identified along SDSS J0950+4831, at d = 94 kpc from the LRG. Contour levels are the same as in Figure A.1b. Not plotted here is component 4 at $dv_c = +96$ km s^{-1}, which has the lowest N(H I) in the absorber ($\log N_c$(H I)/cm$^{-2} = 15.1$) and exhibits associated metal absorption in only C III, resulting in weak constraints on the gas metallicity and density (see Table A.6b).

N(H I) gas in components 1 and 4 are low, $\log n_{\rm H}/{\rm cm}^{-3} \lesssim -3$ under both HM05 and HM12 UVBs. In contrast, models for the optically thick ($\log N({\rm H\,I})/{\rm cm}^{-2} \gtrsim 17$) components 2 and 3 require higher densities to match the observations, from $\log n_{\rm H}/{\rm cm}^{-3} = -2.7^{+0.8}_{-0.4}$ (HM12) to $\log n_{\rm H}/{\rm cm}^{-3} = -2.4^{+0.8}_{-0.6}$ (HM05) for component 2, and from $\log n_{\rm H}/{\rm cm}^{-3} = -2.0^{+0.1}_{-0.3}$ (HM12) to $\log n_{\rm H}/{\rm cm}^{-3} = -1.7 \pm 0.2$ (HM05) for component 3. A caveat from the analysis is that over the allowed gas densities, CLOUDY under-predicts the absorption column density of Si IV by more than 1 dex for optically thick components 2 and 3, indicating that most of the Si IV absorption likely arises from a lower-density gas phase.

Similarly, our CLOUDY photoionization models indicate that the optically thin and thick gases are well-separated in metallicity space (Figure A.6b and Table A.6b). The observed ionic column densities in the lower N(H I) components 1 and 4 are consistent with a low-metallicity gas of [M/H] ~ -1.6 under HM05 or [M/H] ~ -1.0 under HM12, for both components. In contrast, the inferred metallicities for component 2 and 3 are sub-solar, from [M/H] $= -0.8 \pm 0.3$ (HM05) to [M/H] $= -0.6 \pm 0.3$ (HM12) for component 2, and from [M/H] $= -0.9 \pm 0.1$ (HM05) to [M/H] $= -0.8 \pm 0.1$ (HM12). The close agreement between HM05- and HM12-derived metallicities for component 3 is due to the well-constrained O I column density, which scales proportionally with metallicity but is insensitive to different ionizing radiation fields. Finally, we note that the bulk of the absorption (component 3) is consistent with arising from a gas with an $\alpha-$element enhanced abundance pattern of [Fe/α] $\approx -0.2 \pm 0.1$.

This LLS was previously studied in the COS-Halos survey. Using the Haardt & Madau (2001) UVB (which is similar of the HM05 UVB at energies $\lesssim 2$ Ryd), Werk et al. (2014) inferred a mean metallicity of [M/H] $= -1.0^{+1.0}_{-0.5}$ and density of between $\log n_{\rm H}/{\rm cm}^{-3} = -3.8$ and $\log n_{\rm H}/{\rm cm}^{-3} = -3.2$ under the Haardt & Madau (2001) UVB. In an updated analysis using the HM12 UVB, Prochaska et al. (2017) found a mean metallicity of [M/H] $= -0.91^{+0.14}_{-0.10}$ and density of $\log n_{\rm H}/{\rm cm}^{-3} = -2.8 \pm 0.2$. The Prochaska et al. (2017) values are consistent with what we find in our analysis using the single-clump model, after accounting

for the difference in the adopted redshift of the HM12 UVB spectrum used in both studies.

The strong O VI absorption in this system can be fitted by a single component centered at $dv_c = +31$ km s^{-1}. The O VI absorption profile is broad with a Doppler linewidth of 66 km s^{-1}, and a column density of $\log N(\mathrm{O\,VI})/\mathrm{cm}^{-2} = 14.32 \pm 0.03$. No low- or intermediate-ionization metal or H I component is found to correspond with the O VI absorption in velocity space (Figure A.6a), with the O VI doublet situated at $\Delta v = +31$ km s^{-1} from the nearest low-ionization component.

A.7 SDSS J1127+1154 at $d = 99$ kpc

This LRG is found at $z_{\mathrm{LRG}} = 0.4237$. As shown in Figure A.7a, an H I absorber with a total N(H I) of $\log N(\mathrm{H\,I})/\mathrm{cm}^{-2} = 15.81 \pm 0.06$ is present near the LRG redshift. The HI absorption is accompanied by detections of C III, Mg II, Fe II, and O VI metal species.

The HI absorption profile can be decomposed into two individual components of comparable strengths, $\log N_c(\mathrm{H\,I})/\mathrm{cm}^{-2} = 15.4 - 15.6$ (Figure A.7a and Table A.7a). The stronger H I absorption component (component 2) occurs 171 km s^{-1} redward of the LRG at $z_{\mathrm{abs}} = 0.42451$, whereas the weaker component 1 occurs at $dv_c = -72$ km s^{-1} from this component. A curious feature of this absorption system is while the Mg II and C III absorption are of comparable strengths in both components, Fe II is detected only in component 1 (Figure A.7a), which suggests a difference in [Fe/Mg] abundance ratio between the two components.

The velocity spread of the absorbing gas is $\Delta v \approx 75$ km s^{-1} from the bluer to redder components. The observed Doppler b parameters of individual H I and Mg II components indicate that the absorbing gas is relatively cool, $T \sim (2-4) \times 10^4$ K, with only a modest amount of non-thermal broadening in the gas, with $b_{\mathrm{nt}} \lesssim 6$ km s^{-1}.

The matching component structure between H I and low- to intermediate-ionization metals in the absorber justifies a single-phase photoionization model for the gas. As shown in Figure A.7b and Table A.7b, our ionization analysis finds little variation in gas densities

Table A.6a: Absorption properties along QSO sightline SDSS J0950+4831 at d = 94 kpc from the LRG

Component	Species	dv_c (km s^{-1})	$\log N_c$	b_c (km s^{-1})
all	H I	...	$18.51^{+0.05}_{-0.10}$	...
	C II	...	$14.76^{+0.13}_{-0.06}$	...
	C III	...	> 14.60	...
	N II	...	$14.47^{+0.07}_{-0.04}$	...
	N V	...	< 13.55	...
	O I	...	14.35 ± 0.05	...
	O VI	...	14.32 ± 0.03	...
	Mg I	...	11.86 ± 0.06	...
	Mg II	...	$13.80^{+0.06}_{-0.04}$	...
	Si II	...	$13.85^{+0.06}_{-0.05}$	...
	Si III	...	> 13.96	...
	Si IV	...	$14.00^{+0.22}_{-0.07}$	...
	Fe II	...	13.44 ± 0.03	...
	Fe III	...	14.06 ± 0.14	...
1	H I	$-96.9^{+7.5}_{-3.5}$	$15.43^{+0.11}_{-0.07}$	$25.8^{+5.1}_{-2.4}$
	C II	-96.9	< 12.91	10
	C III	-96.9	$13.57^{+0.06}_{-0.11}$	$36.1^{+8.7}_{-7.1}$
	N II	-96.9	< 13.07	10
	O I	-96.9	< 13.47	10
	Mg I	-96.9	< 10.90	10
	Mg II	-96.9	< 11.43	10
	Si II	-96.9	< 12.40	10
	Si III	-96.9	$12.25^{+0.29}_{-0.21}$	$39.3^{+6.6}_{-19.1}$
	Si IV	-96.9	< 12.49	10
	Fe II	-96.9	< 12.12	10
	Fe III	-96.9	< 13.21	10
2	H I	-32.1	$16.94^{+0.35}_{-0.74}$	$15.0^{+2.6}_{-6.5}$
	C II	-32.1	$13.99^{+0.09}_{-0.14}$	$36.9^{+13.8}_{-5.7}$
	C III	-32.1	> 13.72	< 27.5
	N II	-32.1	< 13.27	10
	O I	-32.1	< 13.45	10
	Mg I	-32.1	< 10.85	10
	Mg II	$-32.1^{+1.7}_{-0.8}$	$12.87^{+0.07}_{-0.02}$	$12.5^{+2.1}_{-0.5}$
	Si II	-32.1	$13.45^{+0.09}_{-0.06}$	$23.6^{+7.1}_{-4.1}$
	Si III	-32.1	> 13.38	< 40.1
	Si IV	-32.1	$13.75^{+0.16}_{-0.09}$	$27.5^{+9.0}_{-6.8}$
	Fe II	-32.1	12.58 ± 0.15	13.1 ± 5.4
	Fe III	-32.1	13.92 ± 0.12	23.4 ± 9.2
3	H I	0.0 ± 0.9	$18.50^{+0.05}_{-0.10}$	$24.7^{+0.9}_{-1.1}$
	C II	0.0	$14.68^{+0.15}_{-0.06}$	$27.2^{+3.4}_{-4.1}$
	C III	0.0	> 14.45	< 36.8
	N II	0.0	$14.47^{+0.07}_{-0.04}$	$29.7^{+5.1}_{-2.7}$
	O I	0.0	14.35 ± 0.05	$30.2^{+10.3}_{-3.7}$
	Mg I	0.0	11.86 ± 0.06	18.1 ± 2.5
	Mg II	$0.0^{+0.7}_{-0.3}$	13.75 ± 0.05	$13.0^{+0.4}_{-0.8}$
	Si II	0.0	$13.63^{+0.09}_{-0.10}$	$16.0^{+2.7}_{-3.1}$
	Si III	0.0	> 13.59	< 23.3
	Si IV	0.0	$13.63^{+0.32}_{-0.21}$	$18.8^{+7.3}_{-7.2}$
	Fe II	$+0.4 \pm 1.3$	13.37 ± 0.03	$19.5^{+1.9}_{-1.2}$
	Fe III	0.0	13.49 ± 0.28	20.2 ± 19.5
4	H I	$+95.9^{+2.4}_{-6.0}$	$15.06^{+0.13}_{-0.08}$	$14.4^{+4.1}_{-1.6}$
	C II	$+95.9$	< 12.89	10
	C III	$+95.9$	$13.40^{+0.10}_{-0.11}$	$19.3^{+4.3}_{-5.3}$
	N II	$+95.9$	< 13.06	10
	O I	$+95.9$	< 13.51	10
	Mg I	$+95.9$	< 10.92	10
	Mg II	$+95.9$	< 11.40	10
	Si II	$+95.9$	< 12.23	10
	Si III	$+95.9$	< 12.10	10
	Si IV	$+95.9$	< 12.63	10
	Fe II	$+95.9$	< 12.14	10
	Fe III	$+95.9$	< 13.19	10
high-1	O VI	$+31.1 \pm 3.5$	14.32 ± 0.03	$65.7^{+6.5}_{-5.7}$
	N V	$+31.1$	< 13.55	

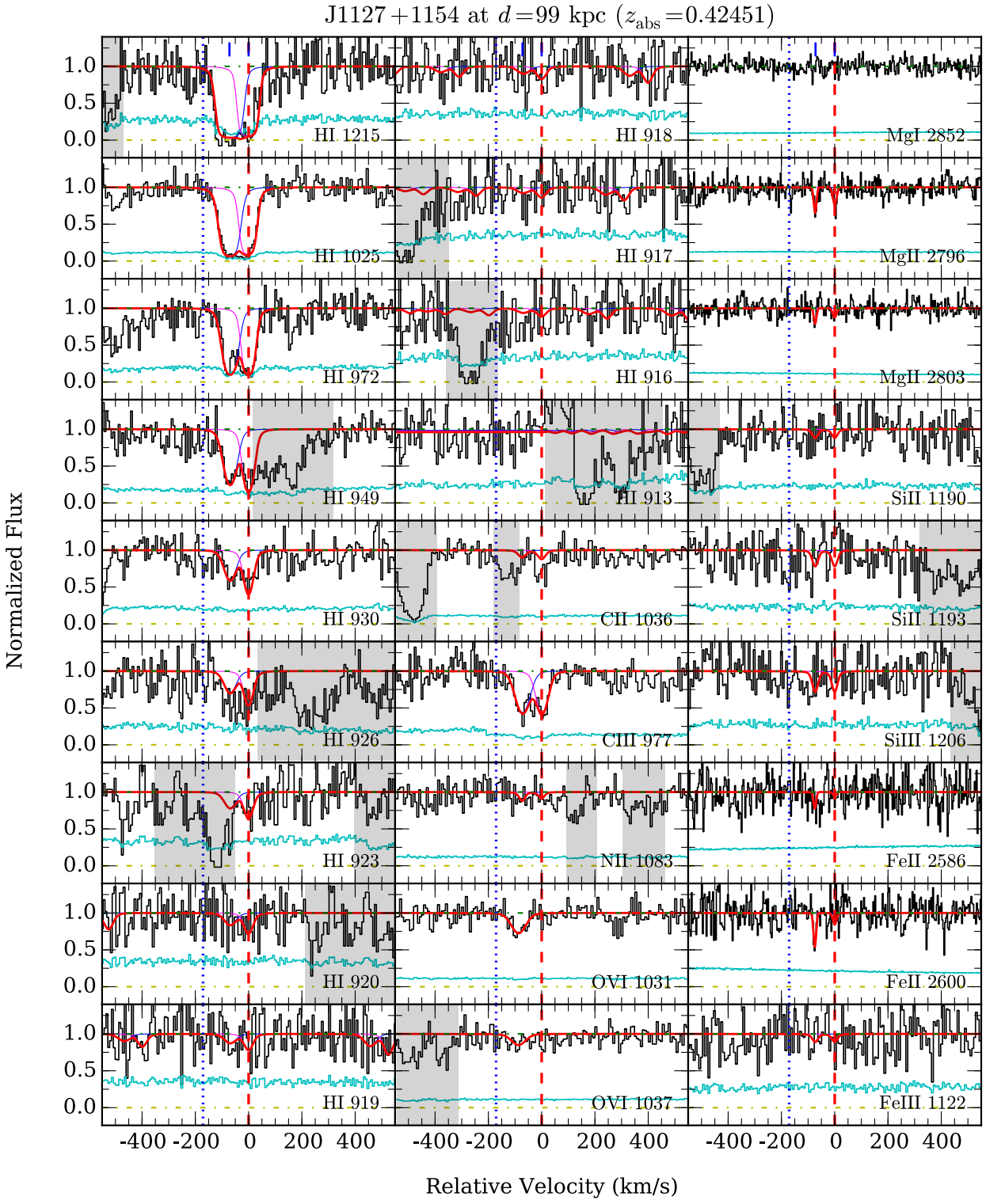

Figure A.7a: Similar to Figure A.1a, but for SDSS J1127+1154 at $d = 99$ kpc from the LRG.

Table A.6b: Ionization modeling results for the absorber along SDSS J0950+4831 at $d = 94$ kpc from the LRG

Component	$N_{\rm metal}$	[M/H]		$\log n_{\rm H}/{\rm cm}^{-3}$	
		HM05	HM12	HM05	HM12
SC	10	-0.97 ± 0.08	$-0.92^{+0.09}_{-0.08}$	$-1.96^{+0.12}_{-0.18}$	$-2.46^{+0.16}_{-0.26}$
1	2	$-1.59^{+0.47}_{-0.15}$	$-1.05^{+0.32}_{-0.14}$	$-3.34^{+0.50}_{-0.16}$	$-3.48^{+0.46}_{-0.16}$
2	7	$-0.76^{+0.36}_{-0.34}$	$-0.57^{+0.37}_{-0.34}$	$-2.42^{+0.86}_{-0.58}$	$-2.68^{+0.82}_{-0.36}$
3	10	-0.93 ± 0.10	$-0.81^{+0.09}_{-0.12}$	$-1.72^{+0.16}_{-0.20}$	$-2.02^{+0.12}_{-0.32}$
4	1	$-1.66^{+0.56}_{-0.17}$	$-0.90^{+0.58}_{-0.15}$	< -3.10	< -3.20

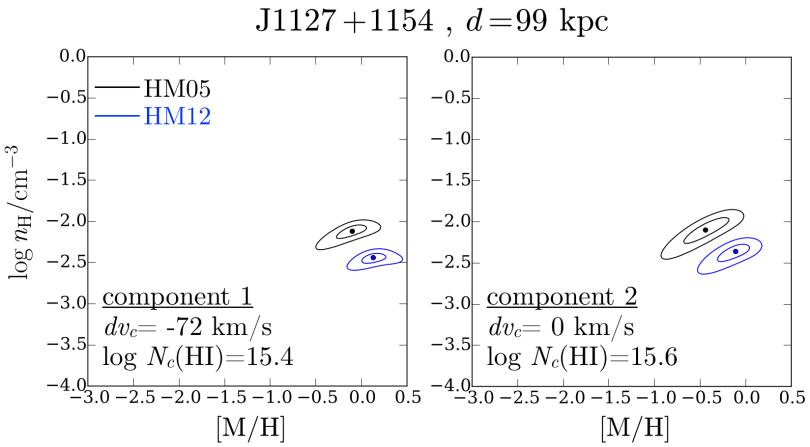

Figure A.7b: Probability distribution contours of gas metallicity and density for individual absorption components identified along SDSS J1127+1154, at $d = 99$ kpc from the LRG. Contour levels are the same as in Figure A.1b.

between the two components, where $\log n_{\rm H}/{\rm cm}^{-3} \approx -2.1$ is inferred under the HM05 UVB and $\log n_{\rm H}/{\rm cm}^{-3} \approx -2.4$ is inferred under HM12 UVB. In contrast, our models indicate a larger variation in chemical abundance. For component 2, we find a sub-solar metallicity of $[{\rm M/H}] = -0.4 \pm 0.2$ under HM05 and $[{\rm M/H}] = -0.1 \pm 0.2$ under HM12. A high chemical abundance, consistent with solar value, is inferred for component 1, where the CLOUDY models constrain the metallicity to $[{\rm M/H}] = -0.1 \pm 0.2$ under HM05 or $[{\rm M/H}] = +0.1 \pm 0.2$ under HM12. Furthermore, the unusual strength of Fe II absorption relative to that of Mg II in component 1 suggests that the gas is particularly iron-rich. The inferred $[{\rm Fe}/\alpha]$ for this component is $[{\rm Fe}/\alpha] \approx +1.0 \pm 0.3$, which is among the highest known in the literature (e.g, Narayanan et al. 2008; Zahedy et al. 2016; 2017b).

Finally, we note that a modest absorption of highly ionized O VI gas is detected at $dv_c = -86$ km s^{-1}. The O VI absorption consists of a single component with $\log N({\rm O\,VI})/{\rm cm}^{-2} = 13.79^{+0.08}_{-0.09}$ and a Doppler b value of of 32 km s^{-1}. No low- or intermediate-ionization metal or H I component is found to correspond with the O VI absorption in velocity space (Figure A.7a), with the O VI doublet situated at $\Delta v = -15$ km s^{-1} from the nearest component.

A.8 SDSS J1243+3539 at $d = 102$ kpc

The LRG is at $z_{\rm LRG} = 0.3896$. As shown in Figure A.8a, no H I absorption is detected within the adopted search window of ± 500 km s^{-1} from the LRG redshift. We are able to place a sensitive 2-σ column density upper limit of $\log N({\rm H\,I})/{\rm cm}^{-2} < 12.7$, calculated for an H I line with $b({\rm H\,I}) = 15$ km s^{-1} that is centered at the LRG redshift (Table A.8a).

A.9 SDSS J1550+4001 at $d = 107$ kpc

The LRG, which is at $z_{\rm LRG} = 0.3125$, has an H I absorber with a total $N({\rm H\,I})$ of $\log N({\rm H\,I})/{\rm cm}^{-2} = 16.61 \pm 0.04$. This pLLS also exhibits corresponding absorption of ionic species C II, C III, N III, Mg II, Si II, Si III, Fe II, and O VI (Figure A.9a).

Table A.7a: Absorption properties along QSO sightline SDSS J1127+1154 at $d = 99$ kpc from the LRG

Component	Species	$\mathrm{d}v_c$ ($\mathrm{km\,s^{-1}}$)	$\log N_c$	b_c ($\mathrm{km\,s^{-1}}$)
all	H I	...	15.81 ± 0.06	...
	C II	...	< 13.43	...
	C III	...	13.73 ± 0.04	...
	N II	...	< 13.52	...
	N V	...	< 13.64	...
	O I	...	< 13.97	...
	O VI	...	$13.79^{+0.08}_{-0.09}$	...
	Mg I	...	< 11.64	...
	Mg II	...	$12.39^{+0.14}_{-0.12}$	...
	Si II	...	< 13.08	...
	Si III	...	< 12.61	...
	Fe II	...	$12.88^{+0.21}_{-0.29}$	...
	Fe III	...	< 14.00	...
1	H I	$-71.5^{+3.0}_{-1.6}$	$15.42^{+0.07}_{-0.06}$	$25.6^{+2.3}_{-0.9}$
	C II	-71.5	< 13.22	10
	C III	-71.5	13.45 ± 0.06	$30.5^{+10.0}_{-5.2}$
	N II	-71.5	< 13.10	10
	O I	-71.5	< 13.50	10
	Mg I	-71.5	< 11.18	10
	Mg II	$-73.3^{+1.4}_{-1.5}$	$12.15^{+0.21}_{-0.15}$	$3.0^{+3.1}_{-1.6}$
	Si II	-71.5	< 12.70	10
	Si III	-71.5	< 12.26	10
	Fe II	$-74.5^{+1.5}_{-1.5}$	$12.88^{+0.21}_{-0.29}$	2.7 ± 2.6
	Fe III	-71.5	< 13.50	10
2	H I	$0.0^{+3.2}_{-2.0}$	$15.59^{+0.06}_{-0.10}$	$18.4^{+1.3}_{-1.4}$
	C II	0.0	< 13.20	10
	C III	0.0	13.41 ± 0.07	$24.8^{+6.8}_{-4.6}$
	N II	0.0	< 13.05	10
	O I	0.0	< 13.48	10
	Mg I	0.0	< 11.19	10
	Mg II	$0.0^{+3.2}_{-3.1}$	$12.02^{+0.09}_{-0.23}$	$7.4^{+6.4}_{-3.7}$
	Si II	0.0	< 12.68	10
	Si III	0.0	< 12.30	10
	Fe II	0.0	< 12.40	10
	Fe III	0.0	< 13.50	10
high-1	O VI	-86.4 ± 5.3	$13.79^{+0.08}_{-0.09}$	$32.2^{+16.8}_{-6.1}$
	N V	-86.4	< 13.64	

Table A.7b: Ionization modeling results for the absorber along SDSS J1127+1154, at $d = 99$ kpc from the LRG

Component	$N_{\rm metal}$	[M/H]		$\log n_{\rm H}/{\rm cm}^{-3}$	
		HM05	HM12	HM05	HM12
SC	3	$-0.22^{+0.11}_{-0.18}$	$+0.07 \pm 0.12$	$-2.10^{+0.04}_{-0.10}$	$-2.40^{+0.02}_{-0.06}$
1	3	$-0.11^{+0.14}_{-0.21}$	$+0.12^{+0.17}_{-0.14}$	$-2.12^{+0.04}_{-0.12}$	$-2.46^{+0.04}_{-0.06}$
2	2	$-0.44^{+0.19}_{-0.26}$	$-0.13^{+0.13}_{-0.22}$	$-2.08^{+0.08}_{-0.20}$	$-2.36^{+0.04}_{-0.16}$

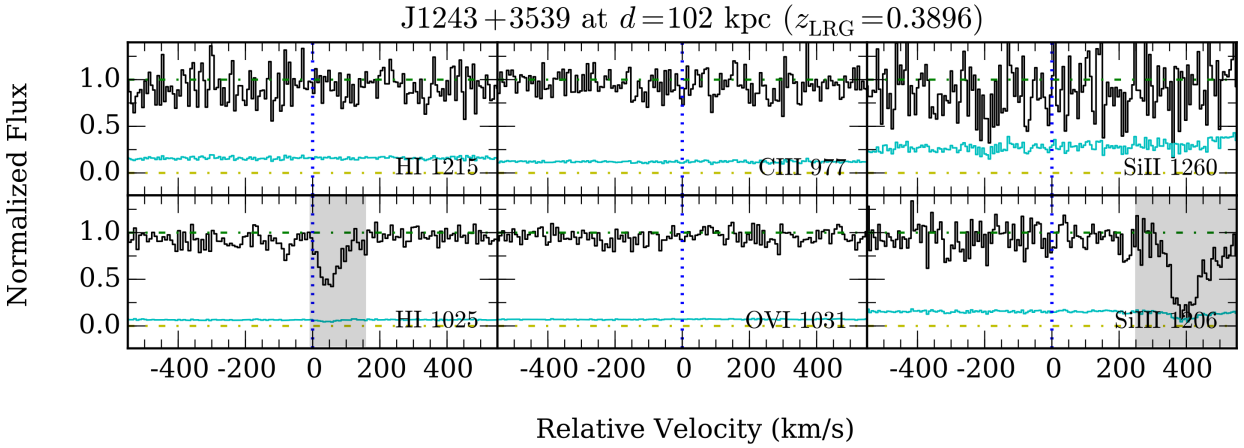

Figure A.8a: Similar to Figure A.1a, but for SDSS J1243+3539 at $d = 102$ kpc from the LRG.

Table A.8a: Absorption properties along QSO sightline SDSS J1243+3539 at $d = 102$ kpc from the LRG

Component	Species	dv_c (km s^{-1})	$\log N_c$	b_c (km s^{-1})
...	H I	0.0	< 12.65	15
	C II	0.0	< 12.80	10
	C III	0.0	< 12.24	10
	N II	0.0	< 12.91	10
	N III	0.0	< 13.06	10
	N V	0.0	< 13.21	30
	O I	0.0	< 13.49	10
	O VI	0.0	< 13.06	30
	Si II	0.0	< 12.38	10
	Si III	0.0	< 11.91	10
	Fe II	0.0	< 12.40	10
	Fe III	0.0	< 13.50	10

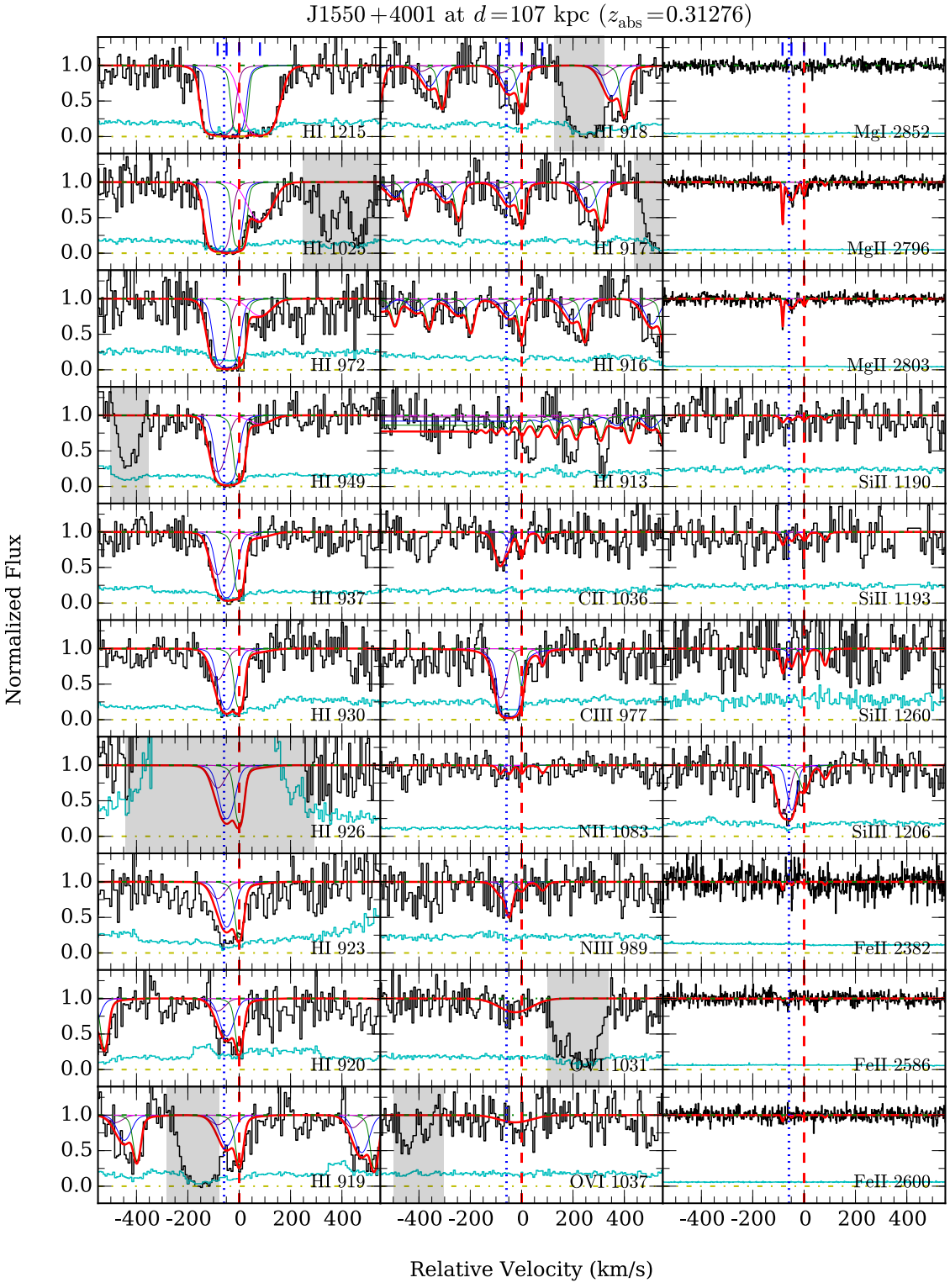

Figure A.9a: Similar to Figure A.1a, but for SDSS J1550+4001 at d = 107 kpc from the LRG. The excess flux seen redward of the Lyman limit can be attributed to a second point source that falls within the same COS aperture as the background QSO (see Paper I).

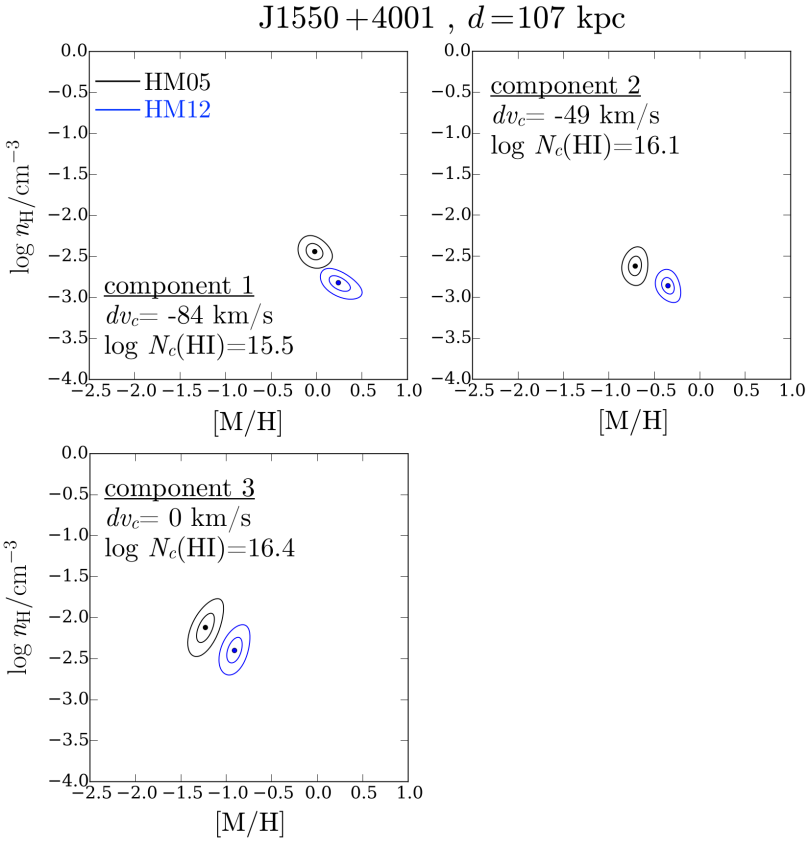

Figure A.9b: Probability distribution contours of gas metallicity and density for individual absorption components identified along SDSS J1550+4001, at $d = 107$ kpc from the LRG. Contour levels are the same as in Figure A.1b. Not plotted here is component 4 at $dv_c = +81$ km s^{-1}, which has the lowest N(H I) in the absorber ($\log N_c$(H I)/cm$^{-2} = 14.6$) and shows only C III metal absorption, resulting in weak constraints on the gas metallicity and density (see Table A.9b).

The HI absorption profile consists of four individual components (Figure A.9a and Table A.9a). The strongest H I absorption is in component 3 at $z_{\rm abs} = 0.31276$, or 58 km s^{-1} redward of the LRG. This component contributes to $\sim$ 60% of the total N(H I) of the absorber. In contrast, the strongest metal absorption corresponds to weaker H I components, component 1 for low ions (e.g., C II and Mg II) and component 2 for intermediate ions (e.g., C III), suggesting a variation in chemical abundance among different components.

The observed velocity spread of the absorbing gas is $\Delta v = 164$ km s^{-1} from the bluest to reddest component. Our Voigt profile analysis shows that the absorption profiles of both low- and intermediate-ionization metals match the component structure of H I very well (see Figure A4a). By comparing the Doppler b linewidths of H I and ionic metal components, we find that the bulk of the absorbing gas (component 3) is cool, $T \sim 10^4$ K, with a modest amount of non-thermal broadening, $b_{\rm nt} \approx 8\,{\rm km\ s^{-1}}$. The other three components are at higher temperatures, $T \sim (3-6) \times 10^4$ K, with inferred non-thermal broadening that varies from $b_{\rm nt} \lesssim 5\,{\rm km\ s^{-1}}$ in component 1 to $b_{\rm nt} \gtrsim 20$ km s^{-1} in components 2 and 4.

As shown in Figure A.9b and Table A.9b, our ionization analysis finds a modest variation in gas densities across different components, which range from $\log n_{\rm H}/{\rm cm}^{-3} \approx -2.6$ to $\log n_{\rm H}/{\rm cm}^{-3} \approx -2.1$ under the HM05 UVB, and from $\log n_{\rm H}/{\rm cm}^{-3} \approx -2.9$ to $\log n_{\rm H}/{\rm cm}^{-3} \approx -2.4$ under the HM12 UVB. To reproduce the observed metal column densities, the required chemical abundances range from sub-solar values of between [M/H] $= -1.2 \pm 0.1$ (HM05) and [M/H] $= -0.9 \pm 0.1$ (HM12) for the strongest component, to at least solar metallicity for component 1, [M/H] $= 0.0 \pm 0.1$ under HM05 and [M/H] $= 0.2 \pm 0.1$ under HM12.

This absorber was also studied in the COS-Halos survey. Using the Haardt & Madau (2001) UVB (which is similar of the HM05 UVB at energies $\lesssim 2$ Ryd), Werk et al. (2014) inferred a mean metallicity of [M/H] $= -0.8 \pm 0.2$ and density of between $\log n_{\rm H}/{\rm cm}^{-3} = -4.0$ and $\log n_{\rm H}/{\rm cm}^{-3} = -3.5$ under the Haardt & Madau (2001) UVB. In an updated analysis using the HM12 UVB, Prochaska et al. (2017) found a mean metallicity of [M/H] $= -0.35^{+0.05}_{-0.05}$ and density of $\log n_{\rm H}/{\rm cm}^{-3} = -2.75 \pm 0.2$, which are in agreement with what

we find in our analysis using the single-clump model (Table A6b).

We detect a weak O VI absorption at $dv_c = -25$ km s^{-1}. The O VI absorption profile consists of a single component with $\log N(\mathrm{O\,VI})/\mathrm{cm}^{-2} = 14.0 \pm 0.1$ and a broad Doppler b value of of 83 km s^{-1}. No low- or intermediate-ionization metal or H I component is found to correspond with the O VI absorption in velocity space (Figure A.9a), with the O VI doublet situated at $\Delta v = -24$ km s^{-1} from the nearest low-ionization component.

A.10 SDSS J0246−0059 at $d = 109$ kpc

This LRG is at $z_{\mathrm{LRG}} = 0.4105$. As shown in Figure A.10a, a LLS with a total N(H I) of $\log N(\mathrm{H\,I})/\mathrm{cm}^{-2} = 17.21 \pm 0.01$ is present near the LRG redshift. The HI absorption is accompanied by ionic metal detections of C II, C III, Mg II, Si II, Si III, and O VI.

Our Voigt profile analysis indicates that the HI absorption profile can be decomposed into six components, with the bulk of the HI gas concentrated on two components with $\log N_c(\mathrm{H\,I})/\mathrm{cm}^{-2} > 16$ (Figure A.10a and Table A.10a). The strongest H I absorption is in component 4 at $z_{\mathrm{abs}} = 0.41172$ or +259 km s^{-1} from the LRG, which contributes to a majority (76%) of the total N(H I). Most of the remaining H I absorption is found in component 2 which is found at $dv_c = -229$ km s^{-1} from the strongest component. An interesting feature of this absorption system, which can be seen in Figure A.10a, is that the strongest low- and intermediate-ionization metal absorption (e.g., Mg II and Si III) occurs in component 2, instead of in component 4 where the N(H I) is almost four times higher. The discrepancy between where the bulk of the H I gas is located, and where most of the heavy metals are, suggests a significant variation in metallicities across different components. We also note that no corresponding absorption of metal ions is detected in the two components with the weakest H I absorption, components 1 and 3.

The observed velocity spread of the absorbing gas is $\Delta v \approx 360$ km s^{-1} from the bluest to reddest component. Based on the Doppler b parameters of individual H I components ($b_c(\mathrm{H\,I}) < 60\,\mathrm{km\ s}^{-1}$), we place a temperature upper limit of $T \lesssim 2 \times 10^5$ K for all compo-

Table A.9a: Absorption properties along QSO sightline SDSS J1550+4001 at $d = 107$ kpc from the LRG

Component	Species	dv_c ($\mathrm{km\,s^{-1}}$)	$\log N_c$	b_c ($\mathrm{km\,s^{-1}}$)
all	H I	...	16.61 ± 0.04	...
	C II	...	$14.16^{+0.11}_{-0.07}$	...
	C III	...	> 14.53	...
	N II	...	< 13.59	...
	N III	...	$13.97^{+0.22}_{-0.19}$	...
	N V	...	< 13.62	...
	O I	...	< 14.26	...
	O VI	...	$13.96^{+0.11}_{-0.12}$	...
	Mg I	...	< 11.27	...
	Mg II	...	12.70 ± 0.02	...
	Si II	...	12.57 ± 0.30	...
	Si III	...	$13.42^{+0.12}_{-0.06}$	...
	Fe II	...	11.84 ± 0.20	...
1	H I	$-84.1^{+3.1}_{-2.4}$	$15.54^{+0.13}_{-0.17}$	$32.6^{+2.2}_{-1.7}$
	C II	-84.1	$14.01^{+0.12}_{-0.09}$	$23.4^{+10.8}_{-4.6}$
	C III	-84.1	$13.58^{+0.44}_{-0.34}$	$26.0^{+10.1}_{-9.9}$
	N II	-84.1	< 13.09	10
	N III	-84.1	< 13.42	10
	O I	-84.1	< 13.78	10
	Mg I	-84.1	< 10.76	10
	Mg II	-84.1 ± 0.3	$12.29^{+0.04}_{-0.03}$	2.8 ± 0.5
	Si II	-84.1	12.57 ± 0.30	$8.0^{+7.1}_{-3.7}$
	Si III	-84.1	$13.12^{+0.14}_{-0.10}$	$32.7^{+9.4}_{-8.3}$
	Fe II	-84.1	11.84 ± 0.20	4.4 ± 4.2
2	H I	$-49.2^{+2.9}_{-2.4}$	$16.12^{+0.08}_{-0.09}$	$30.7^{+4.6}_{-2.9}$
	C II	-49.2	< 13.17	10
	C III	-49.2	> 14.34	< 30.8
	N II	-49.2	< 13.09	10
	N III	-49.2	$13.97^{+0.22}_{-0.19}$	$13.1^{+6.3}_{-2.0}$
	O I	-49.2	< 13.76	10
	Mg I	-49.2	< 10.78	10
	Mg II	-49.2 ± 1.3	12.36 ± 0.03	$19.6^{+2.2}_{-1.7}$
	Si II	-49.2	< 12.37	10
	Si III	-49.2	$12.97^{+0.21}_{-0.25}$	$18.4^{+10.9}_{-6.8}$
	Fe II	-49.2	< 11.60	10
3	H I	0.0 ± 0.3	$16.37^{+0.07}_{-0.08}$	$12.7^{+0.9}_{-1.0}$
	C II	0.0	$13.64^{+0.15}_{-0.19}$	$12.4^{+6.5}_{-4.5}$
	C III	0.0	$13.20^{+0.50}_{-0.44}$	$10.0^{+10.3}_{-3.2}$
	N II	0.0	< 13.07	10
	N III	0.0	< 13.40	10
	O I	0.0	< 13.78	10
	Mg I	0.0	< 10.78	10
	Mg II	0.0 ± 1.2	$11.89^{+0.05}_{-0.07}$	$8.6^{+2.1}_{-1.6}$
	Si II	0.0	< 12.44	10
	Si III	0.0	$12.60^{+0.13}_{-0.22}$	$21.3^{+12.5}_{-7.0}$
	Fe II	0.0	< 11.60	10
4	H I	$+80.7^{+5.1}_{-8.3}$	$14.59^{+0.06}_{-0.05}$	$55.2^{+7.7}_{-4.9}$
	C II	$+80.7$	< 13.20	10
	C III	$+80.7$	$12.84^{+0.19}_{-0.42}$	$48.5^{+18.5}_{-26.1}$
	N II	$+80.7$	< 13.08	10
	N III	$+80.7$	< 13.41	10
	O I	$+80.7$	< 13.82	10
	Mg I	$+80.7$	< 10.80	10
	Mg II	$+80.7$	< 11.31	10
	Si II	$+80.7$	< 12.39	10
	Si III	$+80.7$	< 12.20	10
	Fe II	$+80.7$	< 11.60	10
high-1	O VI	-25.2 ± 18.2	$13.96^{+0.11}_{-0.12}$	82.9 ± 27.1
	N V	-25.2	< 13.62	

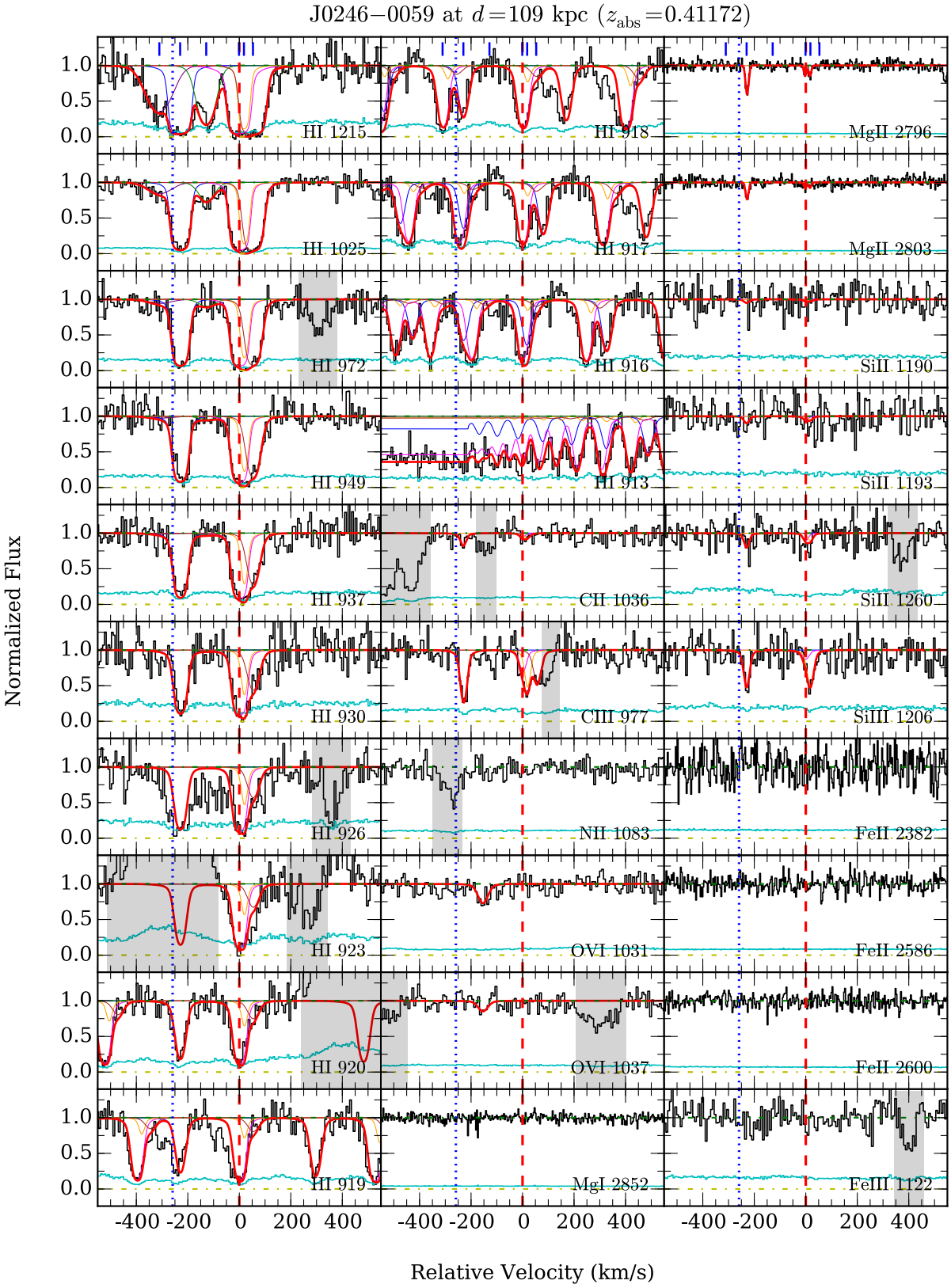

Figure A.10a: Similar to Figure A.1a, but for SDSS J0246−0059 at d = 109 kpc from the LRG.

Table A.9b: Ionization modeling results for the absorber along SDSS J1550+4001, at $d = 107$ kpc from the LRG

Component	$N_{\rm metal}$	[M/H]		$\log n_{\rm H}/{\rm cm}^{-3}$	
		HM05	HM12	HM05	HM12
SC	6	$-0.76^{+0.03}_{-0.04}$	-0.40 ± 0.04	$-2.34^{+0.06}_{-0.08}$	$-2.64^{+0.06}_{-0.08}$
1	6	$-0.03^{+0.10}_{-0.08}$	$+0.24^{+0.11}_{-0.10}$	$-2.44^{+0.06}_{-0.10}$	-2.84 ± 0.08
2	3	$-0.71^{+0.06}_{-0.07}$	$-0.35^{+0.06}_{-0.07}$	$-2.62^{+0.10}_{-0.12}$	$-2.86^{+0.08}_{-0.10}$
3	4	$-1.23^{+0.09}_{-0.10}$	-0.91 ± 0.08	$-2.12^{+0.16}_{-0.18}$	-2.40 ± 0.14
4	1	$-1.48^{+0.78}_{-0.50}$	$-0.71^{+0.59}_{-0.55}$	< -2.26	< -2.54

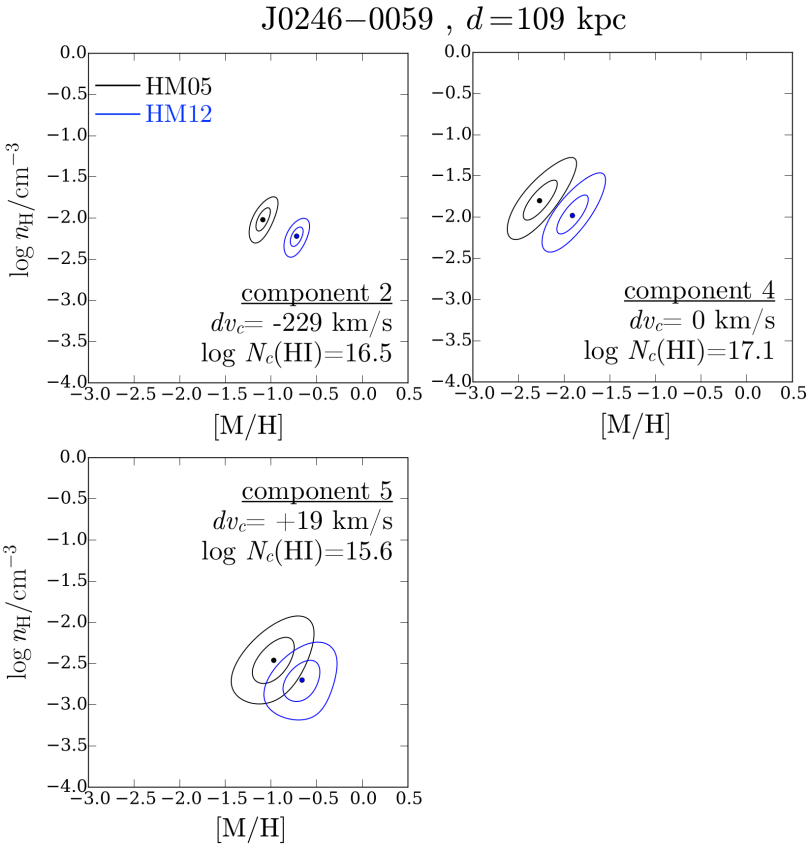

Figure A.10b: Probability distribution contours of gas metallicity and density for individual absorption components identified along SDSS J0246−0059, at $d = 109$ kpc from the LRG. Contour levels are the same as in Figure A.1b. Components 1 and 3 show weaker H I absorption ($\log\ N_c({\rm H\,I}) \lesssim 14$) and are not shown here, because the absence of metal detections for these components result in a lack of strong constraints on the metallicity and density of the gas (see Table A.10b). Also not plotted here is component 6 at $dv_c = +54$ km s^{-1}, which has $\log N_c({\rm H\,I})/{\rm cm}^{-2} = 15.6$ yet shows little metal absorption. The C III absorption seen in component 6, along with upper limits on the column density of other ions, still allows us to constrain the gas density to $n_{\rm H} \lesssim 10^{-3}\,{\rm cm}^{-3}$ and the metallicity of [M/H] $\lesssim -1$ (Table A.10b).

nents. For two components with $\log N(\mathrm{H\,I})/\mathrm{cm}^{-2} > 16$, components 2 and 4, the best-fit line profiles are narrow with $b_c(\mathrm{H\,I}) = 16 - 18\,\mathrm{km\ s}^{-1}$, indicating that the absorption arises in relatively cool gas with $T \lesssim 2 \times 10^4$ K. Moreover, these two components also have associated Mg II detections in the high-resolution MIKE data. Comparing the Mg II and H I linewidths for these two components shows that there is little non-thermal broadening in the gas, with $b_{\mathrm{nt}} \lesssim 3\,\mathrm{km\ s}^{-1}$.

The well-matched component structure between H I and low- to intermediate-ionization metals in this system justifies a single-phase photoionization model. As shown in Figure A.10b and Table A.10b, our ionization analysis indicates only a modest variation in gas densities across different components, where values between $\log n_{\mathrm{H}}/\mathrm{cm}^{-3} \approx -2.5$ and $\log n_{\mathrm{H}}/\mathrm{cm}^{-3} \approx -2.0$ are found under the HM05 UVB. A similar spread in of n_{H} are found under the HM12 UVB albeit at lower (~ 0.2 dex) densities.

In contrast to the relative uniformity seen in n_{H}, a large variation in metallicities is seen in the gas. As previously mentioned, while the strongest H I absorption is found in component 4 ($\log N_c(\mathrm{H\,I})/\mathrm{cm}^{-2} = 17.1$), that component exhibits weak low- and intermediate-ionization metal absorption, suggesting low gas-phase metallicity. Indeed, our analysis infers a very low metallicity for this component, from $[\mathrm{M/H}] = -2.3 \pm 0.2$ under HM05 to $[\mathrm{M/H}] = -1.9 \pm 0.2$ under HM12. For two other components with detection of multiple ionic metal species, components 2 and 5, significantly higher chemical abundances are required to match the data, from $[\mathrm{M/H}] \approx -1$ under HM05 to $[\mathrm{M/H}] \approx -0.7$ under HM12. The large (more than a factor of 10) variations of metallicities seen over $\Delta v = 360$ km s^{-1} in line-of-sight velocity indicates multiple physical origins for the halo gas of this LRG.

Finally, we note that a modest absorption of highly ionized O VI gas is seen in this system at $dv_c = -152$ km s^{-1}. The O VI absorption consists of a single component with $\log N(\mathrm{O\,VI})/\mathrm{cm}^{-2} = 13.66^{+0.08}_{-0.07}$ and a relatively narrow b parameter of 22 km s^{-1}. Although the O VI absorption profile is narrow, no low- or intermediate-ionization metal or H I component is found to match the O VI absorption in velocity space (Figure A.10a), with the

O VI doublet situated at $\Delta v = -25$ km s^{-1} from the nearest low-ionization component.

A.11 SDSS J1357+0435 at $d = 126$ kpc

The LRG, which is at $z_{\rm LRG} = 0.3296$, has a LLS with a total column density of $\log N({\rm H\,I})/{\rm cm}^{-2} = 17.48 \pm 0.01$. Despite the strength of the H I Lyman series absorption in this system, no trace of corresponding metal absorption is found down to very sensitive column density limits (see Figure A.11a and Table A.11a). The HI absorption profile consists of a single component centered at $z_{\rm abs} = 0.32869$, or -205 km s^{-1} from the LRG systemic redshift. Our Voigt profile analysis finds a narrow Doppler parameter of $b_c({\rm H\,I}) = 18\,{\rm km\ s}^{-1}$, which constrains the gas temperature to $T \lesssim 2 \times 10^4$ K.

The most intriguing aspect of this system is the absence of ionic metals in an optically thick absorber occurring at $d = 126$ kpc from an massive quiescent galaxy. To put an upper limit on the metallicity given the observed $N({\rm H\,I})$ and upper limits on ionic column densities (Table A.11a), we make a couple of assumptions about the physical conditions of the gas. First, we assume that the gas is predominantly ionized, $f_{\rm H^+} > 0.9$, which is motivated by previous findings on the physical conditions of $z < 1$ LLSs (e.g., Lehner et al. 2013). Furthermore, we impose an upper limit on the cloud length of ~ 1 kpc, based on observations of Galactic high-velocity clouds (e.g., Putman et al. 2012). Together, these assumptions limit the allowed gas density to $-2.5 \lesssim \log n_{\rm H}/{\rm cm}^{-3} \lesssim -1.1$ under the HM05 UVB, and $-2.3 \lesssim \log n_{\rm H}/{\rm cm}^{-3} \lesssim -1.5$ under the HM12 UVB. Using this prior on gas density, we estimate that the 95 percent upper limit on the metallicity of the gas is [M/H] < -2.3 under HM05 and [M/H] < -2.2 under HM12. The inferred very low metallicity ($\lesssim 5 \times 10^{-3}$ solar) places this absorber among the lowest-metallicity LLSs known to be in the vicinity of $z < 1$ luminous galaxies (c.f., Ribaudo et al. 2011; Prochaska et al. 2017).

Table A.10a: Absorption properties along QSO sightline SDSS J0246−0059 at $d = 108$ kpc from the LRG

Component	Species	$\mathrm{d}v_c$ ($\mathrm{km\,s^{-1}}$)	$\log N_c$	b_c ($\mathrm{km\,s^{-1}}$)
all	H I	...	17.21 ± 0.01	...
	C II	...	$13.31^{+0.12}_{-0.28}$	...
	C III	...	$13.89^{+0.17}_{-0.16}$	...
	N V	...	< 13.27	...
	O VI	...	$13.66^{+0.08}_{-0.07}$	...
	Mg I	...	< 11.32	...
	Mg II	...	$12.43^{+0.05}_{-0.03}$	...
	Si II	...	$12.31^{+0.16}_{-0.35}$	...
	Si III	...	$13.04^{+0.11}_{-0.10}$	...
	Fe II	...	< 12.11	...
	Fe III	...	< 13.83	...
1	H I	$-309.6^{+5.0}_{-4.5}$	13.96 ± 0.06	$59.0^{+2.6}_{-2.5}$
	C II	-309.6	< 12.94	10
	C III	-309.6	< 12.48	10
	Mg I	-309.6	< 10.80	10
	Mg II	-309.6	< 11.35	10
	Si II	-309.6	< 12.24	10
	Si III	-309.6	< 12.02	10
	Fe II	-309.6	< 12.02	10
	Fe III	-309.6	< 13.34	10
2	H I	-228.8 ± 0.9	$16.49^{+0.06}_{-0.05}$	17.4 ± 0.4
	C II	-228.8	$13.31^{+0.12}_{-0.28}$	$10.1^{+6.2}_{-3.5}$
	C III	-228.8	$13.63^{+0.23}_{-0.14}$	9.9 ± 4.6
	N II	-228.8	< 13.05	10
	Mg I	-228.8	< 10.82	10
	Mg II	-227.2 ± 0.5	12.25 ± 0.04	$4.9^{+0.9}_{-1.2}$
	Si II	-228.8	$12.31^{+0.16}_{-0.35}$	$12.2^{+4.3}_{-5.1}$
	Si III	-228.8	$12.72^{+0.15}_{-0.19}$	$8.8^{+4.2}_{-3.4}$
	Fe II	-228.8	< 12.01	10
	Fe III	-228.8	< 13.28	10
3	H I	-127.5 ± 0.6	14.04 ± 0.05	$37.2^{+1.8}_{-1.5}$
	C II	-127.5	< 12.90	10
	C III	-127.5	< 12.46	10
	N II	-127.5	< 13.04	10
	Mg I	-127.5	< 10.80	10
	Mg II	-127.5	< 11.34	10
	Si II	-127.5	< 12.15	10
	Si III	-127.5	< 12.03	10
	Fe II	-127.5	< 12.04	10
	Fe III	-127.5	< 13.32	10
4	H I	$0.0^{+0.8}_{-0.4}$	$17.09^{+0.01}_{-0.02}$	$15.9^{+0.4}_{-0.3}$
	C II	0.0	< 12.76	10
	C III	0.0	$12.84^{+0.18}_{-0.33}$	$13.0^{+6.0}_{-5.1}$
	N II	0.0	< 13.05	10
	Mg I	0.0	< 10.80	10
	Mg II	-1.3 ± 1.4	$11.67^{+0.10}_{-0.15}$	$3.0^{+3.5}_{-1.9}$
	Si II	0.0	< 12.03	10
	Si III	0.0	< 12.19	10
	Fe II	0.0	< 12.02	10
	Fe III	0.0	< 13.33	10
5	H I	$+19.0^{+2.2}_{-0.7}$	$15.61^{+0.24}_{-0.32}$	10.0 ± 0.4
	C II	$+19.0$	< 12.84	10
	C III	$+19.0$	$13.12^{+0.32}_{-0.20}$	$10.3^{+3.7}_{-3.8}$
	N II	$+19.0$	< 13.00	10
	Mg I	$+19.0$	< 10.76	10
	Mg II	$+17.3 \pm 1.4$	11.67 ± 0.11	$3.3^{+6.7}_{-1.3}$
	Si II	$+19.0$	< 12.00	10
	Si III	$+19.0$	12.75 ± 0.15	12.4 ± 4.7
	Fe II	$+19.0$	< 12.02	10
	Fe III	$+19.0$	< 13.26	10
6	H I	$+54.0^{+2.6}_{-2.4}$	15.58 ± 0.08	24.2 ± 0.9
	C II	$+54.0$	< 12.94	10
	C III	$+54.0$	$13.18^{+0.12}_{-0.13}$	$22.8^{+5.8}_{-9.3}$
	N II	$+54.0$	< 13.03	10
	Mg I	$+54.0$	< 10.80	10
	Mg II	$+54.0$	< 11.33	10
	Si II	$+54.0$	< 12.08	10
	Si III	$+54.0$	< 12.02	10
	Fe II	$+54.0$	< 12.00	10
	Fe III	$+54.0$	< 13.23	10
high-1	O VI	-152.3 ± 4.1	$13.66^{+0.08}_{-0.07}$	$21.6^{+12.9}_{-4.3}$
	N V	-152.3	< 13.27	

Table A.10b: Ionization modeling results for the absorber along SDSS J0246−0059, at $d = 108$ kpc from the LRG

Component	$N_{\rm metal}$	[M/H]		$\log n_{\rm H}/{\rm cm}^{-3}$	
		HM05	HM12	HM05	HM12
SC	5	$-1.66^{+0.05}_{-0.06}$	$-1.26^{+0.04}_{-0.06}$	$-2.10^{+0.06}_{-0.10}$	$-2.28^{+0.04}_{-0.10}$
1	0	< 0.69	< 0.71	> -4.56	> -4.66
2	5	-1.09 ± 0.07	$-0.72^{+0.06}_{-0.07}$	$-2.02^{+0.12}_{-0.14}$	$-2.22^{+0.08}_{-0.14}$
3	0	< 0.68	< 0.70	> -4.54	> -4.66
4	2	$-2.27^{+0.19}_{-0.18}$	-1.91 ± 0.17	$-1.80^{+0.26}_{-0.22}$	$-1.98^{+0.26}_{-0.20}$
5	3	$-0.96^{+0.20}_{-0.23}$	$-0.64^{+0.17}_{-0.21}$	-2.48 ± 0.26	$-2.72^{+0.22}_{-0.24}$
6	1	$-2.47^{+0.78}_{-0.12}$	$-1.71^{+0.63}_{-0.12}$	< -2.88	< -3.00

Table A.11a: Absorption properties along QSO sightline SDSS J1357+0435 $d = 126$ kpc from the LRG

Component	Species	$\mathrm{d}v_c$ ($\mathrm{km\,s^{-1}}$)	$\log N_c$	b_c ($\mathrm{km\,s^{-1}}$)
1	H I	0.0 ± 0.4	17.48 ± 0.01	18.3 ± 0.2
	C II	0.0	< 13.11	10
	C III	0.0	< 12.19	10
	N II	0.0	< 12.87	10
	N III	0.0	< 13.19	10
	O I	0.0	< 13.38	10
	O VI	0.0	< 13.19	30
	Mg I	0.0	< 11.18	10
	Mg II	0.0	< 11.71	10
	Si II	0.0	< 12.10	10
	Si III	0.0	< 11.94	10
	Fe II	0.0	< 12.31	10

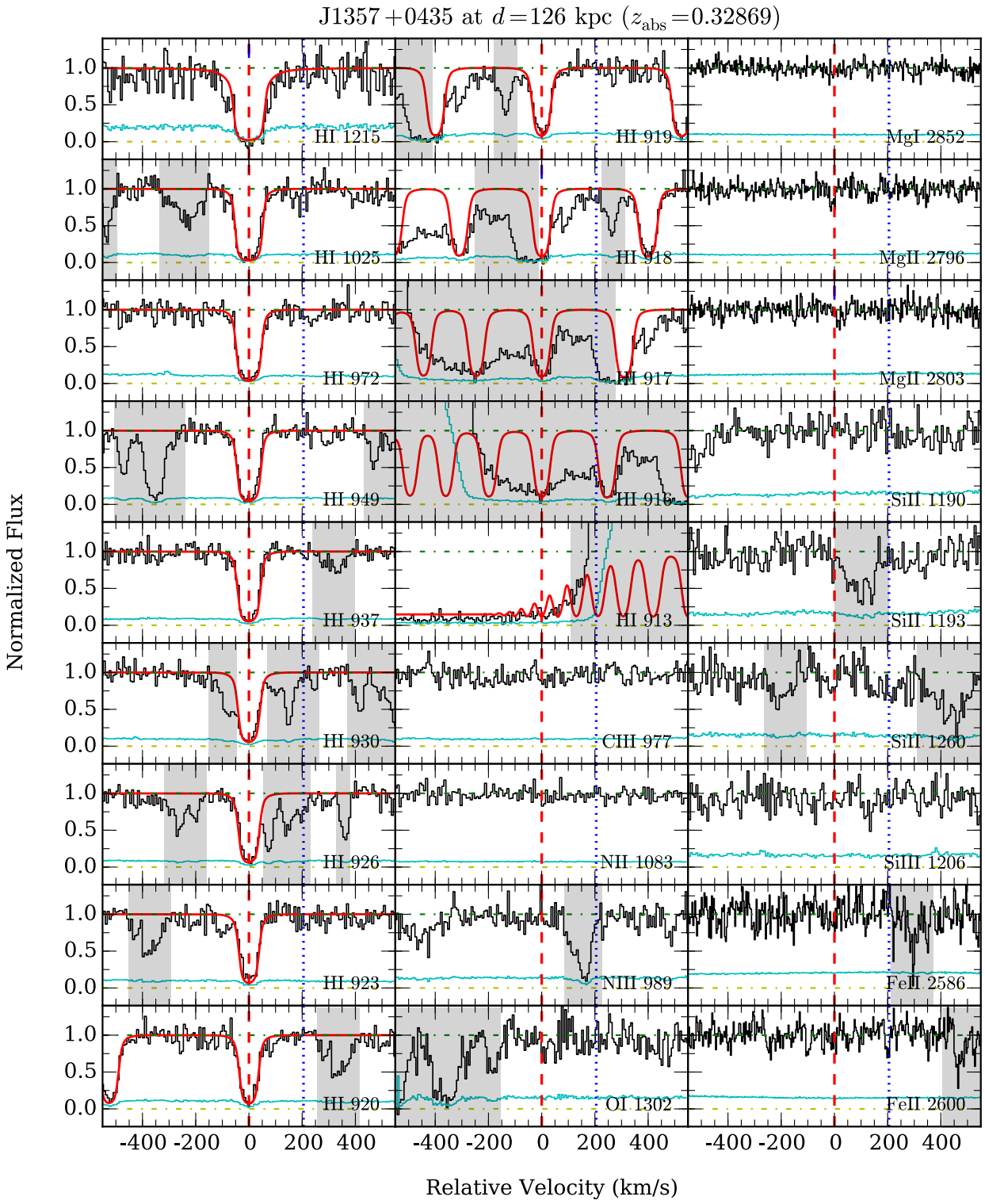

Figure A.11a: Similar to Figure A.1a, but for SDSS J1357+0435 at d = 126 kpc from the LRG.

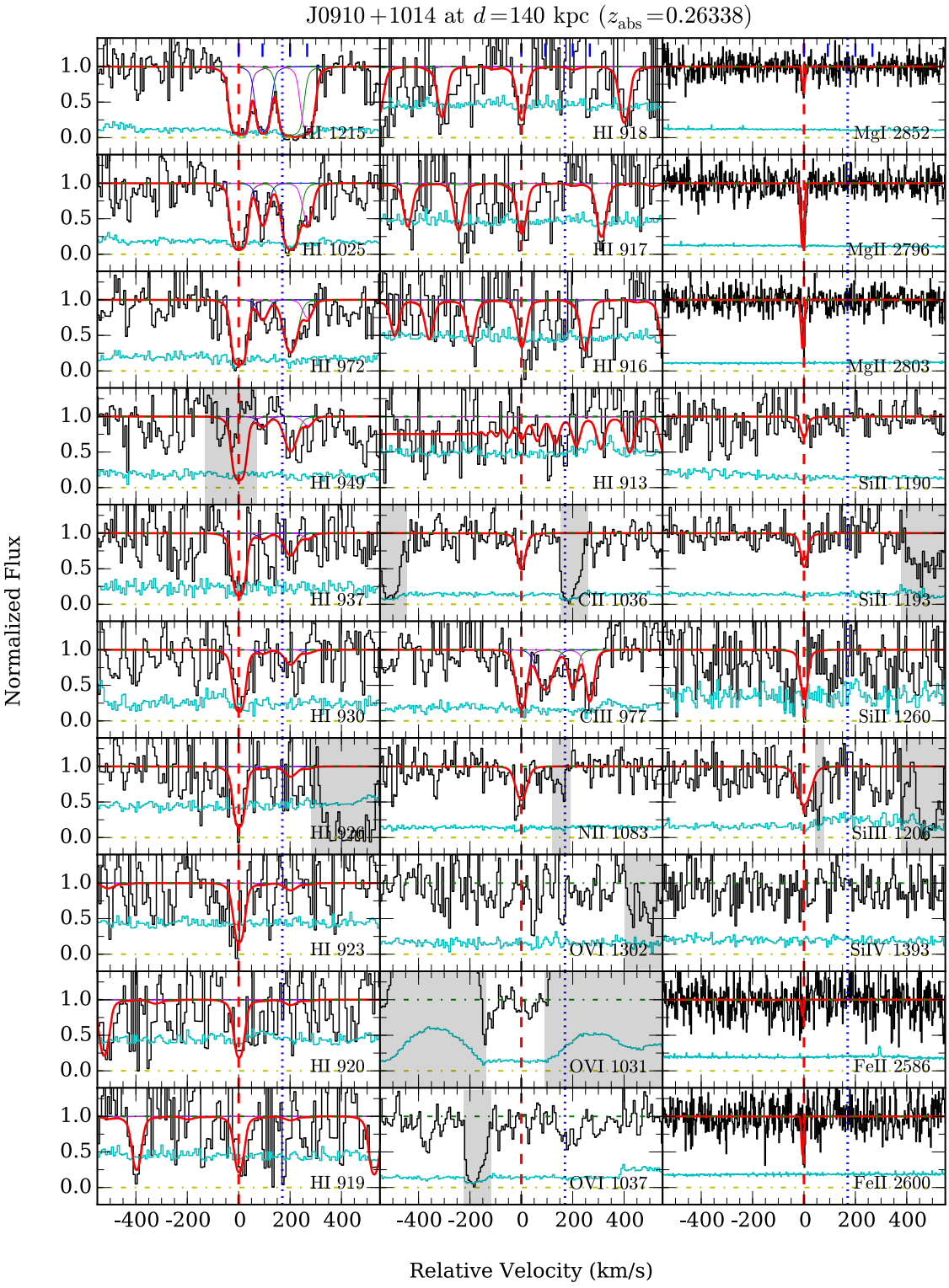

Figure A.12a: Similar to Figure A.1a, but for SDSS J0910+1014 at d = 140 kpc from the LRG. The observed lack of H I λ949 absorption is due to contamination from the geocoronal N I λ1199 emission line.

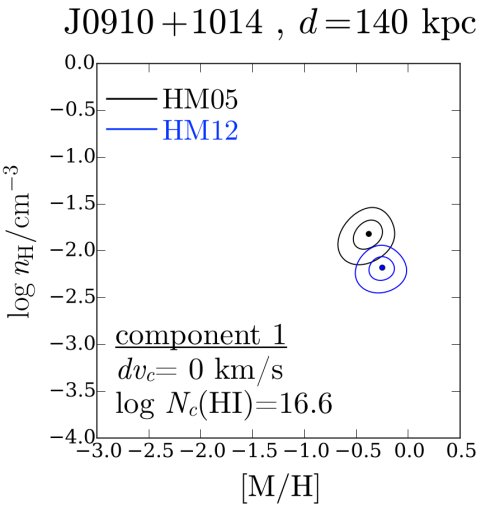

Figure A.12b: Probability distribution contours of gas metallicity and density for the absorbing gas detected along SDSS J0910+1014, at $d = 140$ kpc from the LRG. Contour levels are the same as in Figure A.1b. Not shown here are the probability distributions for components 2 to 4, which have lower H I column densities of log N_c(H I) $\lesssim 15$ and show only C III absorption, resulting in weak constraints on the gas metallicity and density (see Table A.12b).

A.12 SDSS J0910+1014 at $d = 140$ kpc

This LRG occurs at $z_{\rm LRG} = 0.2641$, and it has a pLLS with a total N(H I) of $\log N({\rm H\,I})/{\rm cm}^{-2} = 16.65^{+0.34}_{-0.22}$. In addition to H I, we also detect corresponding ionic absorption of C II, C III, N II, Mg I, Mg II, Si II, Si III, and Fe II (Figure A.12a).

The HI absorption profile consists of four individual components (Figure A.12a and Table A.12a). The strongest H I absorption is in component 1 at $z_{\rm abs} = 0.26338$ or 170 km s^{-1} blueward of the LRG redshift. This component contributes to most (98%) of the absorber's total N(H I). In addition, component 1 also exhibits strong absorption of low- and intermediate-ionization metal species (Figure A.12a), suggesting the gas is chemically enriched. In contrast, C III is the only metal species detected in the other three components, components 2 to 4.

The observed velocity spread of the absorber is $\Delta v \approx 270$ km s^{-1} from the bluest to reddest component. As shown in Figure A.12a, our Voigt profile analysis demonstrates that both low- and intermediate-ionization metal absorption profiles are well-matched to the

component structure of H I. By comparing the measured linewidths for H I and Mg II, we find that the bulk of the absorbing gas (component 1) is cool, $T \sim 10^4$ K, with a modest amount of non-thermal line broadening, $b_{\rm nt} \approx 6\,{\rm km\ s^{-1}}$. For components 2 to 4, the observed H I linewidths of $b_c({\rm H\,I}) \lesssim 25$ km s^{-1} place an upper limit on the gas temperature of $T \lesssim 4\times10^4$ K.

As shown in Figure A.12b and Table A.12b, our ionization analysis finds that the bulk of the absorbing gas (component 1) has a density of $\log n_{\rm H}/{\rm cm^{-3}} = -1.8\pm0.2$ under HM05 and $\log n_{\rm H}/{\rm cm^{-3}} = -2.2 \pm 0.1$ under HM12. To reproduce the observed ionic column densities, the required gas metallicity is sub-solar, between [M/H] $= -0.4 \pm 0.1$ unwed HM05 UVB and [M/H] $= -0.3 \pm 0.1$ under HM12 UVB.

For the weaker components 2, 3, and 4, our analysis determines that the gas is low-density, with an upper limit of $\log n_{\rm H}/{\rm cm^{-3}} \lesssim -2.5$ under HM05 and $\log n_{\rm H}/{\rm cm^{-3}} \lesssim -2.7$ under HM12, constrained by the detection of C III and non-detections of other metal species. Because C III the only metal detection, the inferred metallicity of the gas is subject to large uncertainties, ranging from between [M/H] $= -1.7^{+0.7}_{-0.3}$ (HM05) and [M/H] $= -1.0^{+0.6}_{-0.3}$ (HM12) for component 3, to between [M/H] $= -0.5 \pm 0.5$ (HM05) and [M/H] $= 0.2 \pm 0.5$ (HM12) for components 2 and 4.

This absorber was also studied in the COS-Halos survey. Using the Haardt & Madau (2001) UVB (which is similar of the HM05 UVB at energies $\lesssim 2$ Ryd), Werk et al. (2014) inferred a mean metallicity of [M/H] $= -0.7 \pm 0.5$ and density of between $\log n_{\rm H}/{\rm cm^{-3}} = -4.5$ and $\log n_{\rm H}/{\rm cm^{-3}} = -3.0$ under the Haardt & Madau (2001) UVB. In an updated analysis using the HM12 UVB, Prochaska et al. (2017) found a mean metallicity of [M/H] $= -0.17^{+0.13}_{-0.08}$ and density of $\log n_{\rm H}/{\rm cm^{-3}} = -2.6 \pm 0.2$. The Prochaska et al. (2017) values are consistent with what we find in our analysis using using the single-clump model, after accounting for the difference in the adopted redshift of the HM12 UVB spectrum used in both studies.

Table A.12a: Absorption properties along QSO sightline SDSS J0910+1014 at $d = 140$ kpc from the LRG

Component	Species	dv_c (km s^{-1})	$\log N_c$	b_c (km s^{-1})
all	H I	...	$16.65^{+0.34}_{-0.22}$	...
	C II	...	13.97 ± 0.12	...
	C III	...	> 14.07	...
	N II	...	14.08 ± 0.12	...
	N V	...	< 13.33	...
	O I	...	< 14.20	...
	O VI	...	< 13.53	...
	Mg I	...	11.59 ± 0.10	...
	Mg II	...	12.84 ± 0.04	...
	Si II	...	$13.22^{+0.11}_{-0.08}$	...
	Si III	...	12.98 ± 0.09	...
	Si IV	...	< 12.98	...
	Fe II	...	12.75 ± 0.13	...
1	H I	$0.0^{+0.5}_{-0.4}$	$16.64^{+0.35}_{-0.23}$	$14.8^{+0.9}_{-1.4}$
	C II	0.0	13.97 ± 0.12	$15.6^{+6.6}_{-6.8}$
	C III	0.0	> 13.52	< 25.7
	N II	0.0	14.08 ± 0.12	23.8 ± 9.7
	O I	0.0	< 13.71	10
	Mg I	-1.9 ± 1.1	11.59 ± 0.10	6.0 ± 2.2
	Mg II	0.0 ± 0.4	12.84 ± 0.04	6.5 ± 0.7
	Si II	0.0	$13.22^{+0.11}_{-0.08}$	$12.7^{+8.5}_{-4.1}$
	Si III	0.0	12.98 ± 0.09	$28.8^{+12.0}_{-6.3}$
	Si IV	0.0	< 12.50	10
	Fe II	0.0	12.75 ± 0.13	$4.2^{+3.0}_{-1.6}$
2	H I	$+92.8^{+3.1}_{-2.8}$	14.34 ± 0.15	20.8 ± 2.5
	C II	+92.8	< 13.36	10
	C III	+92.8	$13.47^{+0.18}_{-0.16}$	32.4 ± 15.5
	N II	+92.8	< 13.38	10
	O I	+92.8	< 13.78	10
	Mg I	+92.8	< 11.17	10
	Mg II	+92.8	< 11.67	10
	Si II	+92.8	< 12.44	10
	Si III	+92.8	< 12.19	10
	Si IV	+92.8	< 12.41	10
	Fe II	+92.8	< 12.36	10
3	H I	$+200.1^{+5.4}_{-4.6}$	$15.08^{+0.14}_{-0.13}$	$26.3^{+3.8}_{-2.7}$
	C II	+200.1	< 13.09	10
	C III	+200.1	$13.28^{+0.22}_{-0.14}$	$16.2^{+16.9}_{-6.7}$
	N II	+200.1	< 13.40	10
	O I	+200.1	< 13.66	10
	Mg I	+200.1	< 11.14	10
	Mg II	+200.1	< 11.65	10
	Si II	+200.1	< 12.44	10
	Si III	+200.1	< 12.17	10
	Si IV	+200.1	< 12.47	10
	Fe II	+200.1	< 12.36	10
4	H I	$+266.5^{+7.5}_{-9.3}$	$14.29^{+0.21}_{-0.27}$	$19.9^{+5.6}_{-3.6}$
	C II	+266.5	< 13.35	10
	C III	+266.5	$13.56^{+0.25}_{-0.19}$	$17.1^{+8.8}_{-3.9}$
	N II	+266.5	< 13.43	10
	O I	+266.5	< 13.63	10
	Mg I	+266.5	< 11.16	10
	Mg II	+266.5	< 11.67	10
	Si II	+266.5	< 12.41	10
	Si III	+266.5	< 12.14	10
	Si IV	+266.5	< 12.47	10
	Fe II	+266.5	< 12.39	10

Table A.12b: Ionization modeling results for the absorber along SDSS J0910+1014 at $d = 140$ kpc from the LRG

Component	$N_{\rm metal}$	[M/H]		$\log n_{\rm H}/{\rm cm}^{-3}$	
		HM05	HM12	HM05	HM12
SC	8	$-0.39^{+0.12}_{-0.14}$	$-0.25^{+0.11}_{-0.12}$	$-1.88^{+0.10}_{-0.18}$	$-2.26^{+0.10}_{-0.14}$
1	8	$-0.39^{+0.11}_{-0.15}$	$-0.26^{+0.11}_{-0.13}$	$-1.84^{+0.12}_{-0.16}$	$-2.20^{+0.10}_{-0.12}$
2	1	$-0.68^{+0.49}_{-0.30}$	$0.10^{+0.48}_{-0.28}$	< -2.92	< -3.14
3	1	$-1.73^{+0.68}_{-0.27}$	$-0.99^{+0.63}_{-0.26}$	< -2.50	< -2.70
4	1	$-0.51^{+0.52}_{-0.45}$	$0.23^{+0.42}_{-0.46}$	< -2.90	< -3.10

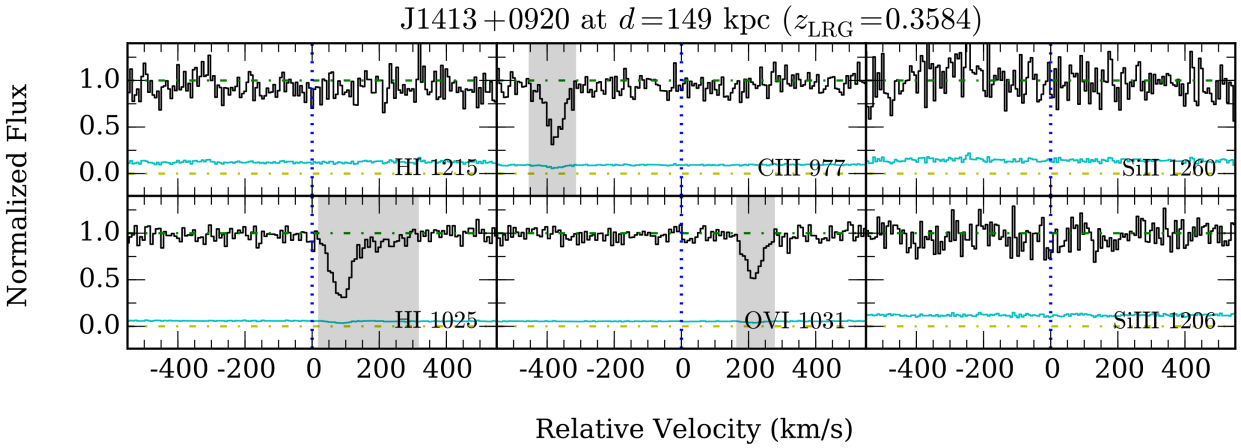

Figure A.13a: Similar to Figure A.1a, but for SDSS J1413+0920 at $d = 149$ kpc from the LRG.

A.13 SDSS J1413+0920 at $d = 149$ kpc

The LRG occurs at $z_{\rm LRG} = 0.3584$. As shown in Figure A.13a, no H I absorption is detected within the adopted search window of ± 500 km s^{-1} from the LRG redshift. We are able to place a sensitive 2-σ column density upper limit of $\log N({\rm H\,I})/{\rm cm}^{-2} < 12.5$, calculated for an H I line with $b({\rm H\,I}) = 15$ km s^{-1} that is centered at the LRG redshift (Table A.13a).

A.14 SDSS J1553+3548 at $d = 156$ kpc

This LRG is at $z_{\rm LRG} = 0.4736$. A H I Lyman absorption series is present near the LRG redshift, with a total $N({\rm H\,I})$ of $\log N({\rm H\,I})/{\rm cm}^{-2} = 15.69 \pm 0.04$. In addition to H I, we detect

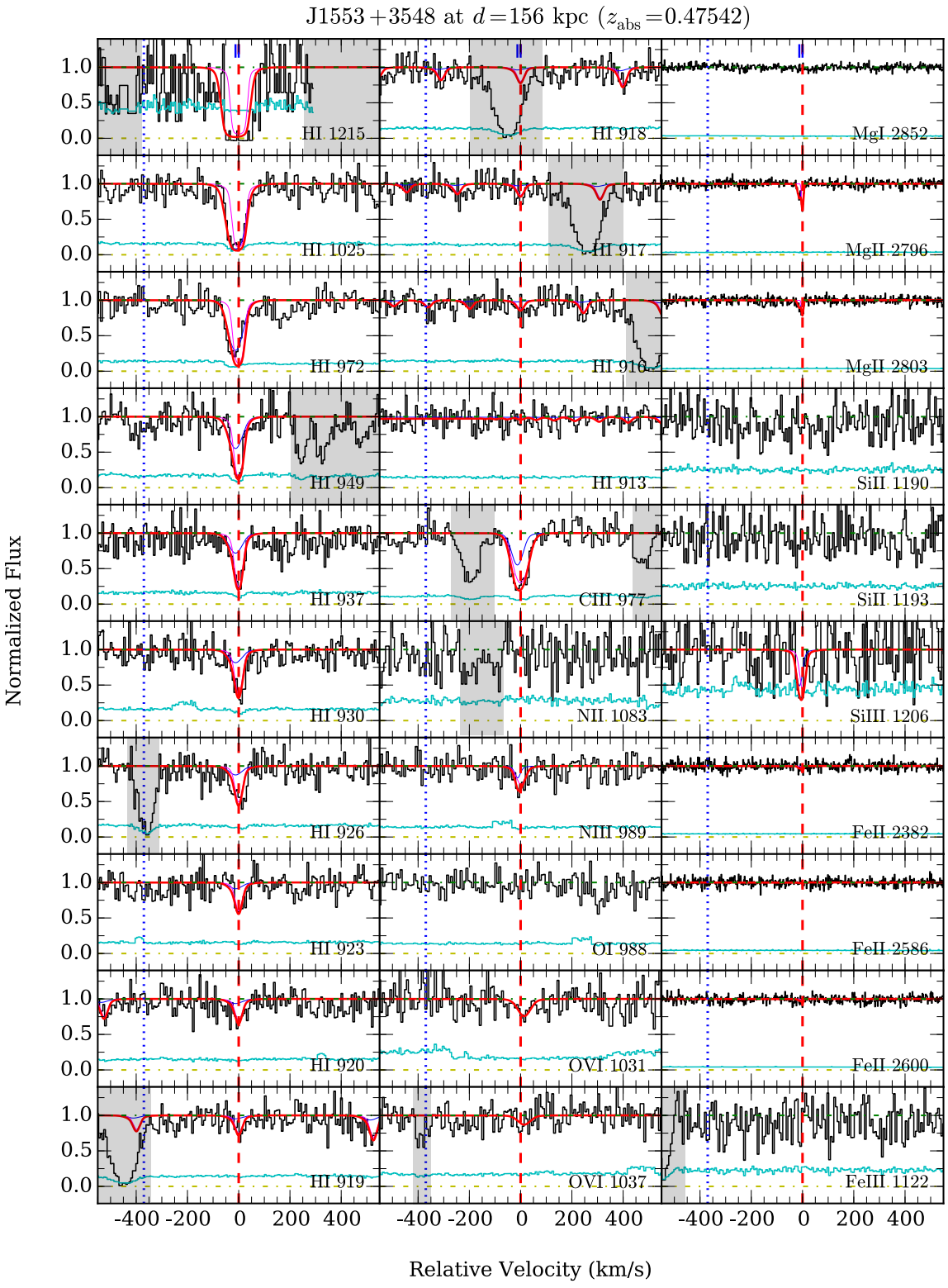

Figure A.14a: Similar to Figure A.1a, but for SDSS J1553+3548 at d = 156 kpc from the LRG. Note that the The H I λ972 line is likely contaminated by O III λ832 and O II λ834 emission lines from the background QSO.

Table A.13a: Constraints on absorption properties along QSO sightline SDSS J1413+0920 at $d = 149$ kpc from the LRG

Component	Species	$\mathrm{d}v_c$ ($\mathrm{km\,s^{-1}}$)	$\log N_c$	b_c ($\mathrm{km\,s^{-1}}$)
...	H I	0.0	< 12.49	15
	C II	0.0	< 12.68	10
	C III	0.0	< 12.15	10
	N II	0.0	< 12.87	10
	N III	0.0	< 13.02	10
	N V	0.0	< 13.16	30
	O I	0.0	< 13.37	10
	O VI	0.0	< 12.92	30
	Si II	0.0	< 12.09	10
	Si III	0.0	< 11.74	10
	Fe III	0.0	< 12.98	10

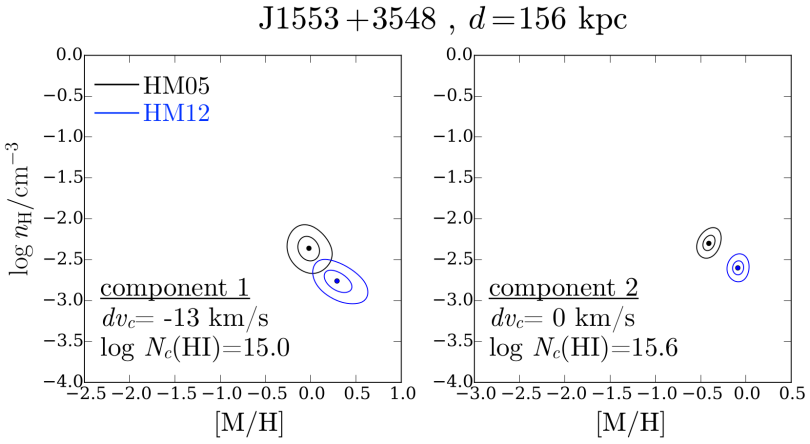

Figure A.14b: Probability distribution contours of gas metallicity and density for individual absorption components identified along SDSS J1553+3548, at $d = 156$ kpc from the LRG. Contour levels are the same as in Figure A.1b.

corresponding absorption of metal species C III, N III, O VI, Mg II, Si III, and Fe II (Figure A.14a).

As presented in Figure A.14a and Table A.14a, our Voigt profile analysis shows that the Mg II absorption profile consists of two individual components which are separated by only 12 km s^{-1} in line-of-sight velocity. The stronger of these two components, component 2, occurs at $z_{\rm abs} = 0.47542$ or +370 km s^{-1} from the LRG redshift. To accurately measure the corresponding N(H I) of each component given the close velocity separation between the two components, we perform a Voigt profile analysis on the H I Lyman series absorption by tying the velocity structure of H I absorption to that of Mg II. The best-fit N(H I) for the two components are $\log N_c({\rm H\,I})/{\rm cm}^{-2} = 15.04^{+0.08}_{-0.18}$ for component 1, and $\log N_c({\rm H\,I})/{\rm cm}^{-2} = 15.57 \pm 0.07$ for component 2.

The observed H I and Mg II Doppler linewidths for component 2 indicate that the absorbing gas is relatively cool, $T \approx 1 \times 10^4$ K, with negligible non-thermal broadening. For the weaker component 1, the b values imply a higher temperature, $T \approx 5 \times 10^4$ K, with a modest non-thermal line broadening of $b_{\rm nt} \sim 5\,{\rm km\ s}^{-1}$.

Our ionization analysis finds little variation (< 0.1 dex) in gas densities across the two components, as shown in Figure A.14b and Table A.14b. For both components, the observed ionic column densities can be reproduced by models with $\log n_{\rm H}/{\rm cm}^{-3} \approx -2.3$ under HM05 and $\log n_{\rm H}/{\rm cm}^{-3} \approx -2.7$ under HM12. Furthermore, the gas appears to have been significantly enriched by heavy metals. For component 2, we find a sub-solar metallicity of [M/H] $= -0.4 \pm 0.1$ under HM05 and [M/H] $= -0.1 \pm 0.1$ under HM12. An even higher chemical abundance is inferred for component 1, where our Cloudy models constrain the metallicity to [M/H] $= 0.0 \pm 0.1$ under HM05 or [M/H] $= +0.3 \pm 0.2$ under HM12. In addition, the strength of N III absorption suggests that the gas is likely to be nitrogen-rich. The inferred [N/α] ratios for the two components are [N/α] $= 0.3 \pm 0.3$ and 0.5 ± 0.2 for components 1 and 2, respectively.

A modest absorption of O VI gas is seen in this system at $dv_c = +10$ km s^{-1}. The

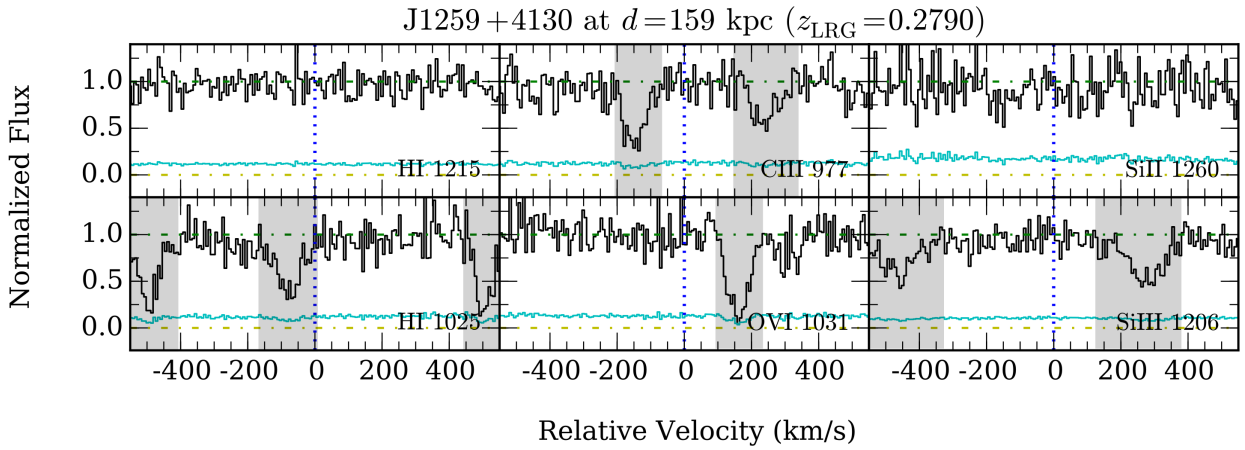

Figure A.15a: Similar to Figure A.1a, but for SDSS J1259+4130 at $d = 159$ kpc from the LRG.

O VI absorption consists of a single component with $\log N(\mathrm{O\,VI})/\mathrm{cm}^{-2} = 13.69^{+0.13}_{-0.18}$ and a b parameter of 29 km s^{-1}. No low- or intermediate-ionization metal H I or component is found to match the O VI absorption in velocity space (Figure A.14a), with the O VI doublet situated 10 km s^{-1} away from the nearest low-ionization component.

A.15 SDSS J1259+4130 at $d = 159$ kpc

The LRG occurs at $z_{\mathrm{LRG}} = 0.2790$. As shown in Figure A.15a, no H I absorption is detected within the adopted search window of ± 500 km s^{-1} from the LRG redshift. We are able to place a sensitive 2-σ column density upper limit of $\log N(\mathrm{H\,I})/\mathrm{cm}^{-2} < 12.5$, calculated for an H I line with $b(\mathrm{H\,I}) = 15$ km s^{-1} that is centered at the LRG redshift (Table A.15a).

A.16 SDSS J1244+1721 at $d = 160$ kpc

This LRG is located at $z_{\mathrm{LRG}} = 0.5591$. We detect absorption from the H I Lyman series near the LRG redshift, with a total $N(\mathrm{H\,I})$ of $\log N(\mathrm{H\,I})/\mathrm{cm}^{-2} = 15.99 \pm 0.04$. In addition to H I, the following metal species are present in absorption: C II, C III, Mg II, and Fe II (see Figure A.16a). Due to the relatively high redshift of the LRG, all transitions above rest-frame $\lambda \approx 1140$ Å fall outside the wavelength coverage of the FUV COS spectrum, including

Table A.14a: Absorption properties along QSO sightline SDSS J1553+3548 at $d = 156$ kpc from the LRG

Component	Species	$\mathrm{d}v_c$ ($\mathrm{km\,s^{-1}}$)	$\log N_c$	b_c ($\mathrm{km\,s^{-1}}$)
all	H I	...	15.69 ± 0.04	...
	C III	...	$13.78^{+0.08}_{-0.05}$	...
	N II	...	< 13.68	...
	N III	...	$13.87^{+0.12}_{-0.09}$	...
	O I	...	< 13.78	...
	O VI	...	$13.69^{+0.13}_{-0.18}$	...
	Mg I	...	< 10.80	...
	Mg II	...	$12.22^{+0.03}_{-0.02}$	...
	Si II	...	< 12.85	...
	Si III	...	$13.00^{+0.24}_{-0.29}$	...
	Fe II	...	$11.81^{+0.08}_{-0.17}$	...
	Fe III	...	< 13.69	...
1	H I	-12.3	$15.04^{+0.08}_{-0.17}$	$30.5^{+5.1}_{-3.2}$
	C III	-12.3	$13.23^{+0.22}_{-0.27}$	$25.1^{+8.6}_{-8.2}$
	N II	-12.3	< 13.48	10
	N III	-12.3	$13.34^{+0.27}_{-0.37}$	10.0 ± 1.9
	O I	-12.3	< 13.57	10
	Mg I	-12.3	< 10.60	10
	Mg II	-12.3 ± 1.9	11.90 ± 0.05	$8.0^{+1.8}_{-1.0}$
	Si II	-12.3	< 12.63	10
	Si III	-12.3	$12.67^{+0.29}_{-0.42}$	$12.0^{+4.3}_{-3.9}$
	Fe II	$-12.8^{+2.2}_{-1.4}$	$11.47^{+0.13}_{-0.31}$	$7.1^{+5.1}_{-5.5}$
	Fe III	-12.3	< 13.51	10
2	H I	$0.0^{+3.2}_{-2.0}$	$15.57^{+0.07}_{-0.07}$	$14.2^{+3.1}_{-1.4}$
	C III	0.0	$13.63^{+0.11}_{-0.10}$	$31.9^{+3.7}_{-4.7}$
	N II	0.0	< 13.50	10
	N III	0.0	$13.72^{+0.14}_{-0.19}$	$19.3^{+7.1}_{-5.7}$
	O I	0.0	< 13.62	10
	Mg I	0.0	< 10.60	10
	Mg II	0.0 ± 0.6	11.94 ± 0.04	3.0 ± 0.7
	Si II	0.0	< 12.64	10
	Si III	0.0	$12.73^{+0.21}_{-0.48}$	$11.1^{+6.4}_{-2.4}$
	Fe II	$0.3^{+1.5}_{-1.6}$	$11.55^{+0.13}_{-0.24}$	$4.5^{+4.7}_{-2.9}$
	Fe III	0.0	< 13.50	10
high-1	O VI	$+9.5 \pm 8.1$	$13.69^{+0.13}_{-0.18}$	$29.2^{+28.5}_{-11.8}$

Table A.14b: Ionization modeling results for the absorber along SDSS J1553+3548 at $d =$ 156 kpc from the LRG

Component	$N_{\rm metal}$	[M/H]		$\log n_{\rm H}/{\rm cm}^{-3}$	
		HM05	HM12	HM05	HM12
SC	5	-0.28 ± 0.04	$+0.05^{+0.03}_{-0.04}$	$-2.28^{+0.04}_{-0.06}$	$-2.60^{+0.04}_{-0.06}$
1	5	$-0.03^{+0.13}_{-0.11}$	$+0.30^{+0.17}_{-0.14}$	$-2.36^{+0.12}_{-0.16}$	-2.78 ± 0.12
2	5	-0.41 ± 0.06	$-0.08^{+0.05}_{-0.07}$	-2.30 ± 0.08	$-2.60^{+0.06}_{-0.08}$

Table A.15a: Constraints on absorption properties along QSO sightline SDSS J1259+4130 at $d = 159$ kpc from the LRG

Component	Species	dv_c ($\rm km\,s^{-1}$)	$\log N_c$	b_c ($\rm km\,s^{-1}$)
...	H I	0.0	< 12.51	15
	C II	0.0	< 13.03	10
	C III	0.0	< 12.33	10
	N III	0.0	< 13.06	10
	N V	0.0	< 13.31	30
	O VI	0.0	< 13.27	30
	Si II	0.0	< 12.20	10
	Si III	0.0	< 11.83	10
	Fe III	0.0	< 13.08	10

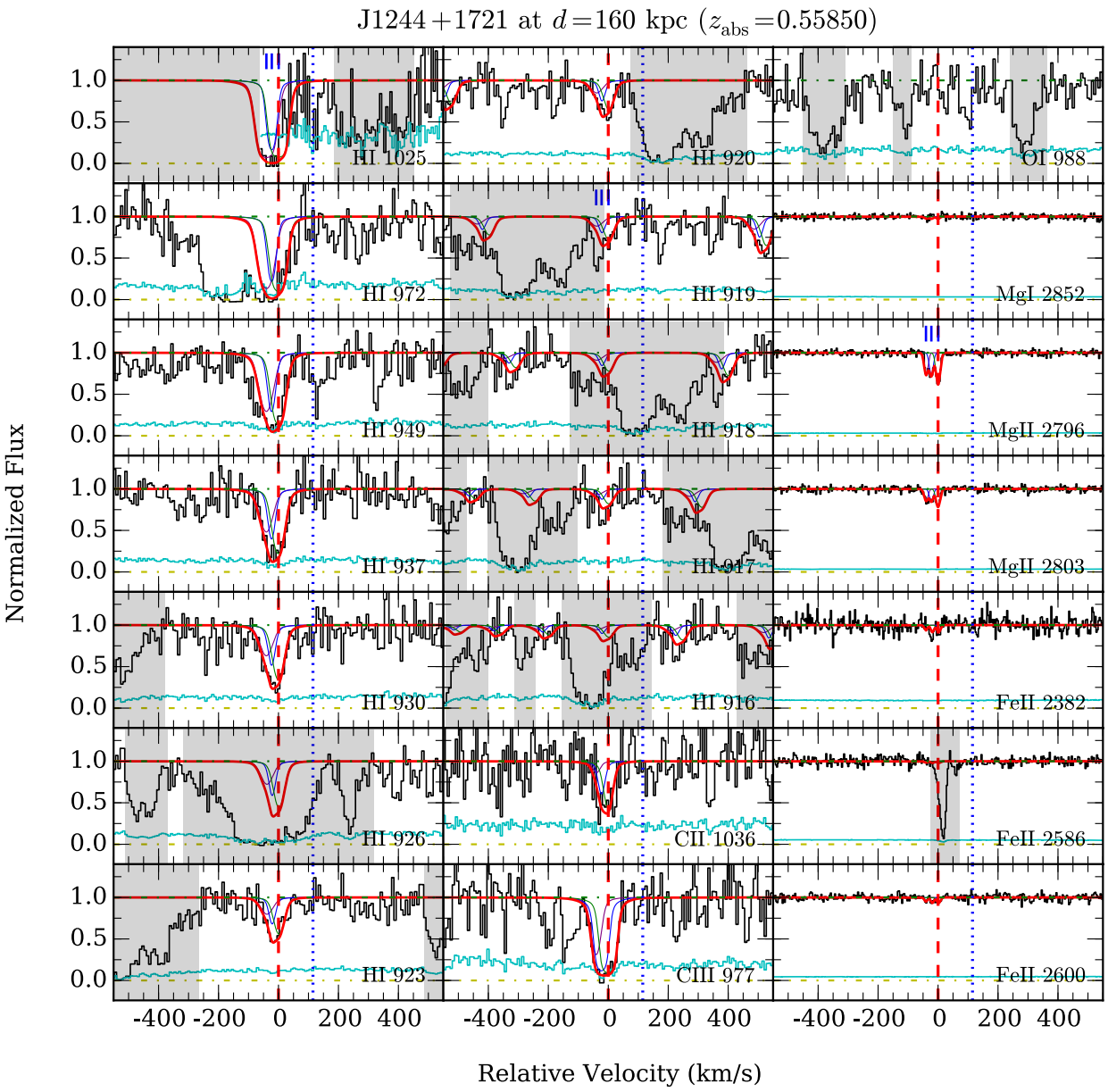

Figure A.16a: Similar to Figure A.1a, but for SDSS J1244+1721 at d = 160 kpc from the LRG.

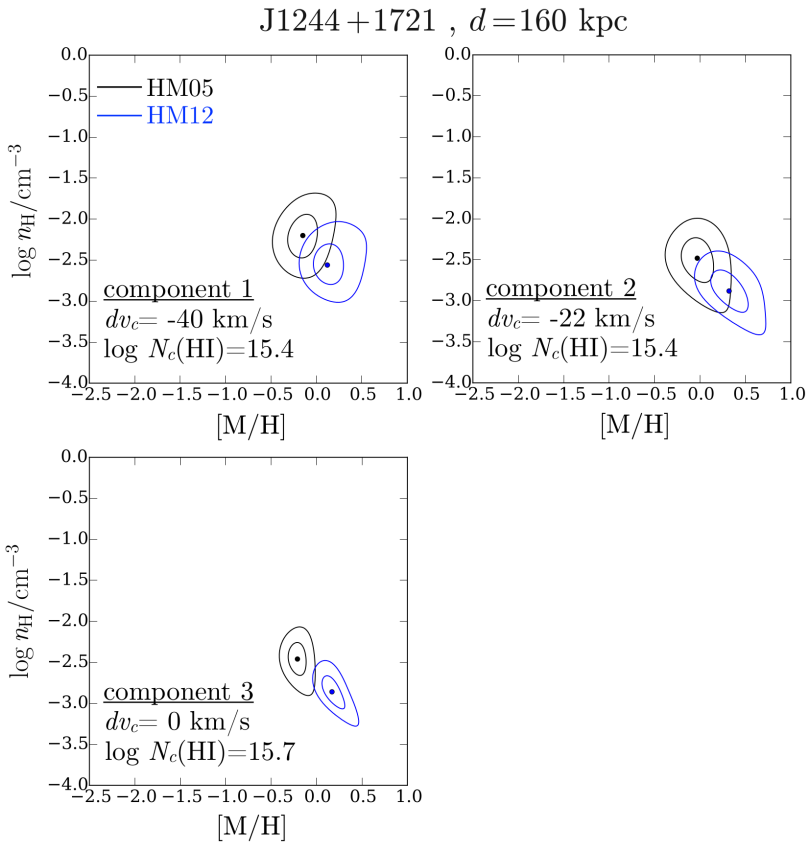

Figure A.16b: Probability distribution contours of gas metallicity and density for individual absorption components identified along SDSS J1244+1721, at $d = 160$ kpc from the LRG. Contour levels are the same as in Figure A.1b.

Lyα, Si II λ1260 and Si II λ1206. We further note that while there is possible N III λ989 absorption in this system, this transition is often blended/contaminated by the adjacent Si II λ989 line. Because no other Si II transition is covered by the data, we are unable to assess how much the N III absorption is contaminated by Si II. For that reason, we chose to exclude this possible N III detection from our subsequent analysis of the absorber.

Our Voigt profile analysis identifies three components in the absorber, which can be seen clearly in the Mg II absorption profile (Figure A.16a and Table A.16a). The observed velocity spread of the absorber is $\Delta v \approx 40$ km s^{-1} from the bluest to reddest component. The strongest H I absorption occurs in component 3 at $z_{\rm abs} = 0.55850$, or -115 km s^{-1} from the LRG. This component comprises half of the total N(H I) of the absorber, with the rest distributed equally between the other two components. As shown in Figure A.16a, the component structure of H I is in very good agreement with those of the metal ions (e.g., Mg II and Fe II). The ratio of the Doppler linewidths of H I and Mg II in each component is consistent with the expectation for a cool gas with $T \sim (1-3) \times 10^4$ K and a modest amount of non-thermal line broadening, $b_{\rm nt} \approx 6$ km s^{-1}.

Our ionization analysis indicates a modest variation (~ 0.3 dex) in gas densities across the three components (see Figure A.16b and Table A.16b). For all components, the observed absorption profile can be reproduced by the models over a gas density range of from $\log n_{\rm H}/{\rm cm}^{-3} \approx -2.5$ to $\log n_{\rm H}/{\rm cm}^{-3} \approx -2.2$ under the HM05 UVB, and $\log n_{\rm H}/{\rm cm}^{-3} \approx -2.9$ to $\log n_{\rm H}/{\rm cm}^{-3} \approx -2.5$ under the HM12 UVB. The observed metal column densities in the absorber are consistent with a high degree of chemical enrichment. The inferred metallicities range from [M/H] $= -0.2 \pm 0.1$ (component 3) to [M/H] $= 0.0 \pm 0.2$ (component 2) under HM05, and [M/H] $= 0.1 \pm 0.2$ (component 1) to [M/H] $= 0.3 \pm 0.2$ (component 2) under HM12. Finally, we note that the observed column densities of carbon ions imply that the absorber is carbon-rich, with estimated [C/α] ratios of [C/α] $= 0.0 - 0.5$.

Table A.16a: Absorption properties along QSO sightline SDSS J1244+1721 at $d = 160$ kpc from the LRG

Component	Species	$\mathrm{d}v_c$ ($\mathrm{km\,s^{-1}}$)	$\log N_c$	b_c ($\mathrm{km\,s^{-1}}$)
all	H I	...	15.99 ± 0.04	...
	C II	...	$14.26^{+0.15}_{-0.10}$	...
	C III	...	> 14.42	...
	O I	...	< 13.83	...
	O VI	...	< 13.74	...
	Mg I	...	< 10.88	...
	Mg II	...	12.61 ± 0.02	...
	Fe II	...	$12.26^{+0.05}_{-0.20}$	...
1	H I	-39.9	$15.35^{+0.07}_{-0.21}$	$23.8^{+10.5}_{-5.5}$
	C II	-39.9	< 13.25	10
	C III	-39.9	$13.50^{+0.20}_{-0.36}$	$15.0^{+9.3}_{-2.8}$
	O I	-39.9	< 13.66	10
	Mg I	-39.9	< 10.60	10
	Mg II	-39.9 ± 1.4	12.04 ± 0.07	$6.2^{+4.4}_{-2.2}$
	Fe II	-40.7 ± 2.9	$11.67^{+0.14}_{-0.46}$	$3.5^{7.3}_{-1.8}$
2	H I	-22.4	$15.38^{+0.23}_{-0.22}$	$11.6^{+5.5}_{-3.0}$
	C II	-22.4	$13.73^{+0.36}_{-0.27}$	$10.0^{+10.2}_{-2.5}$
	C III	-22.4	> 13.62	< 25.6
	O I	-22.4	< 13.65	10
	Mg I	-22.4	< 10.60	10
	Mg II	-22.4 ± 1.1	12.06 ± 0.05	$6.1^{+2.0}_{-1.2}$
	Fe II	-22.4	$11.81^{+0.12}_{-0.44}$	$4.0^{+7.2}_{-1.9}$
3	H I	0.0	$15.71^{+0.06}_{-0.11}$	$19.0^{+4.3}_{-2.2}$
	C II	0.0	$14.05^{+0.17}_{-0.19}$	$24.3^{+7.5}_{-6.5}$
	C III	0.0	> 13.88	< 24.2
	O I	0.0	< 13.70	10
	Mg I	0.0	< 10.60	10
	Mg II	0.0 ± 0.4	12.27 ± 0.03	7.0 ± 0.7
	Fe II	1.5 ± 2.2	$11.86^{+0.11}_{-0.32}$	$5.8^{+5.1}_{-3.3}$

Table A.16b: Ionization modeling results for the absorber along SDSS J1244+1721 at $d = 160$ kpc from the LRG

Component	N_{metal}	[M/H]		$\log n_{\mathrm{H}}/\mathrm{cm^{-3}}$	
		HM05	HM12	HM05	HM12
SC	4	$-0.14^{+0.03}_{-0.04}$	$+0.21^{+0.05}_{-0.04}$	-2.40 ± 0.12	$-2.84^{+0.10}_{-0.12}$
1	3	$-0.14^{+0.19}_{-0.16}$	$+0.15^{+0.24}_{-0.15}$	-2.20 ± 0.26	$-2.54^{+0.26}_{-0.22}$
2	4	$0.00^{+0.19}_{-0.18}$	$+0.33^{+0.22}_{-0.18}$	$-2.50^{+0.22}_{-0.32}$	$-2.86^{+0.22}_{-0.26}$
3	4	-0.20 ± 0.10	$+0.17^{+0.14}_{-0.09}$	$-2.46^{+0.16}_{-0.22}$	$-2.86^{+0.16}_{-0.20}$

APPENDIX B

SUPPLEMENTARY INFORMATION FOR CHAPTER 6: OTHER ABSORPTION SYSTEMS AT $z = 2.7 - 2.8$

Two additional Lyα absorption complexes are found at $z = 2.7 - 2.8$ along the spectrum of background QSO DMS 2139−0405 (see Figure 6.1): Complex X at $z = 2.7147$ and Complex Y at $z = 2.7863$. No known LAE is found within $d < 300$ kpc and $|\Delta v| < 500$ km s^{-1} from these Lyα absorption systems.

A strong, saturated Lyα component dominates the total H I column density of Complex X (Figure B.1), with a best-fit $\log N(\mathrm{H\,I})/\mathrm{cm}^{-2} = 17.9^{+0.2}_{-0.3}$. For this saturated system, we estimate that the range of allowed $N\,(\mathrm{H\,I})$ is $\log N(\mathrm{H\,I})/\mathrm{cm}^{-2} = 15.7 - 18.2$ at 95 percent confidence level. In addition to Lyα, C IV absorption is observed in Complex X as well, which corresponds with the strongest Lyα absorption component in velocity space, with a measured total column density of $\log N_{\mathrm{tot}}\,(\mathrm{C\,IV}) = 13.84 \pm 0.11$. Unfortunately, it is not possible to constrain the Si IV column density, due to contamination from Lyα forest lines at higher redshifts.

Only Lyα absorption is detected in Complex Y (Figure B.2). The range of allowed $N\,(\mathrm{H\,I})$ for this saturated system is $\log N(\mathrm{H\,I})/\mathrm{cm}^{-2} = 16.7 - 17.8$ at 95% confidence level. For the absence of ionic metal absorption, we calculate upper limits on $\log N\,(\mathrm{C\,IV})/\mathrm{cm}^{-2} < 13.2$ and $\log N\,(\mathrm{Si\,IV})/\mathrm{cm}^{-2} < 12.6$ for C IV and Si IV, respectively.

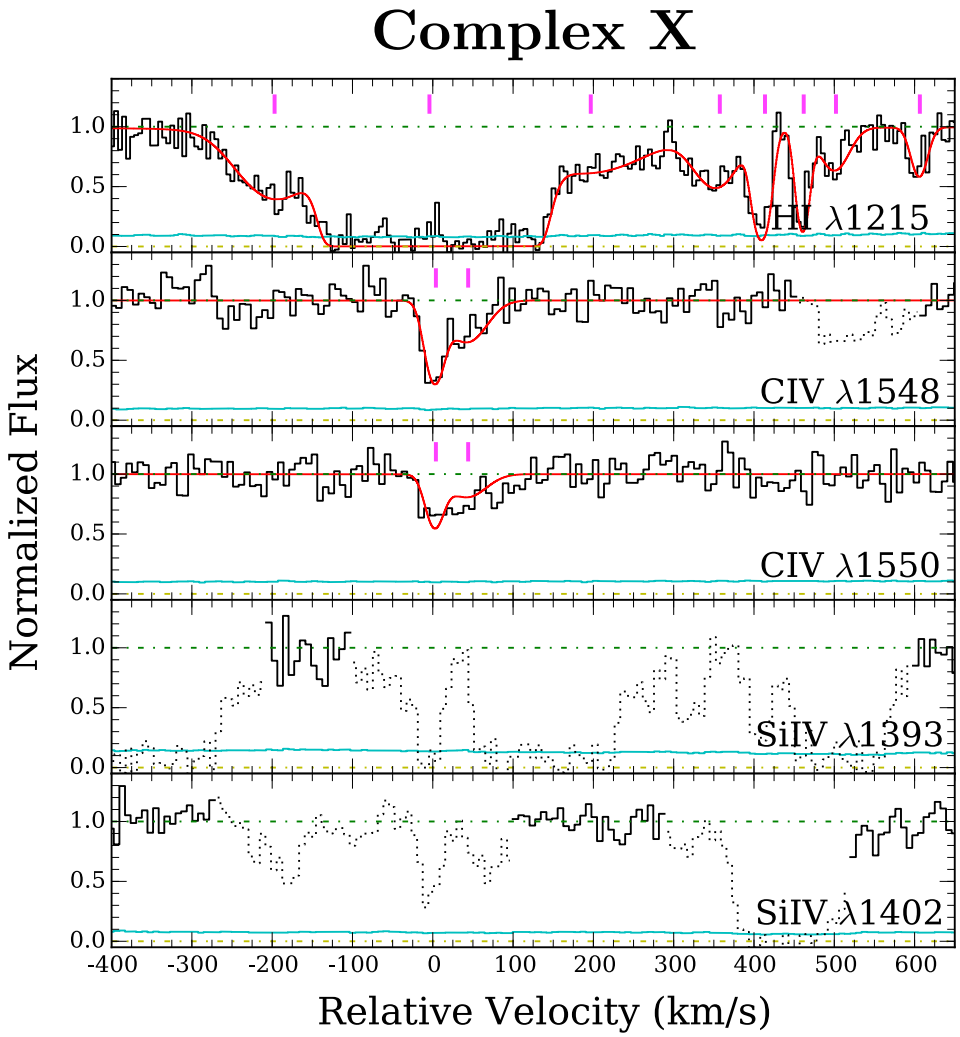

Figure B.1: Continuum-normallized absorption profiles of Complex X at $z = 2.7147$. The absorption spectra and 1σ error array are shown in black and cyan histograms, whereas the best-fitting Voigt profile models are shown in red curves. The magenta tick marks indicate the location of individual components. Contaminating features are dotted out for clarity.

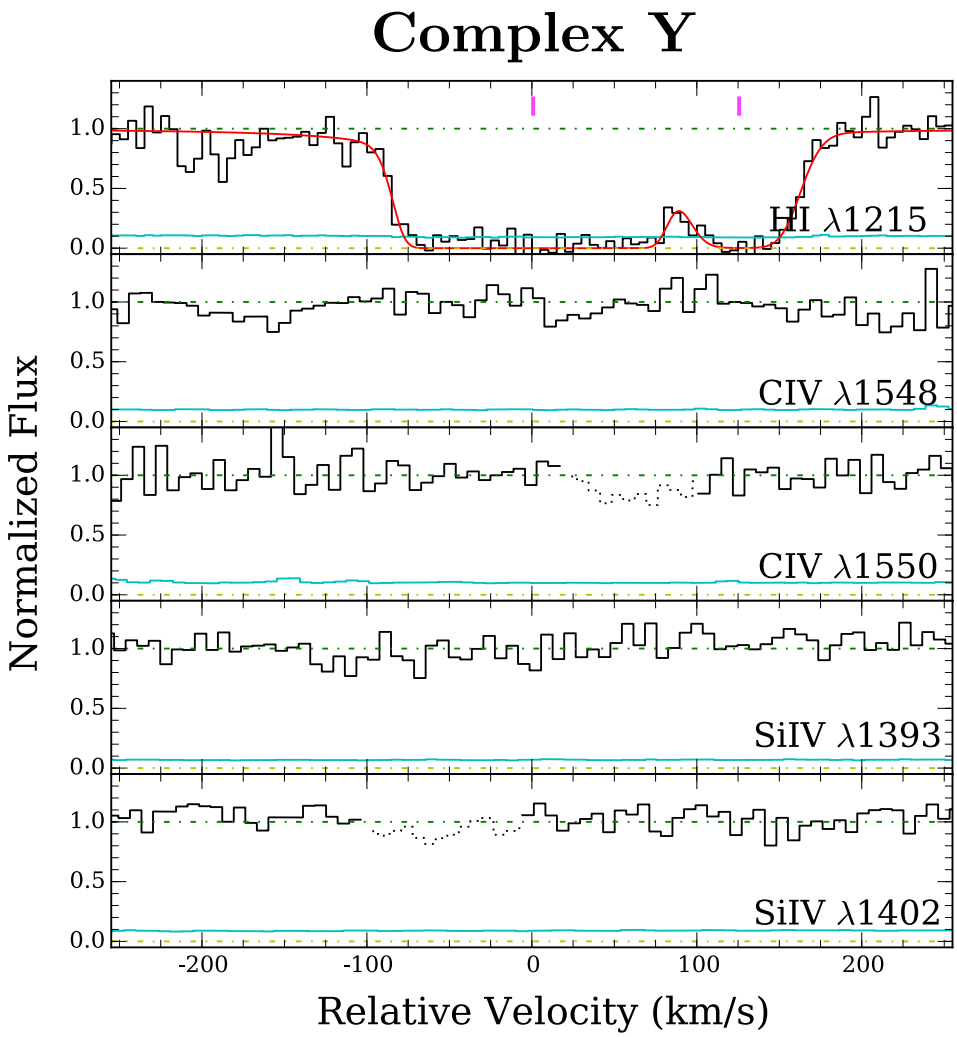

Figure B.2: Continuum-normalized absorption profiles of Complex Y at $z = 2.7863$. The absorption spectra and 1-σ error array are shown in black and cyan histograms, whereas the best-fitting Voigt profile models are shown in red curves. The magenta tick marks indicate the location of individual components. Contaminating features are dotted out for clarity.

Table B.1: Voigt profile fitting results for additional absorption complexes at $z = 2.7 - 2.8$

Species	z_c	$\log N_c/\mathrm{cm}^{-2}$	b_c ($\mathrm{km\,s}^{-1}$)
Complex X at $z = 2.7147$			
H I	2.7122 ± 0.0001	13.82 ± 0.12	57.0 ± 10.7
C IV	...	< 13.0	...
Si IV	...	< 12.7	...
H I	2.71466 ± 0.00003	$17.9^{+0.2}_{-0.3}$	47^{+2}_{-1}
C IV	2.71469 ± 0.00003	13.58 ± 0.14	13.7 ± 3.9
C IV	2.71519 ± 0.00015	13.50 ± 0.18	31.8 ± 13.5
H I	2.71710 ± 0.00037	13.73 ± 0.25	94.3 ± 44.3
C IV	...	< 13.1	...
H I	2.71904 ± 0.00005	13.50 ± 0.09	35.0 ± 8.0
C IV	...	< 12.9	...
H I	2.71974 ± 0.00001	13.71 ± 0.13	11.2 ± 2.0
C IV	...	< 12.7	...
H I	2.72037 ± 0.00002	13.49 ± 0.12	8.3 ± 2.0
C IV	...	< 12.9	...
H I	2.72086 ± 0.00006	13.15 ± 0.11	23.0 ± 7.1
C IV	...	< 13.1	...
H I	2.72217 ± 0.00003	12.99 ± 0.10	12.3 ± 3.8
C IV	...	< 13.0	...
Si IV	...	< 12.4	...
Complex Y at $z = 2.7863$			
H I	2.78630 ± 0.00002	$17.6^{+0.1}_{-0.6}$	27^{+3}_{-1}
C IV	...	< 12.9	...
Si IV	...	< 12.3	...
H I	2.78790 ± 0.00002	14.34 ± 0.15	24.0 ± 3.2
C IV	...	< 12.8	...
Si IV	...	< 12.2	...

REFERENCES

Abgrall, H., Roueff, E., Launay, F., Roncin, J. Y., & Subtil, J. L. 1993, Journal of Molecular Spectroscopy, 157, 512

Adelberger, K. L., Steidel, C. C., Shapley, A. E., et al. 2003, ApJ, 584, 45

Agertz, O., Teyssier, R., & Moore, B. 2009, MNRAS, 397, L64

Alves, D. R., & Nelson, C. A. 2000, ApJ, 542, 789

Asplund, M., Grevesse, N., & Jacques Sauval, A. 2006, Nucl. Phys. A, 777, 1

Asplund, M., Grevesse, N., Sauval, A. J., et al. 2009, ARA&A, 47, 481

Bahcall, J. N., & Salpeter, E. E. 1965, ApJ, 142, 1677

Bahcall, J. N., & Salpeter, E. E. 1966, ApJ, 144, 847

Bahcall, J. N., Sargent, W. L. W., & Schmidt, M. 1967, ApJ, 149, L11

Bahcall, J. N., & Spitzer, L., Jr. 1969, ApJ, 156, L63

Bailly, D., Salumbides, E. J., Vervloet, M., et al. 2010, Mol. Phys., 108, 827

Balogh, M. L., Morris, S. L., Yee, H. K. C., et al. 1999, ApJ, 527, 54

Becker, G. D., Sargent, W. L. W., Rauch, M., et al. 2011, ApJ, 735, 93

Behroozi, P. S., Conroy, C., & Wechsler, R. H. 2010, ApJ, 717, 379

Behroozi, P. S., Wechsler, R. H., & Conroy, C. 2013, ApJ, 770, 57

Benson, A. J., Bower, R. G., Frenk, C. S., et al. 2003, ApJ, 599, 38

Benson, A. J. 2010, Phys. Rep., 495, 33

Bergeron, J. 1986, A&A, 155, L8

Bergeron, J., & Stasińska, G. 1986, A&A, 169, 1

Bernstein, R., Shectman, S. A., Gunnels, S. M., et al. 2003, Proc. SPIE, 1694

Bielby, R. M., Tummuangpak, P., Shanks, T., et al. 2016, MNRAS, 456, 4061

Blanton, M. R., & Roweis, S. 2007, AJ, 133, 734

Boksenberg, A., & Sargent, W. L. W. 1978, ApJ, 220, 42

Boksenberg, A., Danziger, I. J., Fosbury, R. A. E., et al. 1980, ApJ, 242, L145

Booth, C. M., Agertz, O., Kravtsov, A. V., et al. 2013, ApJ, 777, L16

Bordoloi, R., Lilly, S. J., Knobel, C., et al. 2011, ApJ, 743, 10

Bordoloi, R., Tumlinson, J., Werk, J. K., et al. 2014, ApJ, 796, 136

Bordoloi, R., Wagner, A. Y., Heckman, T. M., et al. 2017, ApJ, 848, 122

Borthakur, S., Heckman, T., Strickland, D., et al. 2013, ApJ, 768, 18

Bouché, N., Hohensee, W., Vargas, R., et al. 2012, MNRAS, 426, 801

Bowen, D. V., Blades, J. C., & Pettini, M. 1995, ApJ, 448, 634

Bowen, D. V., & Chelouche, D. 2011, ApJ, 727, 47

Bregman, J. N. 2007, ARA&A, 45, 221

Brocklehurst, M. 1971, MNRAS, 153, 471

Bruzual, G., & Charlot, S. 2003, MNRAS, 344, 1000

Bullock, J. S., & Boylan-Kolchin, M. 2017, ARA&A, 55, 343

Burbidge, E. M., Lynds, C. R., & Burbidge, G. R. 1966, ApJ, 144, 447

Caldwell, N., Rose, J. A., & Concannon, K. D. 2003, AJ, 125, 2891

Carswell, R. F., & Webb, J. K. 2014, VPFIT: Voigt profile fitting program, ascl:1408.015

Cassata, P., Le Fèvre, O., Garilli, B., et al. 2011, A&A, 525, A143

Cecil, G., Bland-Hawthorn, J., Veilleux, S., et al. 2001, ApJ, 555, 338

Cen, R., & Ostriker, J. P. 1999, ApJ, 514, 1

Cen, R., & Ostriker, J. P. 2006, ApJ, 650, 560

Chantry, V., Sluse, D., & Magain, P. 2010, A&A, 522, A95

Chen, H.-W., Lanzetta, K. M., Webb, J. K., et al. 1998, ApJ, 498, 77

Chen, H.-W., Lanzetta, K. M., Webb, J. K., et al. 2001, ApJ, 559, 654

Chen, H.-W., Kennicutt, R. C., & Rauch, M. 2005, ApJ, 620, 703

Chen, H.-W., & Tinker, J. L. 2008, ApJ, 687, 745

Chen, H.-W., & Mulchaey, J. S. 2009, ApJ, 701, 1219

Chen, H.-W., Helsby, J. E., Gauthier, J.-R., et al. 2010, ApJ, 714, 1521

Chen, H.-W., Gauthier, J.-R., Sharon, K., et al. 2014, MNRAS, 438, 1435

Chen, H.-W., Johnson, S. D., Zahedy, F. S., et al. 2017, ApJ, 842, L19

Chen, H.-W. 2017, Outskirts of Galaxies, 291

Chen, H.-W., Zahedy, F. S., Johnson, S. D., et al. 2018, MNRAS, 479, 2547

Chen, H.-W., Johnson, S. D., Straka, L. A., et al. 2019, MNRAS, 484, 431

Chen, S.-F. S., Simcoe, R. A., Torrey, P., et al. 2017, ApJ, 850, 188

Churchill, C. W., Steidel, C. C., & Vogt, S. S. 1996, ApJ, 471, 164

Churchill, C. W., Mellon, R. R., Charlton, J. C., et al. 2000, ApJS, 130, 91

Churchill, C. W., & Vogt, S. S. 2001, AJ, 122, 679

Churchill, C. W., Vogt, S. S., & Charlton, J. C. 2003, AJ, 125, 98

Churchill, C. W., Kacprzak, G. G., Steidel, C. C., et al. 2012, ApJ, 760, 68

Ciotti, L., & Bertin, G. 1999, A&A, 352, 447

Cole, S. 1991, ApJ, 367, 45

Cole, S., Lacey, C. G., Baugh, C. M., & Frenk, C. S. 2000, MNRAS, 319, 168

Conroy, C., van Dokkum, P. G., & Kravtsov, A. 2015, ApJ, 803, 77

Cooper, T. J., Simcoe, R. A., Cooksey, K. L., et al. 2019, arXiv e-prints, arXiv:1901.05980

Cooper, T. J., Simcoe, R. A., Cooksey, K. L., et al. 2015, ApJ, 812, 58

Crighton, N. H. M., Hennawi, J. F., & Prochaska, J. X. 2013, ApJ, 776, L18

Crighton, N. H. M., Hennawi, J. F., Simcoe, R. A., et al. 2015, MNRAS, 446, 18

D'Odorico, S., Cristiani, S., Dekker, H., et al. 2000, Proc. SPIE, 121

Davé, R., Cen, R., Ostriker, J. P., et al. 2001, ApJ, 552, 473

Davis, T. A., Greene, J., Ma, C.-P., et al. 2016, MNRAS, 455, 214

Davis, T. A., Greene, J. E., Ma, C.-P., et al. 2019, MNRAS, 486, 1404

Dawson, K. S., Schlegel, D. J., Ahn, C. P., et al. 2013, AJ, 145, 10

De Cia, A., Ledoux, C., Mattsson, L., et al. 2016, A&A, 596, A97

de Jong, R. S., Simard, L., Davies, R. L., et al. 2004, MNRAS, 355, 1155

de Plaa, J., Werner, N., Bleeker, J. A. M., et al. 2007, A&A, 465, 345

Dekel, A., & Silk, J. 1986, ApJ, 303, 39

Dekel, A., Sari, R., & Ceverino, D. 2009, ApJ, 703, 785

Dessauges-Zavadsky, M., Calura, F., Prochaska, J. X., et al. 2004, A&A, 416, 79

Dessauges-Zavadsky, M., Prochaska, J. X., D'Odorico, S., et al. 2006, A&A, 445, 93

Dessauges-Zavadsky, M., D'Odorico, S., Schaerer, D., et al. 2010, A&A, 510, A26

Draine, B. T., & Salpeter, E. E. 1979, ApJ, 231, 438

Drake, A. B., Guiderdoni, B., Blaizot, J., et al. 2017, MNRAS, 471, 267

Dutton, A. A., & Macciò, A. V. 2014, MNRAS, 441, 3359

Edgar, R. J., & Chevalier, R. A. 1986, ApJ, 310, L27

Efstathiou, G. 1992, MNRAS, 256, 43P

Eigenbrod, A., Courbin, F., Meylan, G., et al. 2006, A&A, 451, 759

Einasto, J. 1965, Trudy Astrofizicheskogo Instituta Alma-Ata, 5, 87

Eisenstein, D. J., Hogg, D. W., Fukugita, M., et al. 2003, ApJ, 585, 694

Ellingson, E., Green, R. F., & Yee, H. K. C. 1991, ApJ, 378, 476

Erb, D. K., Steidel, C. C., Trainor, R. F., et al. 2014, ApJ, 795, 33

Faber, S. M., Willmer, C. N. A., Wolf, C., et al. 2007, ApJ, 665, 265

Fang, J. J., Faber, S. M., Koo, D. C., et al. 2013, ApJ, 776, 63

Faucher-Giguère, C.-A., Lidz, A., Hernquist, L., et al. 2008, ApJ, 688, 85

Faucher-Giguère, C.-A., & Kereš, D. 2011, MNRAS, 412, L118

Faucher-Giguère, C.-A., Hopkins, P. F., Kereš, D., et al. 2015, MNRAS, 449, 987

Faucher-Giguère, C.-A. 2017, Gas Accretion onto Galaxies, 271

Ferland, G. J., Porter, R. L., van Hoof, P. A. M., et al. 2013, Rev. Mexicana Astron. Astrofis., 49, 137

Ferrarese, L., & Merritt, D. 2000, ApJ, 539, L9

Ferreras, I., & Silk, J. 2002, MNRAS, 336, 1181

Ferreras, I., Lisker, T., Pasquali, A., et al. 2009, MNRAS, 396, 1573

Foreman-Mackey, D., Hogg, D. W., Lang, D., et al. 2013, PASP, 125, 306

Fox, A., Richter, P., & Fechner, C. 2014, A&A, 572, A102

Franx, M., van Dokkum, P. G., Förster Schreiber, N. M., et al. 2008, ApJ, 688, 770

Fukugita, M., Hogan, C. J., & Peebles, P. J. E. 1998, ApJ, 503, 518

Fukugita M., 2004, IAUS, 227, IAUS..220

Fukugita, M., & Peebles, P. J. E. 2004, ApJ, 616, 643

Fumagalli, M., Prochaska, J. X., Kasen, D., et al. 2011, MNRAS, 418, 1796

Fumagalli, M., O'Meara, J. M., & Prochaska, J. X. 2016, MNRAS, 455, 4100

Fumagalli, M., Cantalupo, S., Dekel, A., et al. 2016, MNRAS, 462, 1978

Förster, F., & Schawinski, K. 2008, MNRAS, 388, L74

Gao, L., Navarro, J. F., Cole, S., et al. 2008, MNRAS, 387, 536

Gauthier, J.-R., Chen, H.-W., & Tinker, J. L. 2009, ApJ, 702, 50

Gauthier, J.-R., Chen, H.-W., & Tinker, J. L. 2010, ApJ, 716, 1263

Gauthier, J.-R., & Chen, H.-W. 2011, MNRAS, 418, 2730

Gauthier, J.-R., & Chen, H.-W. 2012, MNRAS, 424, 1952

Gauthier, J.-R. 2013, MNRAS, 432, 1444

Gebhardt, K., Bender, R., Bower, G., et al. 2000, ApJ, 539, L13

Gehrels, N. 1986, ApJ, 303, 336

Gnat, O., & Sternberg, A. 2007, ApJS, 168, 213

Goerdt, T., Dekel, A., Sternberg, A., et al. 2010, MNRAS, 407, 613

Green, J. C., Froning, C. S., Osterman, S., et al. 2012, ApJ, 744, 60

Greenstein, J. L., & Schmidt, M. 1967, ApJ, 148, L13

Grossi, M., di Serego Alighieri, S., Giovanardi, C., et al. 2009, A&A, 498, 407

Guillemin, P., & Bergeron, J. 1997, A&A, 328, 499

Guo, Q., White, S., Li, C., et al. 2010, MNRAS, 404, 1111

Haardt, F., & Madau, P. 2001, Clusters of Galaxies and the High Redshift Universe Observed in X-rays, 64

Haardt, F., & Madau, P. 2012, ApJ, 746, 125

Haehnelt, M. G., Steinmetz, M., & Rauch, M. 1996, ApJ, 465, L95

Hafen, Z., Faucher-Giguère, C.-A., Anglés-Alcázar, D., et al. 2017, MNRAS, 469, 2292

Hashimoto, T., Ouchi, M., Shimasaku, K., et al. 2013, ApJ, 765, 70

Hashimoto, T., Verhamme, A., Ouchi, M., et al. 2015, ApJ, 812, 157

Hayashi, E., & White, S. D. M. 2008, MNRAS, 388, 2

Heckman, T. M., Norman, C. A., Strickland, D. K., et al. 2002, ApJ, 577, 691

Heinemann, T., & Papaloizou, J. C. B. 2009, MNRAS, 397, 64

Hodge, J. A., Zeimann, G. R., Becker, R. H., et al. 2009, AJ, 138, 900

Huang, Y.-H., Chen, H.-W., Johnson, S. D., et al. 2016, MNRAS, 455, 1713

Hubble, E. P. 1926, ApJ, 64, 321

Hubble, E. P. 1929, ApJ, 69, 103

Humphrey, P. J., & Buote, D. A. 2006, ApJ, 639, 136

Iwamoto, K., Brachwitz, F., Nomoto, K., et al. 1999, ApJS, 125, 439

Johansson, P. H., Naab, T., & Ostriker, J. P. 2009, ApJ, 697, L38

Johnson, S. D., Chen, H.-W., Mulchaey, J. S., et al. 2014, MNRAS, 438, 3039

Johnson, S. D., Chen, H.-W., & Mulchaey, J. S. 2015, MNRAS, 449, 3263

Johnson, S. D., Chen, H.-W., Mulchaey, J. S., et al. 2017, ApJ, 850, L10

Jones, T., Stark, D. P., & Ellis, R. S. 2018, ApJ, 863, 191

Kacprzak, G. G., Churchill, C. W., Ceverino, D., et al. 2010, ApJ, 711, 533

Kacprzak, G. G., Churchill, C. W., Evans, J. L., et al. 2011, MNRAS, 416, 3118

Kacprzak, G. G., Churchill, C. W., & Nielsen, N. M. 2012, ApJ, 760, L7

Kauffmann, G., Heckman, T. M., White, S. D. M., et al. 2003, MNRAS, 341, 33

Kauffmann, G., Heckman, T. M., White, S. D. M., et al. 2003, MNRAS, 341, 54

Kauffmann, G., Heckman, T. M., De Lucia, G., et al. 2006, MNRAS, 367, 1394

Kawata, D., & Rauch, M. 2007, ApJ, 663, 38

Kawata, D., & Mulchaey, J. S. 2008, ApJ, 672, L103

Keeton, C. R., Kochanek, C. S., & Falco, E. E. 1998, ApJ, 509, 561

Kennicutt, R. C., & Evans, N. J. 2012, ARA&A, 50, 531

Kereš, D., Katz, N., Weinberg, D. H., et al. 2005, MNRAS, 363, 2

Kereš, D., Katz, N., Fardal, M., et al. 2009, MNRAS, 395, 160

Kewley, L. J., Dopita, M. A., Sutherland, R. S., et al. 2001, ApJ, 556, 121

Kewley, L. J., Geller, M. J., & Jansen, R. A. 2004, AJ, 127, 2002

Khaire, V., & Srianand, R. 2015, MNRAS, 451, L30

Kochanek, C. S., Morgan, N. D., Falco, E. E., et al. 2006, ApJ, 640, 47

Kollmeier, J. A., Weinberg, D. H., Oppenheimer, B. D., et al. 2014, ApJ, 789, L32

Konno, A., Ouchi, M., Nakajima, K., et al. 2016, ApJ, 823, 20

Kravtsov, A. V., Vikhlinin, A. A., & Meshcheryakov, A. V. 2018, Astronomy Letters, 44, 8

Krist, J. 1995, Astronomical Data Analysis Software and Systems IV, 349

Kuntschner, H., Emsellem, E., Bacon, R., et al. 2010, MNRAS, 408, 97

Lan, T.-W., & Mo, H. 2018, ApJ, 866, 36

Lanzetta, K. M., & Bowen, D. V. 1992, ApJ, 391, 48

Lanzetta, K. M., Bowen, D. V., Tytler, D., et al. 1995, ApJ, 442, 538

Larson, R. B., Tinsley, B. M., & Caldwell, C. N. 1980, ApJ, 237, 692

Lauroesch, J. T., Truran, J. W., Welty, D. E., et al. 1996, PASP, 108, 641

Lehner, N., Savage, B. D., Richter, P., et al. 2007, ApJ, 658, 680

Lehner, N., Howk, J. C., Tripp, T. M., et al. 2013, ApJ, 770, 138

Lehner, N., O'Meara, J. M., Fox, A. J., et al. 2014, ApJ, 788, 119

Lehner, N., O'Meara, J. M., Howk, J. C., et al. 2016, ApJ, 833, 283

Leitherer, C., Schaerer, D., Goldader, J. D., et al. 1999, ApJS, 123, 3

Li, Y.-P., Yuan, F., Mo, H., et al. 2018, ApJ, 866, 70

Liang, C. J., & Chen, H.-W. 2014, MNRAS, 445, 2061

Liang, C. J., Kravtsov, A. V., & Agertz, O. 2016, MNRAS, 458, 1164

Liang, C. J., & Remming, I. S. 2018, arXiv e-prints, arXiv:1806.10688

Lidman, C., Courbin, F., Kneib, J.-P., et al. 2000, A&A, 364, L62

Loewenstein, M., & Davis, D. S. 2010, ApJ, 716, 384

Loewenstein, M., & Davis, D. S. 2012, ApJ, 757, 121

Lopez, S., Ellison, S., D'Odorico, S., et al. 2007, A&A, 469, 61

Lovegrove, E., & Simcoe, R. A. 2011, ApJ, 740, 30

Lundgren, B. F., Brunner, R. J., York, D. G., et al. 2009, ApJ, 698, 819

Maller, A. H., & Bullock, J. S. 2004, MNRAS, 355, 694

Mandelbaum, R., Seljak, U., & Hirata, C. M. 2008, J. Cosmology Astropart. Phys., 2008, 006

Mannucci, F., Della Valle, M., Panagia, N., et al. 2005, A&A, 433, 807

Maoz, D., Mannucci, F., & Nelemans, G. 2014, ARA&A, 52, 107

Marchesini, D., van Dokkum, P. G., Förster Schreiber, N. M., et al. 2009, ApJ, 701, 1765

Mathews, W. G., & Brighenti, F. 2003, ARA&A, 41, 191

McCourt, M., Sharma, P., Quataert, E., et al. 2012, MNRAS, 419, 3319

McCourt, M., Oh, S. P., O'Leary, R., et al. 2018, MNRAS, 473, 5407

McKee, C. F., Hollenbach, D. J., Seab, G. C., et al. 1987, ApJ, 318, 674

McNamara, B. R., & Nulsen, P. E. J. 2007, ARA&A, 45, 117

McQuinn, M. 2016, ARA&A, 54, 313

McQuinn, M., & Werk, J. K. 2018, ApJ, 852, 33

McWilliam, A. 1997, ARA&A, 35, 503

Mernier, F., de Plaa, J., Kaastra, J. S., et al. 2017, A&A, 603, A80

Mo, H. J., & Miralda-Escude, J. 1996, ApJ, 469, 589

Morgan, N. D., Kochanek, C. S., Pevunova, O., et al. 2005, AJ, 129, 2531

Moster, B. P., Somerville, R. S., Maulbetsch, C., et al. 2010, ApJ, 710, 903

Münch, G., & Zirin, H. 1961, ApJ, 133, 11

Murga, M., Zhu, G., Ménard, B., et al. 2015, MNRAS, 452, 511

Murray, N., Ménard, B., & Thompson, T. A. 2011, ApJ, 735, 66

Muzahid, S., Fonseca, G., Roberts, A., et al. 2018, MNRAS, 476, 4965

Muzahid, S., Kacprzak, G. G., Churchill, C. W., et al. 2015, ApJ, 811, 132

Nagino, R., & Matsushita, K. 2010, PASJ, 62, 787

Narayanan, A., Charlton, J. C., Misawa, T., et al. 2008, ApJ, 689, 782

Navarro, J. F., & Benz, W. 1991, ApJ, 380, 320

Navarro, J. F., & White, S. D. M. 1994, MNRAS, 267, 401

Navarro, J. F., Frenk, C. S., & White, S. D. M. 1995, MNRAS, 275, 56

Navarro, J. F., Frenk, C. S., & White, S. D. M. 1997, ApJ, 490, 493

Navarro, J. F., & Steinmetz, M. 1997, ApJ, 478, 13

Nelson, D., Vogelsberger, M., Genel, S., et al. 2013, MNRAS, 429, 3353

Nelson, D., Kauffmann, G., Pillepich, A., et al. 2018, MNRAS, 477, 450

Nestor, D. B., Johnson, B. D., Wild, V., et al. 2011, MNRAS, 412, 1559

Nielsen, N. M., Churchill, C. W., & Kacprzak, G. G. 2013, ApJ, 776, 115

Nomoto, K., Tominaga, N., Umeda, H., et al. 2006, Nucl. Phys. A, 777, 424

O'Sullivan, E., Forbes, D. A., & Ponman, T. J. 2001, MNRAS, 328, 461

Ofek, E. O., Maoz, D., Rix, H.-W., et al. 2006, ApJ, 641, 70

Oke, J. B. 1963, Nature, 197, 1040

Oke, J. B., Cohen, J. G., Carr, M., et al. 1995, PASP, 107, 375

Oosterloo, T. A., Morganti, R., Sadler, E. M., et al. 2007, A&A, 465, 787

Oosterloo, T., Morganti, R., Crocker, A., et al. 2010, MNRAS, 409, 500

Oppenheimer, B. D., & Schaye, J. 2013, MNRAS, 434, 1063

Oppenheimer, B. D., Crain, R. A., Schaye, J., et al. 2016, MNRAS, 460, 2157

Oppenheimer, B. D., Schaye, J., Crain, R. A., et al. 2018, MNRAS, 481, 835

Osterbrock, D. E., & Ferland, G. J. 2006, Astrophysics of gaseous nebulae and active galactic nuclei

Peeples, M. S., Werk, J. K., Tumlinson, J., et al. 2014, ApJ, 786, 54

Penton, S. V., Stocke, J. T., & Shull, J. M. 2004, ApJS, 152, 29

Persic M., Salucci P., 1992, MNRAS, 258, 14P

Persson, S. E., Barkhouser, R., Birk, C., et al. 2008, Proc. SPIE, 70142V

Petitjean, P., Ledoux, C., & Srianand, R. 2008, A&A, 480, 349

Pettini, M., Rix, S. A., Steidel, C. C., et al. 2002, ApJ, 569, 742

Planck Collaboration, Ade, P. A. R., Aghanim, N., et al. 2016, A&A, 594, A13

Porciani, C., & Madau, P. 2005, ApJ, 625, L43

Prescott, M., Baldry, I. K., James, P. A., et al. 2011, MNRAS, 417, 1374

Prochaska, J. X., Weiner, B., Chen, H.-W., et al. 2011, ApJ, 740, 91

Prochaska, J. X., Werk, J. K., Worseck, G., et al. 2017, ApJ, 837, 169

Prochaska, J. X., & Wolfe, A. M. 1997, ApJ, 487, 73

Putman, M. E., Peek, J. E. G., & Joung, M. R. 2012, ARA&A, 50, 491

Rafelski, M., Wolfe, A. M., Prochaska, J. X., et al. 2012, ApJ, 755, 89

Rao, S. M., Turnshek, D. A., & Nestor, D. B. 2006, ApJ, 636, 610

Rauch, M., Haehnelt, M. G., & Steinmetz, M. 1997, ApJ, 481, 601

Rauch, M., Miralda-Escudé, J., Sargent, W. L. W., et al. 1997, ApJ, 489, 7

Rauch, M. 1998, ARA&A, 36, 267

Rauch, M., Sargent, W. L. W., & Barlow, T. A. 1999, ApJ, 515, 500

Rauch, M., Sargent, W. L. W., & Barlow, T. A. 2001, ApJ, 554, 823

Rauch, M., Sargent, W. L. W., Barlow, T. A., et al. 2001, ApJ, 562, 76

Rauch, M., Sargent, W. L. W., Barlow, T. A., et al. 2002, ApJ, 576, 45

Rauch, M., Haehnelt, M., Bunker, A., et al. 2008, ApJ, 681, 856

Rauch, M., Becker, G. D., Haehnelt, M. G., et al. 2011, MNRAS, 418, 1115

Rauch, M., Becker, G. D., & Haehnelt, M. G. 2016, MNRAS, 455, 3991

Reddy, N. A., Steidel, C. C., Pettini, M., et al. 2008, ApJS, 175, 48

Reddy, N. A., Pettini, M., Steidel, C. C., et al. 2012, ApJ, 754, 25

Rees, M. J., & Sciama, D. W. 1966, ApJ, 145, 6

Rees, M. J., & Ostriker, J. P. 1977, MNRAS, 179, 541

Ribaudo, J., Lehner, N., Howk, J. C., et al. 2011, ApJ, 743, 207

Richter, P. 2006, Reviews in Modern Astronomy, 19, 31

Rigby, J. R., Charlton, J. C., & Churchill, C. W. 2002, ApJ, 565, 743

Rosdahl, J., & Blaizot, J. 2012, MNRAS, 423, 344

Roseboom, I. G., Pimbblet, K. A., Drinkwater, M. J., et al. 2006, MNRAS, 373, 349

Rosenwasser, B., Muzahid, S., Charlton, J. C., et al. 2018, MNRAS, 476, 2258

Rudie, G. C., Steidel, C. C., Trainor, R. F., et al. 2012, ApJ, 750, 67

Rudie, G. C., Steidel, C. C., Shapley, A. E., et al. 2013, ApJ, 769, 146

Rudie, G. C., Steidel, C. C., Pettini, M., et al. 2019, arXiv e-prints, arXiv:1903.00004

Rutkowski, M. J., Cohen, S. H., Kaviraj, S., et al. 2012, ApJS, 199, 4

Ryan-Weber, E. V., Pettini, M., Madau, P., et al. 2009, MNRAS, 395, 1476

Sadler, E. M., Cannon, R. D., Mauch, T., et al. 2007, MNRAS, 381, 211

Sahu, N., Graham, A. W., & Davis, B. L. 2019, ApJ, 876, 155

Sanders, R. L., Shapley, A. E., Kriek, M., et al. 2015, ApJ, 799, 138

Savage, B. D., Narayanan, A., Wakker, B. P., et al. 2010, ApJ, 719, 1526

Savage, B. D., & Sembach, K. R. 1996, ARA&A, 34, 279

Scannapieco, C., Tissera, P. B., White, S. D. M., et al. 2005, MNRAS, 364, 552

Schaye, J., Aguirre, A., Kim, T.-S., et al. 2003, ApJ, 596, 768

Schmidt, M. 1959, ApJ, 129, 243

Schmidt, M. 1963, Nature, 197, 1040

Serra, P., Oosterloo, T., Morganti, R., et al. 2012, MNRAS, 422, 1835

Seyffert, E. N., Cooksey, K. L., Simcoe, R. A., et al. 2013, ApJ, 779, 161

Sharma, P., McCourt, M., Quataert, E., et al. 2012, MNRAS, 420, 3174

Shen, S., Madau, P., Guedes, J., et al. 2013, ApJ, 765, 89

Shibuya, T., Ouchi, M., Nakajima, K., et al. 2014, ApJ, 788, 74

Shull, J. M., Smith, B. D., & Danforth, C. W. 2012, ApJ, 759, 23

Shull, J. M., Moloney, J., Danforth, C. W., et al. 2015, ApJ, 811, 3

Silk, J., & Rees, M. J. 1998, A&A, 331, L1

Silk, J. 2011, Tracing the Ancestry of Galaxies, 273

Simcoe, R. A., Sargent, W. L. W., & Rauch, M. 2004, ApJ, 606, 92

Simcoe, R. A., Sargent, W. L. W., Rauch, M., et al. 2006, ApJ, 637, 648

Simcoe, R. A., Cooksey, K. L., Matejek, M., et al. 2011, ApJ, 743, 21

Singh, P., Majumdar, S., Nath, B. B., et al. 2018, MNRAS, 478, 2909

Skrutskie, M. F., Cutri, R. M., Stiening, R., et al. 2006, AJ, 131, 1163

Smette, A., Robertson, J. G., Shaver, P. A., et al. 1995, A&AS, 113, 199

Som, D., Kulkarni, V. P., Meiring, J., et al. 2015, ApJ, 806, 25

Songaila, A. 2001, ApJ, 561, L153

Spitzer, L. 1956, ApJ, 124, 20

Stalder, B., Stark, A. A., Amato, S. M., et al. 2014, Proc. SPIE, 91473Y

Steidel, C. C., Dickinson, M., Meyer, D. M., et al. 1997, ApJ, 480, 568

Steidel, C. C., Kollmeier, J. A., Shapley, A. E., et al. 2002, ApJ, 570, 526

Steidel, C. C., Erb, D. K., Shapley, A. E., et al. 2010, ApJ, 717, 289

Steidel, C. C., Rudie, G. C., Strom, A. L., et al. 2014, ApJ, 795, 165

Stern, J., Hennawi, J. F., Prochaska, J. X., et al. 2016, ApJ, 830, 87

Stern, J., Faucher-Giguère, C.-A., Hennawi, J. F., et al. 2018, ApJ, 865, 91

Strom, A. L., Steidel, C. C., Rudie, G. C., et al. 2018, ApJ, 868, 117

Suchkov, A. A., Berman, V. G., Heckman, T. M., et al. 1996, ApJ, 463, 528

Tempel, E., Stoica, R. S., & Saar, E. 2013, MNRAS, 428, 1827

Thielemann, F.-K., Nomoto, K., & Yokoi, K. 1986, A&A, 158, 17

Thom, C., Tumlinson, J., Werk, J. K., et al. 2012, ApJ, 758, L41

Tojeiro, R., Percival, W. J., Heavens, A. F., et al. 2011, MNRAS, 413, 434

Trainor, R. F., Steidel, C. C., Strom, A. L., et al. 2015, ApJ, 809, 89

Trainor, R. F., Strom, A. L., Steidel, C. C., et al. 2016, ApJ, 832, 171

Tripp, T. M., Lu, L., & Savage, B. D. 1998, ApJ, 508, 200

Tripp, T. M., Sembach, K. R., Bowen, D. V., et al. 2008, ApJS, 177, 39

Tsujimoto, T., Nomoto, K., Yoshii, Y., et al. 1995, MNRAS, 277, 945

Tumlinson, J., Thom, C., Werk, J. K., et al. 2011, Science, 334, 948

Tumlinson, J., Thom, C., Werk, J. K., et al. 2013, ApJ, 777, 59

Tumlinson, J., Peeples, M. S., & Werk, J. K. 2017, ARA&A, 55, 389

Turner, M. L., Schaye, J., Crain, R. A., et al. 2017, MNRAS, 471, 690

Ubachs, W., Buning, R., Eikema, K. S. E., & Reinhold, E. 2007, Journal of Molecular Spectroscopy, 241, 155

van de Voort, F., Schaye, J., Altay, G., et al. 2012, MNRAS, 421, 2809

Verhamme, A., Schaerer, D., & Maselli, A. 2006, A&A, 460, 397

Verheijen, M., van Gorkom, J. H., Szomoru, A., et al. 2007, ApJ, 668, L9

Viel, M., Haehnelt, M. G., Bolton, J. S., et al. 2017, MNRAS, 467, L86

Vladilo, G., Abate, C., Yin, J., et al. 2011, A&A, 530, A33

Vogt, S. S., Allen, S. L., Bigelow, B. C., et al. 1994, Proc. SPIE, 362

Voit, G. M., Donahue, M., Bryan, G. L., et al. 2015, Nature, 519, 203

Voit, G. M., & Donahue, M. 2015, ApJ, 799, L1

Wakker, B. P., & Mathis, J. S. 2000, ApJ, 544, L107

Wang, B. 1993, ApJ, 415, 174

Weinberg, D. H., Miralda-Escudé, J., Hernquist, L., & Katz, N. 1997, ApJ, 490, 564

Werk, J. K., Prochaska, J. X., Thom, C., et al. 2013, ApJS, 204, 17

Werk, J. K., Prochaska, J. X., Tumlinson, J., et al. 2014, ApJ, 792, 8

Werk, J. K., Prochaska, J. X., Cantalupo, S., et al. 2016, ApJ, 833, 54

Whitaker, K. E., Bezanson, R., van Dokkum, P. G., et al. 2017, ApJ, 838, 19

White, S. D. M., & Rees, M. J. 1978, MNRAS, 183, 341

Wiersma, R. P. C., Schaye, J., Dalla Vecchia, C., et al. 2010, MNRAS, 409, 132

Wild, V., Kauffmann, G., White, S., et al. 2008, MNRAS, 388, 227

Wisotzki, L., Christlieb, N., Bade, N., et al. 2000, A&A, 358, 77

Wilson, M. L., Zabludoff, A. I., Ammons, S. M., et al. 2016, ApJ, 833, 194

Wisotzki, L., Schechter, P. L., Bradt, H. V., et al. 2002, A&A, 395, 17

Wisotzki, L., Schechter, P. L., Chen, H.-W., et al. 2004, A&A, 419, L31

Wolfe, A. M., Gawiser, E., & Prochaska, J. X. 2005, ARA&A, 43, 861

Wotta, C. B., Lehner, N., Howk, J. C., et al. 2016, ApJ, 831, 95

York, D. G. 1999, ApJ, 525C, 752

York, D. G., Adelman, J., Anderson, J. E., et al. 2000, AJ, 120, 1579

Young, L. M., Bureau, M., Davis, T. A., et al. 2011, MNRAS, 414, 940

Young, L. M., Scott, N., Serra, P., et al. 2014, MNRAS, 444, 3408

Young, L. M., Serra, P., Krajnović, D., et al. 2018, MNRAS, 477, 2741

Zahedy, F. S., Chen, H.-W., Rauch, M., et al. 2016, MNRAS, 458, 2423

Zahedy, F. S., Chen, H.-W., Rauch, M., et al. 2017, ApJ, 846, L29

Zahedy, F. S., Chen, H.-W., Gauthier, J.-R., et al. 2017, MNRAS, 466, 1071

Zahedy, F. S., Chen, H.-W., Johnson, S. D., et al. 2019, MNRAS, 484, 2257

Zahedy, F. S., Rauch, M., Chen, H.-W., et al. 2019, MNRAS, 486, 1392

Zhu, G., & Ménard, B. 2013, ApJ, 770, 130

Zhu, G., Ménard, B., Bizyaev, D., et al. 2014, MNRAS, 439, 3139

Zych, B. J., Murphy, M. T., Hewett, P. C., et al. 2009, MNRAS, 392, 1429